

# Mechanical properties of tailored nanostructured alloys produced by electrodeposition

THÈSE N° 7424 (2017)

PRÉSENTÉE LE 17 MARS 2017

À LA FACULTÉ DES SCIENCES ET TECHNIQUES DE L'INGÉNIEUR  
GROUPE SCI STI SM  
PROGRAMME DOCTORAL EN SCIENCE ET GÉNIE DES MATÉRIAUX

ÉCOLE POLYTECHNIQUE FÉDÉRALE DE LAUSANNE

POUR L'OBTENTION DU GRADE DE DOCTEUR ÈS SCIENCES

PAR

Juri Aljoscha WEHRS

acceptée sur proposition du jury:

Prof. P. Murali, président du jury  
Dr S. Mischler, Dr J. Michler, directeurs de thèse  
Prof. C. Motz, rapporteur  
Prof. K. Durst, rapporteur  
Prof. R. Logé, rapporteur



ÉCOLE POLYTECHNIQUE  
FÉDÉRALE DE LAUSANNE

Suisse  
2017



---

*„To see a World in a Grain of Sand  
And a Heaven in a Wild Flower  
Hold Infinity in the palm of your hand  
And Eternity in an hour“...*

— William Blake (1803), *Auguries of Innocence*



---

# Abstract

The studies presented in this thesis aim to extend the current knowledge and understanding of the mechanical behavior of nanocrystalline materials with respect to temperature- and time dependence. Free standing electrodeposited nanocrystalline nickel specimen with mean grain sizes in the order of  $\sim 40nm$  are synthesized and investigated. A miniaturized in situ test rig is developed, capable of performing uniaxial tensile tests on dedicated miniaturized specimen. A novel displacement controlled in situ high temperature indentation system is presented, capable of performing sharp tip indentation and uniaxial micropillar compression experiments up to  $600^{\circ}C$ .

Elevated temperature micropillar strain rate jump tests are performed to extract the strain rate sensitivity factor, apparent activation volume and activation energy. The results suggest grain boundary diffusion to be the rate controlling deformation mechanism. Post deformation imaging also indicates the activity of dislocation based mechanisms. To compare the results to established techniques, micro specimen are tested under three different load cases: uniaxial tension, uniaxial compression and hydrostatic pressure. The results compare well to the previous, suggesting the rate controlling mechanism to be the same for all three load cases. A transient load relaxation tests is developed to assess time dependent plasticity on short and intermediate time scales. The results suggest grain boundary mediated processes to be rate controlling.

To enhance the identification of specific deformation mechanisms, elevated temperature micropillar strain rate jump- and load relaxation tests are also conducted on an inert gas condensated nanocrystalline palladium-gold model alloy. Distinct features of this material are extremely high chemical purity and small, homogeneous grain sizes in the order of  $\sim 10nm$ . Shear transformation mediated plasticity is observed, similar to the deformation of metallic glasses.

The demonstrated methods are relevant for the Swiss watch industry. A series of mechanical tests on standard watch materials are compared. An approach for the electrodeposition of a nickel-tungsten alloy for watch applications with improved thermal stability and less pronounced time dependent plastic behavior is presented.

## Keywords

---

**Keywords:** *nanocrystalline, electrodeposits, thin films, small scale, micromechanical transient tests, micropillar compression, elevated temperature, mechanical properties, deformation mechanisms, activation parameters, watch manufacturing*

---

# Zusammenfassung

Im Rahmen dieser Dissertation wird das mechanische Verhalten nanokristalliner Metalle in Bezug auf Temperatur- und Zeitabhängigkeit untersucht. Hierzu werden galvanisch hergestellte, freistehende nanokristalline Nickel-Proben mit Korngrößen im Bereich von ungefähr  $40\text{nm}$  anhand verschiedener Verfahren geprüft. Zuerst wird ein miniaturisierter Zug-Prüfstand entwickelt, mit welchem es möglich ist Zugversuche an speziellen miniaturisierten Zugproben durchzuführen. Des Weiteren wird ein neuartiges Hochtemperatur-Indentationssystem präsentiert mit dem Mikrosäulenkompressionsversuche bis zu einer Temperatur von  $600^\circ\text{C}$  gefahren werden können.

Ferner werden Dehnraten-Sprung-Versuche bei erhöhten Temperaturen durchgeführt, um den Dehnratenempfindlichkeitsindex, das aktivierte Volumen und die Aktivierungsenergie zu bestimmen. Die Ergebnisse weisen auf Diffusion entlang der Korngrenzen als dominanten Verformungsmechanismus hin. Eine nachgestellte Analyse der Probenoberfläche zeigt Spuren versetzungsbasierter Verformungsmechanismen. Zur Abschätzung der Vergleichbarkeit unterschiedlicher Lastfälle werden identische Versuchsprotokolle auf demselben Material unter einachsigen Zug, einachsigen Druck sowie triaxialem Druck angewandt. Die Ergebnisse im Bezug auf Verformungsmechanismen zeigen keine Abhängigkeit zum vorherrschenden Lastfall. Um zeitabhängige Plastizitätsmechanismen zu untersuchen, wird ein Spannungs-Relaxationsprotokoll entwickelt. Auch hier zeigt sich die Dominanz korngrenzenbasierter Verformungsmechanismen.

Zur Verbesserung der Identifikation spezifischer Verformungsmechanismen werden anschliessend Relaxations- und Dehnraten-Sprung-Versuche an einer inertgaskondensierten Palladium-Gold-Modelllegierung durchgeführt. Charakteristisch für diese Legierung ist, neben ihrer höchstmöglichen chemischen Reinheit, auch ihre, mit ungefähr  $10\text{nm}$  besonders feine, homogene Kornstruktur. Bei den Versuchen wird ein Verformungsverhalten basierend auf der Aktivierung von Schertransformationszonen beobachtet, ähnlich dem metallischer Gläser.

Die im Umfang dieser Dissertation entwickelten Versuchsmethoden sind für die Schweizer Uhrenindustrie von grossem Interesse. Daher werden mechanische Mes-

sungen an unterschiedlichen Uhren-Materialien durchgeführt. Abschliessend wird ein Ansatz für die galvanische Herstellung einer Nickel-Wolfram-Legierung vorgestellt. Diese Legierung weist sowohl eine erhöhte thermomechanische Stabilität als auch eine reduzierte zeitabhängige Plastizität auf.

**Schlüsselwörter:** *Nanokristallin, galvanische Schichten, dünne Schichten, mikro-mechanische Versuche, Mikrosäulen kompression, erhöhte Temperaturen, mechanische Eigenschaften, Verformungsmechanismen, Aktivierungsparameter, Uhrmacherei*



---

# Acknowledgements

Puh! Looks like it's finally done after four years of sweating. As I started my PhD-work in the Laboratory for Mechanics of Materials and Nanostructures at Empa I honestly didn't have much of an idea how working in a research lab will be for me and if I would be able to tackle all the challenges that were waiting ahead. Therefore I was really glad that I got immediately absorbed into the welcoming and stimulating atmosphere at Empa Thun and being able to feel as part of the team right from the start.

It is time to say „Merci viu mou“ to all the great people I was allowed to work with over the past four years. Out-front my supervisor at Empa, Dr. Johann Michler, who basically hired me over the telephone and opened me the door to the world of micromechanics. His kindness, patience, scientific excellence and the ability to always see the positive side of things made him the best supervisor I could have wished for. Further I want to thank Prof.-Dr. Stefano Mischler for supervising me at EPFL and guiding me the way through the EDMX doctoral program, for valuable discussions and of course for all his input which allowed me to look beyond. My special thanks goes to Dr. Jeffrey Martin Wheeler who introduced me into the field of high-temperature micromechanics and, proofed this stack of paper and, most importantly, became a good friend of mine. Giggity! Dr. Gaurav Mohanty I want to thank for his valuable input to my work all along the way, good discussions and mouth-watering Indian food at his home. Further I want to thank Dr. Madoka Hasegawa and Dr. Laetitia Philippe from the electrochemistry group for showing me some of their magic electrochemistry tricks and depositing numerous nickel and nickel tungsten thin films, Dr. Aidan Taylor for doing a great job on the TEM, Dr. Xavier Maeder for the XRD-measurements on our samples and Dr. Rachel Schoeppner for taking care of my cat during I was on conference or vacation. I owe a lot of credit to Dipl.-Ing. Damian Frey who more than just once proved his incredible skills in LabView-programming and solving tricky small scale engineering problems in no time and our microscope technician Gerhard Bürki who always gets the last bit of resolution out of the systems! And speaking about owing: I owe my office (in-)mates Keith and Maxime a drink for giving me such an enjoyable time when

## Acknowledgements

---

I was in my office. Big thanks also go to Katrin Gurtner, Eveline Straubhaar and Sandra Beer - the Empa-team assistants and backbones of our lab! Further I want to thank the Empa workshop technician Anton Böll for his assistance in planning, discussing and (last-minute) manufacturing of many small mechanical components for the miniaturized tensile stage and the high temperature indenter and of course for his, and Bernahard von Gunten's enjoyable company during a cold after work beer on a Friday evening.

Last but not least I am immeasurably grateful to have always had my wife and my family in my back who supported me and always kept the faith in what I did, even when I lost it...

Thank You!

---

# Contents

<b>1</b>	<b>Introduction</b>	<b>1</b>
1.1	Objectives . . . . .	4
1.2	Structure of this thesis . . . . .	7
<b>2</b>	<b>Basic theories of metal plasticity</b>	<b>13</b>
2.1	The mechanical threshold of plasticity . . . . .	13
2.2	Crystallographic defects . . . . .	15
2.2.1	Dislocations . . . . .	15
2.2.2	Dislocation sources . . . . .	17
2.2.3	Planar defects . . . . .	18
2.3	Activation volume and dislocation activity . . . . .	20
<b>3</b>	<b>Nanocrystalline metals</b>	<b>23</b>
3.1	General considerations . . . . .	23
3.1.1	Size effect . . . . .	23
3.1.2	Strength . . . . .	24
3.1.3	Young's modulus . . . . .	28
3.2	Review of the most relevant deformation mechanisms . . . . .	30
3.2.1	Grain boundary sliding . . . . .	30
3.2.2	Grain rotation and grain coalescence . . . . .	32
3.2.3	Stress driven grain boundary migration . . . . .	33
3.2.4	Mesoscopic glide . . . . .	34
3.2.5	Shear transformation zones . . . . .	36
3.3	Conclusion . . . . .	37
<b>4</b>	<b>Experimental methods</b>	<b>39</b>
4.1	Electrodeposition of nanocrystalline nickel micro components . . . . .	39
4.1.1	Sulfamate solution . . . . .	39
4.1.2	LiGA-process . . . . .	41

4.1.3	Determination of chemical composition . . . . .	41
4.2	Electrodeposition of nickel-tungsten alloys . . . . .	45
4.3	Inert gas condensation of nanocrystalline palladium-gold alloy . . . . .	46
4.4	Characterization of specimen nanostructure . . . . .	49
4.4.1	Nanocrystalline nickel . . . . .	49
4.4.2	Palladium-gold alloy . . . . .	51
4.5	Utility of micropillar compression tests on nanocrystalline metals . . . . .	54
4.5.1	Micropillar fabrication with focused ion beam . . . . .	54
4.5.2	Influence of external- and internal pillar dimensions . . . . .	59
4.5.3	Influence of pillar geometry on experimental results . . . . .	61
4.6	High temperature indentation system . . . . .	63
4.6.1	System description . . . . .	63
4.6.2	Key high temperature components . . . . .	64
4.6.3	Thermally calibrated contact temperatures . . . . .	66
4.7	Minaturized tensile tests . . . . .	69
<b>5</b>	<b>Transient tests I: Case studies on electrodeposited nanocrystalline nickel</b>	<b>73</b>
5.1	Elevated temperature micropillar compression . . . . .	73
5.1.1	Material and specimen preparation . . . . .	74
5.1.2	Nanomechanical measurements . . . . .	75
5.1.3	Discussion . . . . .	81
5.1.4	Conclusions . . . . .	85
5.2	Comparison of in situ micromechanical techniques . . . . .	87
5.2.1	Industrial reference material . . . . .	88
5.2.2	Nanomechanical measurements . . . . .	89
5.2.3	Results and discussion . . . . .	92
5.2.4	Conclusions . . . . .	103
5.3	Time-dependent plasticity measurements: load relaxation tests . . . . .	103
5.3.1	Considerations on time-dependent metal plasticity . . . . .	104
5.3.2	Experimental . . . . .	106
5.3.3	Results . . . . .	108
5.3.4	Discussion . . . . .	110
5.3.5	Conclusions . . . . .	118
5.4	Summary . . . . .	118
5.4.1	Technological conclusions . . . . .	118
5.4.2	Scientific conclusions . . . . .	119

---

<b>6</b>	<b>Transient tests II: Model system Palladium-Gold</b>	<b>121</b>
6.1	Introduction and motivation . . . . .	121
6.2	Experimental . . . . .	122
6.2.1	Micropillar compression experiments . . . . .	122
6.2.2	In situ investigation of recrystallization and correlation to mechanical response . . . . .	124
6.3	Results . . . . .	125
6.3.1	Strain rate jump tests . . . . .	125
6.3.2	Repeated load relaxation tests . . . . .	129
6.4	Discussion . . . . .	132
6.4.1	Apparent deformation behavior . . . . .	132
6.4.2	Activation volume . . . . .	134
6.4.3	Activation energy and possible related deformation mechanisms	136
6.5	Conclusions . . . . .	141
<b>7</b>	<b>Technical relevance of nanocrystalline metals and their application in the Swiss watchmaking industry</b>	<b>143</b>
7.1	Motivation . . . . .	143
7.2	Mechanical properties for watch applications . . . . .	145
7.2.1	Young's modulus . . . . .	145
7.2.2	Yield strength and hardness . . . . .	148
7.2.3	Time dependent plastic behavior: load relaxation and creep . . . . .	149
7.3	Case studies: Mechanical testing of watch making alloys on watchpart-scale . . . . .	155
7.3.1	Micro tensile tests . . . . .	155
7.3.2	Micro four point bend tests . . . . .	157
7.4	Development of nickel-tungsten alloys for watch components . . . . .	160
7.4.1	Microstructural characterization . . . . .	161
7.4.2	Indentation results . . . . .	164
7.4.3	Thermal stability . . . . .	164
7.4.4	Texture analysis . . . . .	167
7.4.5	Discussion of NiW results . . . . .	169
<b>8</b>	<b>Summary and outlook</b>	<b>173</b>
8.1	Experimental small scale in situ techniques to assess plasticity mechanisms in nanocrystalline metals . . . . .	173
8.2	Observed deformation mechanisms in nanocrystalline metals . . . . .	175

Contents

---

8.3	Nanocrystalline metals for applications in Swiss watches . . . . .	179
8.4	Outlook . . . . .	183
<b>A</b>	<b>Bibliography</b>	<b>185</b>

---

## List of Figures

2.1	Schematic of the determination of the critical shear stress of a perfect single crystal . . . . .	14
2.2	Common point defects: (a) voids, (b) interstitial atoms, (c) larger (or smaller) foreign atoms . . . . .	15
2.3	Line defects: (a) edge dislocations (b) screw dislocations . . . . .	16
2.4	Activation of a Frank-Read-source . . . . .	17
2.5	Stacking faults: (a) ABC BCA (b) ABC B ABC . . . . .	18
2.6	Schematic of grain boundary (a) and twin boundary (b). . . . .	19
2.7	STEM image of nanotwinned NiW (3.6 at.-%) electrodeposit (a) with corresponding transmission kikuchi diffraction (TKD) pattern quality map (b) and orientation map (c) (see Chapter 7.4). The images suggest the formation of nano twins directly during the deposition process. . . . .	20
2.8	Activation volume . . . . .	21
3.1	Schematic of dislocation pileup in a grain as described by Cottrell [1] (a) and representation of the variation of yield stress as a function of grain size [2] (b). . . . .	25
3.2	Estimation of intercrystalline volume as a function of grain size (a) and grain boundary volume as a function of grain size and boundary width (b) (both [3]). . . . .	26
3.3	Young's modulus as function of porosity in nanocrystalline Cu and Pd [4] (a) and Young's Modulus of electrodeposited nanocrystalline Ni and NiP alloys as a function of grain size [5] (b). Young's moduli for the various directions in the {001}, {011} and {111} planes, calculated using the compliance matrix $[S_{ij}]$ for single crystalline Ni [6] (c). . .	29
3.4	Proposed plastic deformation mechanisms in nanocrystalline <i>fcc</i> -metals.	31
3.5	Schematic of Lifshitz GBS under diffusional creep conditions. $A(A^*)$ and $B(B^*)$ are marker lines. . . . .	32

3.6	Schematic of a stress induced grain rotation process in a nanocrystalline metal. Subsequent grain boundary annihilation creates large elongated grains (after [7]). . . . .	33
3.7	(a) Stress-strain curves #1 and #2 represent two different types of deformation behaviour in nanocrystalline aluminum with a nominal grain size of 40nm. TEM-images reveal the postmortem microstructures: (b) corresponds to curve #1 and shows a uniform grain size distribution whereas (c) corresponds to curve #2 where the nanostructure has obviously coarsened (reprinted from Gianola et al. [8]).	34
3.8	SEM images of macroscopic shear band formation observed after compression of an inertgas condensated Pd <sub>90</sub> Au <sub>10</sub> micropillar at room temperature. The strain rate was $\dot{\epsilon} = 10^{-1} s^{-1}$ . . . . .	35
3.9	Schematic of plastic deformation propagated by a shear transformation zone (STZ) (after Argon et al. [9]). . . . .	36
4.1	The four characteristic steps of a LiGA-process: (a) exposure, (b) development, (c) electrodeposition and (d) stripping/removing parts	42
4.2	Electrodeposited nanocrystalline nickel LiGA tensile dogbone specimen after dissolving the Si-wafer substrate (a) and residual stress induced delamination of nickel layers on flat silicon substrate before deposition parameter and bath chemistry optimization (b) . . . . .	43
4.3	Patterned Si-wafer prepared for LiGA-process (a) and a full wafer with microtensile bars after deposition (b) . . . . .	44
4.4	Effect of electrodeposition conditions on the composition of NiW deposits. . . . .	46
4.5	Schematic of the inert-gas condensation process . . . . .	47
4.6	SEM image of a Pd <sub>90</sub> Au <sub>10</sub> sample. The disc has a diameter of 8mm and is mounted on a SEM stub. . . . .	48
4.7	FIB channeling contrast image of the nickel film deposited at Empa, showing non-columnar microstructure with a broad grain size distribution (a) and TEM bright field image of a FIB-lamellae from the same specimen revealing a crystallite size in the order of 40nm. The grains at the top are larger in comparison to bulk due to grain growth on account of excessive exposure to Ga <sup>+</sup> ions. . . . .	50



4.8	Pd <sub>90</sub> Au <sub>10</sub> -TEM images (STEM) of specimen nanostructure. Both specimen were cut from the bulk section of the identical sample. The upper image (a) represents the initial nanostructure before the elevated temperature experiments whereas image (b) was taken after the thermal treatment. . . . .	52
4.9	XRD-spectra of Pd <sub>90</sub> Au <sub>10</sub> specimen. The blue curve has been acquired before and the grey curve after the heat treatment respectively. Apparently no noticeable grain growth was caused by the heat treatment up to 125°C. . . . .	53
4.10	Quadprobe FIB at Empa Thun. The base system is a Tescan Lyra Gallium-FIB which was equipped with additional XRD, WDX and TOFSIMS detectors. Figure (a) displays the inside view of the vacuum chamber. Figure (b) shows a large micropillar machined with the Tescan Fera Xe-FIB (ETH Zürich) into the gripping section of a nanocrystalline nickel tensile bar. The milling procedure for this pillar takes approximately two hours which is equal to approximately 4-5 days of milling time on a Ga-FIB. . . . .	55
4.11	Principle of focused ion beam milling (a) and imaging (b). . . . .	56
4.12	Typical examples for LMIS-beam damage during specimen preparation: SEM images of amorphized surface layer on a $\langle 123 \rangle$ -Si micropillar which extruded during room temperature compression at low strain rates $\dot{\epsilon} = 10^{-6}$ (a) and formation of a large Ga-compound-sphere next to a $\langle 111 \rangle$ -Si micropillar during in situ annealing at 400°C (b). . . . .	57
4.13	Representative SEM images of a Palladium-Gold micropillar during Gallium-FIB milling. The three-step approach includes coarse- (a) intermediate- (b) and fine milling/polishing (c) at 30kV and sequentially reduced milling currents. . . . .	58
4.14	(a) Number of grains in the cross section of a micropillar as a function of grain size and pillar diameter. The star symbol denotes a down-scaled standard bulk tensile specimen (maraging steel). The brown shaded area marks the regime where bulk like behavior can be expected. (b) Average fraction of FIB-induced damaged volume in a micropillar, assuming damage depths between 10nm and 30nm. The dashed vertical line denotes the average size of micropillars in this study. . . . .	60

4.15	SEM images of Palladium-Gold micropillar before compression (a) and after compression (b) at ambient temperature with a strain rate of $\dot{\epsilon} = 10^{-3}$ . (c) Engineering and true stress-strain curves computed for a particular test run assuming different pillar heights and diameters to study the effect of strain localization and pillar geometry on the resulting stress-strain curves. . . . .	62
4.16	High temperature indentation system with its major components. Joint development between Alemnis and Empa. . . . .	65
4.17	Heat treatment of resistive wire during peg heater assembly (a) and diamond tip during assembly with thermocouple cemented into the ceramic shaft (b). . . . .	66
4.18	Close-up sketch of the independent tip- and sample-heater assembly with the SEM-installation angle of $21.2^\circ$ (adapted from [10]) (a) and cube-corner diamond tip during calibration indent into a thermocouple junction (adapted from [11]) (b). . . . .	67
4.19	Calibration of a $9.5\mu\text{m}$ diameter diamond flat punch tip. Figure (a) shows the temperature offsets as function of surface temperature during calibration at different temperatures. The acquired calibration function is a square fit through the individual data points is provided in Figure (b). . . . .	68
4.20	(a) Adapted miniaturized tensile stage with 500 N load cell, displacement sensor and hard metal grippers. A digital microscope fixed perpendicular to the specimen is used for strain measurement. The inset in the right figure shows a nanocrystalline nickel micro tensile bar (LIGA) right before a tensile test. (b) Micro tensile specimen marked with eight couples of tracking points. . . . .	70
5.1	High resolution SEM images of a micropillar (a) before and (b) after compression to 25% strain at room temperature. The top half accommodates the bulk of the plastic deformation. . . . .	74
5.2	Illustration of test temperature sequence (a) and Engineering stress-strain curves for micro-compression of nanocrystalline nickel at $\dot{\epsilon} = 0.001\text{s}^{-1}$ (b). . . . .	76
5.3	High resolution SEM image of nanocrystalline Nickel micropillar after SRJ-compression. Extensive grain boundary sliding can be observed in the top half of the deformed pillar. Slip traces are observed in the larger grains. . . . .	78

5.4	Engineering stress-strain curves for the SRJ tests on nanocrystalline nickel micropillars at three test temperatures. Each test comprises five SRJs with the strain rates varying from $0.0002$ to $0.005s^{-1}$ , by a factor of 25. . . . .	78
5.5	Raw and corrected experimental data for determination of SRS exponent from engineering stress-strain curve for one of the tests. Values of $m$ were determined instantaneously across the SRJs as well as from the slope of stress-strain rate from the corrected data plotted in log-log scale. . . . .	80
5.6	Log-log plot of flow stress vs. strain rates showing micropillar SRJ and nanoindentation CSR data at room temperature. The hardness $H$ obtained from nanoindentation measurements was converted to stress by division with a factor of 2.8. . . . .	81
5.7	Extrapolation of strain rate at a constant stress level of $\sigma = 1.75GPa$ (a) and corresponding apparent activation energy for deformation, $Q$ , plotted in log scale vs. $1000/T$ (b). . . . .	84
5.8	(a) Apparent activation energy, $Q$ , values calculated from log (stress) vs. $(1/T)$ plots. Here the applied strain rate was $\dot{\epsilon} = 10^{-3}s^{-1}$ . (b) $Q$ plotted as a function of applied strain rates. . . . .	86
5.9	Two types of miniaturized tensile specimen: on the left side an electrodeposited nanocrystalline nickel specimen (LIGA) and an electrode discharge machined maraging steel specimen on the right. . . . .	89
5.10	Bright field TEM image of industrial nanocrystalline nickel. The grain size is in the order of $26nm$ . . . . .	90
5.11	Tensile stress-strain curves of nanocrystalline nickel and polycrystalline maraging steel at constant strain rate (CSR). . . . .	92
5.12	Tensile stress-strain curves for SRJ tests on nanocrystalline nickel. The green curve shows the raw data whereas the green dashed curve represents a fit through the initial and final segment. To account for strain hardening the fit was subtracted and shifted in stress axis to result in zero slope (blue curve). . . . .	93
5.13	Representative load-displacement curve from SRJ indentation of nickel. . . . .	95
5.14	Indentation modulus (blue) and hardness (green) as a function of indentation depth. . . . .	96

5.15	In situ SEM observation of the deformation behavior of nc-nickel (a) and sx-nickel (b) micropillars during compression testing at selected strains. . . . .	97
5.16	Micropillar stress-strain curves of nc-Nickel and $\langle 123 \rangle$ -oriented sx-nickel. . . . .	98
5.17	Post compression high resolution SE micrographs illustrate the differences in deformation behavior: (a) nc-nickel showing displaced grains distributed throughout the pillar and (b) sx-nickel showing deformation confined to discrete slip bands traversing the pillar. . . . .	99
5.18	Flow stress as a function of strain rate for tension, microcompression and nanoindentation ( $H/2.8$ ) tests from the current work and the literature (Maier et al. [12]). Note the jump in the stress axis. . . . .	100
5.19	A large FIB micropillar of nanocrystalline Ni machined in the undeformed gripping section of a micro tensile bar (post mortem). . . . .	107
5.20	(a) An example stress-strain curve for 6 independent relaxations using the miniature tension method. The corresponding stress-strain curve of a constant strain rate test at $\dot{\epsilon}_r = 0.001s^{-1}$ is shown in Figure 5.11. Examples of the fit to extract the apparent activation volume and time constant for the first (b) and the last (c) relaxation segment. The apparent activation volume for these two fits were $8.5$ and $10.4b^3$ respectively. . . . .	109
5.21	An example result from a micropillar compression test with multiple repeated relaxation segments. The entire test is shown in Figure (a). The first and the last segments are shown on a smaller scale in Figure (b) and (c) respectively. . . . .	111
5.22	SEM images during deformation at the onset of deformation (a), and at a strain of 20% (b). . . . .	112
5.23	Examples of raw data and fit for two relaxation segments ( $R_{11}$ and $R_{51}$ ). The correlation coefficient for these fits were $\sim 0.99$ . . . . .	112
5.24	Apparent and effective activation volume for two independent micropillar RLR tests. . . . .	114
5.25	An estimate of the relative dislocation density as it evolves during a sequence of stress relaxation segments from the tensile experiments . . . . .	117
6.1	FIB specimen preparation of a $5 \times 5$ micropillar array on Pd <sub>90</sub> Au <sub>10</sub> (a) and Pd <sub>90</sub> Au <sub>10</sub> micropillar during compression (b). . . . .	123
6.2	Illustration of the applied test temperature sequence for nanocrystalline Pd <sub>90</sub> Au <sub>10</sub> . . . . .	124

6.3	In situ XRD observation of nanostructural stability of Pd <sub>90</sub> Au <sub>10</sub> . The structure remains stable below temperatures of approximately 200°C. Beyond this temperature excessive grain growth occurs. The blue array indicates the constant nanostructure regime in which the micropillar compression tests were performed. . . . .	126
6.4	Eng.stress vs. eng.strain curves of SRJ tests as a function of temperature on thermally-relaxed Pd <sub>90</sub> Au <sub>10</sub> . As the temperature increases, the overall flow stress level decreases and the relative jump height increases. For a better overview, the corresponding strain rates are indicated only for the 250°C curve. . . . .	127
6.5	Log(stress), plotted as a function of log(strain rate). The strain rate sensitivity exponent $m$ increases with increasing temperature. For a better overview within the plot, the individual data points and the fitted slopes for the measurements at 250°C and at room temperature after crystallite growth are not shown. However, the extracted $m$ values are given in the inset. . . . .	128
6.6	Apparent activation volumes from strain rate jump tests, plotted as function of test temperature. . . . .	129
6.7	(a) Eng.stress vs. eng.strain curves of RLR tests as a function of temperature on thermally relaxed Pd <sub>90</sub> Au <sub>10</sub> . As the temperature increases, the relative amount of relaxation with respect to stress increases. (b) Example of a stress relaxation cycle in the fully plastic flow regime as directly obtained from the experiment and the corresponding logarithmic fit of the first segment (c). . . . .	131
6.8	Activation volumes as function of Eng. strain, obtained from repeated load-relaxation tests at variable test temperatures on thermally relaxed Pd <sub>90</sub> Au <sub>10</sub> . The hollow and solid symbols denote apparent and effective activation volumes, respectively. . . . .	132
6.9	SEM overview images of Pd <sub>90</sub> Au <sub>10</sub> micropillars after compression (a and b) and corresponding high resolution SEM images (c and d) at 125°C and 250°C, respectively. Crystallite growth clearly affects the apparent deformation behavior. Increased grain boundary mediated deformation manifests in coarse surface features after compression up to 25% strain. . . . .	133
6.10	Apparent activation energy for deformation calculated by plotting extrapolated strain rate, corresponding to the same stress level in log scale vs. $1/T$ . . . . .	137

6.11	Pd <sub>90</sub> Au <sub>10</sub> TEM cross sections (STEM) of micropillar nanostructure after compression to 25% strain (SRJ). The upper image (a) represents the deformed nanostructure before the elevated temperature experiments whereas image (b) was taken after the thermal treatment at 125°C. Both pillars show no indications of localized grain growth due to GBS or the thermal treatment. . . . .	140
7.1	(a) Nanocrystalline nickel watch micro-cantilevers, obtained from LiGA-process. (b) Mechanical wrist-watch movement (Courtesy: Breitling SA) which utilizes a large number of functional microcomponents. . .	144
7.2	Micropillars, cut in „in-plane“-direction into the side of the gripping section of a nanocrystalline nickel micro tensile specimen (a) and (b). The normal axis of the micropillar corresponds to the tensile-axis. Comparison of modulus from unloading curves in-plane and out-of-plane (c). . . . .	146
7.3	Load-relaxation curves (room temperature) obtained in uniaxial tension above the yield stress on nanocrystalline nickel, nanocrystalline nickel-tungsten and maraging steel (a) and long term prediction of stress relaxation of nanocrystalline nickel and nickel-tungsten at 55% of the elastic limit (b). . . . .	151
7.4	First creep tests on a LiGA sample in air using vision tracking (digital image correlation) over a 24h period. The small LiGA sample (3mm gauge length and 300μm) could bear loads up to 12kg!! These creep tests can be improved and adapted to perform routine tests on industrial specimens using piezo actuation and by performing tests in SEM. . . . .	153
7.5	Prediction of creep deformation as a function of time for accepted creep deformations of 1% and 5%. The experimentally assessed creep rates of $\dot{\epsilon} = 10^{-9} s^{-1}$ are within the blue shaded frame. . . . .	154
7.6	Comparison of micro tensile stress-strain curves for a selection of metals/alloys used in mechanical watches. . . . .	156
7.7	(a) Modified micro-bend test device with four point bending chucks. (b) In situ image of a maraging steel specimen during a test. (c) Bend test specimen from watchmaking alloys, manufactured by EDM or electrodeposition. . . . .	159

---

7.8	Cross-sectional FIB images of NiW electrodeposits with different compositions. NiW deposits were prepared at mean current densities of $J = -10mA/cm^2$ (a-e), and $-15mA/cm^2$ (f) in the ammoniacal citrate baths containing 0 – 20g/L of W. . . . .	162
7.9	Ion channeling contrast images of ncNi-nanostructure (industrial reference) in as deposited condition (a) and after thermal treatment at 250°C for 2 hours (b). . . . .	165
7.10	Ion channeling contrast images of NiW-nanostructure (4.8at. – %W) in different states of thermal treatment (2 hour hold period). (a) as deposited (b) 250°C, (c) 350°C and 450°C. . . . .	166
7.11	Grain growth behavior during heat treatment. The temperatures were held constant for 2 hours at each step. Comparision of nc-NiW (4.8 at% W) and nc-Ni (Industrial reference). . . . .	167
7.12	Texture coefficients for (a) (111), (b) (200), (c) (220) and (d) (311) reflections of Ni and NiW alloy electrodeposits. . . . .	168





---

## List of Tables

4.1	Nominal composition of nanocrystalline Ni plating bath . . . . .	40
4.2	Comparison of nominal composition of nanocrystalline Ni determined from GDOES measurements. Contents in <i>mass.</i> – % . . . . .	45
5.1	Comparison of <i>m</i> values calculated for one of the pillars tested at 100°C using method (a) (instantaneous SRS determination) on raw and slope-corrected engineering stress-strain curves. The <i>m</i> -value determined using method (b) (from the slope of stress-strain rate plot in log-log scale) on slope-corrected data is also shown for comparison.	80
5.2	Activation volumes in nanocrystalline nickel. . . . .	102
6.1	Calculated values for Mechanical work $\Delta W$ and Helmholtz free energy $\Delta F$ . . . . .	139
7.1	Mechanical properties of watchmaking alloys, assessed with uniaxial micro tensile tests. The italicized values are taken from supplier references if available. . . . .	157
7.2	Mechanical properties of watchmaking alloys, assessed with four point bending tests. The italicized values are taken from supplier references if available. . . . .	158
7.3	Young’s modulus and hardness of nanostructured Ni and NiW deposits.	164



---

## List of symbols

Symbol	Unit	Property
$A$	1	Pre-exponential constant
$A$	$m$	FIB aperture
$A'$	1	Constant, experimental values $\sim 10$
$b$	$m$	Burgers vector
$\beta$	1	Proportionality factor
$c$	$s$	Time constant
$d$	$m$	Grain size
$d$	$m$	Pillar diameter
$D$	$m$	Crater diameter
$D$	$m^2/s$	Diffusion coefficient
$D_{GB}$	$m^2/s$	Grain boundary diffusion coefficient
$E$	$N/mm^2$	Young's modulus
$\varepsilon$	1	Strain
$\dot{\varepsilon}$	$s^{-1}$	Strain rate
$\Delta F$	$J/mol$	Helmholtz free energy
$\dot{\gamma}$	$s^{-1}$	Shear strain rate
$\dot{\gamma}_0$	$s^{-1}$	Reference shear strain rate
$\Delta G$	$J/mol$	Gibbs free energy of activation
$\Delta G_0$	$J/mol$	Gibbs free energy of activation
$G$	$N/mm^2$	Shear modulus
$h$	$m$	Pillar height
$\dot{H}$	$N/mm^2$	Indentation hardening rate
$H$	$N/mm^2$	Hardness
$I$	$A$	FIB Probe current
$I_{hkl}$	1	Relative XRD peak intensity
$I_{0,hkl}$	1	Relative XRD peak intensity of randomly oriented powder
$J$	$mA/cm^2$	Current density
$k$	1	Grain boundary strengthening coefficient

---

List of symbols

---

Symbol	Unit	Property
$k$	1	Boltzmann's constant
$\lambda$	$m$	Subgrain size
$m$	1	Strain rate sensitivity exponent
$M$	$N/mm^2$	Modulus of specimen/machine assembly
$n$	1	Creep exponent
$\Omega$	1	Proportionality constant
$\Omega_{STZ}$	1	Size of shear transformation zone
$p$	1	Inverse grain size exponent
$P$	$N$	Applied indentation load
$\dot{P}$	$N/s$	Indentation loading rate
$Q$	$J/mol$	Apparent activation energy
$r$	1	Geometrical ratio
$R$	$J/molK$	Gas constant
$\rho_m$	$m^{-2}$	Dislocation density
$\rho_{m0}$	$m^{-2}$	Initial dislocation density
$r_{nc}$	$m$	Half diameter of a nano grain
$\sigma$	$N/mm^2$	Stress
$\sigma_0$	$N/mm^2$	Peierl's-/lattice stress
$\sigma_Y$	$N/mm^2$	Yield strength
$\sigma_{flow}$	$N/mm^2$	Flow stress
$T$	$K$	Temperature
$\Delta T$	$K$	Temperature difference
$t$	$s$	Time
$\Delta\tau$	$N/mm^2$	Shear stress difference
$\dot{\tau}$	$N/(mm^2s^{-1})$	Shear stress rate
$\Theta$	$^\circ$	Beam incidence angle
$\Theta_{wh}$	1	Work hardening coefficient
$TC_{hkl}$	1	Texture coefficient
$T_m$	$K$	Melting temperature
$UTS$	$N/mm^2$	Tensile strength
$v$	$m/s$	Dislocation velocity
$v_0$	$m/s$	Initial dislocation velocity
$V$	$b^3$	Activation volume
$V_{app}$	$b^3$	Apparent activation volume
$V_{eff}$	$b^3$	Effective activation volume

Symbol	Unit	Property
$\Delta W$	$J/mol$	Mechanical work

---



---

## List of publications

Publishing articles is a process that requires a lot of brain-power, sweat and hands-on work of numerous people. Hence, many people contributed to my first author publications, either with providing experimental data, assistance in the interpretation of results or valuable comments on the language skills of a German student. In return I contributed to many of their publications by spending hours on the FIB, preparing samples and analyzing data and writing up the results or just discussing. And of course I spent many sleepless nights in front of the high-temperature *In-Situ* indenter when compressing their samples at ridiculous temperatures. It is time to thank all these people for the great collaborations, fruitful discussions and amazing materials they brought for testing from various field of materials sciences.

### Articles

- Wehrs, J.; Deckarm, M.; Wheeler, J.M.; Maeder, X.; Birringer, R.; Mischler, S. and Michler, J.: „*Elevated temperature, micro-compression transient plasticity tests on nanocrystalline Palladium-Gold: Probing activation parameters at the lower limit of crystallinity*“, submitted to Acta Materialia in May 2016, currently under review, Elsevier
- Mohanty, G. and Wehrs, J.; Boyce, B.L.; Taylor, A.; Hasegawa, M.; Philippe, L. and Michler, J.: „*Room temperature stress relaxation in nanocrystalline Ni measured by micropillar compression and miniature tension*“, J. Mater. Res., 2016, 31, 1086, Cambridge Univ. Press
- Wehrs, J.; Mohanty, G.; Guillonneau, G.; Taylor, A.; Maeder, X.; Frey, D.; Philippe, L.; Mischler, S.; Wheeler, J.M. and Michler, J.: „*Comparison of In Situ Micromechanical Strain-Rate Sensitivity Measurement Techniques*“, JOM, 2015, 67, 1684-1693, Springer

## Co-authored articles

- Best, J.P.; Zechner, J.; Shorubalko, I.; Oboňa, J.V.; Wehrs, J.; Morstein, M. and Michler, J.: „*A comparison of three different notching ions for small-scale fracture toughness measurement*“, Scripta Materialia, 2016, 112, 71-74, Elsevier
- Gamcová, J.; Mohanty, G.; Michalik, Š.; Wehrs, J.; Bednarčík, J.; Krywka, C.; Breguet, J.M.; Michler, J. and Franz, H.: „*Mapping strain fields induced in Zr-based bulk metallic glasses during in-situ nanoindentation by X-ray nanodiffraction*“, Applied Physics Letters, 2016, 108, 031907, AIP Publishing
- Mohanty, G.; Wheeler, J.M.; Raghavan, R.; Wehrs, J. and Hasegawa, M.; Michler, S.; Philippe, L. and Michler, J.: „*Elevated temperature, strain rate jump microcompression of nanocrystalline nickel*“, Philosophical Magazine, 2015, 95, 1878-1895, Taylor & Francis
- Raghavan, R.; Harzer, T.P.; Chawla, V.; Djaziri, S.; Philippi, B.; Wehrs, J.; Wheeler, J.M.; Michler, J. and Dehm, G.: „*Comparing small scale plasticity of copper-chromium nanolayered and alloyed thin films at elevated temperatures*“, Acta Materialia, 2015, 93, 175-186, Elsevier
- Raghavan, R.; Wheeler, J.M.; Harzer, T.P.; Chawla, V.; Djaziri, S.; Thomas, K.; Philippi, B.; Kirchlechner, C.; Jaya, B.N.; Wehrs, J.; Michler, J. and Dehm, G.: „*Transition from shear to stress-assisted diffusion of copper-chromium nanolayered thin films at elevated temperatures*“, Acta Materialia, 2015, 100, 73-80, Elsevier
- Wheeler, J.M.; Raghavan, R.; Wehrs, J.; Zhang, Y.; Erni, R. and Michler, J.: „*Approaching the limits of strength-measuring the uniaxial compressive strength of diamond at small scales*“, Nano letters, 2015, ACS Publications
- Nadargi, D.; Kelly, C.; Wehrs, J.; Philippe, L.; Michler, J.; and Koebel, M.M.: „*Epoxide assisted metal oxide replication (EAMOR): a new technique for metal oxide patterning*“, RSC Advances, 2014, 4, 36494-36497, Royal Society of Chemistry
- Wheeler, J.M.; Wehrs, J. Favaro, G. and Michler, J.: „*In-situ optical oblique observation of scratch testing*“, Surface and Coatings Technology, 2014, 258, 127-133, Elsevier



## Articles in preparation

- Cryogenic in-situ transient plasticity tests on nanocrystalline Palladium-Gold micropillars
- Variable-temperature in-situ transient creep tests on nanocrystalline Palladium-Gold micropillars
- Influence of various degrees of plastic deformation on the nanostructure of nickel micropillars
- Influence of crystallographic texture on the deformation behavior of nanocrystalline nickel

## Oral presentations

- „*Materials design for structural applications utilizing micro tensile testing and elevated temperature micropillar compression*“, ICSMA 2015, Brno, Czech Republic
- „*Variable temperature time dependent plasticity measurements of thin films: a novel approach using micro compression*“, CINT User Meeting 2015, Santa Fe, NM, USA
- „*Elevated temperature, micro-compression transient plasticity tests on nanocrystalline Palladium-Gold: Probing activation parameters at the lower limit of crystallinity*“, ICEM 2016, Rhodes, Greece

## Posters

- „*Mechanical properties of nanostructured Ni- and NiW- microcomponents produced by electrodeposition*“, GDR CNRS Mecano General Meeting 2013, Cargese, Corsica
- „*Mechanical properties of nanostructured Ni- and NiW- microcomponents produced by electrodeposition*“, GRC 2014 Thin Film and Small Scale Mechanical Behavior, Waltham, MA, USA

List of publications

---

- „*Comparison of in situ micromechanical time dependent plasticity techniques: micropillar compression, nanoindentation and micro-tensile tests*“, ECI 2015, Albufeira, Portugal

---

# 1. Introduction

Nanocrystalline metals provide a few highly desirable mechanical properties which are superior to the properties of their chemically equivalent larger grained polycrystalline counterparts. Out-front their remarkably high strength should be mentioned which is directly connected to their small grain size. As an example we can compare the strength of single crystal nickel which has no internal grain boundaries to the strength of nanocrystalline nickel with a grain size of  $< 100nm$  where billions of internal grain boundaries act as obstacles for classic dislocation based deformation mechanisms. The macroscopic strength of the nanocrystalline nickel is approximately twenty times higher which clearly displays the capability of nanostructural refinement. The combination with reasonably high ductility further increases the attraction of these materials for numerous applications in the field of microtechnology: MEMS-devices, microcomponents or sensing devices.

Looking into the mechanical properties of nanocrystalline metals in general a multitude of studies have been conducted to gain insight into the nature of plastic deformation in this group of materials. For example the previously mentioned classic dislocation based theories like the Hall-Petch relationship which relates the increase in strength to a change in grain size in an inversely proportional manner can only be applied to a certain threshold grain size. After passing this threshold the relation does not hold anymore and the strength decreases again. However, today it is still not clear what governs the plastic deformation in nanocrystalline metals as many studies yield different or even contradictory results. The overall consensus in the community of nanocrystalline metals research is that the decrease in grain size and therewith the tremendous increase in interfacial volume plays a key role here. In fact, a confined volume of material with a grain size at the higher end of the nanocrystalline regime, i.e.  $\sim 100nm$  comprises an interfacial volume of less than 5% when assuming an average grain boundary width of  $1nm$ . Decreasing the grain size by a factor of 10 corresponds to an increase of interfacial volume to approximately 30%. Hence it is somewhat instructive that the interface between individual grains is not negligible anymore when deformation mechanisms are discussed.

Reasons for the pertinent lack of understanding can be addressed to several as-

pects: first of all the mechanical properties of nanocrystalline metals do not only depend on their grain size but also on the way materials have been synthesized and processed. For an example, electrodeposited materials often provide a preferential crystallographic orientation which is caused by the sequence the materials adheres and grows on a substrate and the deposition parameters. Hence, this material will perform differently than a fully randomly oriented one. Also foreign species, additives and spurious elements which may get incorporated in the process of manufacturing alter the mechanical behavior. Another influential factor is the homogeneity of grain size and shape and microstructural damages such as voids or pores. Consequently, it is very difficult to reproduce identical materials which would assist in reducing the experimental scatter in between different materials. Another issue is the availability of materials. In case of nanocrystalline a lot of studies are conducted on material from one and the same commercial supplier where the process parameters are proprietary. Further reasons can be found in the availability of suitable experimental equipment to probe deformation mechanisms on such a small size scale. Well understood bulk techniques such as tensile tests or creep tests for instance are often not possible to be conducted simply because of the fact that the required bulk quantities of nanocrystalline metals are not available. A common and widely spread small scale technique is instrumented nanoindentation which can be used to assess not only the hardness of small quantities of materials or thin films but also to determine their stiffness/ Young's modulus. If advanced systems are available, even time dependent properties like the strain rate dependence of stress or creep properties can be estimated. However, a major disadvantage of these measurements is the complicated triaxial stress state under the sharp indenter tip which is not straight forward to explain and heavily dependent on the tip geometry and sharpness that ideally needs to be assessed accurately before each experiment. Of course the surface preparation of the material is also of interest as only small volumes are probed in one indent and hence the results can be biased by surface inhomogeneities or deformed layers from mechanical surface polishing. Atomistic simulations on the other hand are beneficial for the identification of possible deformation mechanisms but as they are restricted to the assumption of high deformation rates that are far away from experimentally realizable parameters. In between these two groups the field of in situ experiments has evolved. On a specimen scale suitable for available quantities of nanocrystalline metals, etched or heavily ion polished specimen are mechanically tested inside transmission electron microscopes where the motion of dislocations or the activation of dislocation sources can be watched while they happen. On single crystals or coarse grained materials these tests are very instructive as they can easily

---

visualize dislocation based mechanisms. However, on nanometer scale grains even these high resolution in situ experiments fail to provide insight as mechanisms are obscured due to the high density of defects. Hence, ideally a miniaturized classic uniaxial bulk test would be developed which is scaled to a size regime that allows to test thin films and small quantities of nanocrystalline metals while the bulk-character in terms of statistical relevance is maintained. Further this test would be possible to conduct under extreme test conditions like high-/low temperature or in a broad range of strain rates and time frames in order to provide insight into deformation mechanisms that govern plastic behavior in this material.

The studies conducted within the framework of this thesis are aiming to extend the current knowledge and understanding of the mechanical behavior of nanocrystalline materials in two directions: one direction points towards basic research where new experimental small scale and in situ methods are developed and explored and afterward utilized for the mechanical characterization of various nanocrystalline metals and thin films. The other direction is inspired by recent challenges in the Swiss watchmaking industry which has a strong demand for structural microcomponents made of nanocrystalline metals. Traditionally, structural components are produced by manufacturing processes like stamping. This process is feasible as long as large quantities of standardized components are requested since the tool manufacturing costs are comparably high and limitations arise from the geometric dimensionality of the components as only relatively simple geometries can be realized. Also the material itself which is mostly provided the form of rolled sheets is difficult to functionalize as most of the currently used alloys are more than hundred years old. Other manufacturing processes like electrode discharge machining are quite common but expensive for intermediate quantities of parts and still fall below the restrictions of geometry and materials selection. Recent technological advances in the fields of electrochemistry and small-scale manufacturing allow the watch-engineers and designers to apply lithography based manufacturing processes where they can grow high aspect ratio microcomponents into complex cavities and hence integrate various functions into one single part: multiple functional layers, tailored complex geometries, direct incorporation of jewels for esthetic or functional reasons. This so called LiGA-process (LiGA= Litographie, Galvanik, Abformung) which is a German acronym for lithography and subsequent electrodeposition is a key technology in in modern watchmaking as the tradeoff between production costs (design of a mask is approximately 90% cheaper as the manufacturing of a sheet metal stamping tool), flexibility, required time to incorporate design changes or new materials and design freedom is excellent. A drawback from the materials perspective are the partly insuf-

ficient mechanical properties of nanocrystalline metals. Despite their high strength and hardness which is desired, they provide a pronounced time dependent plastic behavior (i.e. load relaxation and creep) which is not appreciated in watch movements where many parts fulfill the function to store energy over an extended period of time in order to keep the watch from running precisely. Those time-dependent plastic properties are currently a bottleneck for increased applications of LiGA components and alternative electrodeposited materials with similarly high strength but better time dependent properties are currently not available.

Therefore, in this thesis a variety of nanocrystalline metals of different grades from highly pure, additive-free alloys which have been synthesized on lab scale up to industrial reference materials from external suppliers, produced by proprietary processes are characterized. Suitable in situ instruments for testing these micro specimens in a meaningful way are developed. These are coupled with new analysis methods and test routines are established which may add to understanding the mechanical behavior of nanocrystalline materials.

### 1.1. Objectives

Based on the literature review we have identified a few white spots where research is needed to gain further insights into the field. One of these white spots is the material itself. Very few studies do an in depth correlation of plating parameters with mechanical properties. In fact most of the available literature is based on electrochemically pure nickel from one commercial source and the plating parameters are not known. This explains also why comparatively few papers deal with alloy development as this requires an interdisciplinary understanding of mechanics and electrochemistry. Further, most studies concentrate on deformation mechanisms while only few studies deal with elastic and time dependent properties (i.e. relaxation and creep). However, these properties are important to assess, especially with respect to applications in a watch movement.

Further, again in the context of watch making applications, the readily available types, sizes and shapes of specimen are not suitable to assess the materials relevant properties as the following example demonstrates: Most mechanical watch components are made by stamping or electrode discharge machining from rolled sheets (polycrystalline bulk metals). However, the dimensions of actual watch parts  $\sim 250\mu\text{m}$  are in ranges where size effects and surface properties start to gain influence, and therefore the known bulk properties are not valid anymore. In contrast, UV-LiGA provides the opportunity to fabricate/deposit hundreds of microcompo-

nents/test specimen in parallel in one single deposition run. These materials are commonly nanocrystalline which proposes other material specific properties that are ultimately connected to their crystallite size: thermal instability, creep and relaxation. Hence this requires that both, plating into UV-LiGA molds and the test methodology for small scale testing is properly developed and in depth studies of different mechanical load cases and loading conditions (temperature, strain rate) are conducted.

### Technological objectives

- A micromechanical test rig capable of performing precise uniaxial micro-tensile tests on the scale of a watchpart needs to be developed and successfully implemented under an optical microscope in the framework of this thesis. Critical points which need to be addressed here are the implementation of DIC algorithms for optical strain measurement and the ability of non-destructive specimen clamping. The setup has to enable variable strain rate tests, stress relaxation experiments and increase the reliability of Young's modulus measurements on small scale specimen.
- A micromechanical test rig under the SEM, capable of high temperature indentation and uniaxial micropillar compression experiments has to be explored. The setup allows for variable strain rate and variable temperature micro compression testing on the scale of thin film specimen. A major task is to learn how to manually build the custom-made high temperature components and operate the system. A few modifications of the load cell, specimen heater and cooling system are required to extend the range of strain rates to  $10^4 s^{-1}$  and temperatures to  $600^\circ C$ . This instrument is unique and at the frontier of micro scale testing.
- A technological/industrial objective is to develop an alloy that shows a Young's modulus above  $200 GPa$  and a creep rate low enough that a watch part can keep a spring load of  $50 MPa$  stress over the lifetime of the watch without stress relaxation. The approach here is to electrochemically alloy the commonly used nanocrystalline nickel with refractory metals (tungsten). Further the influence of plating parameters on modulus (texture, pores), strength and time dependent plastic behaviour (grain size) need to be studied.

### Scientific objectives

- We aim to develop a new test methodology based on variable strain rate and variable temperature micro compression. The method has the potential to gain insight into deformation mechanism as activation energy and volume and strain rate sensitivity can be determined. FIB machined pillars will be used and FIB slices of the whole volume will then be analyzed by TEM to establish unique correlations to the microstructure. As reviewed in Chapter 3, there is a large debate and hundreds of papers deal with this, but none of the papers exploited the advantage of micro compression tests enabling extreme test conditions on a large number of samples with known deposition conditions and the opportunity to analyze the entire volume of the sample by TEM postmortem.
- The plastic deformation of nanocrystalline materials is governed by several mechanisms which act in a convoluted manner. Deconvoluting and identifying the rate controlling mechanism(s) from the multitude of all the active deformation mechanisms is challenging. Grain size and the interfacial volume are closely connected to that and have a strong influence on the mechanical behaviour. However, electrodeposited materials often do not provide fully homogeneous microstructures and feature a comparably wide grain size distribution. Superimposed macrostructures that are a result of deposition may also influence the deformation characteristics on a micron scale. Therefore we aim to extend our studies to a highly pure palladium-gold alloy which provides superior microstructural homogeneity and grain sizes in the order of  $\sim 10nm$  and may serve to gain deeper insight into the deformation mechanisms in nanocrystalline metals.
- We aim to electrodeposit nanocrystalline nickel-tungsten alloys. There are a couple of basic questions: How is the texture influenced by the alloy content? How does the alloy content and deposition parameters influence the microstructure? Do such refractory-metal alloys provide increased thermal stability and enhanced mechanical performance with respect to Young's modulus and time dependent deformation? Is the alloy more temperature stable and yields improved time dependent plastic behavior? Systematic deposition experiments accompanied by XRD and SEM and chemical analysis of the samples in conjunction with miniature tensile and micro compression tests will be used for this purpose.



## 1.2. Structure of this thesis

### Chapter 1

Based on literature review and actual application challenges in the Swiss watch making industry in Chapter 1, the scientific and engineering challenges are identified, and a number of objective tasks are pointed out.

### Chapter 2

In Chapter 2, a selection of basic theories of metal plasticity are discussed.

### Chapter 3

In Chapter 3, the focus is put on reviewing the most relevant deformation mechanisms that can appear in nanocrystalline *fcc*-metals. This review is important to begin with as, although numerous studies dealt with this topic, no general outcome of these studies points out which mechanism are active under which circumstances. Most deformation mechanisms in nanocrystalline materials are not easy to identify as their experimental observation is rather complicated, but it is an overall consensus that plastic deformation strongly depends on the factor „crystallite size“. Thus, it is accepted that the role of grain boundary volume gains more relevance as the grain size reaches lower values whereas the influence of classic intragranular mechanisms fades. However, the process materials have been synthesized with is at least as important as this controls not only the uniformity of crystallite size and shape but also the amount of foreign species on grain boundaries or preferred crystallographic orientations. Further, experimental factors like probed volume, loading case, time scale of experiments, temperature etc. affect the apparent deformation behavior. Hence, in this Chapter, a number of experimentally observed or simulated deformation mechanisms that appeared repeatedly in different studies are discussed with respect to the pertinent literature

### Chapter 4

In Chapter 4, the experimental details of the materials and methods utilized for the studies presented in this thesis are described. First, the studied materials are introduced, starting with the synthesis of nanocrystalline nickel at Empa, which is illustrated and explained from the electrochemical bath to the final deposition into lithography molds (LiGA). Controlling the entire manufacturing process from the bath

to finally free standing microcomponents is highly beneficial from a scientific perspective since this allows to develop a deeper understanding of the convoluted influence of process parameters and composition on the mechanical properties and plastic behavior of the material. In parallel, an industrial reference nickel is introduced which is delivered by a supplier of the Swiss watch industry. The electrochemical bath composition and process parameters of this material are proprietary, but nevertheless this material is the current standard in Swiss watch manufacturing and hence a desirable reference material. Further we discuss the development and deposition of nanocrystalline nickel tungsten alloys which are also investigated in the framework of this thesis. The initial approach was to alloy nickel with refractory metals in order to improve the materials thermal stability and to exceed the mechanical properties of industrial nanocrystalline nickel. Further, the inert gas condensation of highly pure nanocrystalline palladium gold is discussed. Palladium gold, even though not electrodeposited and irrelevant from an industrial application perspective, serves as a model materials for this thesis. First of all inert gas condensation enables to produce highly pure nanocrystalline metals/alloys which is advantageous for the characterization of the materials plastic deformation behavior as the possible influence of spurious atoms, especially for small atom species that segregate preferentially at grain boundaries, is prevailed. Another characteristic feature of inert gas condensed materials is the establishment of randomly textured nanostructures with very small crystallite sizes and narrow, log-normal crystallite size distributions. This is again beneficial for the interpretation of results as texture and crystallite size both show strong influence on the mechanical behavior. Thus, palladium gold may provide useful insight into the deformation characteristics of nanocrystalline metals in a more clear manner which in turn can assist in the interpretation of the behavior of nanocrystalline electrodeposits. The second part of this Chapter deals with the main characterization techniques to assess the materials composition and nanostructural features. Finally in the third part of Chapter 4 the focus is put on two recent nanomechanical characterization techniques that were explored, developed and validated in the framework of this thesis: micropillar compression at elevated temperatures and micro tensile testing. After first discussing the general relevance and utility of uniaxial micropillar compression tests as a highly relevant testing technique in the context of nanocrystalline materials the applied methods for the fabrication of suitable specimen are introduced. Then the high temperature testing system developed at Empa Thun, which is the key experimental technique in this thesis, is described with focus on the high temperature parts. This uniaxial technique is highly relevant, also with respect to engineering applications as it allows

the straight forward assessment and interpretation of engineering properties of thin films and mechanical components manufactured from nanocrystalline materials or more generally: materials which are not readily available in bulk quantities. However, to validate this technique and justify the relatively high required effort of specimen preparation a more conventional system was developed that can be utilized for miniaturized tensile tests of micro dogbone specimen. Tensile tests are probably the most widely spread and well understood mechanical tests and therefore may serve to bridge the gap between well standardized bulk tensile tests, micro tensile tests and pillar compression tests.

## Chapter 5

Chapter 5, contains three case studies on the mechanical behavior of nanocrystalline nickel. In the first part, the plastic behavior of nanocrystalline nickel, which was synthesized at Empa, is experimentally assessed by means of in situ micropillar compression tests at ambient and elevated temperatures. The baseline tests are performed at constant strain rate in order to develop a first understanding of the materials' stress-strain behavior in three temperature regimes up to 100°C. To retain a constant microstructure, the highest test temperature was set below the thermal regime where grains start to grow excessively which would have a pronounced effect on the materials behavior. Then strain rate jump tests, a type of transient test, are introduced where the strain rate is changed instantaneously and repeatedly over several orders of magnitude during one single compression test. The mechanical response of the material, i.e. the change in flow stress is monitored and enables the extraction of parameters (strain rate sensitivity index  $m$  and activation volume  $V$  which are directly or indirectly connected to the active deformation mechanism. Another benefit of performing these tests at room temperature as well as elevated temperatures allows to extract trends in strain rate sensitivity and calculate the activation energy  $Q$  which is another indicator of the apparent type of deformation mechanism. Post compression analysis of the micropillars by means of high resolution SEM gives further indications on the apparent deformation behavior.

In the second part of Chapter 5, a comparative study of three different micromechanical measurement techniques: in situ micro tensile, in situ micropillar compression and nanoindentation is conducted. The idea behind this study is to provide a direct comparison between the test methods by conducting strain rate jump tests on the same specimen from only one batch of material. Although nanoindentation is the most readily available and widely spread technique amongst the three (also in

industrial research), the triaxial stress state and the pronounced influence of the tip geometry render the interpretation of data rather complicated. On the other hand micropillar compression tests are less established since sample preparation (i.e. by focused ion beam milling) is very time consuming and test instruments are less available but from a scientific perspective the interpretation of mechanical data is much more straight forward because of the uniaxial load case. Additionally the permanent observation of the specimen during a in situ test delivers helpful information on the deformation behavior. To bridge the gap between these test methods, the most well established uniaxial mechanical test - the tensile test - was conducted under the same experimental conditions on a dedicated small scale test rig that was developed in the frame work of this thesis. Using only one specimen has the advantage that compositional- or microstructural inhomogeneities between samples can be ruled out and hence this test is also a quantitative validation for micro scale tests. The strain rate sensitivity factor,  $m$ , and activation volume,  $V$ , are extracted as well and compared to the results of the previous section. Since the outcome of this study is also relevant from an industrial perspective as many watch manufacturers utilize only nanoindentation for assessing micromechanical properties of their materials or have to rely on available bulk data, the industrial reference nickel was tested here.

The third part of Chapter 5 introduces a novel approach to access the pronounced time dependent plastic behavior of nanocrystalline metals by a second type of transient test: micropillar load relaxation tests. Contrary to the previously introduced strain rate jump tests in a load relaxation test strain with a constant strain rate is applied up to a desired (plastic) deformation and instantaneously stopped. During the relaxation phase the load drops and the material recovers quasi-elastically. After a desired segment duration the sample is reloaded quasi-elastically to the previous load which is considered as a transient and the test is repeated. The advantage of performing repeated tests versus a single segment tests is that in a single test the microstructure is constantly evolving over the entire segment duration whereas over the short/fast reloading transient in a repeated test the microstructure is considered to remain constant. From a scientific perspective, this test is interesting as the extraction of activation volumes here provides insight into mechanisms that act on a slightly longer timescale and under different load conditions than in a strain rate jump test. Quantitatively this test is also highly relevant for watchmaking applications as many watchparts fulfill a spring function and hence have to store energy over a certain period of time. If this energy is dissipated by relaxation of the material it is no longer available for keeping the watch function at the expected precision.

## Chapter 6

In Chapter 6, the previously developed micropillar strain rate jump and load relaxation tests are applied on inert gas condensated nanocrystalline palladium gold. This material which serves as a binary model system for nanocrystalline metals in this thesis provides the advantage of extremely high purity, random texture and narrow log-normal grain size distribution. Further the grain size of this material is  $\sim 12nm$  and hence already at the lower end of the nanocrystalline regime. All these features enable an enhanced and more clear observability of nanocrystalline behavior and assist to develop a better understanding of the deformation behavior of nanocrystalline metals. Although this material cannot be directly compared to electrodeposited nanocrystalline nickel and further has no obvious applicative relevance it allows to draw conclusions towards the deformation behavior of electrodeposited materials with slightly larger grain sizes as studied in the previous Chapter.

## Chapter 7

Chapter 7 aims to connect the results from the different test methods and tests developed so far and transfer the knowledge into the Swiss watchmaking industry. First, the most relevant mechanical properties for engineering applications for watch movements, namely yield strength, Young's modulus and time dependent plastic behavior are discussed with respect to the previously achieved results.

The second part of Chapter 7 is concerned with the assessment of mechanical properties of watch making materials in a more broad manner. In that context a series of commercially available watchmaking materials, either produced by electrodeposition or hot/cold rolling, were provided in the shape of micro tensile specimen. The specimen were tested by means of room temperature tensile tests and load relaxation tests (tension as well) and the results compared to available (bulk) property values from literature. Additionally, based on the technology of the tensile test setup a small scale bending test was developed in order to test the same materials under bending conditions. From an application perspective this test is even more relevant as most watchparts are subjected to bending stresses inside a watch movement and the watch manufacturers are lacking reliable mechanical data.

The development of an electrodeposited nickel tungsten alloy is described in the third part of this Chapter. As already briefly introduced in Chapter 4 the idea is to alloy nickel with the refractory metal tungsten to impede diffusive mechanisms along grain boundaries and hence increase the thermal stability and decrease the pronounced time dependent plastic behavior which is beneficial for watch applica-

tions. As this study was conducted in the end of this thesis only preliminary results are available and a thorough in depth mechanical characterization is required, nevertheless the results are promising.

### **Chapter 8**

In Chapter 8 the results of the thesis are reviewed and summarized.

---

## 2. Basic theories of metal plasticity

Metals form probably the most important class of solid materials. They provide a series of key properties, e.g. excellent thermal and electrical conductivity. Their generally good ductility in combination with high strength - that can be significantly increased through alloying- designates them to the most reliable and widely used engineering material. Commonly their structure is crystalline, meaning that their atoms are arranged in a highly symmetric, periodical lattice. Each atom has its designated position, held in place by an elastic restoring force. If not perturbed by external forces the atoms can only oscillate around their equilibrium position. If the crystal is subjected to small external forces the whole strain gets homogeneously distributed, meaning that each single atom is moved out of its equilibrium position and the crystal is elastically deformed. This process is fully reversible and as soon as the external force is removed the entire lattice restores its initial shape. However, if the external forces exceed a material specific value the atoms irreversibly overcome their elastic threshold and move to another lattice position. When the external force increases beyond the materials plastic limit the strain cannot be propagated within the crystal anymore and as a final consequence the material fails. The following considerations and drawings are partly adapted and compiled from the following books: [13, 9, 14, 1, 15, 16, 17, 18, 19].

### 2.1. The mechanical threshold of plasticity

As previously mentioned inelastic deformation only happens after a material specific threshold is exceeded. Until this threshold is reached the whole crystal deforms homogeneously elastic. The required stress is known as the ideal shear stress. In the most simple case neighboring lattice planes are displaced against each other as illustrated in Figure 2.1.

The periodical shear stress  $\tau$  is required to displace one atom layer against another

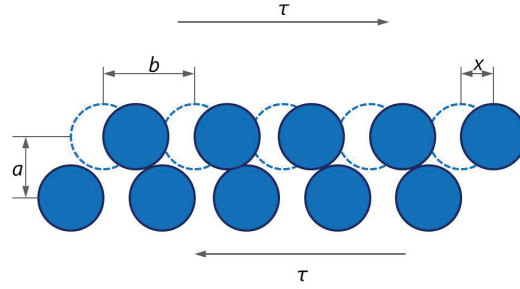


Figure 2.1.: Schematic of the determination of the critical shear stress of a perfect single crystal

and can be calculated by[20]:

$$\tau = \frac{Gb}{2\pi a} \sin \frac{2\pi x}{b} \quad (2.1)$$

where  $G$  is the shear modulus,  $a$  the lattice spacing,  $b$  the distance between atoms of the same plane towards the shear stress and  $x$  the displacement of atoms from their equilibrium position which are drawn with dashed lines in Figure 2.1. For small displacements  $x$  or small shear strains  $\gamma = x/a$  the  $\sin$  term may be approximated by  $\sin \frac{2\pi x}{b} \approx \frac{2\pi x}{b}$  which transforms equation 2.1 to  $\tau = G \cdot \gamma$ . The theoretical critical shear stress corresponds to the maximum of the pre-factor in equation 2.1:

$$\hat{\tau}_{crit} = \frac{b G}{a 2\pi} \quad (2.2)$$

According to this simplification the critical shear stress  $\hat{\tau}_{crit}$  is only a fraction of the shear modulus  $G$ . Less simplified calculations result in values of  $\hat{\tau}_{crit} \approx G/30$  [20]. However, the first bulk experiments on plasticity of single crystal metals yielded results where the stresses were a factor of 1000 below the predicted values. The discrepancy between theoretically predicted and actual experimental values resulted from a series of imperfections and defects which were found in the tested single crystals\*. Representative examples for the most common crystallographic defects are illustrated in Figure 2.2 (point defects), 2.3 (line defects) and 2.5 and 2.6 (planar defects). It can be shown that the stresses which are required to activate such defects are below the critical shear stresses for the activation of slip in entire lattice planes

\*Experiments by S.S.Brenner in the 1950's on defect free iron-, copper- and silicon-whiskers were the first who allowed to confirm the theoretically predicted stress values [21]



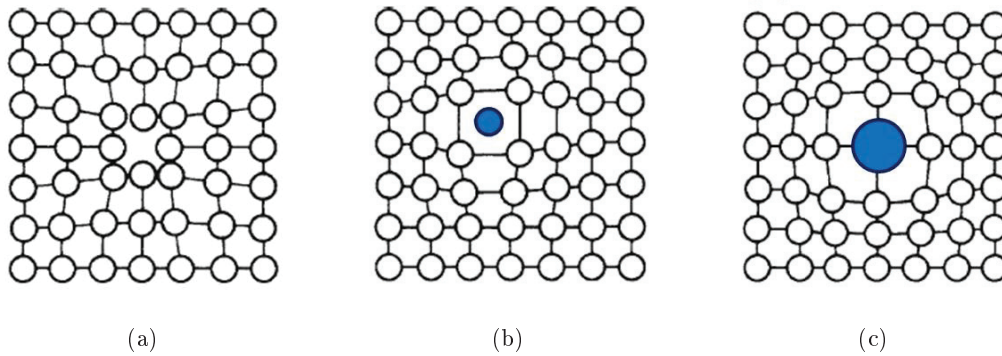


Figure 2.2.: Common point defects: (a) voids, (b) interstitial atoms, (c) larger (or smaller) foreign atoms

[13, 21]. Their activation causes local shear zones in the lattice which result in plastic deformation of the crystal below  $\hat{\tau}_{crit}$ .

Hence, in contrast to any elastic deformation which is homogeneous throughout the crystal, plastic deformation is a localized and inhomogeneous process, at least on the characteristic length scale of the activated mechanism [13]. However, in actual (bulk) experiments the number of flow defects, such as dislocations, included in the deformed volume is large. The contribution of each single defect results in a mostly homogeneous macroscopic deformation behavior of the entire volume.

## 2.2. Crystallographic defects

### 2.2.1. Dislocations

Crystallographic defects play an important role for the deformation of metals. In principle every crystallographic defect can contribute to inelastic deformation. However, under given boundary conditions like strain rate or temperature, there is always a mechanism which propagates the deformation most effectively. Based on experimental results, Orowan [22, 23, 24], Taylor [25, 26] and Polanyi [27] in the year 1934 independently developed theories in order to describe this phenomenon. They expected line defects which first have been introduced by Volterra in the year 1907 to act as the major carrier of plastic flow in metals. However, it took another two decades after Orowan's initial theories until Hirsch [28] in 1956 came up with the first TEM images and of dislocations in heavily plastically deformed aluminum foils, therewith delivering the first visible proof of the existence of dislocations in metals. In the following years, theories were refined and developed further to a much more

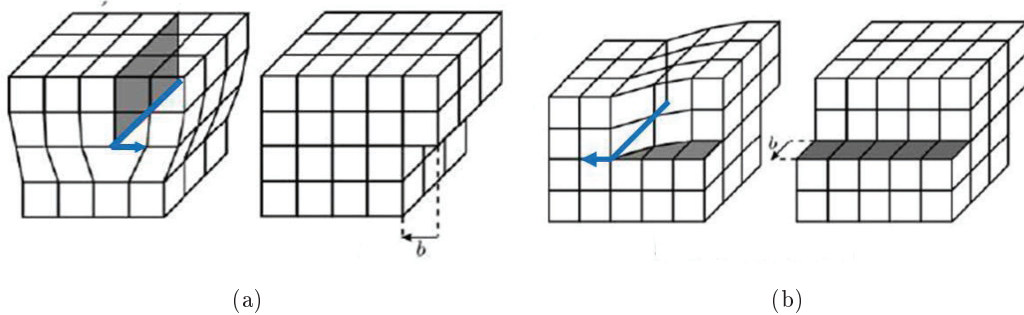


Figure 2.3.: Line defects: (a) edge dislocations (b) screw dislocations

complex level. Nowadays they allow us to understand the plasticity of common metals. Since this is a well understood field of materials science only a few key theories are described in this work. An introduction to the theory of dislocations can be found in [20] and more detailed in [13, 29, 30].

Fundamentally we differentiate between two types of dislocations: screw dislocations where the burgers vector is parallel to the dislocation vector and line dislocations where the burgers vector is orthogonal to the dislocation line. The burgers vector  $b$  indicates the direction into which atoms are transported during the movement of a dislocation segment. Its characteristic length corresponds to the distance of neighboring atoms in a slip plane. Actual dislocations are mostly combinations of various curved segments. Never the less each of these segments by itself has either line- or screw character and can therefore be described.

Only mobile dislocations which are not pinned by other defects may contribute to plastic deformation. They preferably move on planes with the largest lattice spacing towards the direction with the shortest interatomic distance. For *fcc*-metals this corresponds to the  $\{111\}$  plane towards  $\langle 110 \rangle$  directions. Considering a *fcc* unit cell with a lattice constant  $a$ , the shift of atoms per dislocation event corresponds to the shift of one atom from the corner of the unit cell to the center of one of its faces. The Burgers vector then corresponds to  $b = a/\sqrt{2}$  according to the geometrical relation. The combination of slip plane and -direction is denoted as slip system with the usual notation  $\{111\}\langle 110 \rangle$ . The *fcc* unit cell contains 12 slip systems for dislocations, however only two out of the three  $\langle 110 \rangle$ -directions are independent. Further each  $\langle 110 \rangle$ -direction can be reconstructed in one of the four  $\{111\}$  planes as spatial combinations of  $\langle 110 \rangle$ -directions in the three remaining  $\{111\}$  planes. For the sake of completeness it should be mentioned that in materials with a non-primitive lattice to which also *fcc*-metals belong, dislocations can split into partial dislocations

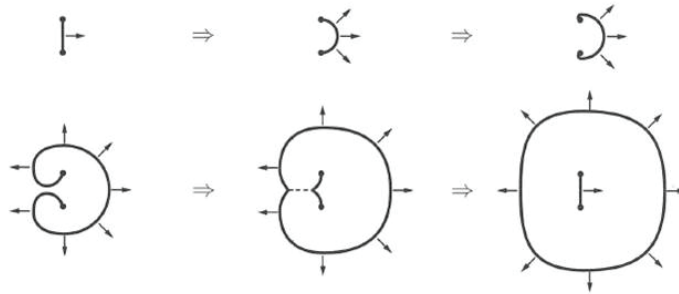


Figure 2.4.: Activation of a Frank-Read-source

with a shorter Burgers vector. This can happen if the dislocation line energy  $E_L \approx Gb^2$  is reduced according to the *Frank-criterion* [31]  $b^2 > b_1^2 + b_2^2$ . Unlike perfect dislocations which do not change the crystal symmetry due to their self similar propagation, individual partial dislocations can leave stacking faults in the lattice. Although a stacking fault can be annihilated by a following partial dislocation, the increase in stacking fault energy is generally considered as evidence for the activation of partial dislocations.

### 2.2.2. Dislocation sources

Mobile dislocations that reach the surface of a crystal disappear, leaving a step with the height of the burgers vector on its surface. Hence, without the ability of dislocation multiplication, flow defects would get exhausted and the plastic deformation would seize already at small plastic strains. However, most metals show decent ductility which means that they must contain dislocation sources. The most common is the so called Frank-Read-source [16] of which a schematic is shown in Figure 2.4.

A line dislocation segment encounters two obstacles in a slip plane and gets pinned. Increasing external stress causes the pinned segment with the length  $l$  to bow out which leads to a decreasing curvature radius  $r$ . The line tension of the dislocation segment acts in the opposite direction, trying to increase  $r$  and keep the segment straight. The stress which is required to bow out a dislocation segment can be estimated by

$$\tau_0 = \alpha \frac{Gb}{r} \quad (2.3)$$

Here  $\alpha$  is a dimensionless factor, commonly with values between 0.5 and 1 [20] and  $G$  is the shear modulus. Equation (2.3) suggests that the stress  $\tau_0$  increases with

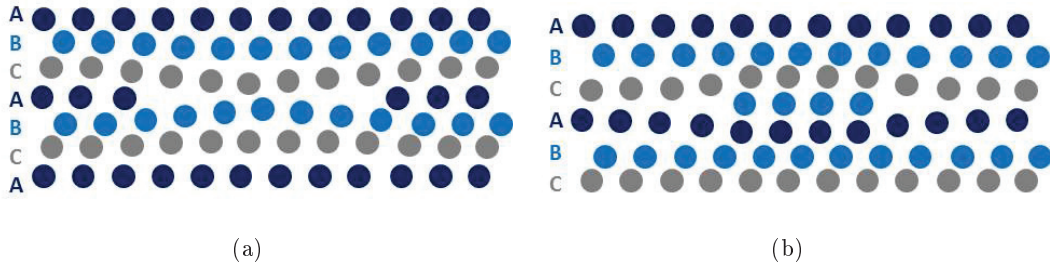


Figure 2.5.: Stacking faults: (a) ABC|BCA (b) ABC|B|ABC

decreasing curvature radius  $r$  which reaches its minimum  $r = l/2$  in the aforementioned half circle configuration. Beyond this point  $r$  increases again which means that any further bow out is no longer driven by external stresses. The two dislocation segments propagate until they collide and create a dislocation ring, as well as a new line segment between the pinning points, allowing the whole process to start again.

Active dislocation sources do not only contribute to the generally decent ductility of metals. They are also responsible for their commonly observed work hardening. After exceeding the yield stress, the stress level which is required to propagate plastic deformation keeps increasing which can be explained by the increase of dislocation density. It takes more energy to move a dislocation through the stress field of another dislocation than through a perfect (defect free) lattice. Hence, the increase of dislocation density hinders their mobility due to dislocation-dislocation interaction.

### 2.2.3. Planar defects

#### Stacking faults

Stacking faults are planar defects and usually disturb the regularity of the common  $ABCABCABC$  stacking sequence of close-packed  $\{111\}$ -planes in the  $fcc$ -lattice. Representative examples are illustrated in Figure 2.5. The stacking sequence in the respective area is interrupted and the four planes in close vicinity to the fault emulate the  $BCBC$ -basal planes of the  $hcp$ -lattice which creates an obstacle for dislocation glide. Stacking faults can be formed directly during the crystallization/ growth process of a metal/alloy or by the movement of partial dislocations during plastic deformation. They readily occur when the stacking fault energy difference between the  $fcc$ - and  $bcc$ -lattice is low.

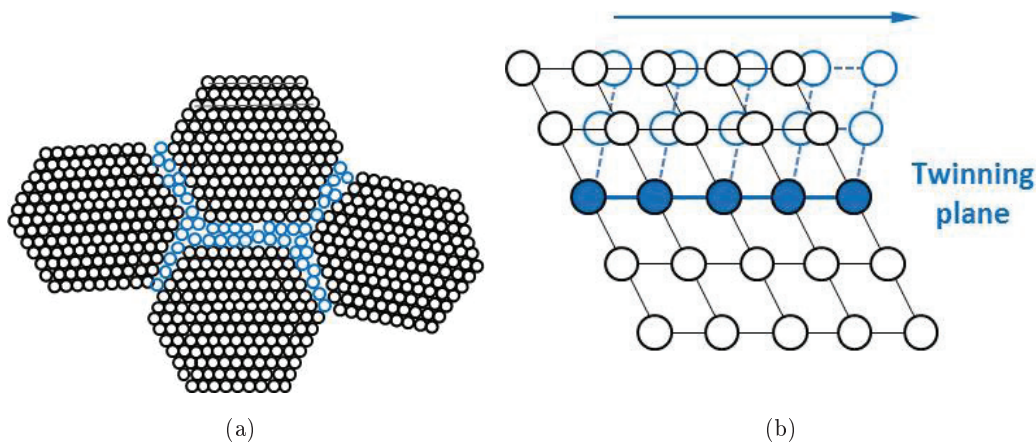


Figure 2.6.: Schematic of grain boundary (a) and twin boundary (b).

### Grain boundaries

The most important group of planar defects are grain boundaries. During growth, crystallization or recrystallization processes the misorientation angle between two neighboring crystallites is usually large ( $\alpha > 5^\circ$ ) [19] which causes the formation of a so-called high angle grain boundary as represented in Figure 2.6(a). The boundary consists of an irregular arrangement of atoms with an approximate width of two to three atoms and creates a highly effective barrier for dislocation glide (see also Chapter 3.1.2). Low angle grain boundaries consist of a series of several ordered dislocations which cause a slight misorientation ( $\alpha < 5^\circ$ ) in neighboring lattices. Two types are differentiated by the nature of the dislocations they are formed of: tilt grain boundaries (edge dislocations) and twist grain boundaries (screw dislocations). However, compared to high angle grain boundaries the energy of both types is lower which causes them to be less effective barriers for dislocation glide.

### Twin boundaries

Twin boundaries are high angle interfaces between lattices with a large number of coincident atom positions. As illustrated in Figure 2.6(b) the mirror plane (blue line) forms the interface and the lattice atoms on both sides remain in fixed angular positions. Twinning is usually observed in the  $\{111\}$ -planes of *fcc*-metals with low stacking fault energies during deformation or thermal treatment where, similar to the formation of a stacking fault, the stacking sequence changes to *ABCABCBCBA*.

A third twinning mechanism is growth twin formation in electrodeposited metals.

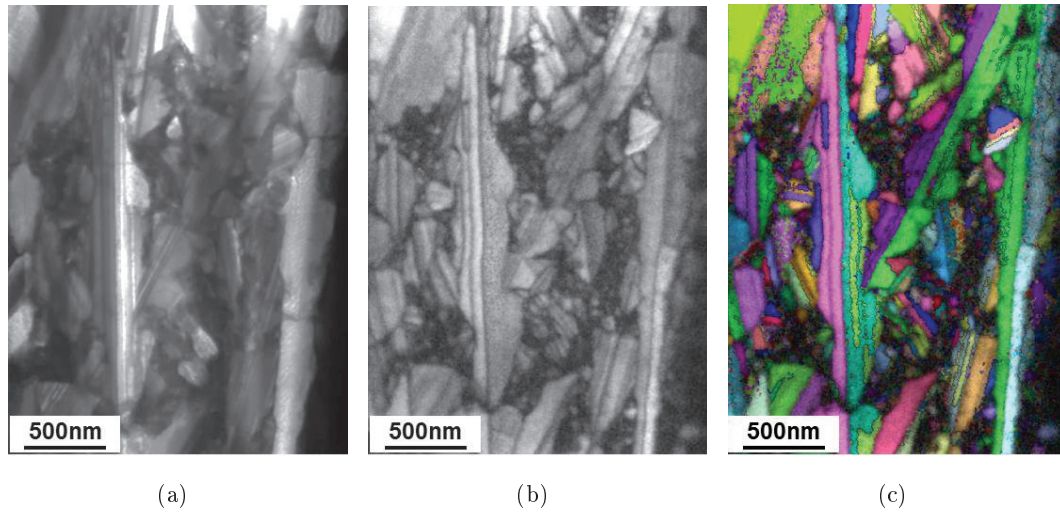


Figure 2.7.: STEM image of nanotwinned NiW (3.6 at.-%) electrodeposit (a) with corresponding transmission kichu diffraction (TKD) pattern quality map (b) and orientation map (c) (see Chapter 7.4). The images suggest the formation of nano twins directly during the deposition process.

Although this mechanism is not fully understood [32] it is probably related to the relatively small excess energy of coherent twin boundaries. Since twins preferentially nucleate at grain boundaries this leads to a decrease in total interfacial energy which is a preferred state. The process itself is kinetically driven and strongly dependent on the bath chemistry as well as the deposition parameters. It has been found experimentally [32, 33] that a high deposition rate which is influenced by high current density, large pH value of solutes and low deposition bath temperatures enhance the formation of twins. There it was argued that under such conditions grain boundaries and triple junctions with higher excess energies were formed because of the limited relaxation what leads to a larger nucleation rate of twins. An illustrative example for growth nano twins that were observed within the framework of this thesis in electrodeposited nickel-tungsten is given in Figure 2.7 and further discussed in Chapter 7.4 .

### 2.3. Activation volume and dislocation activity

The fact that crystallographic defects act as obstacles for dislocation motion allows to draw a simple interpretation of the activation volume as it is illustrated in Figure 2.8. A shear force  $\tau_a b$  acts on a dislocation segment with the length  $2l$ . If no obstacles

are present, the dislocation segment would bow out to a radius  $R_r$ . However, in this scenario an obstacle sits in the middle of the segment and blocks it from bowing out freely. Instead, the segment bows out not as a whole but in two sub-segments, each with a radius  $R_i$ . To pass the obstacle and reach the segments preferred saddle point configuration an activation distance  $\Delta y$  has to be overcome by the aid of thermal fluctuations. During this process both segments sweep an activation area  $\Delta a$ . Multiplying the activation area  $\Delta a$  with the Burgers vector of dislocation  $b$  yields the activation volume  $\Delta v_{\tau a} = b\Delta a$ . When the obstacle is passed, both segments try to minimize their line energy and merge until they have reached the saddle point configuration at  $R_r$ . The entire area which was swept by the dislocation segment(s)  $\Delta A$ , multiplied by the distance between the glide planes  $d$  yields the entire volume  $\Omega_f$  of the flow defect. Accordingly the activation dilatation is  $\Delta\gamma_{af} = b\Delta a/\Omega_f$ . On an atomic scale, all the atoms within the activation volume  $\Delta\gamma_{af}$ , as well as their next neighboring atoms, have to fulfill a collective thermal oscillation towards the saddle point configuration in order to overcome the obstacle.

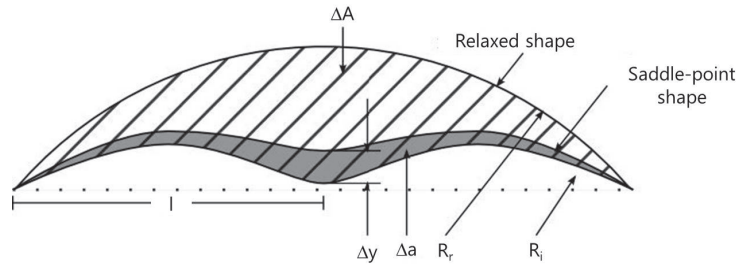


Figure 2.8.: Activation volume





---

## 3. Nanocrystalline metals

### 3.1. General considerations

Metals are mostly not found as single crystals but as polycrystals. In contrast to single crystals, the deformation in polycrystals cannot simply propagate in a single glide system which spreads all over the sample. Neighboring crystals can have significantly different orientations which cause the deformation not to be able to propagate easily from one grain into another. Consequently, the lattice misorientations cause stress concentrations at grain boundaries and triple points until they are able to activate less favorable glide systems in neighboring grains. Hence, in a polycrystal, plastic strain is propagated on an individual percolating trail, defined by the crystal itself. Necessarily the crystallites have to be able to deform freely in order to maintain an overall compatible deformation. A general description of plastic deformation at constant volume requires five independent strain components. Transferring these relations to the plastic regime [25], again five independent slip systems are required in order to propagate a compatible deformation. As explained in more detail in section 2.2.1, *fcc*-metals fulfill these requirements and hence provide good ductility even as polycrystals. These theories are generally well understood since a long time and valid for grain sizes from the higher *mm* down to the lower  $\mu m$  regime. However, a lower grain size limit exists at which the former assumptions as such become invalid. This limit is commonly around  $100nm$  and marks a significant change of material properties and deformation mechanisms. Therefore, in this section some of the key features of these so called „nanocrystalline“ metals are discussed.

#### 3.1.1. Size effect

Miniaturizing materials and components for modern technological applications like MEMS or micromechanical structures is a continuously evolving field of interest. However, employing the unique features of microcomponents is not possible by simply downscaling dimensions and properties from the macro scale since both, material- and component properties may change by varying their length scales over several

orders of magnitude. Key material properties such as yield strength, hardness, wear resistance, magnetic coercivity or electrical resistivity are sensitive to the materials extrinsic and intrinsic length scales. This phenomenon, of which there is still a lack of understanding, is commonly known as size effect [34].

For bulk materials the mechanical behavior is generally well understood and proven experimentally as well as by means of models. It is normally size independent since the length scale of occurring effects (i.e. dislocation-dislocation or dislocation-grain boundary interaction) is several orders of magnitude smaller than the actual component size. Whereas the elastic behavior of materials is determined by the atomic bonds with lengths in the range of ( $\sim 0.1nm$ ), plasticity in metals involves the motion of dislocations. This motion is hindered by obstacles like precipitates or grain boundaries when they are closely spaced, i.e. in the order of less than  $\sim 100nm$ . At larger distances, other effects like fatigue ( $1\mu m$ ) or fracture ( $\sim 100\mu m$ ) can take place [35]. A size effect can therefore be defined as a change in the mechanical properties of metals due to a change in either the dimensions of an internal feature (*intrinsic size effect*) or structure or in the overall physical dimensions (*extrinsic size effect*) of the material [36]. Hence, it can be concluded that it is necessary to probe micromechanical parts which are in a size range from  $< 1mm$  down to  $\sim 1\mu m$  with respect to the length scale of the strengthening effect [35].

### 3.1.2. Strength

Strengthening a material means in principle to increase its ability to withstand irreversible deformation. In case of polycrystalline metals this is commonly achieved by forming obstacles which hinder dislocation motion since they are known to be the major carrier of plastic flow. As an example the formation of precipitates in the matrix during age hardening or introducing foreign atoms as solutes or interstitials can be mentioned [19]. Also dislocations themselves can block their motion as it is the case in strain hardened materials, where high densities of dislocations are introduced on purpose by plastic deformation. However, in the context of nanocrystalline materials, the most significant strengthening effect is considered to be grain refinement. Grain boundaries are defects and therewith obstacles to dislocation motion. When a dislocation moves out of a crystallite (through a grain boundary) it leaves a slip step with the size of one Burger's vector on the surface. However, the neighboring grains are very close and hinder the formation of slip steps due to the already mentioned lattice misorientations. Hence, several dislocations pile up at a grain boundary until the local stress is high enough to activate a slip system in a neighboring crystallite

and create enough space to develop a slip step. This relation, commonly known as the Hall-Petch relation [37, 38], has been described first in the 1960's through the following equation:

$$\sigma_Y = \sigma_0 + \frac{k}{\sqrt{d}} \quad (3.1)$$

where  $\sigma_Y$  is the yield strength,  $\sigma_0$  the Peierl's- or lattice stress,  $k$  a constant and  $d$  the grain size. As illustrated in figure 3.1 (a) stress induced pileup of dislocations in one grain create a stress concentration, leading to the activation of dislocation sources (e.g. Frank-Read source) in neighboring adjacent grains [1]. Other mechanisms related to the Hall-Petch effect have been proposed, introducing the activation of dislocation sources at grain boundary ledges [39] or the formation of a hardening network at grain boundaries due to elastic-/plastic incompatibility stresses [7].

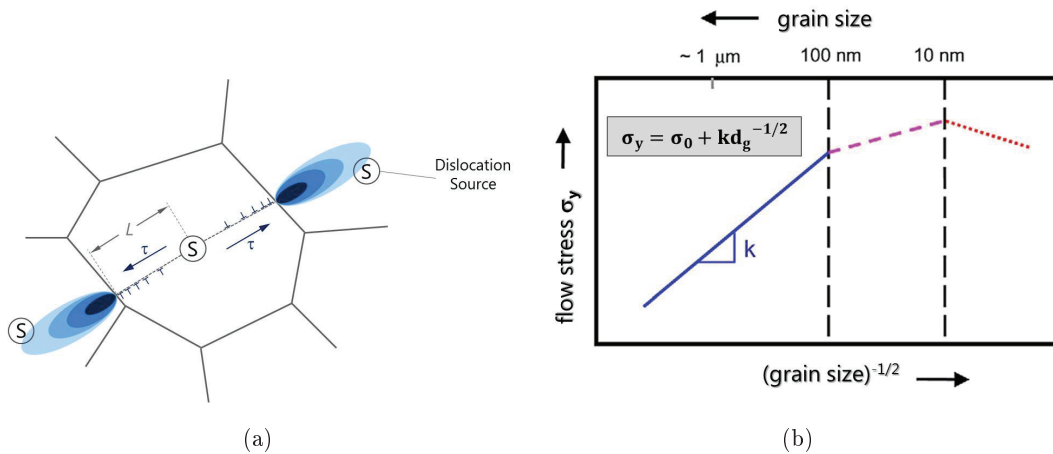


Figure 3.1.: Schematic of dislocation pileup in a grain as described by Cottrell [1] (a) and representation of the variation of yield stress as a function of grain size [2] (b).

The proposed mechanisms have two things in common: They involve dislocation activity and the yield strength scales with the inverse square root of the grain size. Consequently, when decreasing the grain size of a certain metal to the smallest imaginable values, its theoretical strength should be achieved [40]. But in fact, it was found that the HP-relation does not hold for grain sizes below  $\sim 100\text{nm}$ , as can be seen from several series of experiments [41, 42, 43]. Then the extremely small grain size of nanocrystalline metals leads to a fundamentally different plastic deformation behavior as it is found in coarse grained polycrystalline metals. Figure 3.1 (b) displays a model for the dependency of flow stress over the inverse square root of grain

size. In the regime from conventional polycrystalline down to grain sizes of  $\sim 100\text{nm}$  the flow stress increases with decreasing grain size as suggested by conventional Hall-Petch relationship. When the grain size becomes smaller than approximately  $\sim 10\text{nm}$ , a transition from dislocation mediated (intragranular) behavior towards grain boundary mediated (intergranular) behavior takes place. This circumstance is illustrated in Figure 3.2 (a) where the significant increase of relative intercrystalline volume with decreasing grain size is plotted while Figure 3.2 (b) specifically denotes the dependence of grain boundary volume on grain size as a function of grain boundary width [3]. Hence, the absence of dislocation activity inside the grains would be a possible explanation for the negative slope, often referred to as 'inverse' Hall-Petch effect [42]. Possible mechanisms which may be responsible for this transition can include grain boundary sliding, grain rotation and diffusional creep [44] as shown in figure 3.4. But, although the actual trends still have to be determined, it is likely that a combination of some or all of the aforementioned mechanisms operate in this grain size regime [45]. However, the least well understood is the intermediate regime from  $\sim 100\text{nm}$  to  $\sim 10\text{nm}$ . Here, most likely a competition between conventional lattice dislocation slip and diffusional deformation exists with a strong dependence on grain size distribution. How these mechanisms interact with each other is still not completely sorted out [46, 47, 48, 49, 50, 51, 52, 53, 54]. General assumptions are that larger grains may still deform through dislocation slip mechanisms while smaller grains may already deform by grain boundary mediated mechanisms.

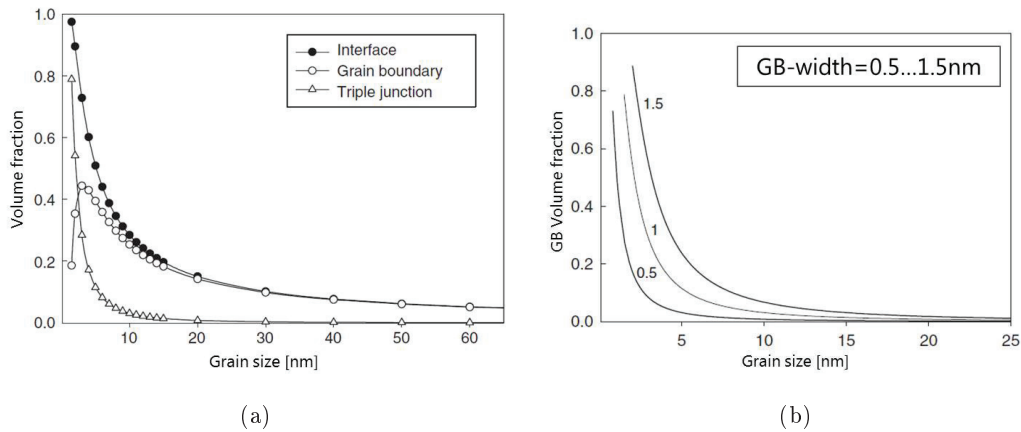


Figure 3.2.: Estimation of intercrystalline volume as a function of grain size (a) and grain boundary volume as a function of grain size and boundary width (b) (both [3]).

Although the actual mechanisms are still under debate (see e.g.: [49, 55, 56, 57])

the overall consensus is that at grain sizes in the nanometer regime the dislocation mediated processes become less and less important and grain boundary mediated mechanisms come into play. Molecular dynamics (MD) simulations indicate that the bulk of deformation in nanocrystalline copper and aluminum is accommodated by means of a combination of grain boundary sliding (see 3.2.1) and the emission of dislocations that do not interact with other dislocations until they are absorbed in neighboring grain boundaries [58, 59, 60]. In situ TEM and XRD experiments confirmed these observations and suggest that nanocrystalline metals do not allow dislocation networks to be established during plastic deformation [61, 62, 2, 63]. The following two simple examples may assist in validating the possibility of these assumptions in the intermediate and the lower nanocrystalline regime. The foundation here is the calculation of the stress which is required to activate a Frank Reed source in a nanocrystal. The dislocation source needs to fit entirely into the crystal. Hence, the minimal bow out radius must not be larger than half the crystal diameter which leads to  $r_{nc} = d/2$ . According to established theories (see 2.3) the minimal activation stress is  $\sigma_0 > \sqrt{3}Gb/d$ . First inserting actual values for electrodeposited nanocrystalline nickel with an average crystallite size  $d_{ncNi} = 30nm$  (measured by XRD), a shear modulus  $G_{ncNi} = 65GPa$  and a Burger's vector  $b_{Ni} = 0.223nm$  results in  $\sigma_{0,ncNi} \sim 0.97GPa$ . This value is well below the average flow stress  $\sigma_{flow,ncNi} \sim 1.5GPa$  and indicates that dislocation sources may still be active in this grain size regime. Secondly, applying the same equations for an inertgas condensated nanocrystalline palladium-gold alloy with  $d_{ncPdAu} = 10nm$ ,  $G_{ncPdAu} = 46GPa$  and  $b_{PdAu} = 0.275nm$  results in  $\sigma_{0,ncPdAu} \sim 2.19GPa$  which is well above the average yield stress  $\sigma_{flow,PdAu} \sim 1.7GPa$ . Therewith, the activation of a Frank-Read source in a  $10nm$  grain seems unlikely. However, dislocation mediated plasticity cannot be entirely ruled out in the lower nanocrystalline regime since other mechanisms can be responsible for the emission of dislocations, e.g. emission of partial dislocations and/or nucleation from triple points [64]. From Figure 3.2 it can be clearly seen that the average grain boundary volume approximately doubles when the crystallite size is decreased from  $30nm$  to  $10nm$  and hence, increases the likelihood of grain boundary mediated processes. The reduced ductility of nanocrystalline metals also points in this direction, since the absence of stable dislocation networks suppresses dislocation multiplication mechanisms and hence less effective deformation mechanisms which are related to grain boundaries come into play. Another aspect which renders the deconvolution of mechanisms rather complex is that materials mostly do not provide a uniform grain size distribution. Especially in electrodeposited materials, it is possible that larger grains are included in the specimen. If these large

grains fall within the examined specimen region they may still deform classically by dislocation slip mechanisms whereas the deformation of smaller grains is localized to the boundary regions.

### 3.1.3. Young's modulus

Most engineering applications consider material deformations which are, at least in a first approximation, reversible. This so called elastic stiffness is an, again in a first approximation, intrinsic property of every material. From an engineering point of view, knowing the elastic properties of a material is crucial to design mechanical components. At an atomic length scale, elastic strain refers to changes in interatomic spacing [19]. Atomic bonds have to stretch when atoms move out of their „equilibrium“ distance, e.g. due to external stress. Consequently and when neglecting other factors that may contribute to the elastic behavior, the macroscopically measured Young's modulus reflects the strength of the atomic bonding. When taking other factors into account, a controversial discussion exists on how the Young's modulus is influenced in nanocrystalline metals. A main feature of this type of materials is that they have a relatively large amount of interface volume. The atomic disorder in grain boundaries is larger than within the lattice [65] as well as the average atomic spacing. Therefore it could be concluded that grain boundaries overall exhibit lower bond strengths than intragranular regions and their Young's moduli are lower than those of their polycrystalline counterparts. In contradiction to this theory, simulations suggest exactly the opposite [66] when taking into account that grain boundary stiffness may be enhanced by a very low number of atoms where inter atomic distances are smaller than equilibrium due to asymmetry in interatomic potential.

In fact, the Young's modulus of nanocrystalline metals depends strongly on the way how materials have been processed since factors like porosity and crystallographic texture may significantly decrease it in certain directions. Grain size influences the Young's modulus only when below  $\sim 10nm$  as can be concluded from Figure 3.3 (a). In Figure 3.3 (b) the Young's moduli of nanocrystalline Cu and Pd measured by a pulse-echo technique are plotted over the fraction of porosity. As can be seen from the fitted curves already for porosities of 1% the moduli of both tested materials lie approximately 5% below the theoretical reference for fully dense material and decrease further with increasing porosity.

The anisotropy of elastic behavior of electrodeposited nanocrystalline nickel has been studied by Hemker and Last [6]. They tried to find an explanation why some reported Young's moduli were very close to the bulk modulus of polycrystalline nickel

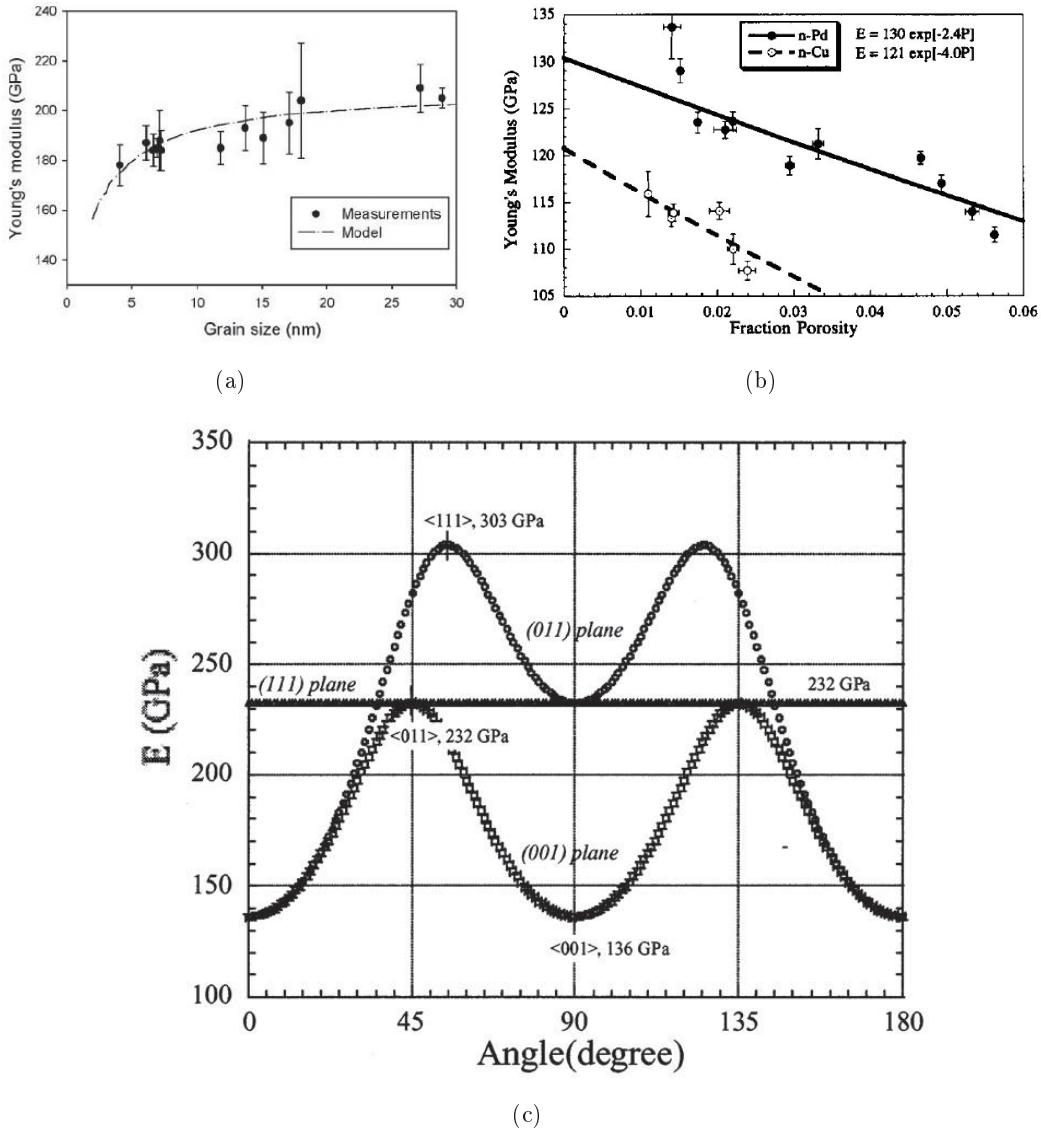


Figure 3.3.: Young's modulus as function of porosity in nanocrystalline Cu and Pd [4] (a) and Young's Modulus of electrodeposited nanocrystalline Ni and NiP alloys as a function of grain size [5] (b). Young's moduli for the various directions in the  $\{001\}$ ,  $\{011\}$  and  $\{111\}$  planes, calculated using the compliance matrix  $[S_{ij}]$  for single crystalline Ni [6] (c).

$E_{Ni,bulk}=207GPa$ , whereas his experimental findings and others were far below. He calculated the Young's moduli for various directions in the  $\{001\}$ ,  $\{011\}$  and  $\{111\}$  planes of a nickel single crystal. A plot of the resulting values as a function of angle  $\Theta$  are given in Figure 3.3(c). According to this model, for the  $\{001\}$ -plane a variation of Young's modulus from  $E_{\langle 001 \rangle}=136GPa$  to  $E_{\langle 111 \rangle}=303GPa$  is possible. Additionally he conducted tensile tests on  $\sim 200\mu m$  thick nanocrystalline nickel samples with a  $\{001\}$  out-of-plane texture, yielding an average of  $E\sim 180GPa$ . The experimental results he obtained match nicely with the average Young's modulus from his calculation of  $E_{\{011\}}=171-177GPa$  when assuming a random in-plane orientation of grains.

## 3.2. Review of the most relevant deformation mechanisms

An abundance of possible deformation mechanisms in nanocrystalline metals is debated in literature. Atomistic simulations usually assume strict boundary conditions, i.e. extremely low temperatures or high strain rates and very short time frames, and hence provide results which are very specific and may not be observable from conventional experiments. On the other hand, the complex ensemble of possible mechanisms which can be studied by means of suitable small-scale experiments makes it difficult to assess specific information but delivers a more broad overview over what happens in the nanostructure upon deformation. In addition, the nomenclature used in different literature sources is not unity which makes it difficult to directly compare the huge number of studies present. Therefore, in this , only the most relevant and accepted mechanisms as depicted in Figure 3.4 will be briefly reviewed.

### 3.2.1. Grain boundary sliding

In a lot of discussions, the term grain boundary sliding (GBS) is used in a broad sense, even when the general term grain boundary mediated deformation appears more appropriate. It should be noted that GBS is a very distinct mechanism which is classically associated to creep but nevertheless relevant in the context of nanocrystalline metals. In polycrystalline metals GBS denotes the displacement of two adjacent grains along a shared interface under the application of external stress. Two mechanically different types of GBS are distinguished: Lifshitz GBS [67] and Rachinger GBS [68]. Both processes occur under creep conditions, i.e. at a higher fraction of the materials melting temperature ( $T > 0.5T_m$  [69]) and produce similar offsets in



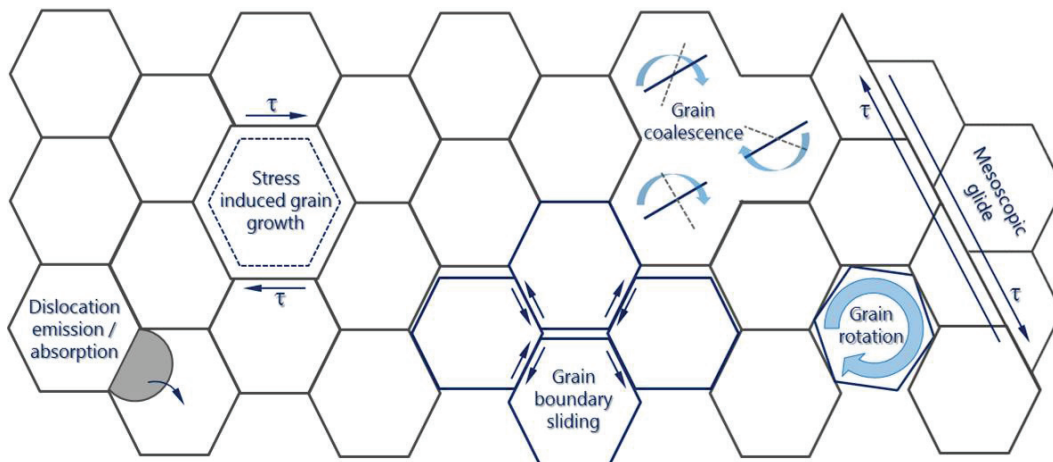


Figure 3.4.: Proposed plastic deformation mechanisms in nanocrystalline *fcc*-metals.

grain boundary marker lines. The Rachinger mechanism requires accommodation by intragranular dislocation glide and climb. The original shape of the sliding grains is generally retained. Lifshitz sliding is self-accommodating and mediated by the stress- and temperature driven diffusion of vacancies, similar to diffusional creep. Hence, the shape of the grains becomes elongated along the axis of the applied tensile stress as depicted in Figure 3.5.

Extending the theory to nanocrystalline materials it is helpful in a first approach to look into the rate equation model for Rachinger GBS and assume the boundary conditions for superplasticity at small grain sizes  $d < \lambda$  where  $d$  denotes the grain size ( $d < 100nm$ ) and  $\lambda$  is the size of an average subgrain which traditionally forms during creep in larger polycrystals:

$$\dot{\epsilon}_{GBS(d<\lambda)} = \frac{A' D_{GB} G b}{kT} \left(\frac{b}{d}\right)^p \left(\frac{\sigma}{G}\right)^n \quad (3.2)$$

where  $A'$  is a dimensionless constant with experimental values  $\sim 10$  and  $D_{GB}$  is the grain boundary diffusion coefficient. As it is assumed that all the creep deformation is accommodated by the Rachinger mechanism, the stress exponent can be experimentally determined to  $n \approx 2$  and an inverse grain size exponent  $p \approx 2$  [70, 71, 72]. Although Equation 3.2 suggests that the described process is diffusion controlled and hence not necessarily relevant at low homologous temperatures there are predictions of GBS in nanocrystalline metals with grain sizes  $< 10nm$  from molecular dynamics simulations [2, 73, 74, 59, 75]. However, it is nearly impossible to experimentally discriminate GBS from other deformation concepts like shear transformations (see

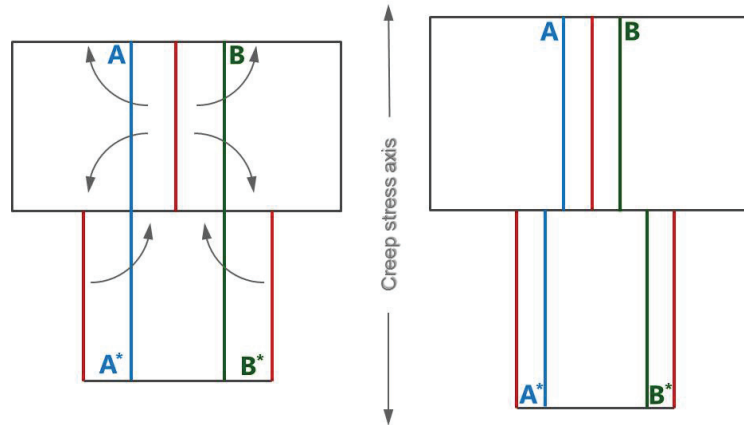


Figure 3.5.: Schematic of Lifshitz GBS under diffusional creep conditions.  $A(A^*)$  and  $B(B^*)$  are marker lines.

section 3.2.5) which themselves lead to grain boundary marker line shifts, even when creep conditions are not fulfilled.

### 3.2.2. Grain rotation and grain coalescence

During a plastic deformation process the stress exerted by their neighbors can force individual grains to rotate [76, 77]. In polycrystalline metals this often leads to the measurable formation of a preferred orientation, caused by the activation of multiple slip systems within the grains. However in very fine grained nanocrystalline metals it is, as previously discussed unlikely that such a scenario is only caused by a wealth of intragranular dislocations. For instance texture formation was not observed in a heavily cold rolled nanocrystalline palladium with a nominal grain size of  $\sim 6nm$  [78]. Another cause for grain rotation can be the previously discussed grain boundary sliding (see section 3.2.1), however this mechanism usually accommodates strain only at rather high homologous temperatures or very small grain sizes. Figure 3.6 depicts a possible grain rotation and grain coalescence scenario, caused during the accommodation of shear stress induced deformation. The slip system with the highest Schmid factors are represented as grey lines in the center of the rotating grains. As the grains rotate their relative misorientations are reduced and eventually the grain boundary between them gets annihilated. The newly created grain provides a severely longer path or fewer barriers for dislocation motion and hence, strain localization or softening can occur.

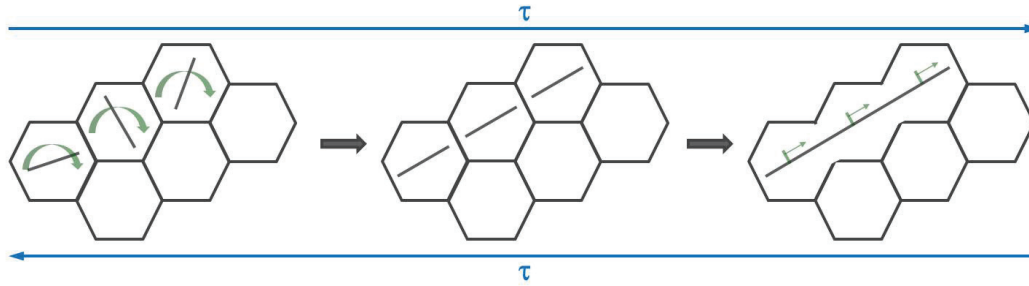


Figure 3.6.: Schematic of a stress induced grain rotation process in a nanocrystalline metal. Subsequent grain boundary annihilation creates large elongated grains (after [7]).

### 3.2.3. Stress driven grain boundary migration

Stress driven grain boundary migration (*SDGBM*) can occur in nanocrystalline metals as they are subjected to external shear stress. It manifests itself in localized growth of individual grains or grain clusters. An overall change in mechanical properties during the deformation process can be observed as larger grains open pathways for more conventional (i.e. dislocation based) deformation mechanisms. In accord to the *LeChatelier-Braun* principle\* external stress can partly be accommodated/relieved by grain growth. Hence in nanocrystalline metals, this mechanism serves as a system-intrinsic softening mechanism as the growth/coalescence of grains opens pathways for extended dislocation motion (see also 3.2.2) and stresses below the work-hardening regime can be maintained. Gianola et al. [8] investigated the nanostructural evolution of nanocrystalline aluminum thin films by means of in situ tensile tests in a synchrotron. They observed that some specimen developed regions of increased and very localized plasticity. Postmortem TEM analysis at different stages of plastic deformation as illustrated in Figure 3.7 revealed patterns of discontinuous grain growth in these specimen whereas other specimen that did not exhibit changes in plastic behavior also did not show microstructural changes.

Similar experimental results were found by indentation studies on nanocrystalline aluminum [80] and nanocrystalline and ultrafine grain copper [81]. Further, molecular dynamics simulations of the behavior of nanocrystalline copper under cyclic

\*The principle which was independently discovered between 1884 and 1888 by Henry Louis Le Chatelier and Ferdinand Braun empirically describes the reactions of a system in equilibrium which is disturbed by external influences. It states that a system tends to partially counteract the effects of the disturbance through establishing a new equilibrium [79]

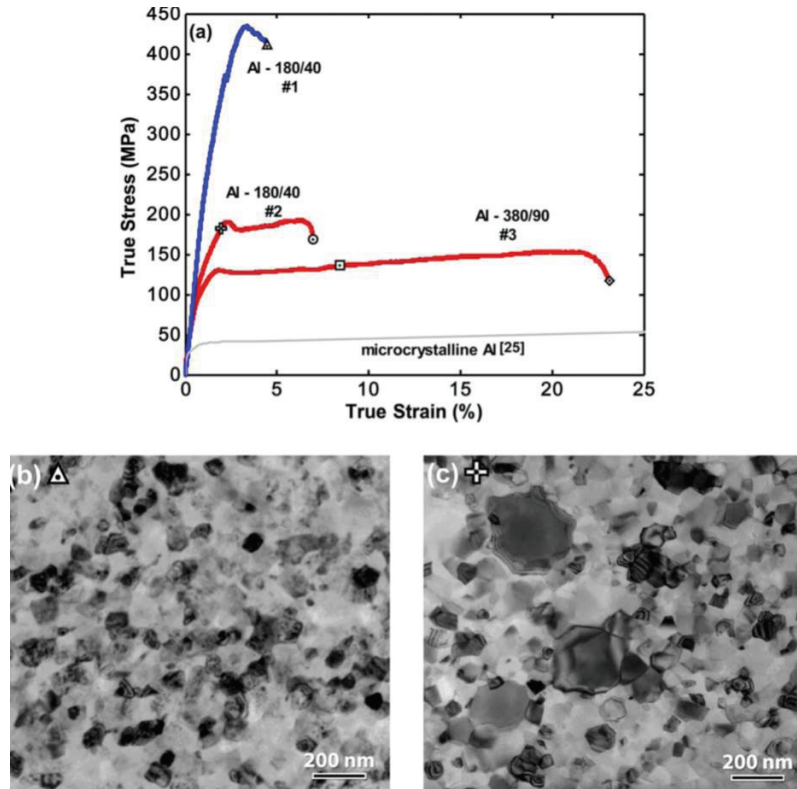


Figure 3.7.: (a) Stress-strain curves #1 and #2 represent two different types of deformation behaviour in nanocrystalline aluminum with a nominal grain size of 40nm. TEM-images reveal the postmortem microstructures: (b) corresponds to curve #1 and shows a uniform grain size distribution whereas (c) corresponds to curve #2 where the nanostructure has obviously coarsened (reprinted from Gianola et al. [8]).

loading conclude that enhanced grain boundary mobility during deformation enables grain boundaries to migrate, resulting in an overall coarsening of the specimen structure [82].

### 3.2.4. Mesoscopic glide

At high plastic strains  $\varepsilon > 0.5$  another deformation mechanism designated as *mesoscopic glide* can be activated. Mesoscopic glide is enabled by antecedent mechanism like grain boundary sliding, grain rotation or -coalescence which preferentially occur at lower plastic strains and closely related to those. In the course of deformation the orientation of individual grains can align and form coplanar clusters of grain boundaries which manifests in the formation of a crystallographic texture localized

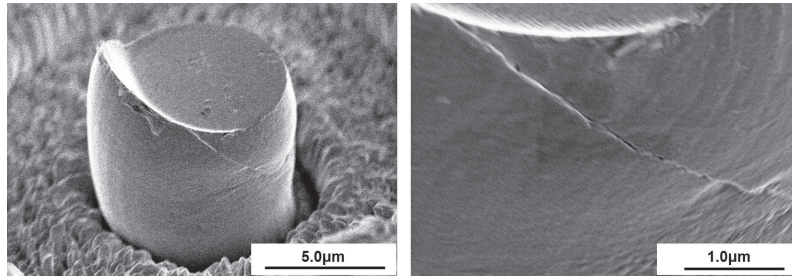


Figure 3.8.: SEM images of macroscopic shear band formation observed after compression of an inertgas condensated  $\text{Pd}_{90}\text{Au}_{10}$  micropillar at room temperature. The strain rate was  $\dot{\epsilon} = 10^{-1} \text{s}^{-1}$ .

to these regions. The reduced grain boundary misorientation consequently assists in the cooperative slip of neighboring crystallites and ultimately forms a mesoscopic glide plane. As such a glide plane encounters obstacles i.e. non-aligned grains it can propagate through the grain by means of intragranular slip.

In the higher nanocrystalline size regime  $d > 40 \text{nm}$  mesoscopic glide was observed in palladium [83] and iron [84] and also in ultrafine grain aluminum [85]. The tested specimen all revealed significantly elongated grains and texture formation, suggesting similarities to the conventional dislocation based shear band formation mechanisms in polycrystalline metals. However, in the lower nanocrystalline regime  $d < 20 \text{nm}$  in situ synchrotron studies on initially randomly textured PdAu-alloys [83, 86, 87] revealed that, even at degrees of deformation larger than  $\epsilon > 0.5$  the grain shape did not change markedly and no (or very small formations of) deformation texture was observed. In those studies the nanostructure remained mostly unchanged and shear band formation occurred already at the onset of the fully developed plastic regime. This suggests that for very small grain sizes the observed shear banding is induced by grain boundary mediated mechanisms rather than by dislocations. Nevertheless these findings cannot serve to exclude the activity of dislocations as they still may be present in grain boundaries or within the nanograins. Macroscopic shear band formation was also observed during in situ micropillar compression experiments on an inertgas condensated  $\text{Pd}_{90}\text{Au}_{10}$  specimen with a nominal grain size of  $\sim 10 \text{nm}$ . Figure 3.8 shows the SEM images of the postmortem state after compression at room temperature to a strain of  $\epsilon \sim 40\%$  at comparably high strain rates in the order of  $\dot{\epsilon} = 10^{-1} \text{s}^{-1}$ . The shear band is traversing the entire micropillar cross section.

### 3.2.5. Shear transformation zones

Another interesting approach to describe the plastic deformation of nanocrystalline metals with very small grain sizes is found in the theory of deformation in metallic glasses. In contrast to highly ordered crystalline metals, metallic glasses provide no crystallographic long range order. They are amorphous and in absence of any translation symmetry. Hence, stable dislocation networks are not available to accommodate plastic strain in these materials. Characteristically metallic glasses deform via shear transformation zones (STZ) [9, 88]. STZ are flow defects which evolve in individual regions where strain is heavily localized [17, 89]. Figure 3.9 illustrates the principle. Although the nature of plastic deformation in metallic glasses is not fully understood, the STZ-model is essentially referred to as a local cluster of atoms which fulfills a shear movement in-between two low energy configuration by overcoming a state of higher energy. Unlike dislocations on GBS this mechanism is not observable, i.e. in a TEM. It actually is considered as a fluctuation of a cluster of up to  $\sim 100$  atoms and not a microstructural feature.

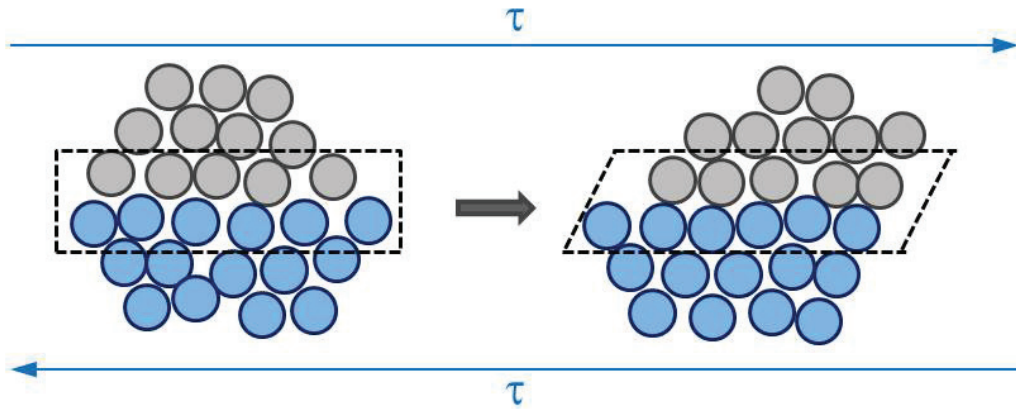


Figure 3.9.: Schematic of plastic deformation propagated by a shear transformation zone (STZ) (after Argon et al. [9]).

In nanocrystalline metals, the grain boundaries help to accommodate misorientations between neighboring grains. Atoms in the center of these boundaries do not possess perfect lattice positions. This local disorder leads to shear softening of the adjacent grain boundaries [90]. Hence it is likely that inelastic deformation rather propagates through the soft grain boundary network. Although in metallic glasses STZs need to be activated, whereas grain boundaries are present in nanocrystalline

materials at any time, the similarities are intriguing. Comparing hardness values and strain rate sensitivities of a multitude of metallic glasses [91] one can find that they are in close vicinity to those of very fine grained nanocrystalline palladium-gold alloys [92, 93]. Using established equations to calculate  $V_{app}$  for amorphous metals results in activation volumes in the order of  $\sim 2 - 15b^3$ . These values are well within in the ballpark found for nanocrystalline metals (see i.e. [94]) which may indicate the activity of STZs. Another distinct feature of the mechanical behavior of metallic glasses is a well pronounced tension-compression asymmetry which is also observed in nanocrystalline metals [95]. Hence, it is possible that crystalline metals, at least at the lower end of the crystalline regime are susceptible for plastic deformation via the propagation of STZs. However, it remains unclear how great the share of STZ in the overall plastic deformation in these metals is and at which stress levels they preferably occur.

### 3.3. Conclusion

The pertinent literature provides a vast variety of possible deformation mechanisms for nanocrystalline materials - regardless of lattice structure and crystallite size (if below  $100nm$ ). Nevertheless, it is very difficult to name a single mechanism as the rate limiting one or at least quantify its contribution to the overall deformation, since most of the possible mechanisms can not clearly be separated. They rather act in parallel or at least overlap [96], which makes it almost impossible to experimentally access a single mechanism. Even TEM-studies are mostly restricted post mortem results which means that only the deformation mechanisms that leave visible traces may be seen. For observing e.g. the dislocation motion in a nanocrystalline material in situ, the instrument resolutions are not sufficient. Nevertheless, a key to access these mechanisms may be combinatorial experiments where the same sample of a specific material is probed consequently by various types of experiments. For instance in situ tensile tests on electrodeposited micro tensile specimen can help to access bulk properties of these materials. Further, in situ micropillar compression tests at variable strain rates and temperatures can provide qualitative and quantitative insight into the rate controlling mechanisms on a much smaller scale. Next to mechanical properties, activation volumes and -energies can be determined which are considered to be footprints of plastic deformation mechanisms. The following chapters of this thesis deal with exactly these types of experiments and are an attempt to contribute valuable insights into these promising materials from a research as well as from an industrial perspective.





---

## 4. Experimental methods

### 4.1. Electrodeposition of nanocrystalline nickel micro components

In the following subsection, we discuss the manufacturing and chemical characterization of freestanding electrodeposited nanocrystalline nickel components on laboratory scale. The nickel electroplating solutions commonly used for electrodeposition are the „Watts“- and conventional „nickel sulfamate- solutions“ with and without additive agents. Both methods are well established, but in the framework of this study the focus is put on the second bath type, since thick deposits in the order of  $250\mu m$  are required. The Watts-solution is mainly used to deposit very thin layers. The sulfamate solution allows fabrication with low internal stresses in the deposits and high rates of deposition, which makes them interesting from a commercial point of view. As reference material, we use an industrially-produced nanocrystalline nickel material from a proprietary deposition process\*. Further, we describe the electrodeposition of thick  $\sim 200\mu m$  nickel-tungsten films which were developed with the aim of improving the mechanical properties of nanocrystalline electrodeposits (i.E. high Young’s modulus and high yield stress) with respect to applications of the Swiss watch industry.

#### 4.1.1. Sulfamate solution

Basically two types of nickel sulfamate solutions are distinguished: the conventional and the concentrated solution. In case of the conventional solution, the created internal stress is comparably low. Even zero stress may be obtained by maintaining the solution at high state of purity and by constantly eliminating the nickel chloride which forms as a byproduct during the electrochemical reaction. Further, to ensure an efficient dissolution of nickel anode materials, it is essential to activate these with sulfur. However, even with great care, a zero stress level in such thick deposits is

---

\*The electrodeposited reference material was provided by Mimotec SA, Route des Iles 20, CH-1950 Sion, Switzerland

Table 4.1.: Nominal composition of nanocrystalline Ni plating bath

Component	Content (Gram/Liter)
Ni(SO <sub>3</sub> NH <sub>2</sub> ) <sub>2</sub> 6H <sub>2</sub> O	450
NiCl <sub>2</sub> 6H <sub>2</sub> O	30
Boric acid	20
Sodium dodecyl sulphate	0.1
Saccharin	2.5

difficult to maintain without using small amounts of organic additives. By adding nickel chloride to the bath composition an overall tensile stress condition can be obtained. To avoid oxidation of the sulfamate anion, using an adequate anode area, commonly 1.5 to 2 times the area of the cathode, and a fully-active nickel anode material to maintain the potential on the anode basket as low as possible is also required. Under these conditions, the tensile stress level normally is between 35 and 55 MPa. A phenomenon which apparently only occurs in sulfamate solutions is anodic oxidation of the anion to form species which diffuse to the cathode where they are reduced. In some cases, this results in incorporation of sulphur, which lowers internal stress and brightens the deposit. This occurs for example at insoluble primary or auxiliary anodes or at nickel anodes that are operating at high potentials. More than one sulfamate oxidation product may form, and the one that forms depends on the anode potential. The second type are concentrated nickel sulfamate solutions. They permit the deposition of nickel at high rates and at low stress levels in the deposit. They are particularly useful for electroforming where zero-stress conditions are required. Because low- to zero-stress conditions can be achieved without organic addition agents, there is no incorporation of sulphur and the deposits do not become embrittled when heated above 200°C.

The plating bath used in the framework of this thesis is a slight modification of the sulphamate bath used by Zheng et al. [97]. Its composition is listed in Table 4.1. The pH of the solution was adjusted to 3.5 by the addition of sulphamic acid. Electrodeposition was carried out galvanostatically at  $J = -8\text{mA}/\text{cm}^2$  at 60°C for 8 minutes by employing a computer-aided potentiostat system PGSTAT30 (Metrohm Autolab B.V., Utrecht, The Netherlands).

### 4.1.2. LiGA-process

LiGA is the German acronym for lithography, electroplating and polymer replication and describes a key technology for manufacturing micromechanical devices with high aspect ratios and precision by means of electroplating [98]. The whole process consists basically of four different steps as illustrated in Figure 4.1.

The sequence according to Figure 4.1 is as follows: (a) a flat substrate, mostly Si-wafer with a few nanometers thin PVD-metal layer on top, is covered with a photoresistive polymer layer. A photo mask which projects the component geometry, in this case micro tensile bars, is placed above the photoresist and then exposed to radiation in order to transfer the projected geometry into the photoresist. Depending on the applied technology the radiation source can be either X-rays (synchrotron) or UV-light. (b) Afterwards the photoresist is developed and the unexposed structure can be removed from the substrate. This step leaves behind the voids which already have the negative shape of the actual part geometry as also displayed in Figure 4.3 (a). (c) By means of electrodeposition the molds are filled from the metalized bottom (substrate) to the top (see also Figure 4.3 (b)). (d) In a final step the remaining photoresist is stripped by dissolving in acetone or oxygen plasma and the micro parts can be removed from the substrate. The main difference in this technology is the type of irradiation used to expose the photoresist. In the framework of this study the emphasis is put on the UV-LiGA process due to two reasons: First of all the achievable aspect ratios of approximately 1 : 10 and geometrical precision still meet the requirements of the final application, e.g. in a wrist watch. Further, the application of a UV-light source is cheaper, quicker and easier to realize on lab scale, since no synchrotron beamline is required.

### 4.1.3. Determination of chemical composition

Electrodeposited films contain higher amounts of impurities in comparison to vacuum sputtered films. Although the effect of solid solution alloying elements, like tungsten [99], on the mechanical deformation behaviour of nanocrystalline nickel has been of primary interest to the community, the influence of impurities can be significant. For example, segregation of sulphur above 330°C has been reported to form Ni-sulphide at the grain boundaries resulting in substantial decrease in flow stress [100]. The effect of B and C doping on the mechanical properties has also been investigated [101, 102, 103]. These impurities hamper grain growth and render microstructural stability to the grains. Hence, it is crucial to thoroughly determine the materials composition. In case of the nickel films deposited at Empa, the chemical composition

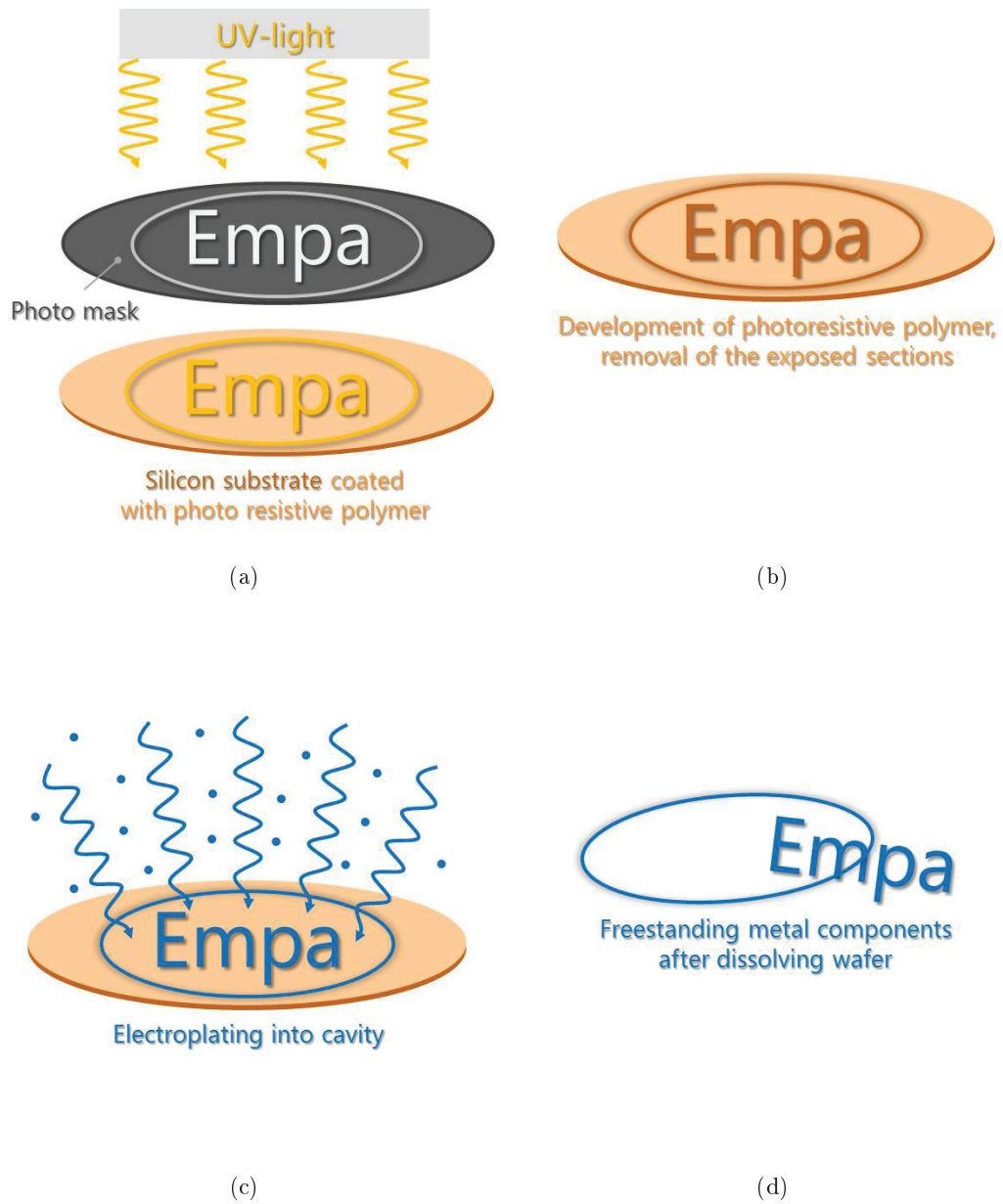


Figure 4.1.: The four characteristic steps of a LiGA-process: (a) exposure, (b) development, (c) electrodeposition and (d) stripping/removing parts

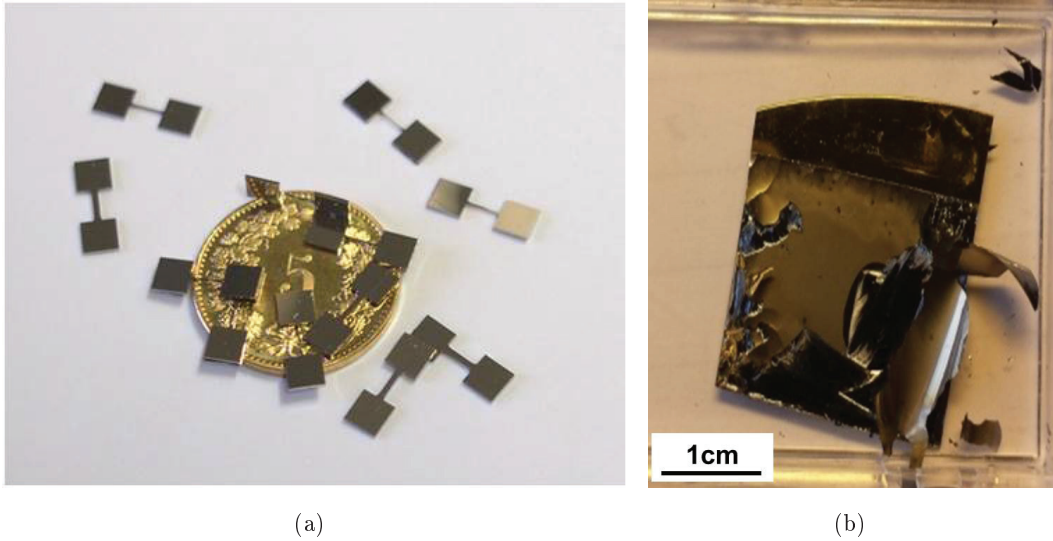
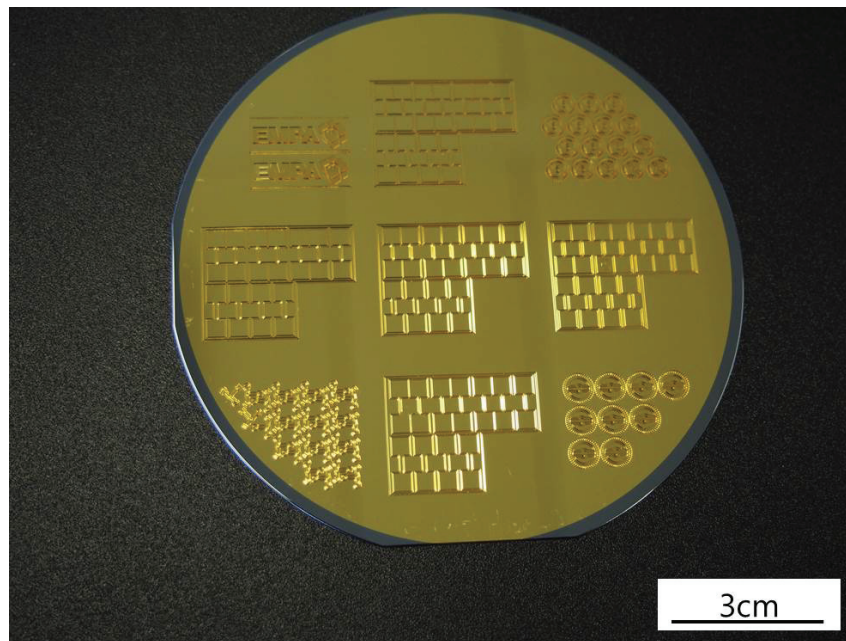


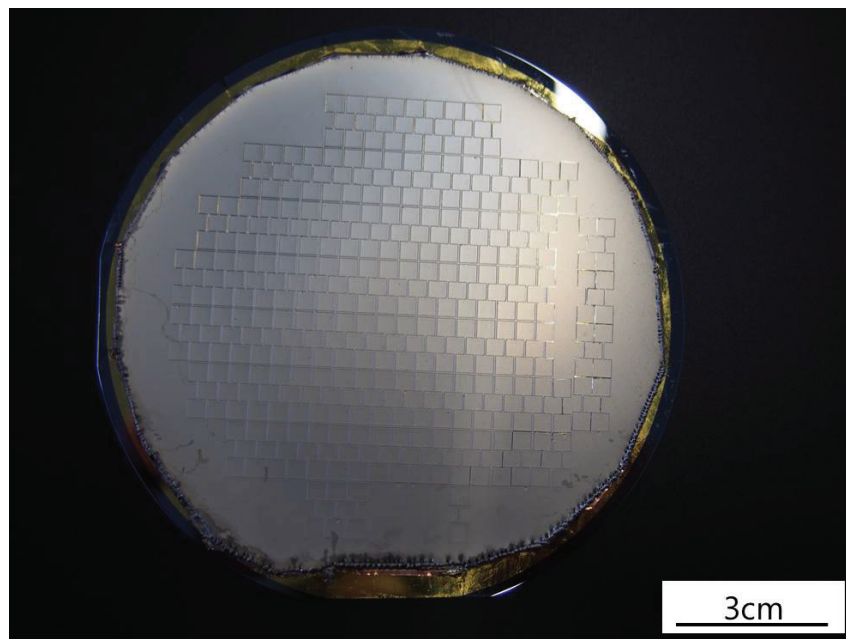
Figure 4.2.: Electrodeposited nanocrystalline nickel LiGA tensile dogbone specimen after dissolving the Si-wafer substrate (a) and residual stress induced delamination of nickel layers on flat silicon substrate before deposition parameter and bath chemistry optimization (b)

and the thickness were measured by Glow Discharge Optical Emission Spectroscopy (GDOES) using a JY5000 RF instrument (HORIBA Jobin Yvon GmbH, Bensheim, Germany). For comparative reasons, the industrial reference nickel was analyzed as well.

The nominal compositions are reported in Table 4.2. The nickel concentration in the Empa-nickel was found to be  $98.7 \text{ mass.} - \%$  versus  $99.9 \text{ mass.} - \%$  in the industrial reference nickel. Both materials contain trace amounts of other components, i.e. Al, C, Cu and S. With amounts  $> 0.45 \text{ mass.} - \%$  the Co concentration appears relatively high which can be addressed to traces of contamination in the electrochemical bath as well as interference effects during the measurements. However, in any case, solid solution strengthening effects due to cobalt in the nickel matrix are low [104] and hence, for such low concentrations, the effect of Co on the strength of electrodeposited nickel can be neglected. Although the plating process of the industrial reference nickel is proprietary, it is likely that a similar, but of course heavily optimized, type of bath has been used there on a much larger scale. The average film thickness was around  $8 \mu\text{m}$  for the Empa-nickel. The average thickness of the industrial reference nickel was  $\sim 250 \mu\text{m}$  and has been measured with a gauge dial since these films were delivered as free standing mechanical components.



(a)



(b)

Figure 4.3.: Patterned Si-wafer prepared for LiGA-process (a) and a full wafer with microtensile bars after deposition (b)

Table 4.2.: Comparison of nominal composition of nanocrystalline Ni determined from GDOES measurements. Contents in *mass.* – %

Alloy	Ni	Co	Al	C	Cu	S
This study	98.740	1.191	0.005	0.025	0.025	0.010
Industrial reference	99.874	0.45	–	0.0386	–	0.060

## 4.2. Electrodeposition of nickel-tungsten alloys

The major challenge of electrodeposited NiW is its high intrinsic tensile stress which results in bending, cracking and delamination of deposits. Hence, in this study, we employed, the ammoniacal-citrate NiW bath as with this type of bath promising results have already been achieved [105, 106, 107, 108]. The bath consists of nickel sulfate hexahydrate ( $NiSO_4 \cdot 6H_2O$ , Sigma-Aldrich), and sodium tungstate dehydrate ( $Na_2WO_4 \cdot 2H_2O$ , Sigma-Aldrich) as well as sodium citrate tribasic dehydrate ( $C_6H_5Na_3O_7 \cdot 2H_2O$ , Sigma-Aldrich) as a complexing agent and ammonium chloride (Sigma-Aldrich) as a pH buffering agent. The concentrations of Ni ions and tungstate ions are  $0.4mol/L$  and 0 to  $0.1mol/L$  respectively. Citrate ions were added and the solution pH was adjusted by ammonium hydroxide (Sigma-Aldrich) to 8 at a plating temperature of  $70^\circ C$ .

In order to reduce the residual stress, pulse plating [109] as well as pulse reverse plating [105, 110] have been employed, and these techniques have been shown to be effective to some extent. Both the pulse-on and pulse-off times were set at  $5ms$ , while the mean current density was varied in the range between  $J = -10mA/cm^2$  and  $-25mA/cm^2$ . Pulse plating seemed to have positive effects on the residual stress in the deposited films as none of the films deposited in this study delaminated from the substrate in the aimed current density range (similar deposition experiments in DC-mode resulted in severe delamination). Electrodeposition was carried out using a potentiostat (PGSTAT 30, Autolab) controlled by NOVA (version 1.7) software. A Si substrate sputter-coated with a  $100nm$ -thick Au seed layer and a  $10nm$ -thick Cr adhesion layer was used to deposit NiW films. The surface of the conducting part of the substrate was covered with a masking tape, leaving a plating area of  $1.5cm$  by  $1.5cm$ . A Ti mesh basket filled with Ni pellet was used as the counter electrode. After the deposition, samples were rinsed in deionized water and dried under clean air flow.

The chemical compositions of NiW deposits as well as the film thickness ( $20-25\mu m$ ) were measured by X-ray fluorescence (XRF, FISCHERSCOPE X-RAY XDV-SDD,

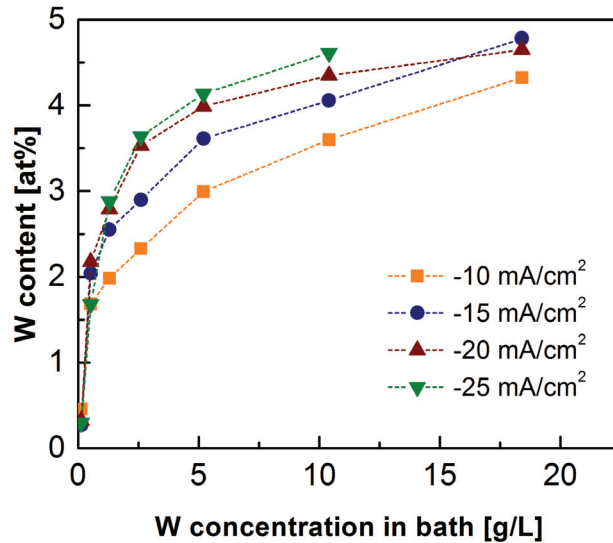


Figure 4.4.: Effect of electrodeposition conditions on the composition of NiW deposits.

Fischer Technology, Switzerland). GDOES measurements (JY 5000 RF, HORIBA Jobin Yvon) were also performed in order to obtain the concentration of impurities such as carbon, sulfur, nitrogen and oxygen. Figure 4.4 shows the influence of deposition conditions on the achieved tungsten content in the deposits. Impurity content in NiW films, analyzed by GDOES, were found to be less than  $0.03wt. - \%$  for C and  $0.02wt. - \%$  for S, regardless of the bath composition and deposition current density for NiW films. The concentration of oxygen was  $\sim 1wt. - \%$  which is lower than the reliable detection limit.

### 4.3. Inert gas condensation of nanocrystalline palladium-gold alloy

For more basic studies of the characteristics deformation of nanocrystalline *fcc*-metals it is desirable to have access to an „ideal“ nanocrystalline material which comprises features like chemical purity, full density, random texture, homogeneous and adjustable grain size distribution, miscibility with other alloying components to adjust stacking fault energies or thermal stability up to high homologous temperatures. However, using electrodeposition it is so far impossible to achieve materials which fulfill more than just a few of the above mentioned requirements. However, neglecting any industrial relevance, there are materials available which are produced by



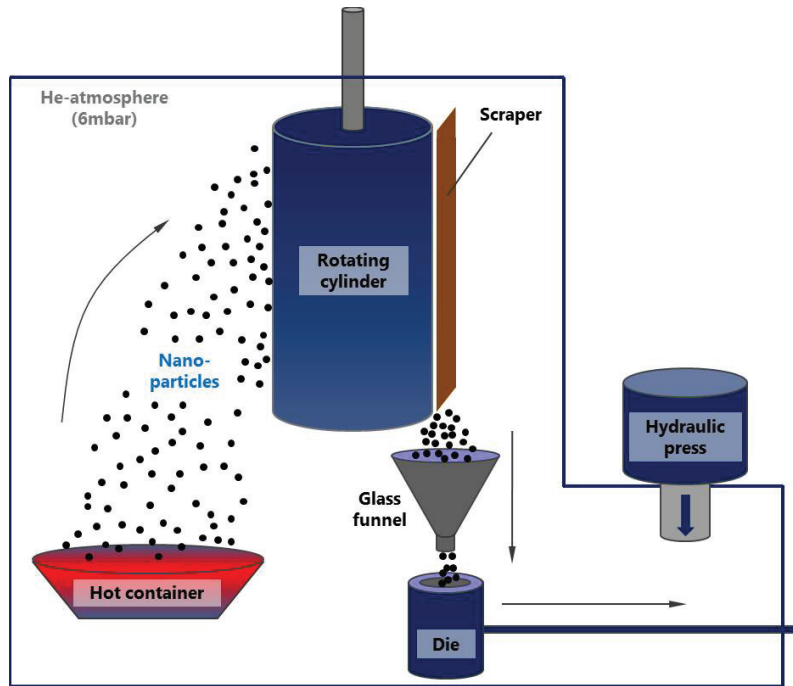


Figure 4.5.: Schematic of the inert-gas condensation process

other process routes which are promising candidates for basic research. One of these candidates, inert gas condensed Palladium-Gold is described and pre-characterized in this section.

Inert gas condensed (IGC) nanocrystalline Palladium-Gold [111] has been chosen as a reference material for in-depth studies of the deformation behaviour of nanocrystalline metals. The specimen with a nominal gold concentration of 10at.% was prepared/provided by the group of Professor Rainer Birringer from the *Lehrstuhl für technische Physik* at Universität des Saarlandes in Saarbrücken, Germany which is gratefully acknowledged.

The IGC principle is illustrated in Figure 4.5. As base materials, high purity palladium and gold rods ( $Pd99.5\%$ ,  $Au99.99\%$ ) were used. In a first step, the two materials are weighed in accord to the desired composition. Then both materials are transferred into a crucible into a fully encapsulated environment and molten under a high vacuum atmosphere at  $10^{-7}bar$ . Both elements form a fully miscible PdAu alloy [112] which, in a second step, is evaporated from the liquid phase under a partial helium pressure of  $6mbar$ . The evaporated metal atoms agglomerate on the helium atoms and form nanoscale particles. Finally they move towards a liquid nitrogen cooled cylinder where the particles condense. The cylinder is rotated and

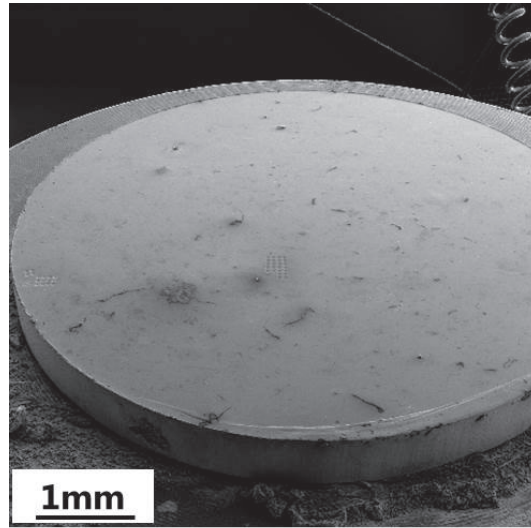


Figure 4.6.: SEM image of a Pd<sub>90</sub>Au<sub>10</sub> sample. The disc has a diameter of  $8\text{mm}$  and is mounted on a SEM stub.

the condensed particles get wiped off by a flexible copper-beryllium scraper and fall into a die. Subsequently, the full die is transferred within the vacuum chamber into a press where a tungsten-carbide plate is used to compress the powder with a pressure of  $1.85\text{GPa}$  with a dwell time of  $30\text{s}$  into the shape of a disc. The disc-shaped specimen as displayed in Figure 4.6 with a diameter of  $8\text{mm}$  and a thickness of  $1\text{mm}$  is randomly textured and has about 6% of residual porosity. The material composition was verified to be Pd<sub>90</sub>Au<sub>10</sub> by energy dispersive X-ray spectroscopy (EDAX TSL Trident system) in a scanning electron microscope (SEM, JEOL F 7000). Afterwards, the sample was subjected to a thermal annealing treatment at  $130^\circ\text{C}$  for 3 hours in order to structurally and energetically equilibrate the grain boundaries and reduce residual stresses without causing noticeable grain growth. Despite the materials very fine grain size in the order of  $\sim 13\text{nm}$  and narrow grain size distribution which is helpful for the interpretation of the mechanical tests, this material is of remarkably high purity. In contrast to electrodeposited nanocrystalline materials, where usually several additives are necessary to deposit a homogeneous and reasonably low stressed thin film without a lot of defects, the condensed material is free of additives and spurious elements. This is beneficial for the interpretation of experimental results, since it allows to rule out the effects of foreign species on deformation mechanisms.

## 4.4. Characterization of specimen nanostructure

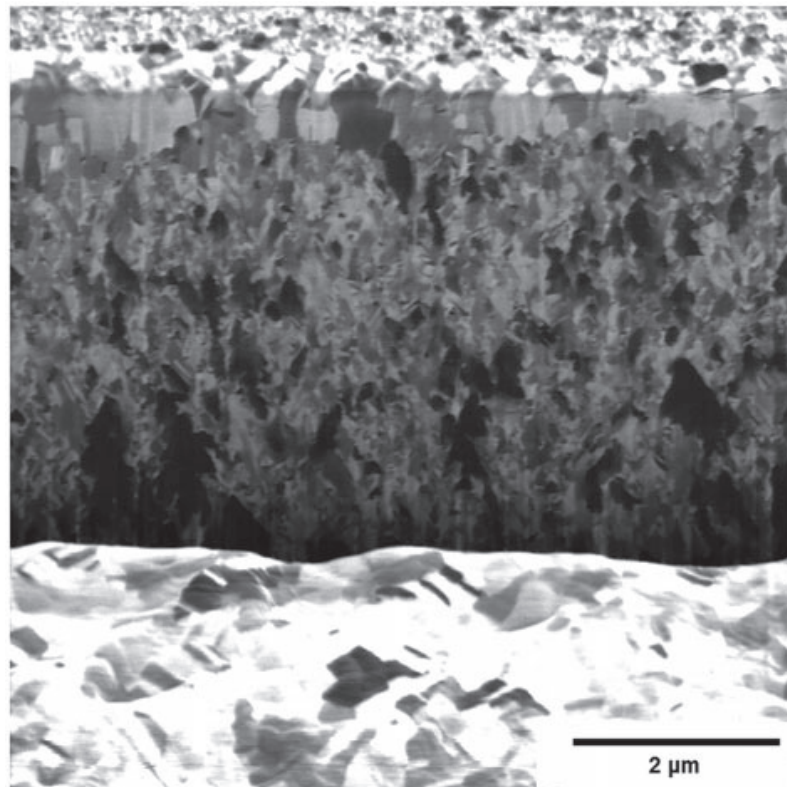
### 4.4.1. Nanocrystalline nickel

#### **Ion channeling contrast imaging and transmission electron microscopy**

In order to gain information about the present grain morphology, a sample of the electrodeposited film was prepared for cross-sectional imaging with a Tescan Vela dual-beam FIB/SEM (Tescan s.r.o., Brno, Czech Republic). Specimens were sectioned by a FIB using an acceleration voltage of  $30kV$  and a probe current of  $1000pA$ . The samples were observed with the ion-channeling contrast at an acceleration voltage of  $30kV$  and the lowest possible probe current ( $5pA$ ). Figure 4.7 shows a representative specimen cross-section with non-columnar grains throughout the trench. The grains at the surface are larger in comparison to the bulk on account of grain growth due to prolonged exposure to high-energy beams. Since the grains grow during FIB milling as well as during imaging, such images provide a qualitative idea about the grain shape and size distribution. TEM lamellae of the deposits were manufactured by the FIB lift-out technique [113] using a Vela dual-beam FIB (TESCAN s.r.o., Brno, Czech Republic). The surface of the deposits were coated using a gas injection system (GIS) with  $2\mu m$  of platinum prior to lift-out to provide a protective layer to limit the extent of any ion beam damage. Final polishing of the lamellae was performed using a  $5kV$  ion beam at  $1^\circ$  incidence to the lamellae surfaces. A JEM-2200FS TEM (JEOL GmbH, München, Germany) was used to image the sample displayed in Figure 4.7 (b) in scanning mode (STEM) at  $200kV$  and  $0.7nm$  spot size. In all cases, the material's nanostructure displayed a homogeneous grain size distribution with an average grain size of  $26 \pm 10nm$ , calculated for over fifty grains applying grain area analysis using the ImageJ software package.

#### **XRD crystallite size determination**

To determine the crystallite size of the electrodeposited Ni films, a BRUKER Discover D8 X-ray Diffraction machine (Bruker GmbH, Karlsruhe, Germany) with  $Cu-K\alpha$  radiation at  $40kV/40mA$  was employed. Spectra of the specimens were recorded in a  $2\Theta$  range between  $20^\circ$  and  $90^\circ$  which revealed a strong characteristic Ni-peak [111] at  $2\Theta = 44.56^\circ$ . The mean crystallite size, which is the average size of a coherent scattering domain, was calculated by measuring the full-width half-maximum of these peaks and applying the basic form of the Scherrer equation, which is valid in crystallite size range from approximately 2 to  $100nm$  [114, 115]. However, care must be taken here since this approach only estimates the average coherence length of a



(a)



(b)

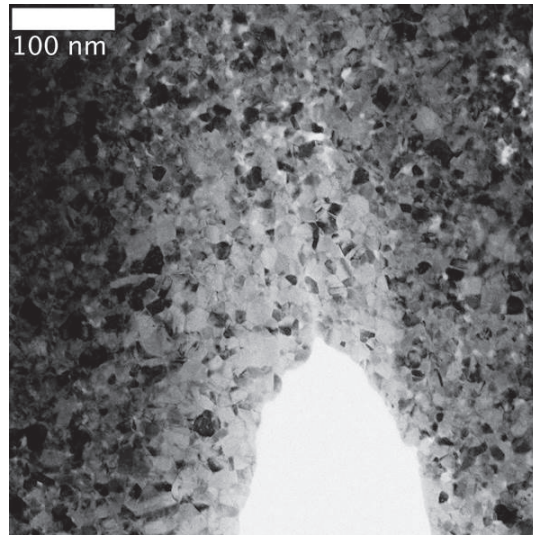
Figure 4.7.: FIB channeling contrast image of the nickel film deposited at Empa, showing non-columnar microstructure with a broad grain size distribution (a) and TEM bright field image of a FIB-lamellae from the same specimen revealing a crystallite size in the order of  $40\text{nm}$ . The grains at the top are larger in comparison to bulk due to grain growth on account of excessive exposure to  $\text{Ga}^+$  ions.

scattering domain. Microstructural features like grain boundaries, sub-grain boundaries or twins can contribute to this estimation which may lie well below the actual grain size. The mean crystallite size of the deposits estimated from XRD was  $27nm$ . Further it should be noted that crystallite size is different from grain size since one grain can consist of several crystallites [116]. However, in case of mechanical deformation behavior, these microstructural features like low-angle grain boundaries, sub-grain boundaries and twins impede dislocation glide. Therefore, crystallite size has also been widely reported as grain size in the literature for nanocrystalline materials. Apart from the average grain size, the grain shape and distribution also affects the mechanical behavior. Limitations of XRD measurements include measurement of grain size only in the direction perpendicular to the surface. Hence information about grain size distribution [117] and their shape is not included.

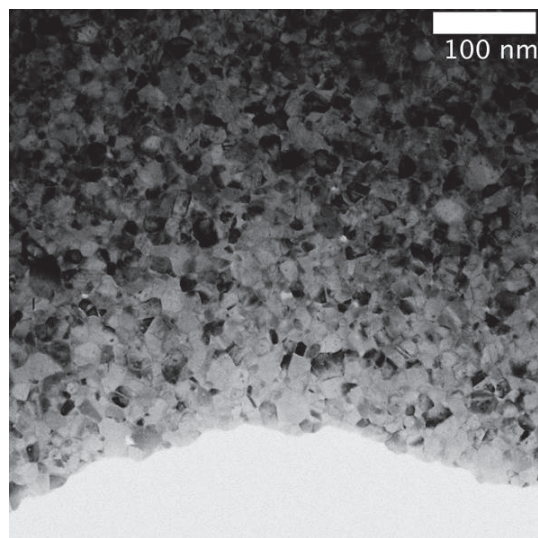
#### 4.4.2. Palladium-gold alloy

##### Transmission electron microscopy

To confirm the uniformity and crystallite size of the  $Pd_{90}Au_{10}$ -material before and after the elevated temperature experiments as described in Chapter 6, TEM lamellae were manufactured by the FIB lift-out technique as described in the previous section. Both lamellae were cut from mechanically untested regions of the PdAu-disc before and after annealing and not from compressed micropillars as the original nanostructure had to be accessed. A JEM-2200FS TEM (JEOL GmbH, München, Germany) was used to image the sample in scanning mode (STEM) at  $200kV$  with  $0.7nm$  spot size. Figure 4.8 (a) and (b) display the remarkably homogeneous nanostructure of the present material. The crystallites are uniform and equiaxed, and the overall structure appears fully dense without pores. Statistical grain size measurements of 60 to 70 grains per image revealed a mean crystallite size of  $13 \pm 5nm$  on both specimen. For the grain size measurements, the ImageJ software package was used. The diffraction rings in the insert of the figures allow the conclusion that both specimen are of nearly random texture which has also been reported in previous studies [92, 93]. The grain size distribution was found to be log normal [92]. Hence, with respect to all these nanostructural properties the  $Pd_{90}Au_{10}$ -material investigated in the present study may indeed be considered to be very close to an ideal nanocrystalline model material. However, the alloy's limited thermal stability will be investigated in Chapter 6



(a)



(b)

Figure 4.8.:  $\text{Pd}_{90}\text{Au}_{10}$ -TEM images (STEM) of specimen nanostructure. Both specimen were cut from the bulk section of the identical sample. The upper image (a) represents the initial nanostructure before the elevated temperature experiments whereas image (b) was taken after the thermal treatment.

### XRD crystallite size determination

X-ray diffraction (XRD) measurements were performed (Discover D8 diffractometer with a  $\text{Cu-K}\alpha$  source, Bruker GmbH, Karlsruhe, Germany) in order to assess the crystallite size from Bragg-Brentano  $\Theta - 2\Theta$  diffractograms. Figure 4.9 depicts two representative spectra of the  $\text{Pd}_{90}\text{Au}_{10}$  specimen before and after the thermal treatment. For a better readability the curves have been shifted apart on the intensity-axis. The Scherrer equation [114, 115] at full width half maximum of the (111) peak, yields a mean grain size value of  $d_{\text{XRD},\text{Pd}_{90}\text{Au}_{10}} \sim 12\text{nm}$ . As for the nanocrystalline nickel this result is only a lower boundary estimate since some parameters such as the presence of twins, crystal defects and residual stresses, can also contribute to the peak broadening [118]. However the results are assumed to be reasonable since the XRD-grain size corresponds well to the findings of the TEM-analysis on the same specimen as described above. Previous studies on exactly the same composition of material yielded values which are in close agreement [119, 93] to this analysis. The XRD-measurments further did not indicate any preferred crystallographic orientation (texture) of the specimen, which again is in good agreement with previous studies [119, 120].

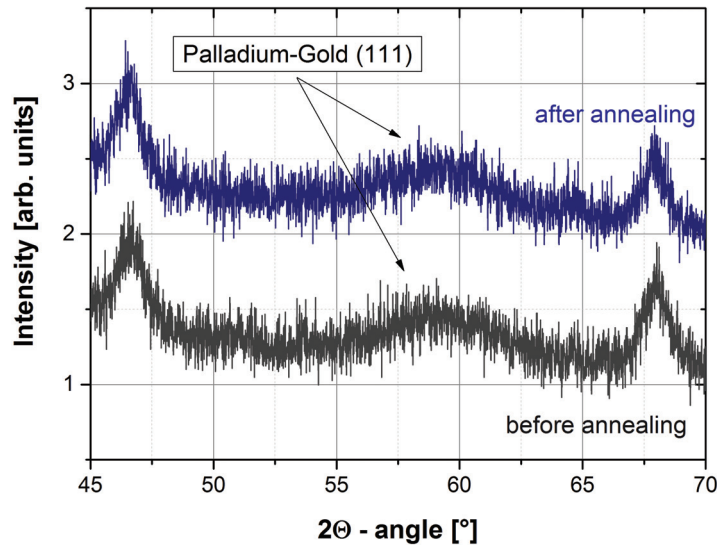


Figure 4.9.: XRD-spectra of  $\text{Pd}_{90}\text{Au}_{10}$  specimen. The blue curve has been acquired before and the grey curve after the heat treatment respectively. Apparently no noticeable grain growth was caused by the heat treatment up to  $125^\circ\text{C}$ .

## 4.5. Utility of micropillar compression tests on nanocrystalline metals

### 4.5.1. Micropillar fabrication with focused ion beam

Gallium ion sources are still the most widely distributed liquid metal ion sources (LMIS). They are successfully used for various applications, such as imaging, micromachining or ion beam induced deposition and chemical analysis, in numerous laboratories around the world. Average micropillar dimensions that can be achieved with this type of ion source are in the order of  $> 200nm$ . At Empa Thun, two Ga-FIB systems are operational: a Tescan Vela and a Tescan Lyra system (Quadprobe). The latter instrument also combines a multitude of detectors as shown in Figure 4.10 (a) which offers unique features for the simultaneous assessment of chemical and microstructural features. Less destructive plasma ion sources are operated on i.e. Helium and are therefore more suitable for imaging or even for milling patterns in the lower nanometer regime. A more recent development in the opposite direction is the Xe-plasma ion source which allows for much larger milling rates than LMIS-devices and therefore give the opportunity to mill larger micro specimen  $> 100\mu m$  in a few hours which would take days in a LMIS instead. Figure 4.10 (b) shows a large „micropillar“ which was milled with a Tescan Fera Xe-FIB<sup>†</sup>. Another major advantage of the plasma-FIB compared to LMIS-FIB systems is that, especially with respect to machining microspecimen for miniaturized mechanical testing, the unavoidable implantation of metal ions from the LMIS into the substrate surface and the possible related effects (see next subsection) can be avoided. Hence, this technology for instance enable specimen manufacturing for uniaxial micropillar compression tests on metals which are prone to metal ion damage - i.e. Aluminum. However, currently only a few of these instruments exist worldwide which limits their availability.

### Principle

The interaction of high energy incident ions on a substrate are various and cover interactions with both: substrate electrons and substrate atoms. Amongst the most important interactions are sputtering of neutral and ionized atoms which enables milling and secondary electron emission which enables imaging. As these interactions are mainly required for the specimen production and characterization in the

---

<sup>†</sup>The Tescan Fera Xe-FIB belongs to ScopeM at ETH-Zürich. The possibility to work with this system is kindly acknowledged.



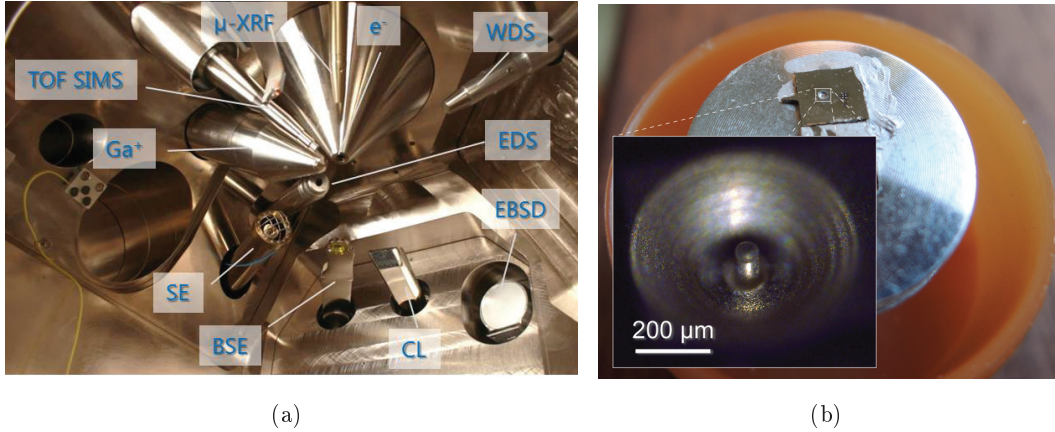


Figure 4.10.: Quadprobe FIB at Empa Thun. The base system is a Tescan Lyra Gallium-FIB which was equipped with additional XRD, WDX and TOFSIMS detectors. Figure (a) displays the inside view of the vacuum chamber. Figure (b) shows a large micropillar machined with the Tescan Fera Xe-FIB (ETH Zürich) into the gripping section of a nanocrystalline nickel tensile bar. The milling procedure for this pillar takes approximately two hours which is equal to approximately 4-5 days of milling time on a Ga-FIB.

framework of this thesis, their principles are depicted in Figure 4.11 (a) and (b) respectively. Other effects are breaking of chemical bonds, phonon emission and the dislocation of substrate atoms, which is considered as so called ion beam damage.

Removing material from a substrate requires ion beams with high currents, and acceleration voltages of usually  $> 15\text{keV}$ . The incident beam penetrates the substrate and sputters away atoms or atom clusters as illustrated in Figure 4.11 (a). The typical sputter yield mainly depends on the electron density of the material and the applied beam currents. The beam incidence angle also has a strong influence as the sputter yield increases with  $1/\cos(\Theta)$  with  $\Theta$  being the incidence angle between the surface normal and the ion beam direction. However, with respect to the restrictions of micropillar manufacturing with a top-down approach, the beam incidence angle is  $\Theta = 90^\circ$ . Another approach would be lathe milling after Uchic [121] where the beam incidence angle is more shallow and the micropillars are milled from the side. However, for calculating a sputter yield another factor has to be taken into account. The sequence of the applied milling patterns, i.e. the sequence how the ion beam scans over the substrate, may lead to redeposition of sputtered material which in turn can cover or refill milled trenches. Hence, it is important to adjust the milling strategy to the desired pattern as discussed in the following subsection.

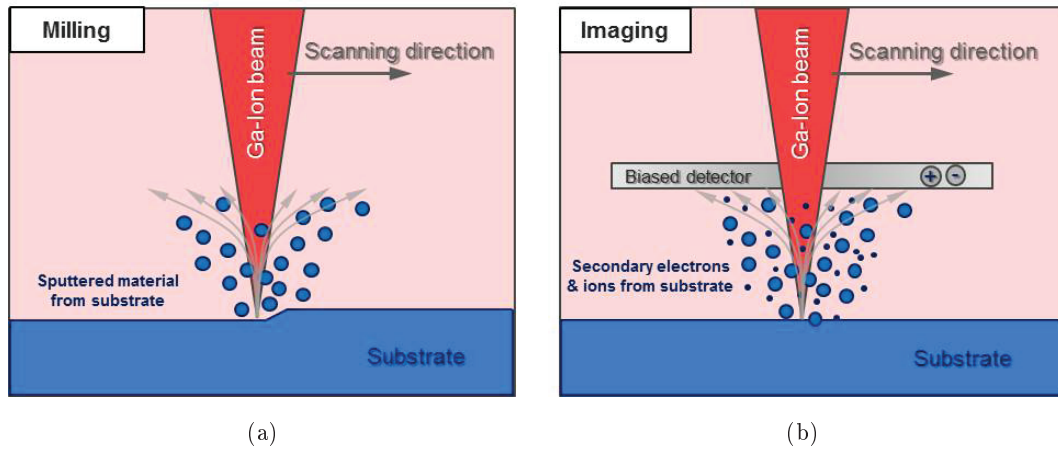


Figure 4.11.: Principle of focused ion beam milling (a) and imaging (b).

It should be noted that, although most ions leave the substrate during sputtering, a small amount of ions is implanted. This irradiation damage is mostly restricted to the specimen surface and can cause several different types of defects, i.e. locally increased dislocation density [122], surface amorphization (see Figure 4.12 (a)) [123], point defects [124] or the formation of intermetallic Ga-compounds (see Figure 4.12 (b)) [125]. On light metals like Aluminium or semiconductor materials, the effect of implantation is generally more pronounced.

Sample imaging requires that the ion beam is scanned across the substrate surface like an electron beam during conventional scanning electron microscopy. Figure 4.11 (b) depicts the principle. The average resolution of ion images is in the order of the minimum spot size of  $\sim 10nm$ . During scanning the ions sputter secondary particles (neutral atoms, electrons and ions) away from the substrate and destroy the surface. Hence, ion imaging is a surface destructive process, which is an important parameter since imaging cannot be repeated without topological changes in the imaged region. However, working with a fine ion beam at low probe currents reduces this effect considerably. Both charged species are accelerated towards a voltage biased detector which can either detect electrons or ions, according to their respectively negative or positive charge. Further, the Quadprobe at Empa (see Figure 4.10 (a)) has the capability of using the emitted secondary ions for TOF-SIMS. Another advantageous feature of ion imaging is the capability of mapping grains in a crystalline metal. As particular lattice orientations open channels, ions can penetrate deeply into crystal lattices. Due to the dependence of electron emission on the ion penetration depth

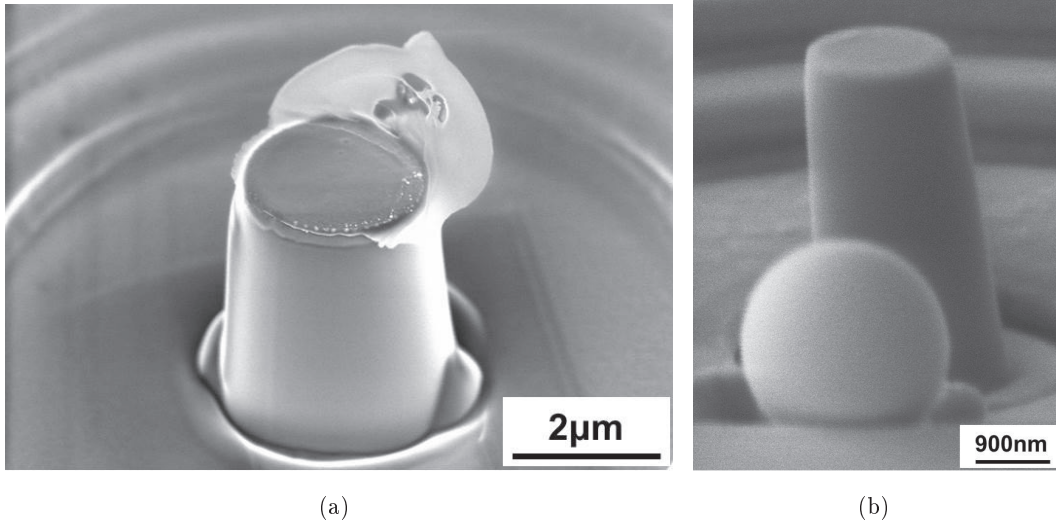


Figure 4.12.: Typical examples for LMIS-beam damage during specimen preparation: SEM images of amorphized surface layer on a  $\langle 123 \rangle$ -Si micropillar which extruded during room temperature compression at low strain rates  $\dot{\epsilon} = 10^{-6}$  (a) and formation of a large Ga-compound-sphere next to a  $\langle 111 \rangle$ -Si micropillar during in situ annealing at  $400^\circ\text{C}$  (b).

this effect can reveal different crystallographic orientations. Figure 4.7 (a) provides an example of a FIB-channeling contrast image of a nanocrystalline Nickel specimen. Despite the fine grain size the nano-grains are clearly distinguishable from each other. Interestingly, the larger domains which appear in dark color throughout the structure are grains which grow due to ion penetration during repeated scanning. An explanation for this observation may be their crystallographic orientation which allows for a particularly deep ion penetration. The ions traverse through the crystallites and get stopped at the grain boundaries, where they loose their energy and cause the grains to grow.

### Milling strategy for micropillar fabrication

The pillar dimensions are restricted to a fixed ratio between pillar diameter  $d$  and -height  $h$ , which should be in the order of  $d/h \approx 2 - 3$ . Pillars which are below that ratio may not be tall enough to allow for fully developed macroscopic deformation features (i.e. shear bands in single crystals), whereas pillars above that ratio tend to buckle. A remarkable advantage of micropillar testing inside an SEM, as already claimed, is the continuous observation of the pillar before, during and after the

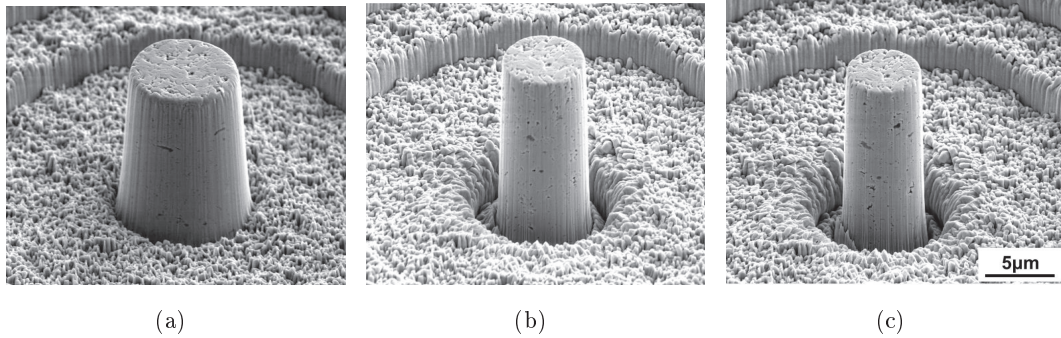


Figure 4.13.: Representative SEM images of a Palladium-Gold micropillar during Gallium-FIB milling. The three-step approach includes coarse- (a) intermediate- (b) and fine milling/polishing (c) at  $30kV$  and sequentially reduced milling currents.

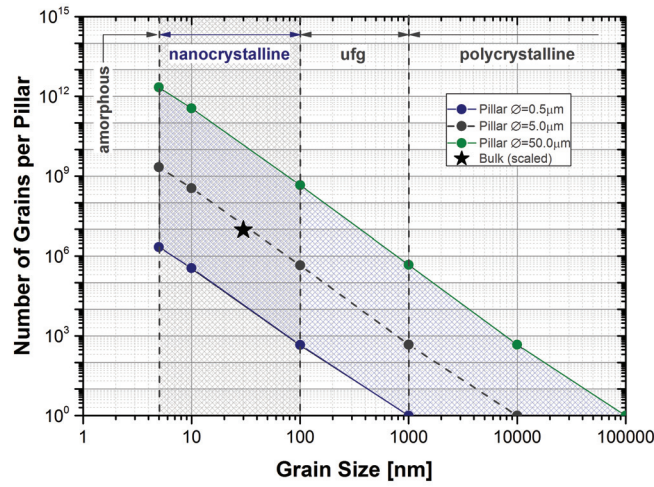
experiment. That is beneficial not only for the correlation of mechanical data and apparent deformation behavior but also to exclude the disturbing effects of debris or misalignment. However, in order to enable observation of the entire pillar and measure the pillar height correctly, it is necessary to have a free path of view to the base of each pillar. Hence, the crater diameter  $D$  should be approximately six times the pillar height ( $D/h \sim 6$ ). Milling this crater consumes the largest quantity of time during the milling process. Therefore, a three step milling strategy for micropillars up to a final diameter of  $\sim 5\mu m$  was chosen in the framework of this thesis, consisting of: coarse-, intermediate- and fine-milling. Representative examples for this sequence are presented in Figure 4.15. For the coarse milling step the largest beam aperture,  $A = 400\mu m$ , was chosen with a set probe current,  $I \sim 3600pA$ , which allows for relatively fast milling. Unfortunately, the less sharp beam and the larger spot sizes allow to achieve only a very rough pillar shape which requires to set the initial pillar diameter around 30% larger than desired (see Figure 4.13 (a)). The subsequent intermediate milling step requires a smaller beam aperture,  $A = 200\mu m$ , which results in probe currents around  $I \sim 1500pA$  and allows to refine the pillar shape towards the desired cylindrical geometry (see Figure 4.13 (b)). The pillar diameter after intermediate milling is still  $\sim 10\%$  above the final diameter. Finally, the pillar is polished with a very fine beam ( $A = 100\mu m, I = 250pA$ ) to the final shape as depicted in Figure 4.13 (c). This step also reduces the amount of beam damage on the surface. Larger pillars with diameters in the range of  $d \sim 10\mu m$  as they were used for load relaxation tests where enhanced displacement resolution is beneficial, a preliminary coarse milling step with probe currents at the technical limit of the Gallium source  $> 10nA$  was employed to mill a very roughly shaped pillar/crater. This

procedure saves time on one hand but the rough patterns are not well defined which may in turn increase the intermediate milling considerably. It should be mentioned that the amount of beam damage is mainly concentrated to the top surface, as the beam is scanning perpendicular to that but parallel to the side walls. There the amount of damage is decreased.

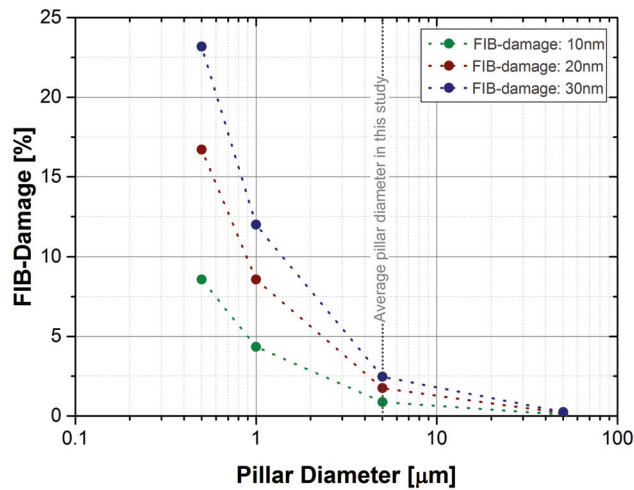
#### 4.5.2. Influence of external- and internal pillar dimensions

Especially for thin films, hard coatings, multilayers, or nanocrystalline metals [118, 126, 127, 128] where bulk quantities are usually not available, (elevated temperature-) micropillar compression tests can provide valuable insights into mechanical properties and deformation mechanisms of these materials. Furthermore, the method is of interest for addressing orientation- and size-specific mechanical properties of single crystal metals [129], semiconductors [130, 131, 123] or even extremely hard materials such as diamond [132]. However, it is important to consider the representativity of such a micro-scale experiment compared to a bulk test with respect to its internal length scale [36]. For single crystals, the situation is clearly defined as measured properties can be correlated to the activated slip systems, failure mechanisms and pillar sizes [130, 129]. But as soon as several crystallites are contained in one micropillar, it is important to keep an eye on the number and orientation of these crystallites, since they may cause size effects and yield properties which do not represent the overall material system. In case of nanocrystalline materials, where crystallite sizes by definition are  $< 100nm$  some simple calculations allow an estimate for the correlation of actual bulk to microscale testing.

Recent studies [94] compare the activation parameters extracted from SRJ-tests on nanocrystalline nickel from microtensile- and micropillar compression tests. Although the loading cases and probed volumes in these tests were different, the results agreed very well. Also when put in context to the presented results in Chapter 6 where the crystallite size is with  $\sim 10nm$  at the lower end of the nanocrystalline regime. Idealizing the crystallite morphology to be spherical with ideal packing density and a grain boundary width of  $1nm$  between two neighboring grains [7], the cross section of a  $5\mu m$  diameter pillar consists of approximately  $2 \times 10^5$  grains. Yang et al. [133] studied the mechanical properties of micro-sized polycrystalline Cu wires as a function of crystallite size and specimen diameter. Based on their experimental data, they developed a composite-model which describes the relation of mechanical properties with respect to specimen- and crystallite size. They concluded that bulk-like mechanical behavior can be expected if the ratio  $r = D/d \geq 10$  where  $D$  is the



(a)



(b)

Figure 4.14.: (a) Number of grains in the cross section of a micropillar as a function of grain size and pillar diameter. The star symbol denotes a downscaled standard bulk tensile specimen (maraging steel). The brown shaded area marks the regime where bulk like behavior can be expected. (b) Average fraction of FIB-induced damaged volume in a micropillar, assuming damage depths between 10nm and 30nm. The dashed vertical line denotes the average size of micropillars in this study.

pillar diameter and  $d$  the diameter of a crystallite. Figure 4.14(a) visualizes these general considerations with respect to the present study. The shaded area marks the regime which meets the  $D/d \geq 10$  criterion [133]. Compared to the cross section of a downscaled bulk tensile bar made of maraging steel, which consists of  $10^4$  grains, the pillars in this thesis generally range one order of magnitude higher.

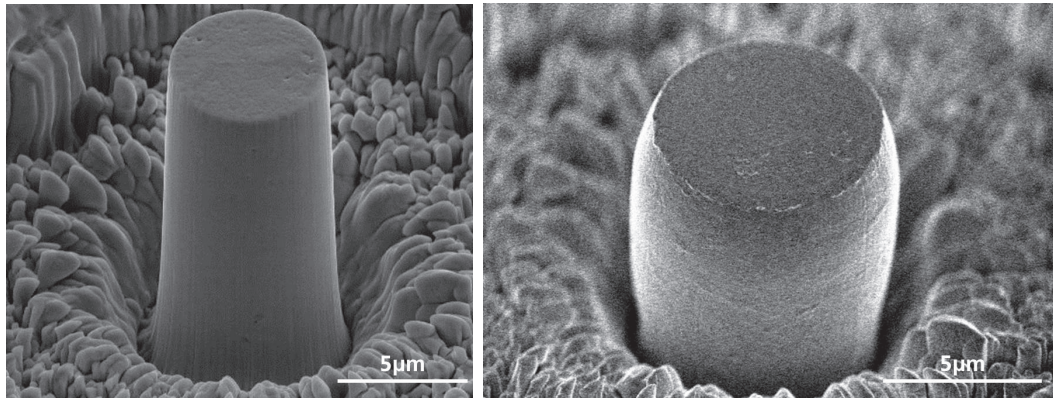
Additionally, Figure 4.14(b) depicts the computed influence of surface damage from FIB-milling with average depths ranging from  $10nm$  (green curve) to  $30nm$  (blue curve). Assuming a FIB damage layer of  $\sim 20nm$  into the pillar surface, the damaged volume of the same  $5\mu m$  diameter pillar is on the order of  $< 2\%$ , which is considered to have minor influence on the overall deformation behavior. Further, the average damage which is introduced to a bulk specimen as an effect of machining i.e. from cold-working- and heat-influence of cutting tools for lathe-milling is found in depth regimes in the order of  $\sim 50\mu m$ . Again considering a specimen diameter of  $5mm$  this damage would be in the same order of magnitude. Hence, micropillar compression can be considered as a valid and highly repeatable test to assess bulk-like mechanical behavior and activation parameters in nanocrystalline *fcc*-metals.

### 4.5.3. Influence of pillar geometry on experimental results

The geometric effect of pillar taper and plastic strain localization in the top segment during compression might explain the apparent strain hardening as observed i.e. in Section 5.1 for nanocrystalline nickel. The geometric issue of pillar taper has been addressed by Yang et al. [134] for accurate extraction of elastic modulus from micropillar compression tests. Nevertheless, it is instructive to explore the reason for the observed apparent strain hardening in engineering stress-strain data using some simplistic assumptions. Figure 4.15 (a and b) shows a Palladium-Gold micropillar with a nominal diameter  $d \sim 5.9\mu m$  and a height  $h \sim 14.4\mu m$  which was compressed at ambient temperature and a strain rate  $\dot{\epsilon} = 10^{-3}s^{-1}$ .

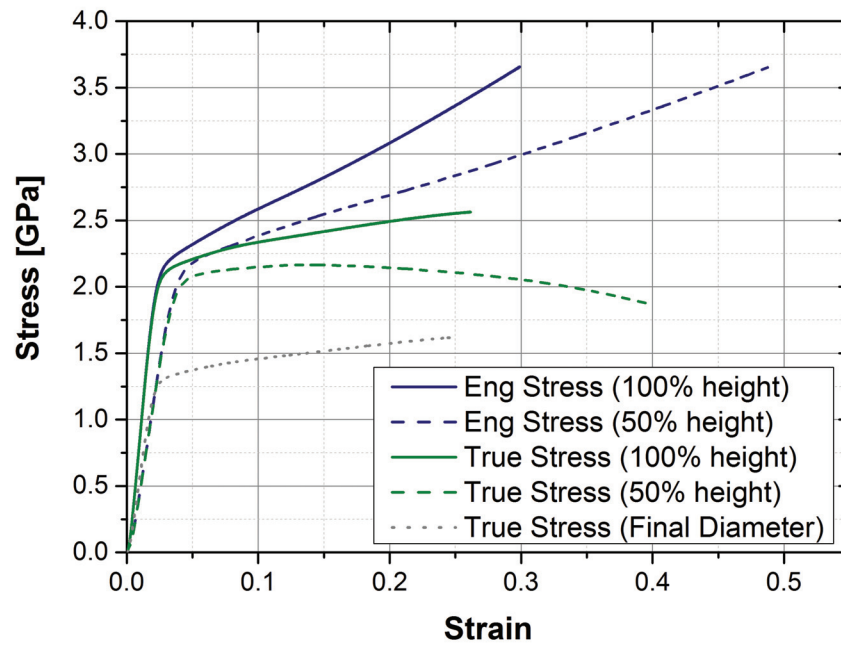
As a rough first approximation to determine the effect of the strain localization in the top segment of the micropillar, engineering stress-strain curve for a particular test run was recomputed by assuming the pillar height to be half of its original height. The true stress-strain curves for the original and reduced pillar heights were also calculated based on the assumption of constant volume and homogeneous deformation. Additionally, the stress-strain curve was calculated for the top diameter after compression. These results are shown in Figure 4.15 (c).

Reducing the pillar height by half increases the overall strain but has minor influence on the strain hardening rate. Increasing the pillar diameter (final diameter



(a)

(b)



(c)

Figure 4.15.: SEM images of Palladium-Gold micropillar before compression (a) and after compression (b) at ambient temperature with a strain rate of  $\dot{\epsilon} = 10^{-3}$ . (c) Engineering and true stress-strain curves computed for a particular test run assuming different pillar heights and diameters to study the effect of strain localization and pillar geometry on the resulting stress-strain curves.



after compression  $>$  initial diameter) decreases the yield point but does not affect the slope of the stress-strain curve beyond the yield point. Therefore, pillar height and diameter, considered separately, do not seem to affect the strain hardening behavior of the engineering stress-strain curves. However, the true stress-strain curve for the original pillar height, which takes into consideration simultaneous change in pillar height and diameter, does show significant reduction in strain hardening. For the case of half pillar height, the true stress-strain curve exhibits significant strain softening. From these results, it is clear that the apparent strain hardening observed in engineering stress-strain curves is likely a geometric effect due to strain localization resulting from taper and inhomogeneous deformation throughout the height of the pillar.

## 4.6. High temperature indentation system

All micropillar compression experiments reported in this thesis were performed using a customized micromechanical in situ testing system based on a commercial micro- and nano-indentation system from Alemnis<sup>‡</sup> inside a scanning electron microscope (SEM) . A unique feature of this particular instrument is its high temperature (HT) capability which has been developed at EMPA. The details have been reported previously [10, 11]. Hence only the key concept and details are reviewed in the following section.

### 4.6.1. System description

The original version of the room temperature Alemnis-indenter has been developed by R.Rabe et al. [135]. It consists of a stable and compact load frame which is equipped with a piezo positioning device and a load cell on the specimen side as well as a stepper motor for coarse- and a stack-piezo actuator for the application of the displacement on the specimen side. This version, installed in a Zeiss DSM 962 SEM<sup>§</sup>, combines versatile and highly accurate in situ, room temperature testing of a vast variety of materials in compression or indentation with permanent visual observation of the experiment, all within a fully encapsulated and stable environment. The system is intrinsically displacement-controlled as a piezoelectric actuator (with a travel range of  $20\mu m$  and a noise floor standard deviation of  $0.3nm$ ) used to apply a preset displacement to a sample. Via this path the resulting force is transmitted

---

<sup>‡</sup>Alemnis GmbH, Feuerwerkerstrasse 39, 3602 Thun, Switzerland

<sup>§</sup>Carl Zeiss Microscopy GmbH, Oberkochen, Germany

into the load cell (with a maximum load capacity of  $500mN$  and a load noise floor standard deviation of  $6\mu N$ ) that sits directly behind the sample. In contrast to load controlled systems this feature is beneficial for variable strain rate testing as the imposed strain rates can be varied easily. Especially for studies which require deformations above the sample yield point the advantage of a displacement controlled system is marked as, due to yielding, a load controlled system would respond with a rapid increase in strain rate. However, the load frame compliance has influence on the actual strain which is delivered to the sample and hence a precise compliance correction is required for adjusting desired strains in a specimen. The LabView-based control software features a PID-loop which further enables system operation in a pseudo load-controlled mode. More common indentation profiles with load- or drift-hold segments or high-load periods for indentation-creep measurements are possible.

Enabling measurements at elevated temperatures required extensive modifications of this system. Figure 4.16 provides an overview of the HT-system and shows the major components. The standard back plate was exchanged with a highly conductive copper back plate with integrated cooling pipes. A dedicated feed through on the SEM chamber is used to connect these cooling pipes to a circulation pump which uses a water-glycol mixture as cooling fluid and transports any excess heat out of the system. The water cooling does not influence the system noise floor in a significant manner. To protect the heat sensitive positioning stage and the load cell from heat, both components are connected to the cooled back plate by ether screws or a nickel coated low stiffness copper braid. The stepper motor and piezo actuators on the tip side are both directly clamped against the back plate so that heat can be drawn out instantaneously. For better insulation between the heat source and the „cold“ parts of the system, the sample heater and the tip assembly and -holder are made of low conductivity ceramic components. With respect to the high temperature applications testing in the stable high-vacuum environment of an SEM is even more advantageous since all heated components are protected from excess oxidation during high temperature cycles.

#### 4.6.2. Key high temperature components

The two key components of the high temperature setup are the independently controllable specimen- and tip heater. Figure 4.17 (a) depicts a ceramic peg heater during assembly. The resistive heating coil is pre-oxidized through overheating in air before being cemented into the peg. The formed oxide layer helps to prevent

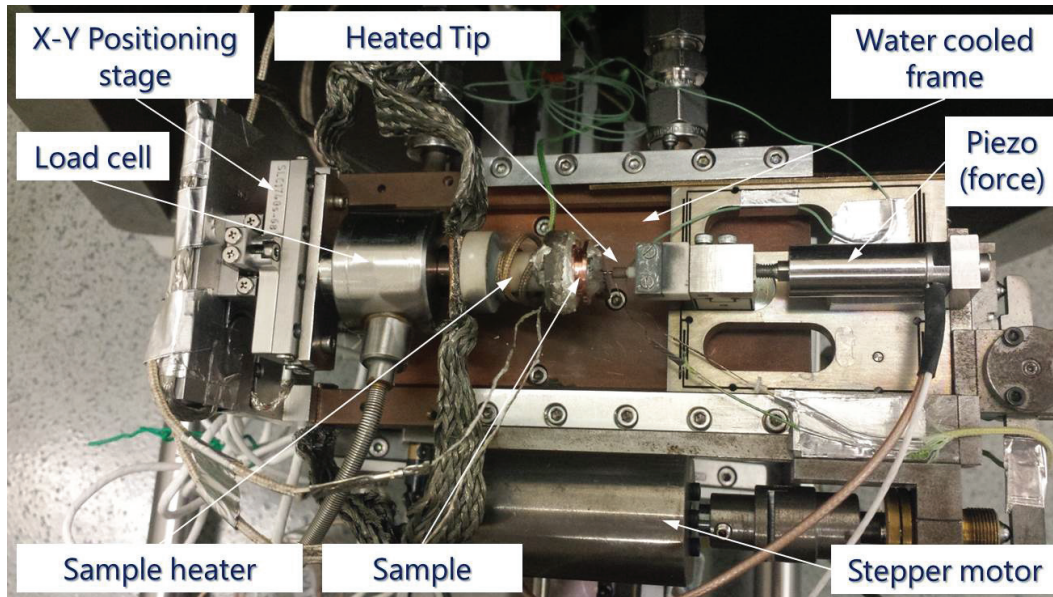


Figure 4.16.: High temperature indentation system with its major components. Joint development between Alemnis and Empa.

shortening between the wires and provides a more even heat distribution over the heater surface. Before the coil is installed a thermocouple is cemented into the peg for a more accurate heater temperature readout. After filling the preform with high temperature cement the assembly needs to be dried and cured before it is ready for installation into the indenter.

The second key component, the heated tip assembly, is shown exemplarily in Figure 4.17 (b). Similar to the sample heater, a resistive wire is wound around the inner shaft of the tip assembly and covered with cement and a protective ceramic tube. A thermocouple is cemented into the backside of the shaft, right behind the actual tip to allow for a temperature readout as close to the tip as possible. As for the sample heater the entire process is manual and requires several steps until the components are ready to be installed. Figure 4.18 (a) illustrates the setup as it is installed inside the SEM under a tilt angle of  $21.2^\circ$ . The color gradients represent the thermal gradients in the hot parts of the system as measured in various spots [10]. These measurements demonstrate the highly localized hot-spots in the specimen- and tip area and confirm the efficiency of the water cooling. Both of heated components are independently controlled by a PID-controller which can be switched to manual (constant voltage) control. With the current setup it is possible to reach specimen surface temperatures of  $\sim 600^\circ\text{C}$ .

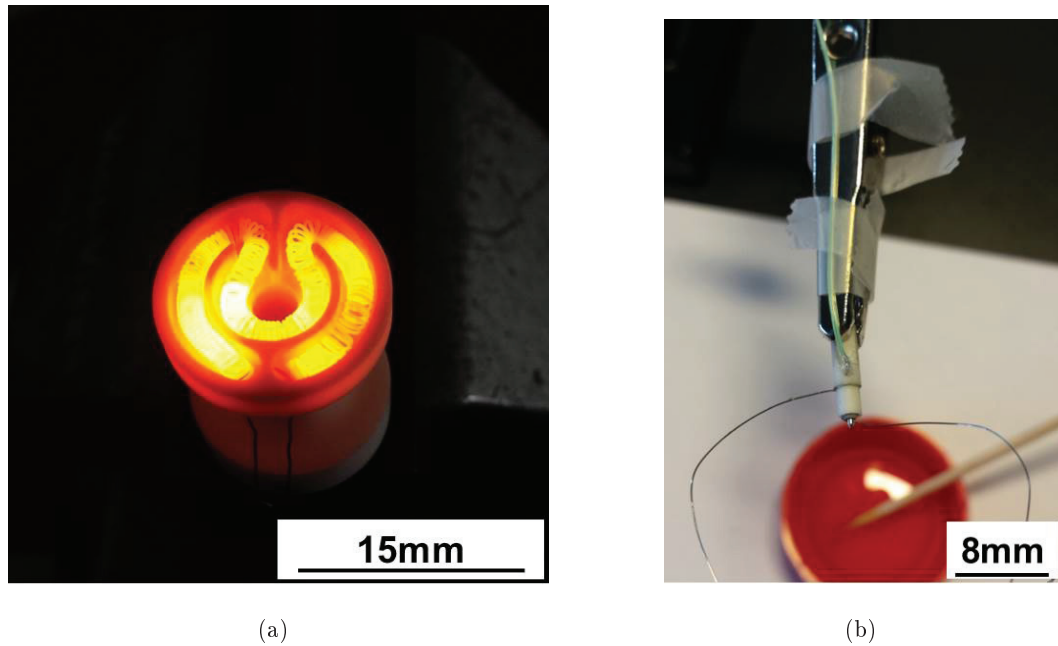


Figure 4.17.: Heat treatment of resistive wire during peg heater assembly (a) and diamond tip during assembly with thermocouple cemented into the ceramic shaft (b).

### 4.6.3. Thermally calibrated contact temperatures

To prevent thermal drift upon contact between sample and tip it is a requirement to have both sides at exactly the same temperature. However, as can be seen from Figure 4.18 (a) there are two separate thermal gradients which need to be adjusted. Additionally the read out temperatures of the thermocouples originate from somewhere inside the devices they are mounted into, i.e. the shaft of the tip or the sample heater but in both cases not from the very surface of either of them. Further, the sample surface temperature is not the same as the heater surface temperature because the sample material, thickness and also the amount and type of cement which is used to bond the specimen to the heater may vary. Hence, it is not only important to minimize the thermal drift but also to know the actual surface temperatures. A method developed by Wheeler [11] suggests to circumvent this problem by using the tip temperature as a reference temperature. This procedure requires to calibrate each tip in order to determine the thermal gradient between the apex of a tip and the thermocouple in the shaft. For this calibration, a dedicated copper stub with a thermocouple embedded below the surface is ground down until the thermocouple (TC) is exposed at the surface. An auxiliary temperature read out port in the SEM-

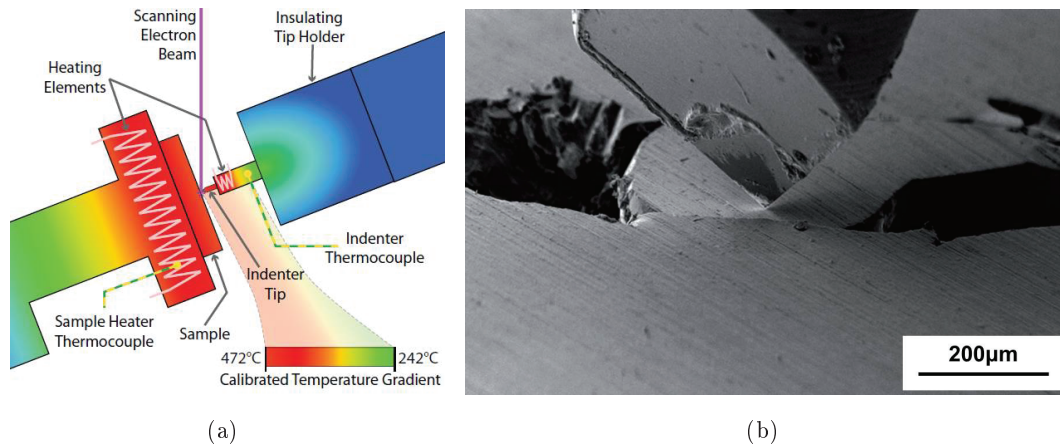
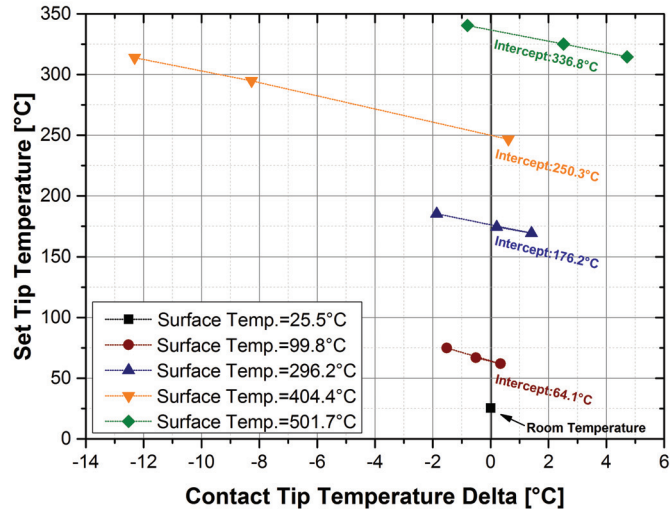


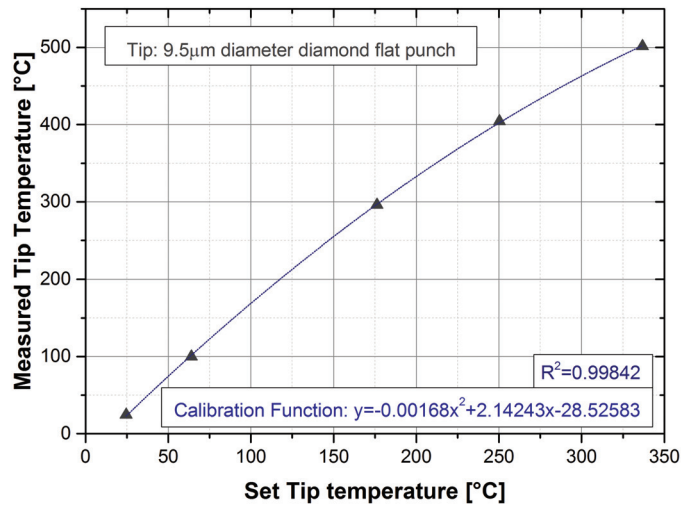
Figure 4.18.: Close-up sketch of the independent tip- and sample-heater assembly with the SEM-installation angle of  $21.2^\circ$  (adapted from [10]) (a) and cube-corner diamond tip during calibration indent into a thermocouple junction (adapted from [11]) (b).

chamber allows to read the temperature of the surface TC while the heater is tuned to the desired calibration temperature. Once the surface temperature corresponds to the desired calibration temperature the tip is heated up in constant voltage mode until it roughly is at the same temperature as the calibration TC and then brought into contact. Figure 4.18 (b) illustrates this scenario. The sharp cube corner tip sits right above the auxiliary TC on the sample side, ready to indent into the TC. A loading profile which should be the same for all calibration indents with one single tip is set up and the thermal drift during the indentation is monitored. Due to the large difference in thermal mass, the thermal change within the heater is negligible and only the thermal drift of the tip is relevant.

For each desired calibration temperature, i.e.  $100^\circ\text{C}$ ,  $200^\circ\text{C}$ ,  $300^\circ\text{C}$ ,  $400^\circ\text{C}$ ,  $500^\circ\text{C}$  and if required  $600^\circ\text{C}$ , the heater temperature is adjusted until the approximate calibration temperature is reached on the auxiliary surface temperature TC and has stabilized. Average heating rates are  $15^\circ\text{C}/\text{minute}$ , and stabilization requires about 20 minutes for each temperature step. Then, the tip is heated stepwise in manually set constant voltage steps. As the tip temperature stabilized at the desired voltage, an indent with the previously set calibration indentation profile is performed. Before, during and after the indentation the evolution of the tip temperature is monitored. Once the drift has stabilized after indentation a linear function is fitted through the stable segments at the onset and the offset of the drift segment and the  $\Delta T$  between



(a)



(b)

Figure 4.19.: Calibration of a  $9.5\mu\text{m}$  diameter diamond flat punch tip. Figure (a) shows the temperature offsets as function of surface temperature during calibration at different temperatures. The acquired calibration function is a square fit through the individual data points is provided in Figure (b).

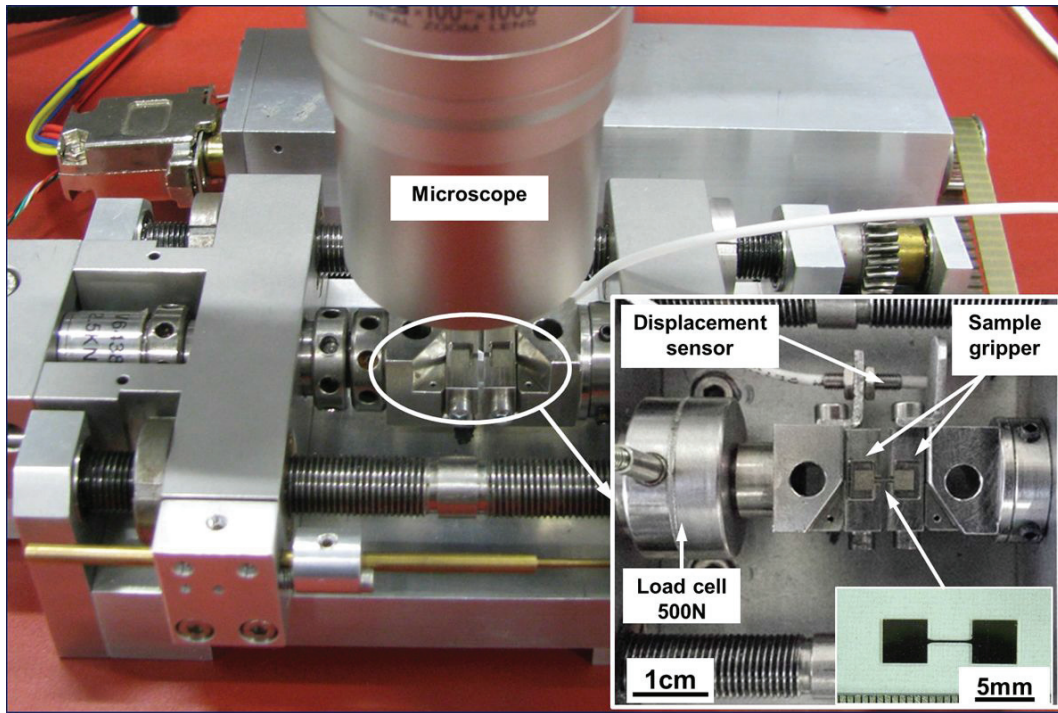
the fit- and the temperature curve is measured. The direction and significance of the  $\Delta T$  provides information if the tip is gaining heat (tip is colder than the calibration TC) or loosing heat (tip is hotter than the calibration TC). Ideally the calibration is accomplished with, at least three indents per temperature step as displayed in Figure 4.19 (a) with one data point above, one data point below and finally one data point in close vicinity to the reference temperature. A linear fit through the data points yields the actual tip TC readout temperature and thus this value can be correlated to the surface TC temperature. As this procedure is repeated for the other desired calibration temperatures a calibration function as exemplarily shown in Figure 4.19 (b) can be fit through the interception temperatures. This function describes the offset between the actual- and the set tip temperature and is finally integrated into the heater control software. Now the tip is calibrated and can serve as a reference probe for measuring the temperature of an actual sample. Figure 4.19 (b) also illustrates the thermal gradient between the tip TC output value and the tip surface temperature which in the presented case of the  $9.5\mu\text{m}$  diamond flat punch tip is apparently only  $\sim 337^\circ\text{C}$  at a true tip temperature of  $\sim 502^\circ\text{C}$ .

## 4.7. Minaturized tensile tests

Uniaxial tensile tests are probably the most common and well accepted mechanical tests in material science and engineering. Specimen geometries, at least on a macroscopic scale, are standardized and bulk properties of a vast variety of engineering materials are readily available from a multitude of sources. Specimen production from bulk materials can be accomplished in a common workshop by lathe milling, electrode discharge machining or stamping. Consequently, results from such well standardized tests are i.e. available, comparable and reliable. However, when specimen sizes encounter the micronmeter regime, as usually the case for nanostructured materials or thin films, the application of tensile tests is not as simple anymore. Mainly two reasons account for that: first, the available testing equipment on the free market does not provide the required resolutions (load and displacement) and secondly the lack of bulk quantities of free standing specimen materials. The latter case limits the common specimen manufacturing techniques and also prevails that samples can be manufactured within standardized aspect ratios. In the framework of this study, a Kammrath& Weiss<sup>¶</sup> micro tensile stage (See Figure Figure 4.20 (a)) with a nominal load capacity of originally up to  $< 25\text{kN}$  was utilized and modi-

---

<sup>¶</sup>Kammrath Weiss GmbH, Im Defdahl 10F, 44141 Dortmund, Germany



(a)



(b)

Figure 4.20.: (a) Adapted miniaturized tensile stage with 500 N load cell, displacement sensor and hard metal grippers. A digital microscope fixed perpendicular to the specimen is used for strain measurement. The inset in the right figure shows a nanocrystalline nickel micro tensile bar (LIGA) right before a tensile test. (b) Micro tensile specimen marked with eight couples of tracking points.



fied for testing small scale LIGA samples as shown in the insert of Figure 4.20 (a). The commercially available version of this setup is already compact enough to be installed inside a SEM for in situ measurements. It mainly consists of a robust load frame with parallel spindles that translate rotational- into linear movement of the two cross heads. However it is originally not designed for testing specimen with an overall length below  $\sim 10mm$  which is mainly due to the large sample gripping system and the incapability of precise measurement of small strains. Hence, the system was adapted and heavily modified. A compact load cell (Measurement Specialties Ltd., Hampton, VA, USA) with a noise floor of  $0.03N$  and a maximum load capacity of  $500N$  was installed. To minimize the elasticity of the loading path the load cell was directly attached to the crosshead. The fragile, small scale tensile specimens require careful handling and specimen gripping via a clamping device would induce damage to the specimen gauge section or enable premature failure during the test. A small gripping device was designed and machined from high strength austenitic steel which allows to insert samples from the top and transfer the crosshead displacement through shape locking. An inductive displacement sensor was directly attached to the sample grip support. However, this sensor is only used as a reference signal for applying desired displacement rates during the experiment. To avoid any error in displacement arising from the compliance of the setup or deformation outside of the gauge section, the actual displacement of the sample gauge section was measured in situ by optical measurement from high definition video. Videos are acquired using a VHX-500F digital microscope (KEYENCE International SA, Mechelen, Belgium) which is mounted perpendicular to the specimen. A Lucas and Kanade algorithm [136] was implemented in LabView-based software to measure the time-dependent displacement between selected points on the gauge section. Figure 4.20 (b) depicts a silicon dogbone specimen with eight couples of selected tracking points. Although other MATLAB-based approaches for measuring strain fields in miniaturized specimen exist [137], we decided to continue with this simple point to point correlation approach and use reference measurements on standardized specimen (steel, silicon) for validation of the setup as demonstrated in Section 5.2.



---

## 5. Transient tests I: Case studies on electrodeposited nanocrystalline nickel

This chapter aims to extend the repertoire of nanomechanical testing approaches for thin films and nanostructured bulk-like specimen by developing multiple micropillar test procedures on nanocrystalline nickel. As these metals are known for their strongly pronounced time- and temperature-dependent plastic deformation behavior, micropillar transient tests (i.e. strain rate jump, load-relaxation and repeated creep tests) at ambient and elevated temperatures are introduced. A study of the rate controlling and activation parameters as function of temperature on nanocrystalline nickel is conducted. This chapter also intends to bridge the gap between uniaxial testing on micropillars versus conventional uniaxial tensile tests and triaxial stress state testing in small volumes by nanoindentation.

The structure is as follows: In Section 5.1.2, we develop the elevated temperature capability of the indentation system (see Section 4.6 for details) when testing nanocrystalline nickel films and outline the data evaluation procedures we adapted for microscopic tests. Then we compare these results to room temperature compression test on the industrial reference nickel in Section 5.2. In the same study, the identical industrial samples are also characterized by in situ nanoindentation and in situ uniaxial tensile test on a heavily modified small scale tensile testing frame. In the third section of this Chapter, we investigate the time dependent plastic behavior of nanocrystalline nickel developed at Empa and compare load relaxation measurements under uniaxial tension with a novel approach on repeated relaxation tests on unusually large micropillars.

### 5.1. Elevated temperature micropillar compression

The experimental details and results in this section have been published as an article in the „Philosophical Magazine“\*

---

\***Elevated temperature, strain rate jump microcompression of nanocrystalline nickel**, Mohanty, Wehrs et al., Phil.Mag., 2014, Volume 95, pp 1-18 [118]

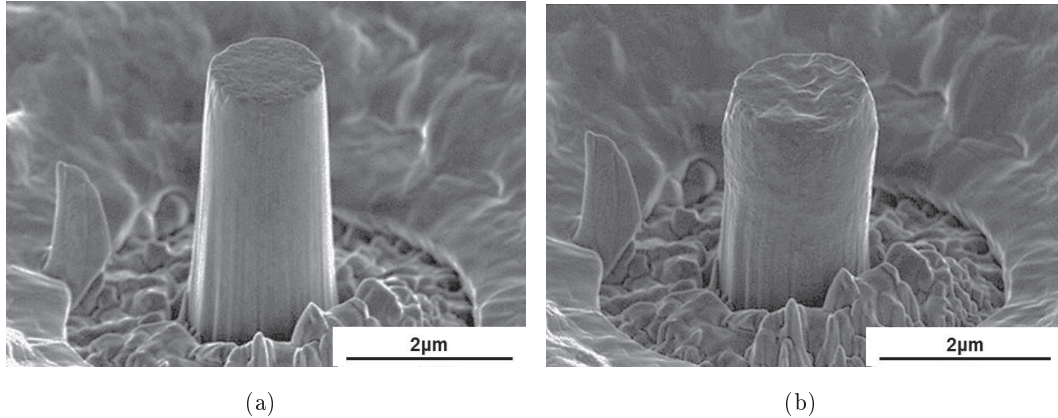


Figure 5.1.: High resolution SEM images of a micropillar (a) before and (b) after compression to 25% strain at room temperature. The top half accommodates the bulk of the plastic deformation.

### 5.1.1. Material and specimen preparation

Nanocrystalline nickel thin films (non-free standing) have been deposited on a copper substrate. The plating bath composition and deposition parameters are provided in Section 4.1 and Table 4.2. Small micropillars with diameters of  $\sim 1.5\mu\text{m}$  and aspect ratios of  $\sim 2.5$  were milled, utilizing a Tescan Vela Ga-ion FIB. The pillars were milled in three sequential stages: coarse milling ( $A = 30\text{KV}$ ,  $I \sim 5\text{nA}$ ), intermediate milling ( $A = 30\text{KV}$ ,  $I \sim 1\text{nA}$ ) and final polishing ( $A = 30\text{KV}$ ,  $I \sim 220\text{pA}$ ). The micropillars were imaged using a Hitachi S4800 high-resolution scanning electron microscope before and after compression tests, as displayed in Figure 5.1. Microstructural stability is important for the current study on account of elevated temperature testing. Grain growth between different temperature runs and during testing can exhibit anomalous mechanical deformation behavior that can make interpretation of experimental data difficult. Hence, it was important to ascertain the highest testing temperature, so that we can be reasonably sure of absence of grain growth and perform all tests with the same starting microstructure. Previous studies on nanocrystalline nickel have reported appreciable grain growth above  $200^\circ\text{C}$  [97, 117, 138, 139]. Therefore, we decided to keep the maximum temperature of testing at  $100^\circ\text{C}$ . For direct experimental verification of absence of substantial grain growth, an electrodeposited nanocrystalline nickel sample was annealed at  $100^\circ\text{C}$  for over  $24\text{h}$ . The average crystallite size increased from  $27\text{nm}$  in as-deposited condition to  $31\text{nm}$  for the annealed sample, which is similar to the observations reported by Zheng et al. [97].

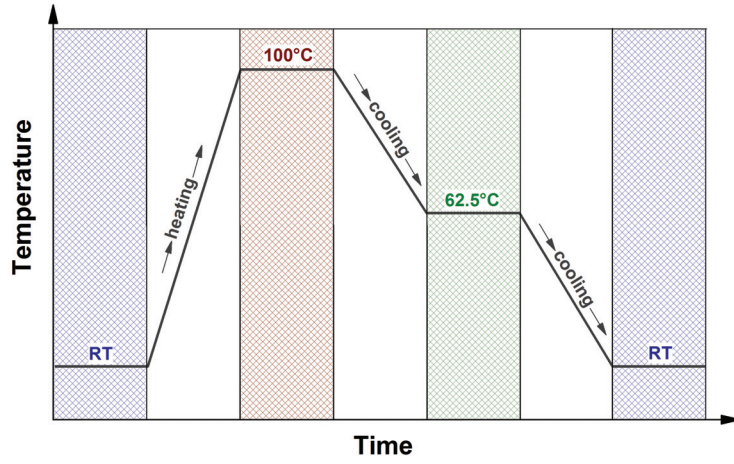
### 5.1.2. Nanomechanical measurements

#### Nanoindentation

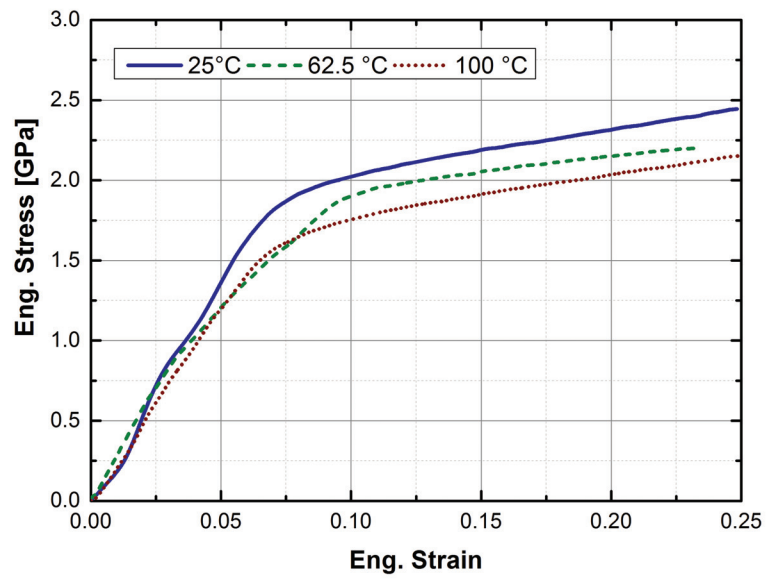
Nanoindentation tests were carried out in a UNHT system (CSM Instruments, Neuchâtel, Switzerland) using a sapphire Berkovich tip for comparison with similar data from literature. Hardness and modulus were measured continuously using the *sinus mode* whereby a small sinusoidal function is superimposed on the primary load signal. For these measurements, load amplitude of  $1mN$ , sinus oscillation frequency of  $10Hz$  and a maximum load of  $100mN$  were used. Constant indentation strain rates ranging from  $2.5 \times 10^{-3}$  to  $2.5 \times 10^{-1} s^{-1}$  were applied by keeping  $\dot{P}/P$  (rate of load change/instantaneous applied load) ratio constant. This resulted in loading times for a single measurement varying between 13 and 1400s. Hardness values corresponding to depth of  $\sim 1\mu m$  were considered for analysis in order to provide a consistent comparison between the different strain rates. A minimum of seven indents were performed at each strain rate and the results were averaged.

#### Micropillar compression

Micropillar „constant strain rate“ (CSR) and „strain rate jump“ (SRJ) tests were carried out in an Alemnis in situ elevated temperature indentation system in a Zeiss DSM 962 SEM (see Section 4.6 for details). Micropillar compressions, as well as micropillar strain rate jump tests, were carried out at three different temperatures as illustrated in Figure 5.2(a):  $25^{\circ}C$ ,  $62.5^{\circ}C$  and  $100^{\circ}C$ . The sequence of testing was  $100^{\circ}C$ ,  $25^{\circ}C$  followed by  $62.5^{\circ}C$ , so that the initial tests at  $100^{\circ}C$  relax the grain boundaries and allow in case of apparent grain growth to reach a steady state size distribution. The high vacuum of the SEM chamber ( $\sim 10^{-4}Pa$ ) prevents excess sample surface oxidation. Thermal drift at elevated temperature testing was minimized by tuning the tip temperature with the sample surface temperature [11]. All test temperature values reported in this paper correspond to the sample surface temperatures measured by the calibrated indenter tip. The accuracy of surface temperature measurement and tip temperature tuning was  $<0.5^{\circ}C$ . Since an intrinsically displacement controlled indenter was utilized for these experiments, the SRJs could be incorporated easily. The strain rate was varied by a factor of 25 from  $0.0002$  to  $0.005s^{-1}$ . A diamond flat punch was used for the experiments. Although diamond indenters are not optimal for elevated temperature measurements on nickel, as reported recently in the landmark paper of Wheeler and Michler [140], dissolution or reaction of a flat punch is not of as much concern in micropillar measurements,



(a)



(b)

Figure 5.2.: Illustration of test temperature sequence (a) and Engineering stress-strain curves for micro-compression of nanocrystalline nickel at  $\dot{\epsilon} = 0.001s^{-1}$  (b).

unlike sharp conical or pyramidal tips and for test temperatures up to only 100°C. Six micropillars were tested at each temperature: three for CSR micro-compression and three for SRJ tests.

Figure 5.2(b) shows representative engineering stress-strain curves from CSR micropillar compression results obtained at three test temperatures. The nanocrystalline film exhibits 1% offset yield strength<sup>†</sup> of  $1.89 \pm 0.05 \text{ GPa}$  at room temperature, and the yield strength decreases with increasing test temperature ( $1.80 \pm 0.09 \text{ GPa}$  at 62.5°C and  $1.63 \pm 0.09 \text{ GPa}$  at 100°C, measured for six micropillars each). It should be noted that the room temperature tests were preceded by 100°C tests. The engineering stress-strain data obtained at room temperature on this annealed sample were compared with another sample in as-deposited condition. The room temperature results from both samples overlapped nicely suggesting negligible grain growth and no noticeable change in mechanical properties on account of initial testing at 100°C. An intriguing observation in the engineering stress-strain curves is the apparent strain hardening for micropillar compression results. Nanocrystalline materials do not typically exhibit strain hardening [7], which is attributed to saturation of dislocation density due to dynamic recovery or due to annihilation of dislocations into the grain boundaries [7]. So, the observed strain hardening might be a geometrical artefact. On careful observation of the micropillars before and after compression (Figure 5.1 (a) and (b) respectively), it was noticed that the pillars have a taper of  $2.5 \pm 0.3^\circ$  (calculated for 18 micropillars), and the bulk of the plastic deformation is accommodated by the top half segment of the micropillar. In situ testing videos obtained during compression also show the top half deforming the most, with grains rotating and sliding out of the free pillar surface, while the bottom half segment is not greatly affected. Traces of grain boundary sliding can be observed in the scanning electron micrographs at the surface of the deformed pillars (Figure 5.3) as the now roughened structure indicates. The larger grains show slip traces.

### Elevated temperature strain rate jump tests

Figure 5.4 shows the engineering stress-strain curves for the SRJ tests at the three test temperatures. After each jump, the flow stress reached a steady state value rather quickly and SRJs were sharp with very small transients. The strain rates have been marked on one of the curves to provide an idea about the magnitude and sequence of the rate jumps. The same rate jump sequence and testing methodology was used on

---

<sup>†</sup>1% offset yield strength is taken at the point where the stress-strain curve deviates 1% in strain from the extrapolated linear portion

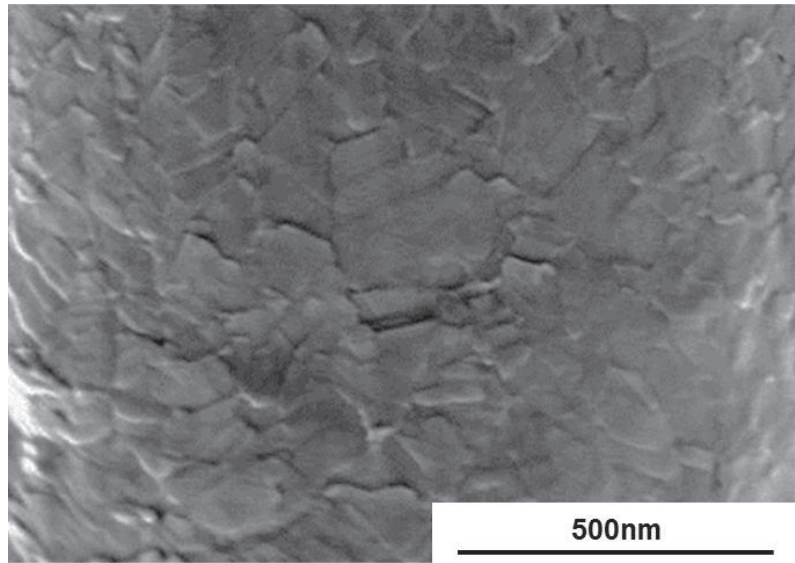


Figure 5.3.: High resolution SEM image of nanocrystalline Nickel micropillar after SRJ-compression. Extensive grain boundary sliding can be observed in the top half of the deformed pillar. Slip traces are observed in the larger grains.

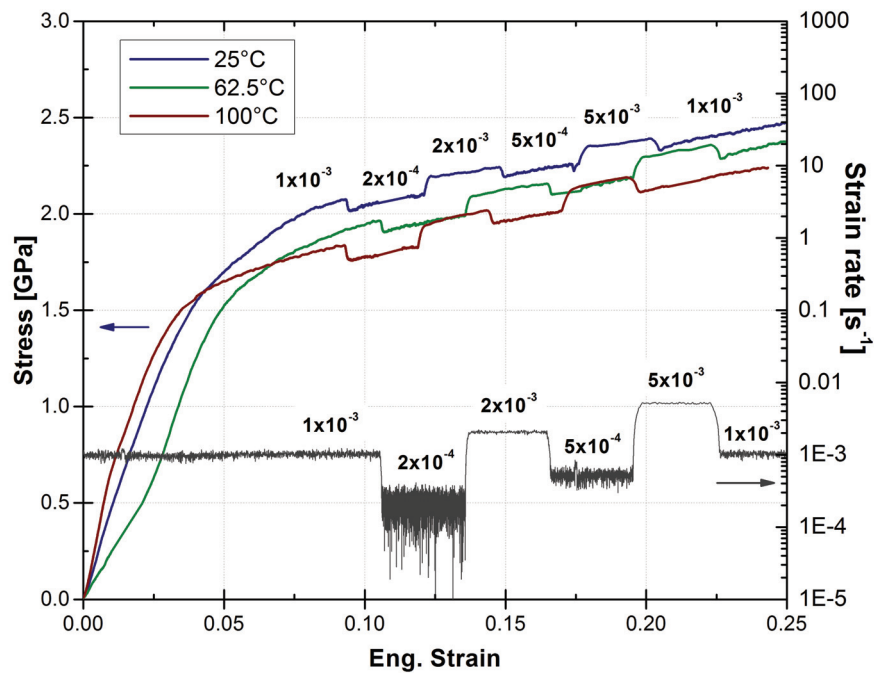


Figure 5.4.: Engineering stress-strain curves for the SRJ tests on nanocrystalline nickel micropillars at three test temperatures. Each test comprises five SRJs with the strain rates varying from  $0.0002$  to  $0.005s^{-1}$ , by a factor of 25.



all the pillars. The strain rate sensitivity (SRS) exponent,  $m$ , is the measure of the dependence of change in flow stress,  $\sigma$ , as a function of change in applied strain rate,  $\dot{\epsilon}$ , at constant temperature,  $T$ , as defined in Equation 5.10 and can be calculated from SRJ tests using two analysis methods: (a) instantaneously for each SRJ, and (b) from the slope of stress-strain rate data plotted in log-log scale, an analysis often used for SRS determination from CSR measurement data. In method (a), the change in flow stress is calculated from experimental data just before and after the rate jump by ignoring the transients. This method of computation does not depend on the slope of the stress-strain curve in the plastic regime and hence, is independent of strain hardening or softening in the material being tested. However, it is sensitive to any noise present in the data during the jump and on jump transients. On the other hand, the value of  $m$  calculated using method (b) is strongly influenced by the slope of the stress-strain curve. In case of strain hardening behaviour, an average value for the flow stress corresponding to an applied strain rate cannot be ascertained for computing the value of  $m$ . Since nanocrystalline materials do not exhibit excessive strain hardening, this has not been an issue with bulk measurements. However, the apparent strain hardening behavior noticed in engineering stress-strain curves from tapered micropillars precludes the direct use of method (b) on experimental data. Data corrections must be introduced before using this method. To remove the influence of the slope on analysis method (b), a straight line was fitted through the initial and final segments of the stress-strain curves that were compressed at the same strain rate of  $0.001s^{-1}$ . The fitted segment was shifted in stress axis to result in zero slope  $\sigma - \epsilon$  curve so as to subtract the apparent strain hardening (Figure 5.5). The value of  $m$  was then calculated from the corrected data using method (b). This correction uses the assumption of reversibility of the strain rate dependent flow [12] to allow all other variations in the  $\sigma - \epsilon$  curve to be subtracted, leaving only the SRS. It allows better statistics to be obtained in comparison to method (a), where the stress needs to be calculated over a very narrow range of strain to avoid jump transients and apparent strain hardening behavior from affecting the results. A comparison of values of  $m$  determined using different methods for a micropillar tested at  $100^{\circ}C$  is shown in Table 5.1. The results from all three analyses are in good agreement.

In order to compare these results with other techniques, room temperature SRS data obtained from micropillar SRJ tests and nanoindentation CSR tests performed on the same sample have been plotted in Figure 5.6. The flow stress values from nanoindentation data were calculated by dividing hardness by a factor 2.8 [12]. Nanoindentation CSR hardness values from the current work are lower due to sub-

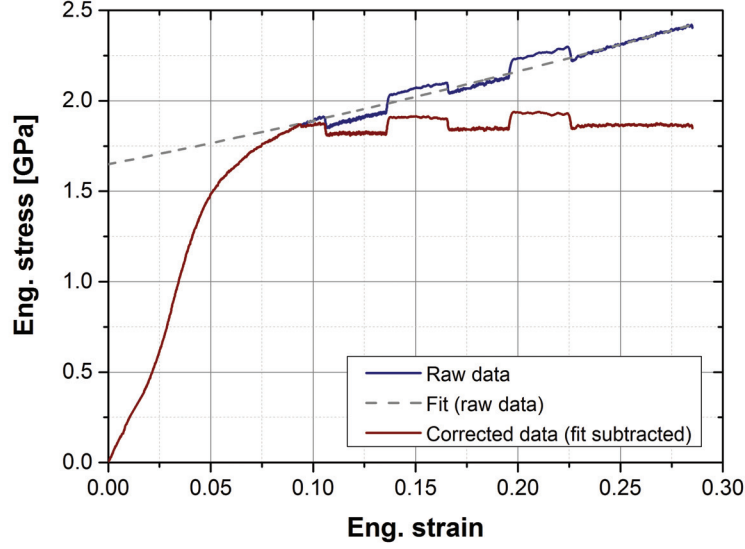


Figure 5.5.: Raw and corrected experimental data for determination of SRS exponent from engineering stress-strain curve for one of the tests. Values of  $m$  were determined instantaneously across the SRJs as well as from the slope of stress-strain rate from the corrected data plotted in log-log scale.

Table 5.1.: Comparison of  $m$  values calculated for one of the pillars tested at 100°C using method (a) (instantaneous SRS determination) on raw and slope-corrected engineering stress-strain curves. The  $m$ -value determined using method (b) (from the slope of stress-strain rate plot in log-log scale) on slope-corrected data is also shown for comparison.

Strain rate jump segment ( $s^{-1}$ )	Method (a) on raw data	Method (a) on corrected data	Method (b) on corrected data
0.001-0.0002	0.026	0.029	
0.0002-0.002	0.027	0.030	
0.002-0.0005	0.022	0.028	
0.0005-0.005	0.025	0.026	
0.005-0.001	0.020	0.027	
Average	0.024	0.028	0.027

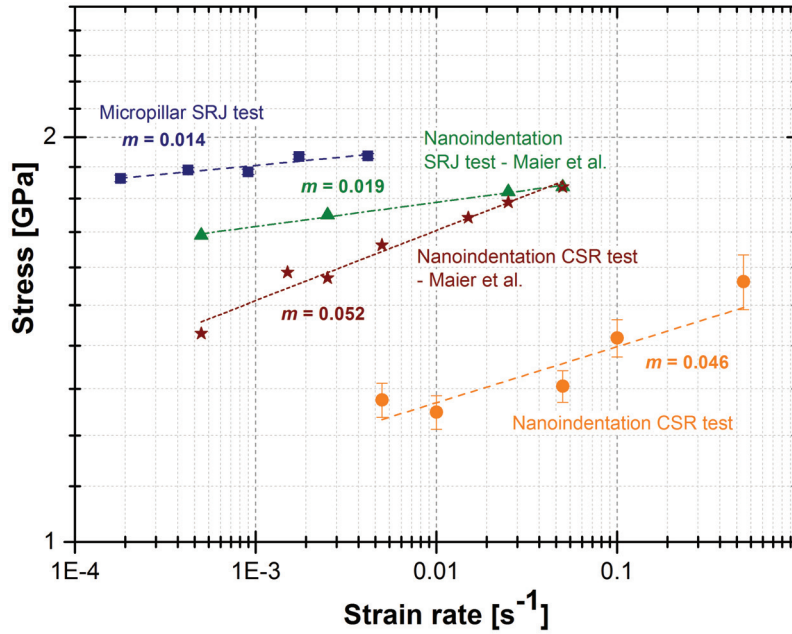


Figure 5.6.: Log-log plot of flow stress vs. strain rates showing micropillar SRJ and nanoindentation CSR data at room temperature. The hardness  $H$  obtained from nanoindentation measurements was converted to stress by division with a factor of 2.8.

strate effect [141] as the indentation-depth-to-film thickness ratio was around 15%. It should be noted that nanoindentation CSR tests yield higher  $m$  values due to influence of thermal drift and creep for lower strain rates [12]. For comparison with literature, nanoindentation SRJ and CSR data from Maier et al. [12] are also shown. Values of  $m$  obtained from both SRJ techniques and both CSR measurements show good agreement. The average grain size of the nanocrystalline sample, determined from XRD analysis, used by Maier et al. [12] was  $80\text{nm}$  in comparison to  $27\text{nm}$  in this study.

### 5.1.3. Discussion

#### Apparent activation volume

The apparent activation volume,  $V_{app}$ , was calculated from SRJ tests using Equation 6.2. The apparent activation volume is directly related to the plastic deformation and

is often used to obtain an idea of the governing rate controlling mechanism(s). The variation in SRS exponent,  $m$ , and apparent activation volume,  $V_{app}$ , as a function of temperature obtained from micropillar SRJ tests is shown in Figure 5.4. Literature data [142] on bulk uniaxial tensile SRJ tests performed on nanocrystalline samples of average grain size  $29nm$ , determined using TEM, is also shown. The values of  $m$  and  $V$  match reasonably well for both cases. These results are consistent with previous literature on bulk deformation of nanocrystalline nickel that report SRS exponent,  $m$ , of around 0.02 and activation volume,  $V_{app}$ , in the range of  $10 - 20b^3$  [7, 12, 143, 142, 144, 145]. Activation volumes of  $\sim 1b^3$  correspond to grain boundary diffusion processes [7].

### Apparent activation energy for deformation

For many mechanical deformation processes, multiple deformation mechanisms will be active at any time. If the deformation mechanisms are in series, the mechanism having the highest activation energy will be the rate-controlling mechanism. In case of parallel mechanisms, the one having the lowest activation energy will dominate [96]. Due to stress and temperature dependence of the activation energies, only an apparent activation energy value can be calculated which is devoid of any stress dependence. Traditionally, the apparent activation energy for deformation has been calculated from the slope of  $\log(\dot{\epsilon})$  vs.  $(1/T)$ , particularly in the field of creep testing. This follows from the widely used steady state creep equation that correlates the overall strain rate,  $\dot{\epsilon}$ , with the applied stress,  $\sigma$ , through an Arrhenius formulation:

$$\dot{\epsilon} = A\sigma^n \exp\left(\frac{-Q}{RT}\right) \quad (5.1)$$

where  $A$  is a pre-exponential constant,  $R$  is the gas constant and  $T$  is the temperature in degrees  $K$ . On taking logarithm of both sides, this equation reduces to:

$$\log(\dot{\epsilon}) = \log(A) + n \log(\sigma) - \frac{Q}{RT} \quad (5.2)$$

Assuming  $\log(A) + n \log(\sigma)$  to be constant, the slope of  $\log(\dot{\epsilon})$  vs.  $(1/T)$  provides the value of  $\left(\frac{-Q}{RT}\right)$ . The inherent assumptions are the attainment of steady state strain rates at each test temperature and strain rate values plotted for the same stress levels. This follows from the assumption of constant microstructure in steady state creep regime. For SRJ tests, the case is slightly different, although

some parallels can be drawn to the creep tests. Due to absence of strain hardening or strain softening in nanocrystalline materials [7], the assumption of constant microstructure can be considered to hold true. Also, the strain rate remains constant, which can be considered analogous to CSR in secondary state creep tests. The only difference is that the stress values are not the same for the pillars measured at different temperatures. Since flow stress is a strong function of the applied strain rate for nanocrystalline nickel pillars tested, the strain rates can be extrapolated to constant stress values to calculate the apparent activation energy for deformation. Figure 5.7(a) illustrates this extrapolation at a flow stress level of  $\sigma = 1.75\text{GPa}$ . The slope of the curve in Figure 5.7(b) yields an apparent activation energy value of  $102.5\text{kJ/mol}$ , which is close to the boundary diffusion activation energy for nickel ( $115\text{kJ/mol}$ ) [146]. It should be pointed out that similar apparent activation energy values were also obtained from bulk compression experiments on nanocrystalline nickel by Kottada and Chokshi [147] from creep measurements and by Li et al. [148] from SRS measurements.

Another approach for calculating the apparent activation energy using the same concept from hardness values as suggested by Sherby and Armstrong [149], involves slight modification of Equation 5.2 to compensate for the creep stress exponent,  $n$ , in the exponential term. Taking this logic further and equating  $m = (1/n)$ , the following equations are obtained:

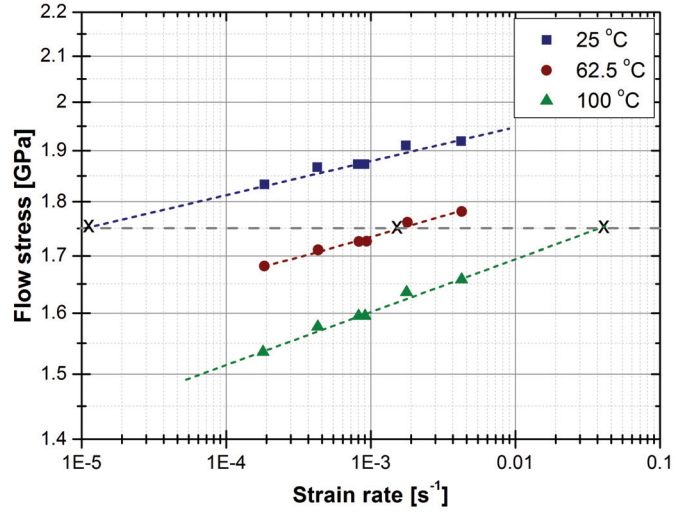
$$\dot{\varepsilon}^{(\frac{1}{n})} = A^{(\frac{1}{n})} \sigma \exp\left(\frac{-Q}{nRT}\right) \quad (5.3)$$

$$\dot{\varepsilon}^{(m)} = A^{(m)} \sigma \exp\left(\frac{-mQ}{RT}\right) \quad (5.4)$$

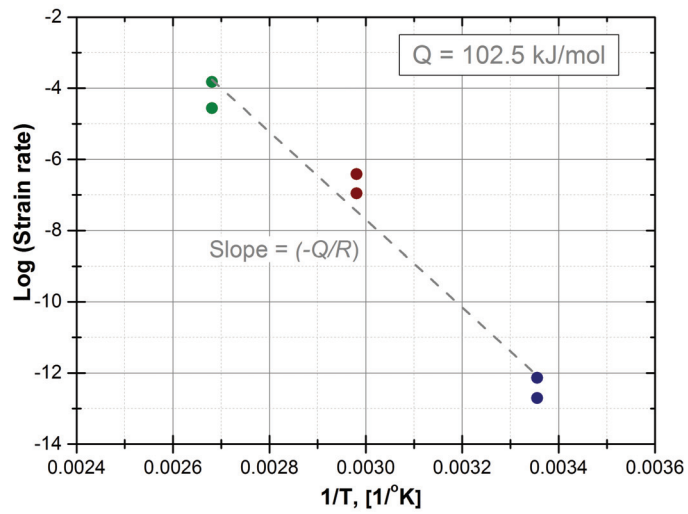
$$\sigma = \frac{1}{A^{(m)}} \dot{\varepsilon}^{(m)} \exp\left(\frac{mQ}{RT}\right) \quad (5.5)$$

$$\log \sigma = \log \left\{ \frac{1}{A^{(m)}} \right\} + m \log(\dot{\varepsilon}) + \left(\frac{mQ}{RT}\right) \quad (5.6)$$

$$\log \sigma = B + \left(\frac{mQ}{RT}\right) \quad (5.7)$$



(a)



(b)

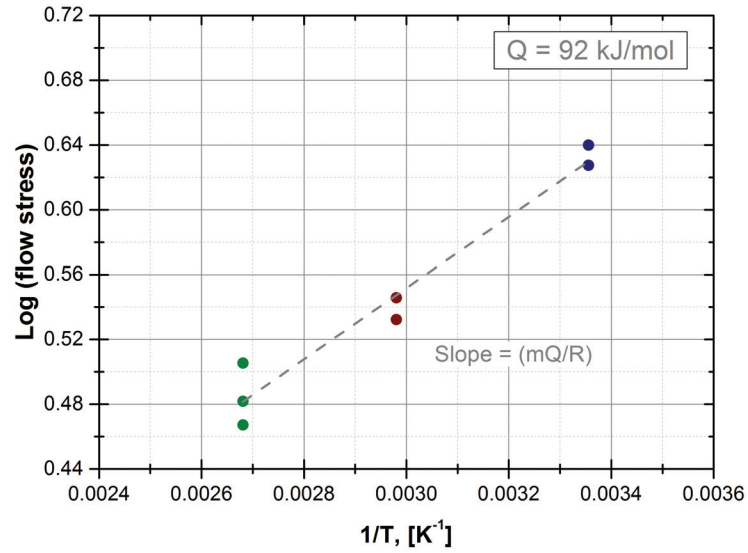
Figure 5.7.: Extrapolation of strain rate at a constant stress level of  $\sigma = 1.75\text{GPa}$  (a) and corresponding apparent activation energy for deformation,  $Q$ , plotted in log scale vs.  $1000/T$  (b).

Assuming a constant average value of  $m = 0.02$ , an apparent activation energy value of  $Q_{average} = 92 \pm 9 \text{ kJ/mol}$  is obtained over the tested strain rates (Figure 5.8(a)) that corresponds well with the previously calculated value. Changing  $m$  from 0.014 to 0.026 (values for RT and 100°C, respectively) changes the apparent activation energy from 135 to 72 kJ/mol. These values are still in the range for boundary diffusion. It should be noted that the activation energies for nickel for lattice diffusion and core diffusion are 284 and 170 kJ/mol, respectively, quite far off from the values calculated from SRJ tests. The apparent activation energy seems to decrease with the applied strain rate (Figure 5.8(b)), indicating that more deformation is accommodated by dislocation plasticity at higher strain rates.

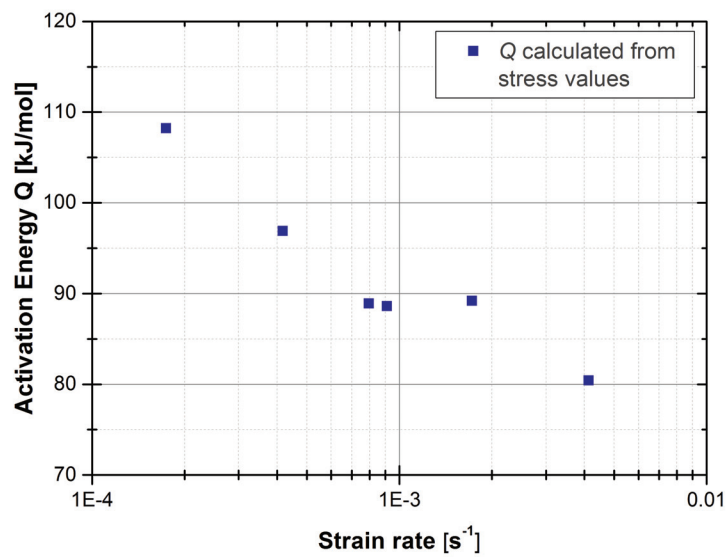
Lohmiller et al. [96] reported on the sequence of deformation mechanisms in nanocrystalline Ni with an average grain size of 30 nm. They reported that the deformation behaviour proceeds in the following sequence: (a) elasticity, (b) grain boundary shear and slip, (c) dislocation glide and (d) finally grain growth at large strains. They further stated that the deformation is governed by succession of these different, partly overlapping mechanisms. In case of deformation mechanisms in series, the deformation mechanism that has the highest activation energy becomes the rate controlling mechanism. The apparent activation energy extracted for the deformation should match closely with the activation energy of the rate controlling mechanism in this case [150]. Since the activation energy for slip is very small in comparison to that for grain boundary diffusion, and these mechanisms can be considered to be in series, we obtain an apparent activation energy value that matches closely with grain boundary diffusion. These observations are consistent with large volume fraction of grain boundaries present in the sample and extensive grain boundary sliding observed in the deformed pillars.

#### 5.1.4. Conclusions

Microcompression SRJ technique has been successfully demonstrated on nanocrystalline nickel. Good agreement was obtained for SRS exponent,  $m$ , and apparent activation volume,  $V_{app}$ , between microcompression and bulk compression SRJ tests from 25°C to 100°C. The apparent activation energy extracted from SRJ tests matched well with grain boundary diffusion activation energy for nickel suggesting it to be the rate controlling deformation mechanism. Electron microscopy of the deformed pillars showed extensive grain boundary sliding and rotation to accommodate the plastic strain. Slip traces were also observed in case of large grains. These observations are consistent with the existing literature. The microcompression testing



(a)



(b)

Figure 5.8.: (a) Apparent activation energy,  $Q$ , values calculated from  $\log(\text{stress})$  vs.  $(1/T)$  plots. Here the applied strain rate was  $\dot{\epsilon} = 10^{-3} \text{ s}^{-1}$ . (b)  $Q$  plotted as a function of applied strain rates.



technique and the analysis methodology described in this section enable determination of SRS parameters from micro-pillar samples prepared from thin films and coatings as well as site specific small length-scale microstructural features.

## 5.2. Comparison of in situ micromechanical techniques

Today, mechanical testing of nanocrystalline metals is mostly restricted to nanoindentation. Nanoindentation systems are readily available in many facilities and in the context of nanomechanical- or thin film applications this technique provides two distinct benefits: only a reduced amount of sample surface preparation like a thorough mechanical or chemical surface polishing is required which is beneficial for accelerated materials characterization and secondly, already small/thin amounts of material are sufficient to yield representative test results. On the downside, the interpretation of nanoindentation data is not straight forward, mainly because of the complex hydrostatic stress state underneath the indenter tip which is heavily influenced by the shape of the tip apex. Further, the volumes which are probed during an indentation are rather small and may therefore not be representative for the overall properties of the material as localized compositional gradients, microstructural inhomogeneities (i.e. growth gradients in electrodeposited films) can easily occur. With respect to industrial applications as discussed in more detail in Chapter 7, microcomponents which are manufactured from electrodeposited nanocrystalline metals also show a strong directional (textural) dependence of mechanical properties. For instance, in mechanical watches many parts fulfill a function as a spring and thus require to store energy. Hence, the elastic properties of these materials need to be assessed with respect to the main loading direction a microcomponent encounters over its lifetime. However, with nanoindentation this is not possible as the method is somewhat insensitive to textural effects. Therefore and also from an interpretation point of view, uniaxial tests are much more favorable. Tensile tests, for example, are straight forward to perform and provide easy understandability and interpretation of micromechanical data, as the load case is uniaxial. During such a test always the entire cross-sectional area of a specimen is accessed which improves the statistical relevance and diminishes the influence of microstructural inhomogeneities or localized compositional gradients. However the limited availability of thick ( $> 10\mu\text{m}$ ), freestanding quantities of nanocrystalline materials or thin films prevails their application. Consequently, in our attempt to bridge the gap between the three load cases and assist in the validation of their comparability, freestanding nanocrystalline nickel LiGA specimen (industrial reference material) were tested in this study. The

industrial reference nickel was chosen, as this study was partly conducted in the framework of a CTI-project<sup>‡</sup>. To enhance the comparability of results and avoid any sample to sample variations in composition and/or microstructure obtained from a single electrodeposited wafer, the full series of nanoindentation and micropillar compression tests in this work were performed on the undeformed ends of one of the dogbone tensile specimens postmortem. The experimental details and results in this section have been published as an article in „JOM: Journal of The Minerals, Metals & Materials Society (TMS)“<sup>§</sup>.

### 5.2.1. Industrial reference material

Nominally pure nanocrystalline nickel was produced by means of a proprietary electrodeposition process on a silicon wafer. The material is used as an industrial reference. A UV-LIGA [98] method was utilized to produce individual free-standing, dogbone-shaped microtensile bars, as shown in Figure 5.9. Further details about the material composition and the sample production method are provided in Section 4.1 and 4.1.2 respectively. A compositional characterization did not yield any major impurities as can be seen from Table 4.2. The dogbone-shaped samples had a gauge length of  $3.0\text{mm}$ , gauge width of  $0.15\text{mm}$  and thickness of  $0.25\text{mm}$ . The top surface of the deposited samples was lightly polished with a final grit size of  $< 0.05\mu\text{m}$ , using standard metallographic techniques to reduce surface roughness.

In order to determine the electrodeposited industrial reference material’s texture and crystallite size, X-ray diffraction (XRD) measurements were performed using a Discover D8 diffractometer (Bruker GmbH, Karlsruhe, Germany) with a Cu-K $\alpha$  source operated at  $40\text{kV}/40\text{mA}$ . The texture of the samples was estimated from the (111), (200), (220) and (311) peaks from the Bragg-Brentano  $\Theta$ - $2\Theta$  diffractograms, using the Harris method [151]. The results indicate a strong  $\langle 111 \rangle$  texture. The average crystallite size was estimated with the Scherrer formula [115, 114] from the full width at half maximum of the (111) peak, which yielded a mean value of  $d_{(\text{XRD},\text{Ni})} = 15\text{nm}$ . As already mentioned in Section 4.4, this estimation is only a lower boundary estimate, since some parameters, such as the presence of twins, crystal defects and residual stresses, can also contribute to the peak broadening [118]. For additional characterization of the material’s microstructure and grain size, transmission electron microscopy (TEM) was performed in accord to Section

---

<sup>‡</sup> *Accelerated materials design of alloys for LIGA parts with high Young’s modulus and creep resistance comparable to maraging steel CTI-209673*

<sup>§</sup> **Comparison of in situ Micromechanical Strain-Rate Sensitivity Measurement Techniques**, Wehrs et al., JOM, August 2015, Volume 67, Issue 8, pp 1684-1693 [94]

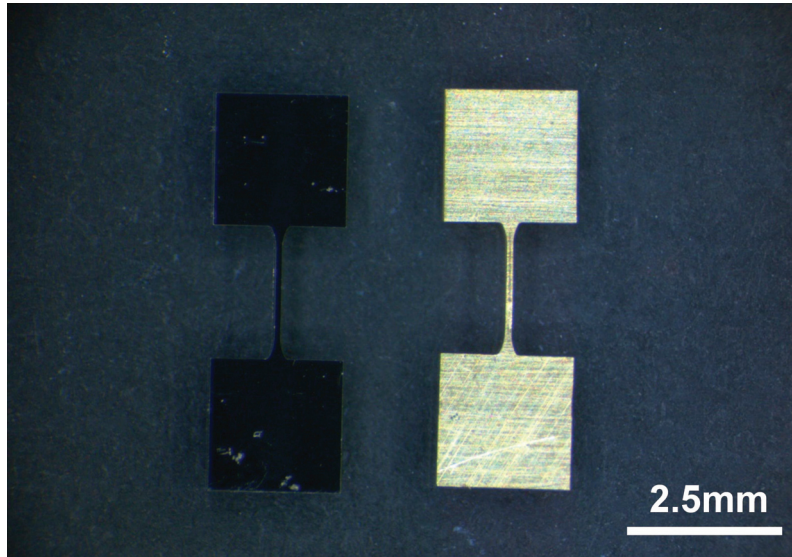


Figure 5.9.: Two types of miniaturized tensile specimen: on the left side an electrodeposited nanocrystalline nickel specimen (LIGA) and an electrode discharge machined maraging steel specimen on the right.

4.4. A representative TEM image of the specimen used in the present section was taken in scanning mode (STEM) at  $200kV$  and  $0.7nm$  spot size and is given in Figure 5.10. The material's nanostructure displayed a homogeneous grain size distribution with an average grain size of  $26 \pm 10nm$ , calculated for over fifty grains applying grain area analysis using the ImageJ software package.

### 5.2.2. Nanomechanical measurements

#### Minaturized tensile tests

Displacement-controlled miniature tensile experiments to investigate the bulk mechanical behavior of nanocrystalline nickel were conducted on the modified Kammrath & Weiss in situ tensile test frame as described in Section 4.7 and displayed in Figure 4.20. Tests were performed by means of monotonic, constant strain rate (CSR) and transient strain rate jump (SRJ) techniques. CSR tensile tests were conducted on a minimum of three samples of nc-nickel and maraging steel at a strain rate of  $\dot{\epsilon} = 10^{-4}$  until specimen failure. Strain rate jump tests were performed on five nc-nickel samples where the strain rate was varied over two orders of magnitude from  $\dot{\epsilon} = 10^{-3}$  to  $\dot{\epsilon} = 10^{-5}$ , following the same sequence of jumps as described in Section 5.1.

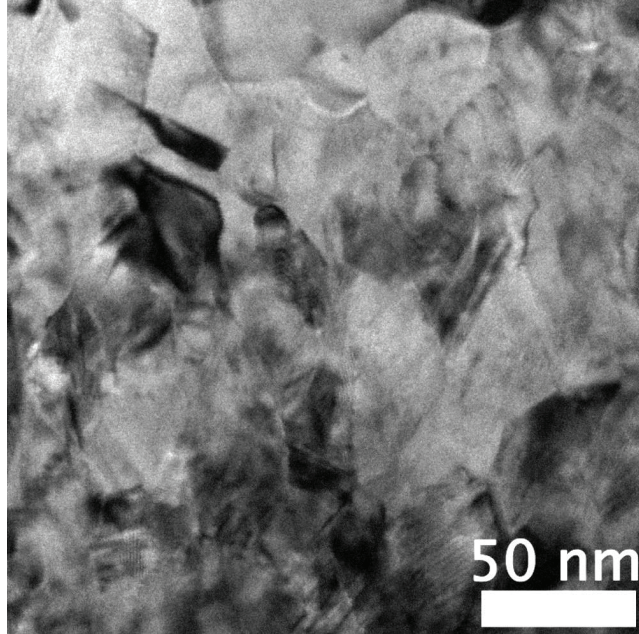


Figure 5.10.: Bright field TEM image of industrial nanocrystalline nickel. The grain size is in the order of  $26\text{nm}$ .

### Nanoindentation

In situ nanoindentation was performed at room temperature using the SEM Indenter system as described in Section 4.6. In order to ensure that the representative strain level was comparable to both the tension and the microcompression testing, nanoindentation testing was performed using a calibrated [11] diamond Berkovich indenter,  $\varepsilon_{\text{R}} = 8\%$  rather than a Cube Corner indenter,  $\varepsilon_{\text{R}} = 22\%$  [12], which would have provided superior in situ observation. A limitation of previous work [152] using this system to characterize strain rate sensitivity using indentation was the lack of Continuous Stiffness Measurement (CSM, also alternately referred to as sinus mode or dynamic testing) capability [153] to measure the hardness and modulus as a function of depth during the jump segments. However, in collaboration with Alemnis GmbH, this has now been developed. An oscillation with constant voltage amplitude was superimposed on the excitation of the displacement piezoelectric stack. This resulted in a displacement amplitude of approximately  $5\text{nm}$  at a frequency of  $25\text{Hz}$ . The indentation modulus and the hardness were extracted from each sinus segment using the Oliver and Pharr method [154]. Strain rate jumps were incorporated during each indentation cycle using the method described by Maier et al. [12]. The indentation strain rate, defined as the ratio of the loading rate,  $\dot{P}$ , to the current load,  $P$ , has

been shown [155] to be proportional to the strain rate when the hardness,  $H$ , is constant with depth  $\dot{H}/H = 0$  at depths above that where an indentation size effect is observed:

$$\dot{\epsilon} = \frac{\dot{h}}{h} = \frac{1}{2} \left( \frac{\dot{P}}{P} - \frac{\dot{H}}{H} \right) \approx \frac{1}{2} \frac{\dot{P}}{P} \quad (5.8)$$

The indentation strain rates were varied from  $\dot{\epsilon}_{\text{SRJ,Indentation}} = 2 \times 10^{-2} s^{-1}$  to  $5 \times 10^{-5} s^{-1}$  during the loading cycle. The hardness was measured for depths greater than  $500nm$  in order to avoid any size effects [12]. During unloading, the strain rate was kept constant at  $\dot{\epsilon}_{\text{SRJ,Indentation,Unloading}} = 2 \times 10^{-3} s^{-1}$  and the thermal drift was corrected by applying a constant load hold segment at 5% of maximum load. A relatively high data acquisition rate of  $2500Hz$  was used to capture the sinus oscillations with sufficient resolution at the higher strain rates. The modulus and hardness results obtained were averaged over five sinus oscillation cycles. More than ten indentations were performed with different strain rate jump profiles (i.e. varying the order of the strain rate magnitudes occurring at different indentation depth segments) to illustrate the reversibility of the jumps [12], and ensure that the hardness is a function of indentation strain rate and independent of indentation depth.

### Micropillar compression

Nanocrystalline nickel micropillars with a nominal diameter of  $3.5\mu m$  were machined by employing the milling strategy described in Section 4.5.1. For further comparison, micropillars were also fabricated on a  $\langle 123 \rangle$ -oriented single crystal of pure nickel, acquired from Goodfellow Ltd., Cambridge, UK. Microcompression testing was performed with the in situ indentation system described in Section 4.6, utilizing a  $5\mu m$  diameter diamond flat punch tip. CSR tests were conducted with a strain rate of  $\dot{\epsilon}_{\text{CSR,Compression}} = 7 \times 10^{-4} s^{-1}$  to a total strain of 11%. The applied strain rates were varied from  $\dot{\epsilon}_{\text{SRJ,Compression}} = 2 \times 10^{-2} s^{-1}$  to  $4 \times 10^{-5} s^{-1}$  on each micropillar. Similar to the nanoindentation experiments, the strain rate for the last segment was kept the same as for the first segment to demonstrate reversibility. Additionally the order of the strain rate jumps was changed for a few tests in order to ensure that the strain hardening of the material did not influence the test results. A minimum of three pillars were compressed on both the nc-nickel and the  $\langle 123 \rangle$ -oriented  $sx$ -nickel samples.

### 5.2.3. Results and discussion

#### Miniature Tension

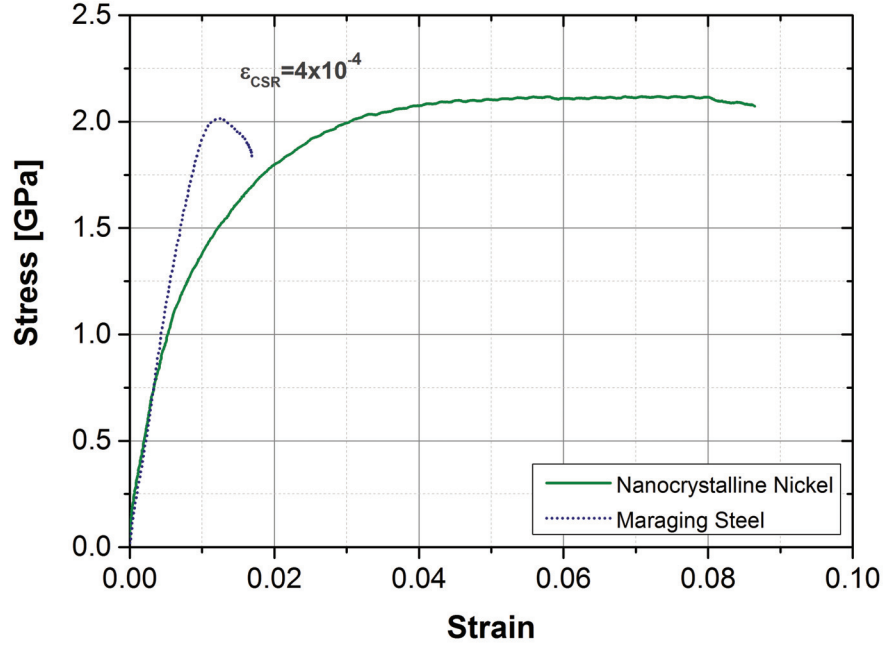


Figure 5.11.: Tensile stress-strain curves of nanocrystalline nickel and polycrystalline maraging steel at constant strain rate (CSR).

Tensile testing is perhaps the most standard technique for measuring mechanical properties and, as such, provides a good baseline against which to compare the results of more novel techniques. Figure 5.11 shows representative stress-strain curves obtained from CSR tension tests performed at a strain rate of  $\dot{\epsilon}_{\text{CSR, Tension}} = 4 \times 10^{-4} \text{ s}^{-1}$ . Results from nc-nickel samples indicate a Young's modulus of  $E_{\text{nc Ni}} = 180 \pm 12 \text{ GPa}$  and yield strength at 1% offset of  $\sigma_{\text{y,nc Ni}} = 1.8 \pm 0.2 \text{ GPa}$ . Significant work hardening and ductility is also observed.

These results are difficult to directly compare to other researchers results in the literature, since it is known that the mechanical properties of nanocrystalline materials depend heavily on factors like grain size, texture, impurities and processing parameters. To ensure the accuracy of the applied testing apparatus and method, reference measurements on a well-characterized bulk material were also conducted. Miniature tensile bars were made using electrical discharge machining (EDM) from rolled

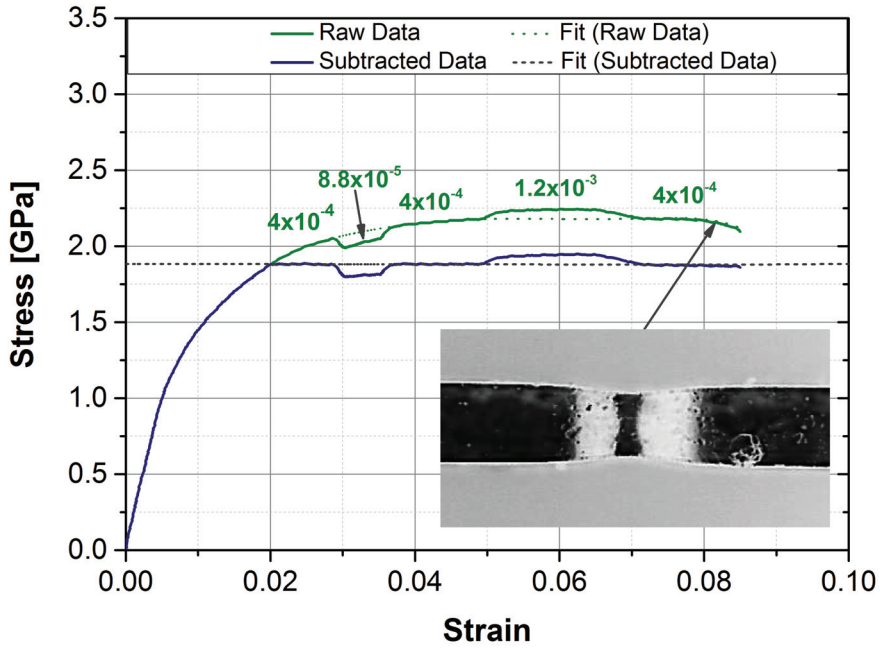


Figure 5.12.: Tensile stress-strain curves for SRJ tests on nanocrystalline nickel. The green curve shows the raw data whereas the green dashed curve represents a fit through the initial and final segment. To account for strain hardening the fit was subtracted and shifted in stress axis to result in zero slope (blue curve).

maraging steel sheets of similar thickness to the nc-nickel LIGA samples. Tensile results from these samples yielded a Young's modulus,  $E_{\text{maraging steel}} = 205 \pm 10 \text{ GPa}$ , and ultimate tensile strength  $UTS_{\text{maraging steel}} = 2.0 \pm 0.12 \text{ GPa}$ . These results match very well with the bulk properties given by the manufacturer ( $E_{\text{maraging steel,ref}} = 208 \text{ GPa}$  and  $UTS_{\text{maraging steel,ref.}} = 2.05$ ). This suggests that the applied testing and data evaluation method is valid and delivers reasonable results for the nanocrystalline nickel. The majority of studies on the SRS of nanocrystalline metals under tensile loading have concentrated on series of monotonic, CSR tests where individual specimens are strained at a single strain rate for the entire duration of the test. This is repeated for several different strain rates with a different specimen for each test. Transient tests, where the strain rate changes during the test, provide the advantage of extracting rate sensitivity from a single test by varying the strain rate and monitoring the materials response in flow stress [14]. This allows measurement of the rate sensitive flow behavior of a constant microstructure and removes the influence of any

microstructural variation between samples. However, the ductility of nanocrystalline materials is generally limited to a few percent strain before plastic instability (non-uniform deformation such as necking) occurs, and this generally limits the feasibility of transient testing. Furthermore, the lack of strain hardenability, due to the small grain size, reduces the magnitude of the plastic regime further. The location of this plastic instability is generally attributed to defects (e.g. pores or foreign species), which lead to localized stress concentrations. The nature and quantity of these defects can vary heavily with the production method of the samples. After onset of plastic instability, which is described by the Considère-criterion [156]:

$$\left(\frac{\delta\sigma}{\delta\varepsilon}\right)_{\dot{\varepsilon}} \leq \sigma \quad (5.9)$$

The stress state is no longer purely uniaxial, so experimental observations will differ from the theory. The inset in Figure 5.12 shows a tensile bar during necking, which is first observed at around 8.2% strain. In a well-designed transient test, all of the rate jumps will be completed well before the onset of necking. Therefore, the number of possible strain rates (in the strain rate range of interest) that can be accommodated within one test using this apparatus was limited to three. Figure 5.12 displays the sequence of SRJ on a representative stress-strain curve. The initial strain rate was set to  $\dot{\varepsilon}_{\text{SRJ,tension,1}} = 4 \times 10^{-4} \text{ s}^{-1}$  until well into the plastic regime. Reducing the strain rate to  $\dot{\varepsilon}_{\text{SRJ,tension,2}} = 8.8 \times 10^{-5} \text{ s}^{-1}$  showed an immediate reduction in flow stress. Increasing the strain rate back to  $\dot{\varepsilon}_{\text{SRJ,tension,1}}$  resulted in an increase in flow stress back to the previous level as predicted by the fitted curve. This shows the flow stress transient testing to be fully reversible, indicating a mostly constant microstructure. This same reversibility was observed after increasing the strain rate further by another order of magnitude to  $\dot{\varepsilon}_{\text{SRJ,tension,3}} = 1.2 \times 10^{-3} \text{ s}^{-1}$ . After each SRJ, the flow stress level was observed to quickly reach a steady state.

### Nanoindentation

A representative load-displacement curve from nanoindentation SRJ experiment is shown in Figure 5.13. The individual SRJ segments are marked with their corresponding strain rates and can be clearly distinguished from the baseline strain rate of  $2 \times 10^{-2} \text{ s}^{-1}$ . The strain rate was kept constant up to  $700 \text{ nm}$  to allow that the indentation hardness values to stabilize to a constant value.

Hardness and modulus results as a function of indentation depth are plotted in Figure 5.14. The indentation modulus (shown in blue) remains roughly constant as a function of depth, similar to the trends observed by Maier et al. [12]. The scatter



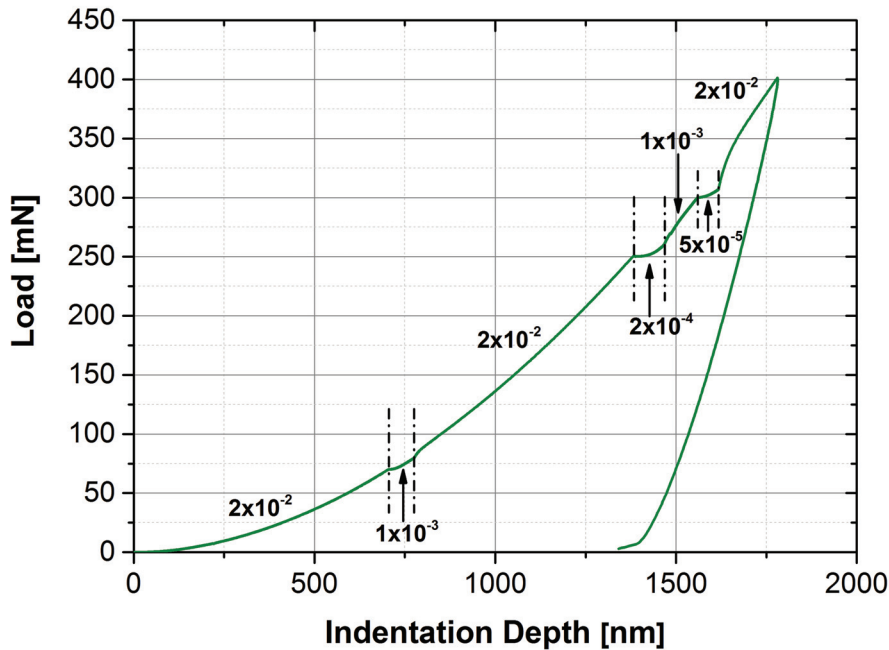


Figure 5.13.: Representative load-displacement curve from SRJ indentation of nc-nickel.

in modulus data increases with depth due to the increasing contribution of load cell compliance at higher loads. Since the applied sinus displacement amplitude is not compliance-corrected, the compliance-corrected displacement - used for computation of modulus and hardness values - decreases with increasing load. This increases scatter at higher loads/ depths. Although not applied here, data smoothing can be additionally used to further reduce the scatter in modulus values. Similar trends have been observed for calibration tests performed on fused silica using this instrument. Hardness values (shown in green) can be clearly observed to vary directly with the applied strain rate due to the rate jumps. The magnitude of  $\Delta H$  is more pronounced for larger  $\Delta \epsilon$  values. Hardness stabilizes back to the baseline values as soon as the initial strain rate is restored. Initial hardness and modulus values from depths less than  $400\text{nm}$  have not been shown as they are more likely to be affected by tip area calibration and other errors.

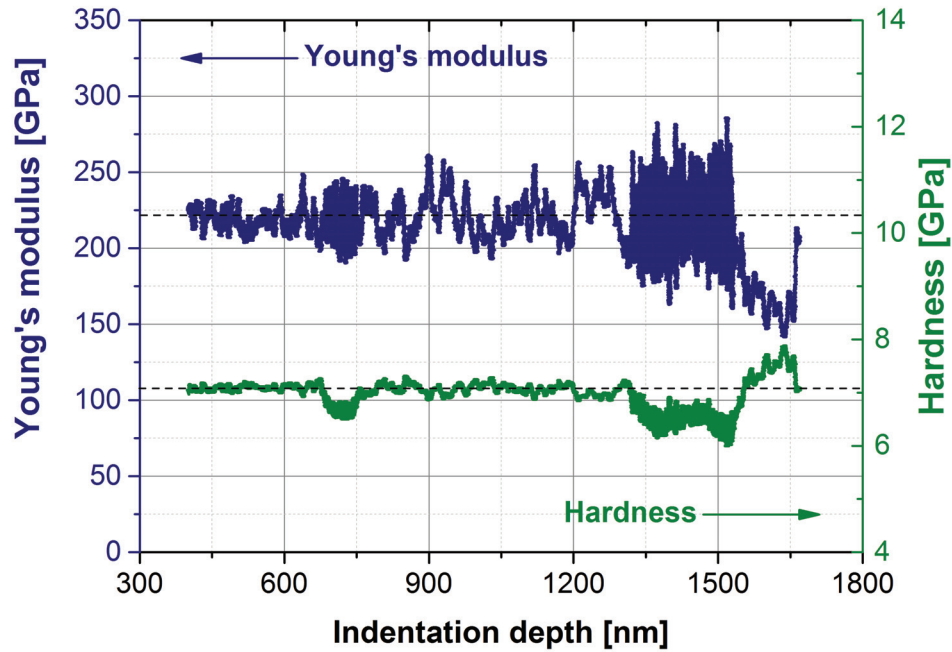


Figure 5.14.: Indentation modulus (blue) and hardness (green) as a function of indentation depth.

### Microcompression

Prior to performing strain rate jump microcompression tests, constant strain rate tests were conducted with a strain rate of  $\dot{\epsilon}_{\text{CSR, Microcompression}} = 7 \times 10^{-4} \text{ s}^{-1}$  to determine the appropriate strain levels after general yielding to perform rate jumps. Figure 5.15 illustrates the differences in deformation behavior between the two materials observed in situ during testing at selected strain levels. While the nc-nickel micropillar (Figure 5.15 (a)) accommodate most of the plastic deformation by somewhat homogeneous barreling localized in its upper half, the single crystal pillar (Figure 5.15 (b)) develops several large, discrete slip steps over the entire pillar diameter. These slip steps increase in number with increasing strain. However, at higher strain levels, the slip steps near the top of the pillar slide downwards and towards the direction of observation to occlude slip steps lower down the pillar.

The stress-strain behavior typical of these CSR tests is shown by the blue curve in Figure 5.16. The yield strength observed at 1% offset was  $2.55 \text{ GPa}$ . The apparent strain hardening observed in the curve can be partly attributed to geometric

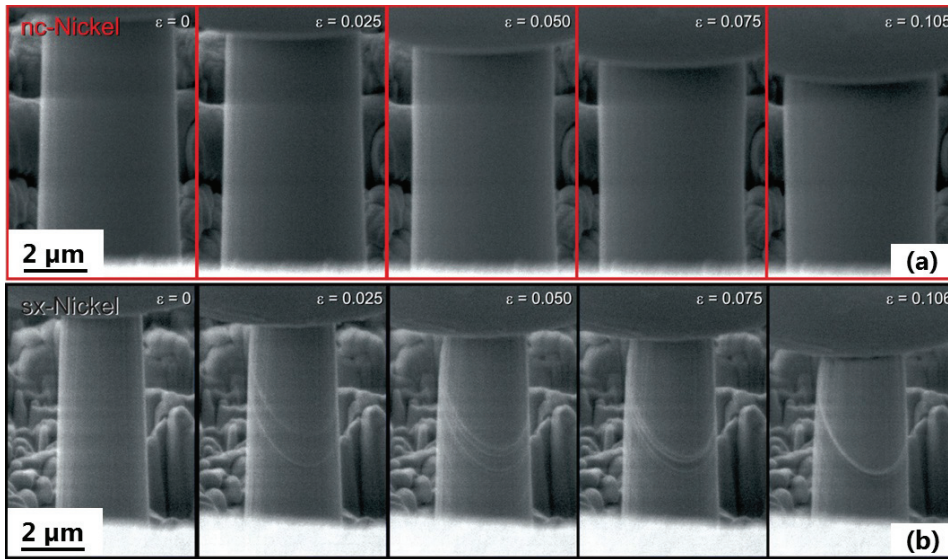


Figure 5.15.: In situ SEM observation of the deformation behavior of nc-nickel (a) and sx-nickel (b) micropillars during compression testing at selected strains.

effects and inhomogeneous deformation throughout the pillar height (Figure 5.15), as discussed in our previous work [118]. For all further considerations, only true stress-strain curves were taken into account.

The green curve in Figure 5.16 shows the representative stress-strain behavior observed during the SRJ tests. Strain rates were varied over four orders of magnitude from to within each test. The jumps are observed to be sharp with rather quick stabilization of the flow stress and minor transients. Following the sequence of the jumps, it is obvious that the increasing strain rates result in a significant increase in flow stress due to the pronounced SRS of nanocrystalline nickel. The first and the final jump segments were both performed at the same strain rate (the same rate as the CSR tests) to allow correction for any influence of apparent work hardening or strain softening. However, the SRJ and CSR tests are shown to agree exceptionally well. This suggests that these tests are highly repeatable due to a uniform microstructure within the material and a high geometric fidelity of the pillars due to their relatively large diameters and careful preparation. Since the flow stress returns to its monotonic/CSR levels upon decreasing the strain rate in the final segment, this suggests that any microstructural evolution within the material is effectively independent of strain rate, and that no change in deformation mechanism occurs within this range of strain rates.

To illustrate the tremendous strengthening effect of the nanocrystalline microstruc-

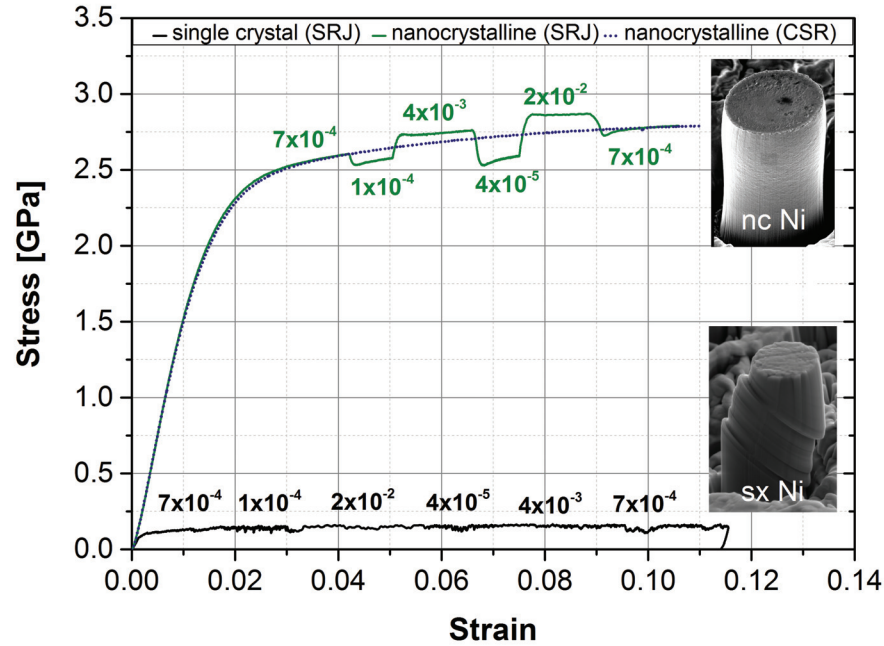


Figure 5.16.: Micropillar stress-strain curves of nc-Nickel and  $\langle 123 \rangle$ -oriented *sx*-nickel.

ture, microcompression testing was also performed on a  $\langle 123 \rangle$ -oriented single crystal of nickel. Both CSR and SRJ tests were conducted on a total of three pillars with exactly the same strain rates and similar diameters as the nanocrystalline micropillars. The single crystal's yield strength at 1% offset is observed to be only  $0.13\text{GPa}$  (Figure 5.16) - nearly a factor of twenty less than its nanocrystalline counterpart! Due to these low strengths, the indenter was operated close to the resolution limit of the load cell, so some additional noise is observed in the data during the rate jumps. However, the deformation of single crystals in experiments similar to this has been frequently observed to display flow serration which is often attributed to dislocation avalanches [157] as shown in Figure 5.17 (b). Due to this increased noise, no pronounced strain rate sensitivity can be observed at first glance, and statistical analysis is needed.

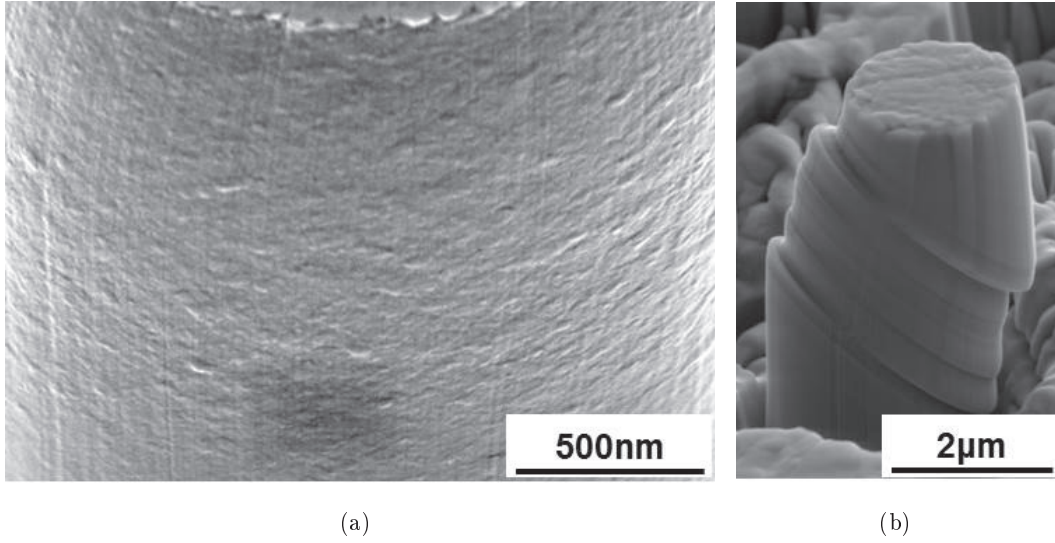


Figure 5.17.: Post compression high resolution SE micrographs illustrate the differences in deformation behavior: (a) nc-nickel showing displaced grains distributed throughout the pillar and (b) sx-nickel showing deformation confined to discrete slip bands traversing the pillar.

### Strain rate sensitivity

For uniaxial mechanical tests (e.g. tension or compression), the strain rate sensitivity (SRS) exponent,  $m$ , can be extracted by using the following equation [158]:

$$m = \left[ \frac{d(\ln\sigma)}{d(\ln\dot{\epsilon})} \right]_T \quad (5.10)$$

where  $d(\ln\sigma)$  is the change in flow stress as a function of the change in applied strain rate  $d(\ln\dot{\epsilon})$  at constant temperature  $T$ . To determine the SRS from indentation tests, the representative indentation strain rate and the representative indentation stress should be used instead [159]. As in Section 5.1, two analysis methods were applied to extract values of  $m$  from the different data sets. Method (a) allows the direct calculation of the  $m$  values from the raw data across the strain rate jump by ignoring the transients using the assumption that the nanostructure right after the SRJ remains constant. This method is less sensitive to the slope of the curve (strain hardening/softening), but it is susceptible to noise in the data, long transients and local yield changes immediately before and after the strain rate jump. Method (b) allows determining the SRS from the slope of a plot of stress vs. strain rate on a log-log scale, but it is sensitive to any increase/decrease in stress between jumps due to apparent work hardening in the stress-strain curve. It can be seen in both

Figure 5.12 and Figure 5.16 that the nc-nickel does show moderate apparent strain hardening, so additional steps are required to correct for this in order to use method (b). This is accomplished by subtracting the apparent work hardening from the curve by fitting a polynomial relationship to the segments with the same strain rate (i.e.  $\dot{\epsilon}_{\text{SRJ},1}$  for the curves from tensile tests) and subtracting it from the raw data, as illustrated for the tension tests in Figure 5.12. The resulting curves are then flat in regions of constant strain rate, so that the variation in flow stress due to changes in strain rate are directly apparent.

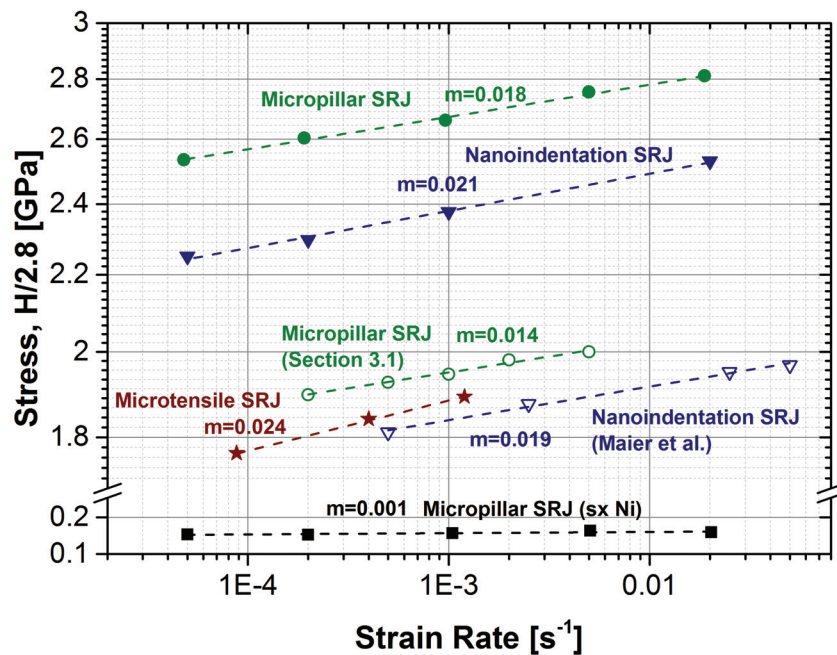


Figure 5.18.: Flow stress as a function of strain rate for tension, microcompression and nanoindentation ( $H/2.8$ ) tests from the current work and the literature (Maier et al. [12]). Note the jump in the stress axis.

The log-log plot in Figure 5.18 compares the resulting yield stress as a function of strain rate for the three applied testing methods. For comparison, the hardness values obtained by nanoindentation were converted into representative stress values by dividing them with a confinement parameter of 2.8 [12]. Although Figure 5.18 compares three different loading cases and three different nc-nickel samples with grain sizes of  $26\text{nm}$  (current study),  $27\text{nm}$  (Section 5.1) and  $80\text{nm}$  (Maier et al. [12]), the results are all fairly consistent, especially when comparing the  $m$  values between

measurements. The variation in terms of absolute strength, rather than relative rate sensitivity, between the small scale and larger scale measurements from this study can be attributed to crystallographic texture, since XRD measurements revealed a  $\langle 111 \rangle$  fiber texture in the loading direction of indentation/microcompression experiments. Furthermore, the nanoindentation results are observed to fall between those of the tension and compression tests, which were conducted normal to and parallel to the  $\langle 111 \rangle$  fiber texture direction respectively. This is consistent with the triaxial expanding cavity of the indentation plastic zone of a sharp pyramidal tip being less sensitive to anisotropic material properties [160]. The results from the single crystal nickel sample, however, vary significantly from the nanocrystalline results in both absolute strength values and strain rate sensitivity exponent values. As mentioned before, the noise in the measurement made extraction of  $m$  values difficult, but a value of  $m_{\text{sxNi}} = 0.001$  was determined by averaging the noise in each jump segment to determine the relative difference. This is one order of magnitude lower than the nanocrystalline nickel results for both rate sensitivity and strength (N.B. the break in scale of the stress-axis for sx-nickel results).

### Apparent activation volume

The strain rate sensitivity exponent measured in the previous sub-section can be used to determine the apparent activation volume of the deformation mechanism using the following relationship [152, 144, 161]:

$$m = \frac{\sqrt{3}kT}{V_{app}\sigma_f} = \frac{2.8\sqrt{3}kT}{V_{app}H} \quad (5.11)$$

where  $k$  is the Boltzmann constant,  $T$  is the absolute temperature,  $V_{app}$  is the apparent activation volume for plastic deformation and  $\sigma_f$  is the flow stress. It should be noted that an apparent activation volume is used in this context instead of a true or effective activation volume, because in strain rate jump tests it is not possible to infer whether the observed change in flow stress on varying the applied strain rate is due to variation of dislocation density or average dislocation velocity or both [14]. Although the concept of activation volume is derived from thermal activation theory of dislocations, it is equally applicable to other non-dislocation mechanisms like grain boundary diffusion processes. This is mainly true for nanocrystalline metals where diffusive mechanisms like grain boundary sliding, grain rotation and grain boundary migration are active and may predominate [7]. Furthermore, multiple deformation mechanisms may be active simultaneously, so the apparent volume may not be indicative of a single rate controlling deformation mechanism.

Table 5.2.: Activation volumes in nanocrystalline nickel.

Test Method	Reference	$V_{app}[b^3]$
Tension	Current study	9
	Wang et al.[142]	21
Compression	Current study	10
	Mohanty et al.[118]	21
Indentation	Current study	9
	Maier et al.[12]	14
	Shen et al.[145]	10
	Vehoff et al.[162]	10-12

The room temperature activation volumes for deformation of nc-nickel from the present study and the literature [142, 162, 145, 118, 12] are summarized in Table 5.2. The present study reveals nearly identical values of  $10b^3$  for all the different loading cases for the nanocrystalline nickel sample. According to Meyers et al. [7], this corresponds to grain boundary diffusion processes which usually act in a range from 1 to  $20b^3$ . However, it is also within the typical range for dislocation glide-based plasticity, so either or both mechanisms may be active. The literature data summarized in Table 5.2 is also in good agreement with the observed values.

Another indication for grain boundary-mediated deformation mechanisms is provided by the surface topology of a micropillar after compression. Figure 5.17 (a) shows evidence of grain rotation or grain boundary sliding of the unconstrained, near-surface grains during the deformation process. This is similar to the relief of surface grains observed during the nanoindentation of ultrafine-grained aluminum [152] and nanocrystalline nickel [12]. The deformation observed in the case of the single crystal nickel (Figure 5.15 and Figure 5.17 (b)) is very different than that of the nanocrystalline material. Giant slip offsets are observed across the entire diameter of the micron-scale pillar, rather than the nano-scale protrusions observed in Figure 5.17 (a). It is not too surprising, therefore, that the resulting apparent activation volumes are much larger:  $\sim 350b^3$ . This is consistent with a significant amount of dislocation-dislocation interactions occurring within the pillar, but not to the extent of dislocation forest cutting, which would produce volumes  $\geq 1000b^3$  [15]. Jennings et al. [163] observed that for copper pillars with diameters  $> 0.15\mu m$  the rate sensitivity decreases and apparent activation volume increases with increasing pillar diameter. Extrapolating their data to a pillar diameter of  $3.5\mu m$ , the expected activation volume would be  $\sim 333b^3$ , in good agreement with our observed



values. This offers further evidence that the applied microcompression methodology for strain rate sensitivity measurements is robust and useful for a wide range of materials and microstructures, even those with very low strain rate sensitivities.

#### 5.2.4. Conclusions

Three different micromechanical measurement techniques for assessing strain rate sensitivity were applied on the same nanocrystalline nickel specimen in order to study the comparability and consistency of the test results. The extracted SRS exponents and apparent activation volumes from these three methods were found to be in excellent agreement. This suggests that the rate controlling deformation mechanism(s) was the same for all three loading cases. The obtained apparent activation volume,  $\sim 10b^3$ , for nanocrystalline nickel is consistent with grain boundary diffusion processes and dislocation glide-based plasticity. Due to grain size variation in electrodeposited nickel, it is plausible that both of these mechanisms are simultaneously operative. In contrast, the SRS results obtained from microcompression of single crystal nickel showed much lower strain rate sensitivity and a high apparent activation volumes of  $\sim 350b^3$ , which is indicative of significant dislocation-dislocation interactions in the pillars. Nevertheless, this study suggests that the techniques compared herein can be reliably and interchangeably used to accurately measure strain rate sensitivity in a wide variety of materials. However, for materials with mechanical anisotropy, such as crystallographic texture, it is suggested that investigators be aware that nanoindentation techniques underestimate the magnitude of the anisotropy, so alternatives such as tension and microcompression are suggested. This comparative study, however, provides the foundation for further studies on other transient testing techniques, like creep and stress relaxation as discussed in the following sections, to understand deformation mechanisms in thin films and nanostructured materials by accurate extraction of deformation parameters.

### 5.3. Time-dependent plasticity measurements: load relaxation tests

Plastic deformation in nanocrystalline metals is known to be strongly time dependent. This viscoplasticity manifests itself as a high degree of strain rate sensitivity and susceptibility to creep and stress relaxation even at room temperature. Numerous studies have reported on creep behavior [164, 101, 103, 165, 166] and strain rate sensitivity [148, 138, 142, 144, 167] of nanocrystalline materials using conventional

tensile or compression tests on bulk specimens. Stress relaxation properties, on the other hand, have not received as much attention, with very few studies [168, 169, 144] reported. Time-dependent deformation is an important criterion for designing micro-components made up of nanocrystalline materials. Both creep and stress relaxation contribute, in a convoluted manner, towards the failure of nanocrystalline micro-components when placed under contact stresses. Apart from the engineering aspect, time-dependent studies provide fundamental insights into the rate controlling deformation mechanism(s) in these materials. The load relaxation tests (LRT) described in this section were conducted on the industrial reference nickel which has been characterized in the previous section. The experimental details and results in this section have been published as an article in the „Journal of Materials Research“<sup>¶</sup>.

### 5.3.1. Considerations on time-dependent metal plasticity

For proper understanding of the analysis and results presented in this work, it seems helpful to recapitulate the early concepts of transient tests by Cottrell and Stokes [170] and Caillard and Martin [14] on which the micropillar experiments (i.e. load relaxation and strain rate jump tests) presented here are based upon. Therefore a brief overview of the basic concepts of these tests and their applicability with reference to nanocrystalline metals is presented in this section.

The most general approach is to write,  $\dot{\gamma}$ , the net shear strain rate, for stresses close to the athermal threshold stress in the form of an Arrhenius term:

$$\dot{\gamma} = \dot{\gamma}_0 \exp(-\Delta G/kT) \quad (5.12)$$

. Here,  $\Delta G$  is the Gibbs free energy of activation which manifests an energy barrier height that has to be overcome by thermal activation of a mechanism(s) for it to contribute to strain propagation. We adopt standard notation where  $k$  is the Boltzmann constant and  $T$  is the absolute temperature. The pre-exponential factor,  $\dot{\gamma}_0$  represents a reference strain rate, which is usually regarded as a constant; a supposition that seems valid whenever a specific mechanism dominates strain propagation. The thermal energy barrier,  $\Delta G$ , can be lowered by applying shear stress  $\tau$  as shown in Equation 5.13:

$$\Delta G(\tau) = \Delta G_0 - \tau V_{app} \quad (5.13)$$

---

<sup>¶</sup>**Room temperature stress relaxation in nanocrystalline Ni measured by micropillar compression and miniature tension**, *Mohanty, Wehrs et al.*, J.Mater.Res., 2016, Volume 31, 1086

, where  $\Delta G_0$  is the stress-free energy barrier, and  $V_{app}$  is the apparent activation volume. The apparent activation volume can be inferred from Equation 5.12 and Equation 5.13:

$$V_{app} = kT \left. \frac{\delta \ln \dot{\gamma}}{\delta \tau} \right|_{T,P} \quad (5.14)$$

. The magnitude of the activation volume may help to identify and discriminate between different possible thermally-activated and rate-controlling deformation mechanisms. It can be extracted from any transient test: strain rate jump, creep or load-relaxation tests. Generally, the smaller the activation volume is the more localized the rate-controlling mechanism has to act in order to propagate plastic deformation. Large mechanisms like forest dislocation cutting have characteristic activation volumes on the order of  $1000b^3$  ( $\approx 2 \times 10^1 nm^3$ ), whereas small mechanisms like kink pair formation or point defect migration, being characteristic of creep processes, exhibit values in the range of  $0.02 - 1b^3$  ( $\approx 2 \times 10^{-3} - 4 \times 10^{-4} nm^3$ ) [146]. Intermediate values of activation volumes associated with mechanisms like shear transformation plasticity  $5b^3$  [171, 91] and partial dislocation activity  $10b^3$  [172] both represent deformation modes which are considered as plastic strain carrying mechanisms in nanocrystalline materials.

Subsequently, we will focus exemplarily on the analysis routine for load-relaxation tests under constant-strain conditions. For strain rate jump tests (SRJ) please see available references, i.e.: [12, 118, 94, 152, 173]. In a load-relaxation test (RL), the externally applied deformation is stopped and the stress drop  $\Delta\tau$  recorded over time, while the applied strain is held constant. This decay in shear stress  $\Delta\tau$  varies with time  $t$  according to [14] as:

$$\Delta\tau = \frac{-kT}{V_{app,r}} \ln \left( 1 + \frac{t}{c} \right) \quad (5.15)$$

, where  $\Delta V_{a,r}$  is the apparent activation volume under stress relaxation conditions and  $c$  is a time constant. In general, the apparent activation volume is a complex activation volume reflecting the proportional shares of all deformation mechanisms acting at a specific stress-strain state in the material. It can be extracted from different evaluation protocols and is subjected to microstructural evolution during data collection. As a result, the apparent activation volume does not necessarily relate to a single deformation mechanism. In the context of dislocation plasticity, the effective activation volume,  $V_e$ , has been introduced, which is characteristic for dislocation mobility [14]. To assess  $V_e$ , a transient test can be exploited which is based on the rigorous assumption that the microstructure of the specimen does not

change during a short/fast transient [174, 14]. Hence, a repeated micropillar stress relaxation test (RLR) has been recently developed [175] in order to probe  $V_e$  in thin films or in cases where bulk material is not readily available. In detail, constant strain relaxation is sequentially measured while in between each relaxation segment the sample has been reloaded (apparently elastically) to the initial stress condition. The effective activation volume can then be extracted from the reloading steps by means of Equation 5.16.  $V_e$  is then related to subsequent strain rate values at the end ( $f$ ) and beginning ( $i$ ) of relaxation segments and the associated stress difference  $\tau_{i,j+1} - \tau_{f,j} = \Delta\tau$ , where  $j$  denotes the  $j$ -th relaxation segment in a given relaxation cycle (see Figure 6.8):

$$V_{eff} = kT \frac{\ln(\dot{\gamma}_{i2}/\dot{\gamma}_{f1})}{\Delta\tau_{i2-f1}} = kT \frac{\ln(\dot{\tau}_{i2}/\dot{\tau}_{f1})}{\Delta\tau_{i2-f1}} \quad (5.16)$$

### 5.3.2. Experimental

#### Miniaturized tensile experiments

Displacement-controlled miniature tensile experiments were performed to provide an independent verification of the mechanical response of the industrial reference nanocrystalline Ni. The modified Kammrath & Weiss in situ tensile testing system as described in Section 4.7 and displayed in Figure 4.20, was utilized for the load relaxation tests under uniaxial tension. Reference measurements to assess and compensate the load frame relaxation at the desired testing load were conducted on zero gauge tensile bars cut from hot rolled maraging steel by means of micro-EDM. The steel samples did not show any stress relaxation, since their grain size is in the range of several microns. Due to the much larger gauge cross section the applied load, which was exactly the desired load for the nanocrystalline nickel specimen, results in stresses well below 10% of the maraging steel's elastic limit.

#### Micropillar compression

The nanocrystalline Ni was machined into the shape of a „large“ compression pillar using a Tescan Lyra gallium focused ion beam (FIB) system. The approximate pillar dimensions were  $30\mu m$  tall and  $10\mu m$  diameter, as shown in the inset of Figure 5.19. These pillars are much larger than most pillars produced by FIB, requiring  $\sim 10$  hours each of dedicated FIB time for the manufacture. To reduce the required milling time for the much larger crater around the pillar a fourth coarse milling step at a beam current of  $16nA$  was added before the common three step procedure described in

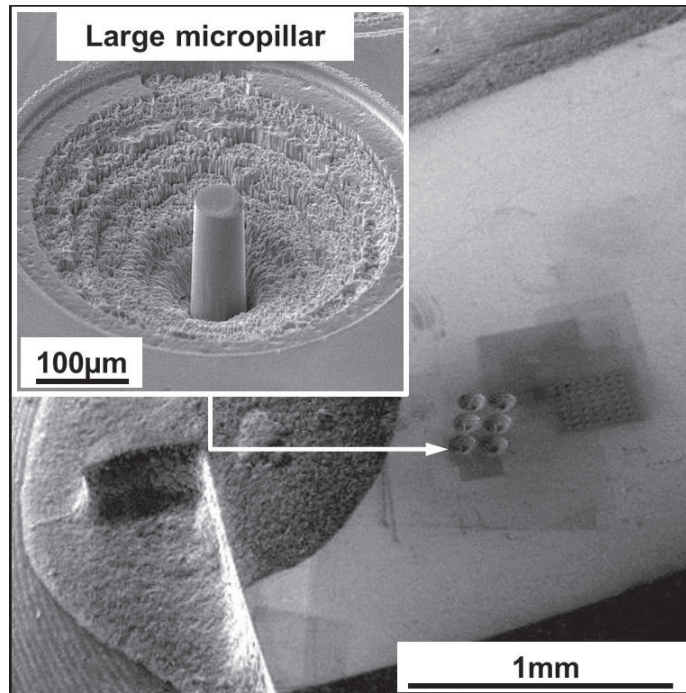


Figure 5.19.: A large FIB micropillar of nanocrystalline Ni machined in the undeformed gripping section of a micro tensile bar (post mortem).

Section 4.5.1. The large size was chosen to minimize the impact of thermal drift on the stress-relaxation measurements. As can be seen from Figure 5.19, micropillars have been milled into the gripping section of a tensile bar which has been strained to failure after the relaxation experiments. This allows to perform multiple experiments on one single sample and enhances the comparability of experimental results by reducing variations in microstructure and composition.

Micropillar compression experiments were performed using a custom in situ scanning electron microscope (SEM) micromechanical testing system based on a commercial micro- and nano-indentation system from Alemnis, the details of which have been reported in the previous Section 4.6. The Alemnis system is particularly well-suited for load-relaxation experiments, because it is intrinsically a displacement-controlled device and is very stable over long periods of time with little susceptibility to time-dependent drift. By providing sufficient stabilization times, it was ensured that the load and displacement drift rates were below  $10\text{ nN}/\text{min}$  and  $5\text{ nm}/\text{min}$ . The SEM has the advantage of a direct visual observation before, during, and after the relaxation experiment. This allows direct confirmation of reasonable alignment (at least in one axis), quality of the pillar, and absence of unwanted spurious features

such as debris. It also allows for the observation of surface evolution during deformation, such as the emergence of slip steps, shear bands, or grain boundary relief. A  $15\mu\text{m}$  diameter diamond flat punch was used to compress the pillars. The compression tests were performed in displacement-controlled mode. Multiple repeated stress relaxation tests were performed on these micropillars with each repeated relaxation segment separated from others by sufficient plastic strain. The strain rate was  $\dot{\epsilon}_r = 0.001\text{s}^{-1}$  in all cases.

### 5.3.3. Results

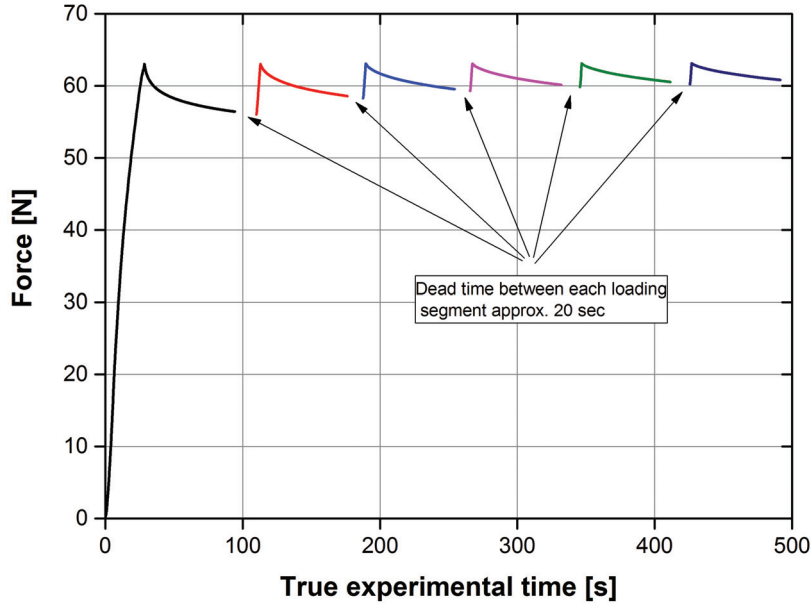
#### Miniature tension

The results of miniature tension experiments which are (at least on bulk scale) more conventional and extensively studied tests, are discussed first. A consecutive series of six load relaxation sequences were performed under uniaxial tension on a total number of three micro tensile specimens. Figure 5.20 (a) shows a representative example of the experimental results obtained from one specimen where the engineering stress is plotted over the true experimental time. Due to software limitations of the experimental setup, the relaxation segments had to be performed individually. As a consequence of that, a dead time of approximately 20s between each segment arises which was taken into account for the further analysis of relaxation data. Each segments starts at the same stress of  $1.925\text{GPa}$  with a duration of 60s. As suggested by the red curve in Figure 5.11, which denotes the stress-strain curve of the examined nanocrystalline nickel obtained from a constant strain rate tensile test, this stress is well above the 0.2% offset yield strength  $1.25\text{GPa}$  but still in the low strain regime where substantial work hardening is observed.

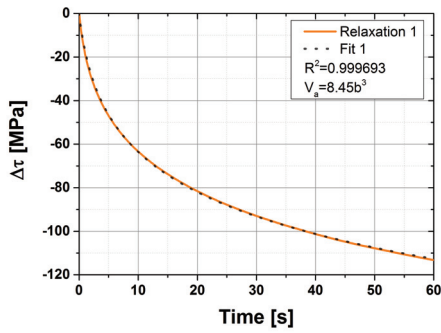
Each individual relaxation segment was fit to the logarithmic decay function suggested in Equation 5.15 by applying a least square algorithm. Figure 5.20 shows two representative examples of the fit for the first (b) and the last (c) relaxation segment of one specimen, respectively. The raw data (red curve) and the fit (black dots) are in excellent agreement, providing correlation coefficients of  $R^2 > 0.99$  in all cases.

#### Micropillar compression

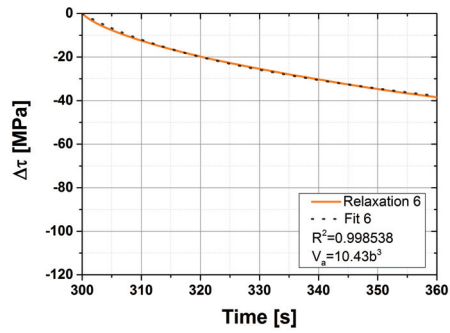
A series of several repeated relaxation experiments were performed on each micropillar. In total, up to 25 relaxations were measured on each pillar, in groups of five repeated stress relaxations. An example of the repeated pillar relaxation curves is shown in Figure 5.21 (a). The dwell time for each relaxation measurement was 60s.



(a)



(b)



(c)

Figure 5.20.: (a) An example stress-strain curve for 6 independent relaxations using the miniature tension method. The corresponding stress-strain curve of a constant strain rate test at  $\dot{\epsilon}_r = 0.001s^{-1}$  is shown in Figure 5.11. Examples of the fit to extract the apparent activation volume and time constant for the first (b) and the last (c) relaxation segment. The apparent activation volume for these two fits were  $8.5$  and  $10.4b^3$  respectively.

After the first 60 second relaxation measurement, the pillar was reloaded to the same stress level and another 60 second relaxation measurement was performed. The entire 25 relaxation measurements were identified by a two-digit index - for example,  $R_{11}$  corresponds to the 1<sup>st</sup> relaxation segment of the 1<sup>st</sup> group of 5, and  $R_{53}$  corresponds to the 3<sup>rd</sup> relaxation segment of the 5<sup>th</sup> group of 5, as shown in Figure 5.21 (b) and (c) respectively. Nearly all prior studies only examined time-dependent plasticity in the work hardening regime at strains  $\gg 1\%$ . However, in this study stress relaxation was measured even at stresses below the 0.2% offset yield strength. This relaxation provides further confirmation that plasticity readily occurs well below the typically reported values for yield strength.

The SEM allows the direct observation of the shape of the micropillar during all stages of the compression experiment. Some example images taken at the start of the compression experiment, and after 20% strain are shown in Figure 5.22. The images were carefully analyzed during the relaxation segments, and as expected there was no discernible change in the pillars during relaxation.

Each of the individual relaxation segments was fitted using a logarithmic decay function (see Figure 5.23) using a minimum least squares method to estimate the values for the apparent activation volume and the time constant. Examples of the fit are provided in Figure 5.23. Generally, the correlation coefficients for this fit of each relaxation curve were very good, with  $R^2 > 0.99$ . Only in a few cases were the correlation coefficients  $< 0.99$ . Specifically, the relaxation segments  $R_{13}$ ,  $R_{14}$  and  $R_{15}$  had correlation coefficients of 0.97 – 0.90, likely because the relaxation behavior was very shallow ( $\sim 0.2MPa/s$ ), such that contributions from instrumental drift were no longer negligible. These suspicious relaxation curves were excluded from detailed analysis of activation volume.

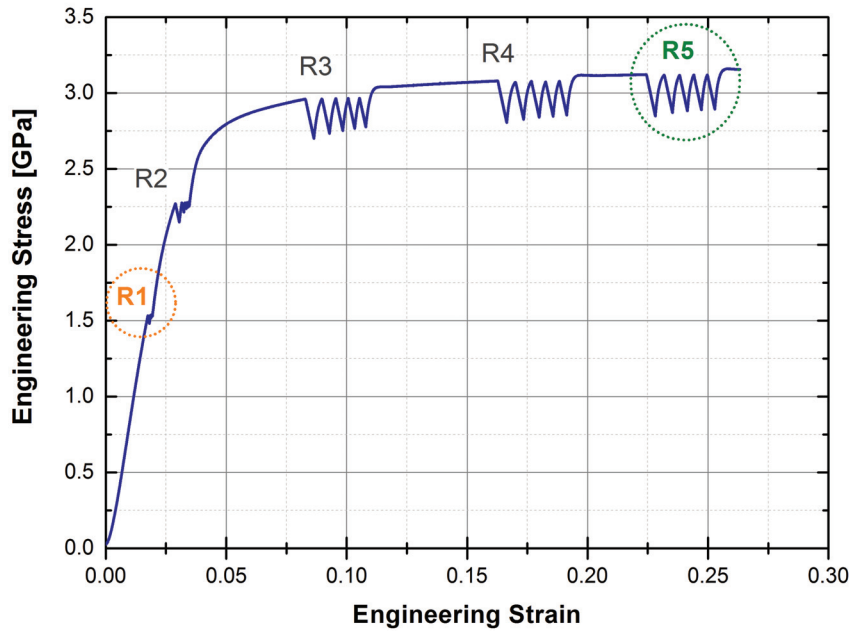
### 5.3.4. Discussion

#### Mechanism for time-dependent plasticity during microcompression

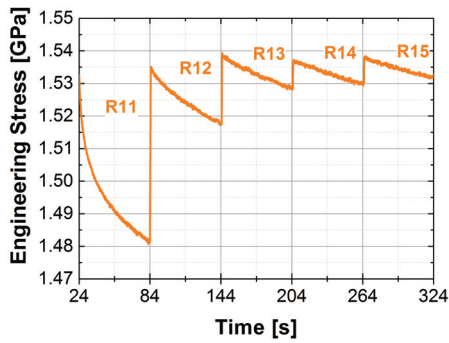
The activation volume for time-dependent plasticity provides an indication of the operative mechanism. The apparent activation volume was determined for each load relaxation segment by fitting the experimental data to Equation 5.15 while the effective activation volume was determined based on the jumps between relaxation segments using Equation 5.16. The plot of apparent and effective activation volume as a function of engineering strain is shown in Figure 5.24.

The apparent activation volume shows a strong strain dependence in the low strain regime, transitioning from  $\sim 30 - 40b^3$  at  $\sim 1\%$  strain to values of  $11 - 13b^3$  at  $\sim 4\%$

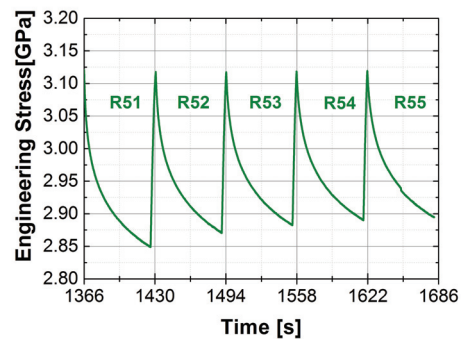




(a)



(b)



(c)

Figure 5.21.: An example result from a micropillar compression test with multiple repeated relaxation segments. The entire test is shown in Figure (a). The first and the last segments are shown on a smaller scale in Figure (b) and (c) respectively.

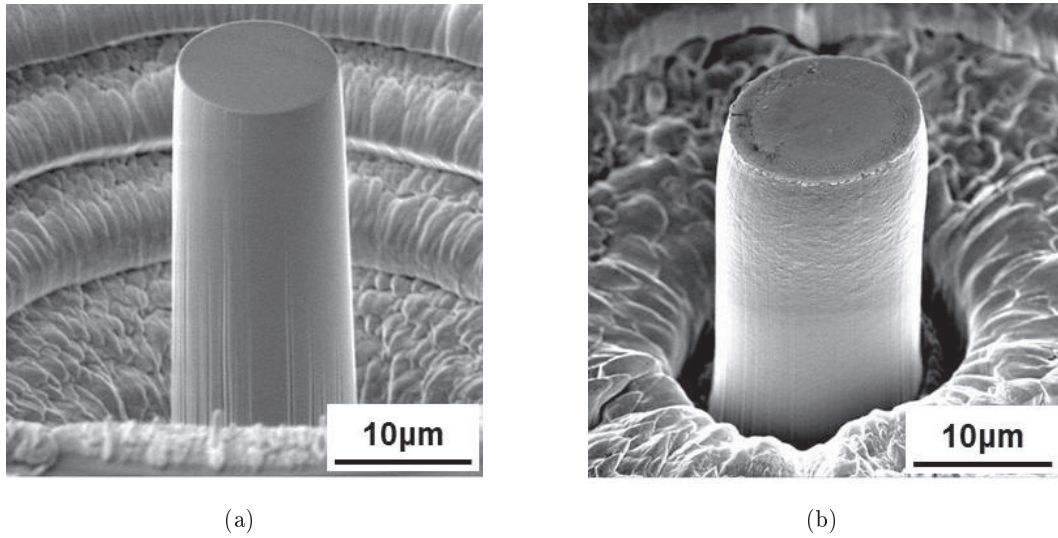


Figure 5.22.: SEM images during deformation at the onset of deformation (a), and at a strain of 20% (b).

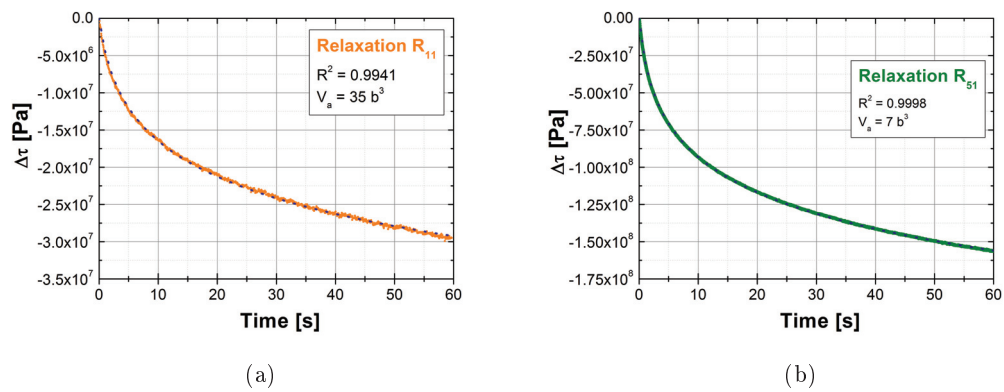


Figure 5.23.: Examples of raw data and fit for two relaxation segments ( $R_{11}$  and  $R_{51}$ ). The correlation coefficient for these fits were  $\sim 0.99$ .

strain. In spite of this sharp transition, the apparent activation volume becomes remarkably stable at strains in excess of 8%, always producing a value of  $7.1 - 7.5b^3$ . The effective activation volume, on the other hand, shows little or no strain dependence over the entire range of strain. The effective activation volume is always lower than the apparent activation volume, but the difference is large at low strains and becomes almost negligible at strains  $> 8\%$ .

One possible interpretation of Figure 5.24 is that the fundamental deformation mechanism does not change significantly over the entire range of strains from 1–25%, hence the stable effective activation volume measured using essentially instantaneous jumps. The elevated apparent activation volumes at small strains is believed to be an artifact induced by the evolving microstructure. At such low strains, the deformation microstructure (e.g. dislocation content) is limited and evolves rapidly during the 60s transient used to measure apparent activation volume. This deformation substructure evolves rapidly with strain, and hence the high work hardening observed in early deformation of nanocrystalline metals. At higher strains, more sources have become activated, more dislocations are present, therefore the evolution is, relatively, not as substantial over the same period of time. Moreover, at these high strain levels the deformation substructure is relatively constant, and there is no strain-dependent evolution in forest hardening.

### Connection to other forms of viscoplastic behavior

The stress relaxation test described in the current study is one of several manifestations of viscoplasticity. The mechanism that gives rise to stress relaxation will also give rise to strain rate sensitivity and creep behavior. Thus, a similar activation volume for the viscoplastic mechanism should be attainable through constant strain stress relaxation tests, constant stress creep tests, or strain rate jump tests. In fact, Equation 5.16, which was originally presented for the interpretation of repeated stress relaxation segments, can also be applied to estimate the effective activation volume for a strain rate jump test where the instantaneous change in strain rate leads to an abrupt change in flow stress. Such strain rate jump tests were previously performed on the same electroplated nanocrystalline nickel alloy and yielded a similar activation volume of  $\sim 10b^3$  [94].

The activation volume provides a scalar metric that can be used to interpret the rate-limiting deformation mechanism. While the current technique of micropillar stress relaxation is new, activation volumes on nanocrystalline nickel in the range of  $15 - 20b^3$  have previously been reported from other groups using both bulk and

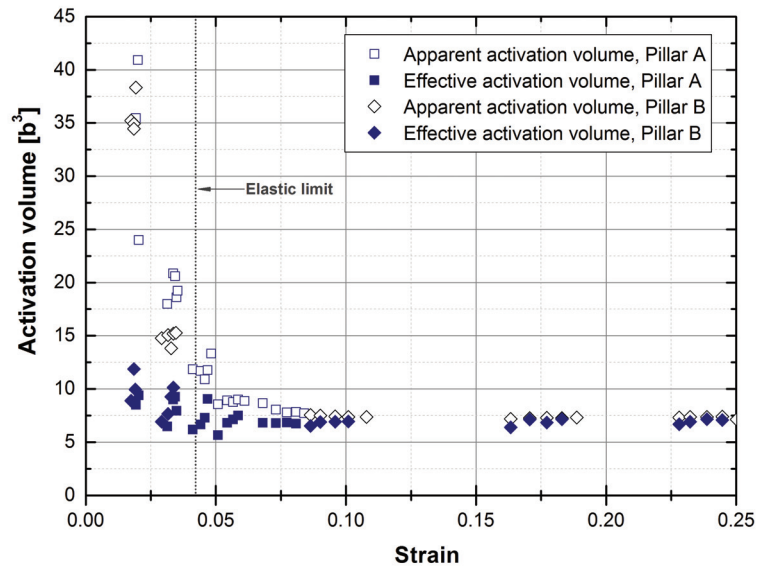


Figure 5.24.: Apparent and effective activation volume for two independent micropillar RLR tests.

micromechanical strain rate jump tests [12, 142]. These results also compare reasonably well with effective activation volume of  $\sim 10b^3$  reported by Wang et al. [169] from bulk repeated stress relaxation measurements. An activation volume of  $\sim 10b^3$  has also been reported for other nanocrystalline *fcc*-metals [144]. It should also be noted that a change of activation volume from 10 to  $20b^3$  is not generally interpreted as a substantial change in deformation mechanism.

Values in the vicinity of  $\sim 10b^3$  are often interpreted that the rate controlling step is the generation of dislocations from grain boundaries (e.g. [144]), rather than dislocation glide past obstacles. However, grain boundary-mediated dislocation nucleation may be an overly simplistic interpretation of the important deformation mechanism in nanocrystalline metals. For example, after strain rate jump tests on micropillars at room temperature, the deformed pillar shows both evidence of dislocation slip steps and clear grain boundary ledges associated with grain boundary sliding, as shown in [94, 118]. As previously mentioned, these strain rate jump tests also yielded similar activation volumes. Therefore activation volume may not be sufficient to rule out other forms of grain boundary mediated deformation.

**A comparison between pillar compression and miniature tension.**

As expected, the mechanism for time-dependent plasticity is relatively independent of the test method (tension vs compression) or the sample size. While coarse grained or single crystal metals show size dependent plasticity in the micron regime, in nanocrystalline metals the plasticity mechanisms are governed instead by the length scale of the grain structure, which is much smaller than the present pillars.

**An estimate for dislocation exhaustion - tension tests**

The Orowan equation shows that the shear strain rate,  $\dot{\gamma}$ , on a slip plane is directly proportional to the mobile dislocation density,  $\rho_m$ , and the average dislocation velocity  $v$ :

$$\dot{\gamma} = A\rho_m b v \quad (5.17)$$

. The shear strain rate is related to the shear stress rate by the following equation:

$$\dot{\gamma} = \frac{-\dot{\tau}}{M} \quad (5.18)$$

, where  $M$  is the elastic modulus of the sample-machine assembly.  $M$  is calculated from the loading/unloading stiffness without performing any instrument compliance correction.

Within a given relaxation transient, the instantaneous rate of change in the shear stress can be estimated from the derivative of Equation 5.15, and the fit values for the apparent activation value and time constant:

$$\dot{\tau}(t) = \frac{-kT}{V_{app}} \cdot \frac{1}{(c+t)} \quad (5.19)$$

. This nearly instantaneous measurement of effective activation volume is also less sensitive to sources of instrumentation error such as drift. It should be noted that it is possible to extract the effective or true activation volume from a repeated stress relaxation test, because previous studies have demonstrated that the plastic strain rate does not change across a stress jump segment suggesting that the microstructure is held constant [14] (refer Equation 5.17). In contrast, in a strain rate jump test, it is not possible to attribute the observed change in stress to variation in mobile dislocation density or average dislocation velocity, or both, which precludes extraction of effective activation volume. Therefore, strain rate jump tests always provide an apparent activation volume. This makes repeated stress relaxation tests very attractive for studying operative deformation mechanisms.

The relative change in the mobile dislocation content can be estimated from apparent and effective activation volume as the apparent activation volume,  $V_{app}$ , and the effective activation volume,  $V_{eff}$ , are related to each other by a proportionality constant  $\Omega$ :

$$\Omega = \frac{V_{app}}{V_{eff}} \quad (5.20)$$

. Rewriting Equation 5.17 for the actual relaxation segment time  $t$  and at the onset of relaxation ( $t = 0$ ), dividing both the expressions and substituting Equations 5.18 and 5.19 yields:

$$\frac{c}{(c+t)} = \left( \frac{\rho_m}{\rho_{m0}} \right) \cdot \left( \frac{v}{v_0} \right) \quad (5.21)$$

, where the subscript „0“ corresponds to the start of relaxation. The mobile dislocation densities and average dislocation velocities are coupled by a factor  $\beta$  such that:

$$\left( \frac{\rho_m}{\rho_{m0}} \right) = \left( \frac{v}{v_0} \right)^\beta \quad (5.22)$$

, and hence:

$$\beta = \frac{\Omega}{1 + \frac{K}{M}} - 1 \quad (5.23)$$

, where  $K$  is the hardening coefficient during the stress relaxation test. Since  $K$  cannot be determined independently, it can be approximated to  $\Theta_{wh}$  which is the work hardening coefficient of the stress-stress curve. Rearrangement of Equation 5.21 and Equation 5.23 results in the expression for estimating the mobile dislocation exhaustion rate as a function of test duration in a relaxation test:

$$\left( \frac{\rho_m}{\rho_{m0}} \right) = \left( \frac{c}{(c+t)} \right)^\beta \quad (5.24)$$

. Figure 5.25 results from applying Equation 5.24 and suggests that the total mobile dislocation content is approaching an exhaustion state where there are no more mobile dislocations available. Extrapolation of the curve suggests that the remnant dislocation density should be below 1% of the initial dislocation content in  $\sim 15$  minutes. After this time, the material is expected to be stable against further evolution. High resolution, long term stress relaxation experiments would be necessary to confirm this prediction.

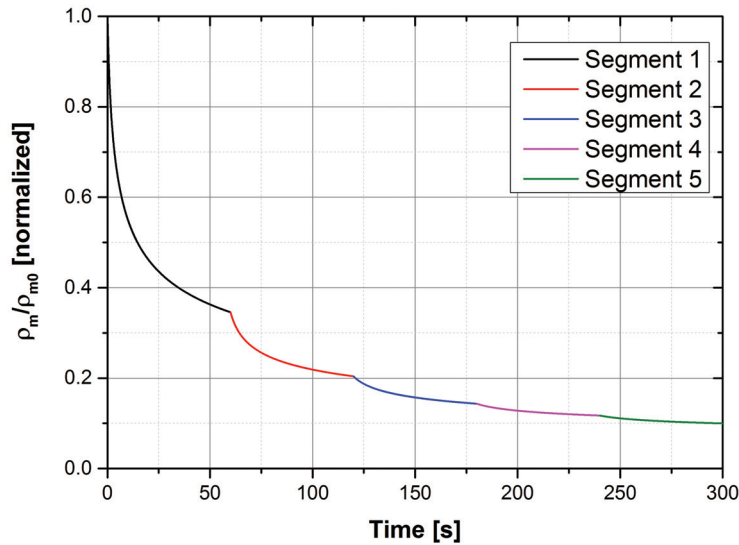


Figure 5.25.: An estimate of the relative dislocation density as it evolves during a sequence of stress relaxation segments from the tensile experiments

### Practical implications of stress relaxation

While stress relaxation is often used as a means to understand the underlying plasticity mechanisms, it is also of practical relevance in several applications. As this matter will be discussed in detail in Chapter 7, only a short practical example is given here. Springs are often relied upon to exert a constant restoring force while held in a flexed position for sustained periods of time. However, springs made from these nanocrystalline alloys will lose their restoring force over time: when loaded near the yield point, the restoring force will decay by  $\sim 3 - 5\%$  even within a single minute, and further decay  $\sim 10\%$  within a week. Moreover, stress relaxation is relevant to applications that rely on residual stresses for functionality, such as shot peening and laser shock peening used to induce compressive residual stresses for fatigue crack initiation suppression. This stress relaxation can also be important in solid state electronics and microdevice fabrication, where an evolving stress state can lead to distorted shapes or altered performance.

### 5.3.5. Conclusions

Microcompression stress relaxation experiments were successfully performed on nanocrystalline nickel sample, and the results were directly compared with bulk tensile relaxation measurements. The results are in good agreement with each other, suggesting that microcompression relaxation experiments can be used to extract time dependent properties of thin films and small length scale features. The effective activation volumes of  $\sim 10b^3$  obtained from these experiments are in good agreement with previous studies using strain rate jump tests, suggesting grain boundary mediated processes being the rate controlling mechanism. To the best of my knowledge, this is the first demonstration and validation of the technique for extracting time-dependent relaxation plasticity using microcompression. Although a displacement controlled machine was employed in this study, similar tests can, in principle, be performed with load-controlled indenters with a very high feedback loop to keep the displacement constant during a stress relation. These tests may also pave the way for development of indentation based stress relaxation tests.

## 5.4. Summary

The studies discussed in this Chapter show a variety of recent micromechanical test techniques and how they can be utilized to assess the mechanical behavior of nanocrystalline metals. For the sake of comparability, we focused on testing nanocrystalline nickel. However all the demonstrated small scale techniques should be applicable for the majority of thin film materials. Hence, it is hoped that the presented work encourages further studies and, more importantly, assists in understanding and validating micropillar compression tests to assess temperature- and time-dependent mechanical behavior of materials.

### 5.4.1. Technological conclusions

- We have successfully synthesized nanocrystalline nickel and deposited it into LiGA-molds. Micro tensile and micropillar compression tests were performed on these specimen and compared to industrial reference materials. The advantage of testing the nickel synthesized at Empa was to know the bath chemistry, the specimen composition and deposition parameters since all these factors have a strong influence on the mechanical behavior of the deposits (texture, porosity, impurities,etc.). Comparing this material directly to samples which originate from a proprietary, heavily commercialized bath improves our knowledge of



the influence of additives and deposition parameters on the nanostructure and mechanical performance.

- A micromechanical tensile test rig has been developed in the first year of my doctoral studies. It has been successfully implemented under an optical microscope. Along with that, DIC algorithms have been implemented to allow for optical strain measurement on small scale mechanical tensile specimen. Further adaptations in the specimen gripping and load cell setup enabled variable strain rate tests. As well this increased the reliability of the Young's modulus measurements and allowed for time dependent plasticity tests. The performance of the setup was validated by testing a variety of materials with well known mechanical properties i.e. silicon, pure copper and steel.
- A micromechanical test rig under the SEM has been explored and modified to allow for variable strain rate and variable temperature micro compression testing. A major task was to learn how to manually build and handle the fragile high temperature components. Parts of the heating- and cooling system have been optimized for better performance and handling. Modifications in the heater controller enables improved sample heating and cooling with fixed rates. The modifications were beneficial with respect to develop new test procedures to assess time dependent plastic behavior. Based on this work we are now developing the existing setup further to enable precise micropillar compression tests at cryogenic temperatures.
- We developed new test methods to assess the pronounced time dependent plastic behavior of nanocrystalline metals. To the already developed strain rate jump tests, other transient tests, i.e. single and multiple load relaxation tests were developed to be performed on the micropillar compression setup. Further, we validated these types of tests by conclusively studying the materials response in different load cases and strain rates over four orders of magnitude.

#### 5.4.2. Scientific conclusions

- Three different micromechanical load cases for assessing strain rate sensitivity were applied on the same nanocrystalline nickel specimen in order to study the comparability and consistency of the test results. The extracted SRS exponents and apparent activation volumes from these three methods were found to be in excellent agreement. This suggests that the rate controlling deformation mechanism(s) was the same for all three loading cases. The obtained

apparent activation volume,  $\sim 10b^3$ , for nanocrystalline nickel is consistent with grain boundary diffusion processes and dislocation glide-based plasticity. The study suggests that the techniques compared herein can be reliably and interchangeably used to accurately measure strain rate sensitivity in a wide variety of materials.

- Elevated temperature microcompression SRJ tests from 25°C to 100°C yielded good agreement for SRS exponent,  $m$ , and apparent activation volume,  $V_{app}$ , among the current tests and literature data. The apparent activation energy extracted from SRJ tests matched well with grain boundary diffusion activation energy for nickel suggesting grain boundary diffusion to be the rate controlling deformation mechanism.
- Microcompression stress relaxation experiments were successfully performed on nanocrystalline nickel (industrial reference grade), and the results were directly compared with bulk tensile relaxation measurements. Time-dependent plasticity and activation parameters were extracted from the data. To the best of my knowledge, this is the first demonstration and validation of the technique for extracting relaxation behavior by using micro compression. The results are in good agreement with each other, suggesting that microcompression relaxation experiments can be used to extract time dependent properties of thin films and small length scale features. The effective activation volumes of  $< 10b^3$  obtained from these experiments suggest grain boundary mediated processes being the rate controlling mechanism in nanocrystalline nickel at grain sizes  $< 50nm$ . However, the activation volumes are still in a regime where dislocation-based plasticity is possible.
- Electron microscopy of all deformed nanocrystalline nickel pillars showed extensive grain boundary sliding and rotation to accommodate the plastic strain. Slip traces were also observed in case of large grains. These observations are consistent with the existing literature. The SRS results obtained from microcompression of single crystal nickel showed much lower strain rate sensitivity and a high apparent activation volumes in the order of  $\sim 350b^3$ , which is indicative of significant dislocation-dislocation interactions in the pillars. Due to the grain size variation in electrodeposited nickel, it is hence plausible that both grain boundary and dislocation based mechanisms are simultaneously operative. Experimentally these mechanisms cannot be deconvoluted at this stage.

---

## 6. Transient tests II: Model system

### Palladium-Gold

This chapter is an approach to probe activation parameters on a binary Palladium-Gold alloy with a nominal crystallite size of  $\sim 12nm$  and a very narrow size distribution. Elevated temperature, micro-compression transient plasticity tests are employed to gain insight into the apparent rate-controlling deformation mechanisms at the lower limit of crystallinity.

#### 6.1. Introduction and motivation

Compared to conventional polycrystalline *fcc*-metals, nanocrystalline metals provide excellent mechanical properties [2, 7, 176], which makes these materials very attractive for a variety of engineering applications: MEMS devices, microcomponents for medical applications or watch parts. The key parameter that determines the mechanical properties in these materials is their extremely fine grain size, which is the cause of both, their greatly improved strength and their time-dependent plastic behavior. However, although numerous studies have dealt with the determination of the rate limiting processes in nanocrystalline materials it has not been possible so far to clearly identify the dominant mechanisms.

Looking at the upper limiting case of grain size, which is represented by conventional polycrystalline metals, pronounced ductility prevails and is caused by two essential features. One feature is the presence and stress-driven multiplication of mobile dislocations which act to propagate strain. The other feature is their work hardening capability which is an effect of intraplane dislocation interactions and autonomous cell structure formation [13]. The lower limit of grain size, where crystallinity vanishes, is the metallic glass where dislocations as such are unstable and therefore not available as carriers of plastic flow. Due to the lack of any long-range order, straining of metallic glasses promotes the occurrence of localized shear transformation zones (STZ) [9] which propagate strain by shuffling and flipping of entire groups of atoms. At higher strains, STZs accumulate in regions of strain localization

and form shear bands which may consequently propagate through the material and lead to failure [17]. However, the plasticity of nanocrystalline metals, which in terms of crystallite size resides in-between these two extreme cases, is much more complex to understand. As the grain size is reduced, the relative amount of volume occupied by grain boundaries increases reciprocally. For example, the grain boundaries occupy volume fractions as large as  $\sim 5 - 10\%$  for grain sizes of  $50nm$  [177, 40]. Smaller grains are less effective in generating dislocations, so their ability to interact across intercrystalline domains is reduced. Particularly, when grain sizes approach the limit of crystallinity towards the amorphous regime, grain boundary-mediated deformation processes gain influence while dislocation-mediated processes fade. Mechanisms which essentially emerge from the core regions of grain boundaries, such as grain boundary sliding [59, 178, 179], grain boundary migration [180], STZ activity in the grain boundary core region [9, 181, 93, 95] and dislocation nucleation [2, 46] are under debate. Consequently, both thermally-activated and stress-driven deformation processes can be simultaneously operative in these materials [182, 183]. All of these mechanisms contribute to the marked time-dependent plasticity of nanocrystalline metals, manifesting itself as a high degree of strain rate sensitivity and susceptibility to load relaxation and creep even at room temperature.

In this study, we explore the strain rate sensitivity and the load relaxation properties of a highly pure nanocrystalline  $Pd_{90}Au_{10}$  alloy with a nominal grain size of  $d_{Pd90Au10} \sim 12nm$  by means of dynamic micropillar compression experiments (SRJ and LRT) at elevated temperatures. First we briefly discuss the testing technique, our experimental considerations and data analysis methods. Then we focus on the applicability of this type of micromechanical experiment for probing activation parameters in nanocrystalline materials. Finally, the results of both types of tests are discussed and compared to literature data to gain insights into the possible rate controlling deformation mechanisms in these materials.

## 6.2. Experimental

### 6.2.1. Micropillar compression experiments

The  $Pd_{90}Au_{10}$  was machined into the shape of compression pillars using a Tescan Lyra (Tescan s.r.o., Brno, Czech Republic) gallium focused ion beam (FIB) system. As illustrated in Figure 6.1 (a) a three step milling procedure was chosen to machine an array of  $5 \times 5$  micropillars into each specimen beginning with coarse milling at  $10nA$  beam current (Figure 4.13 (a)) and followed by intermediate milling at

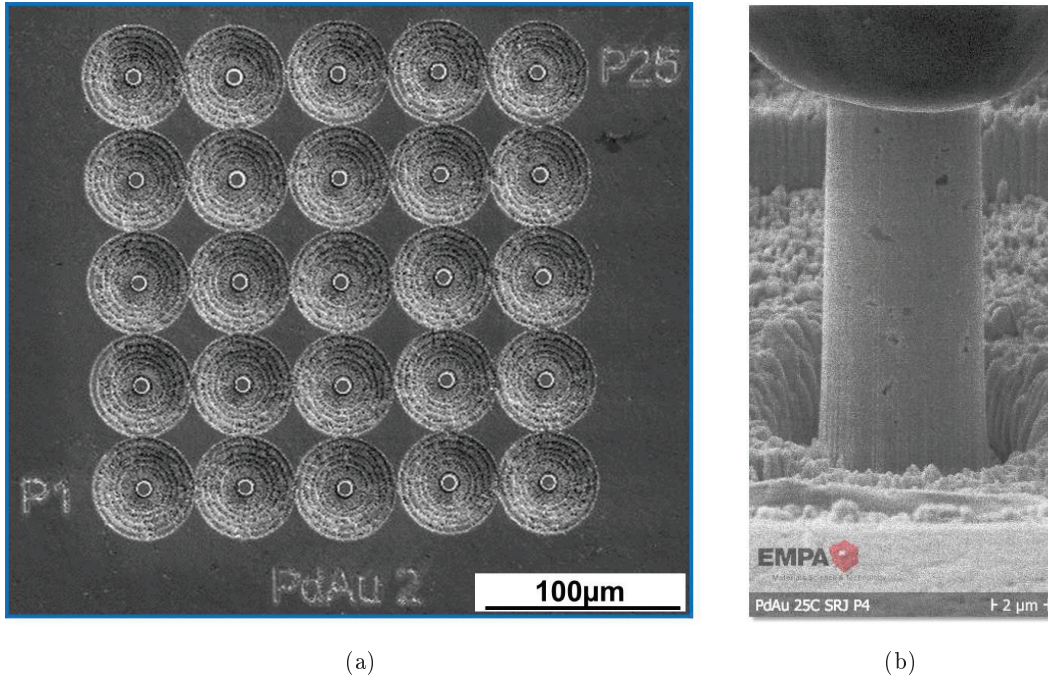


Figure 6.1.: FIB specimen preparation of a  $5 \times 5$  micropillar array on  $\text{Pd}_{90}\text{Au}_{10}$  (a) and  $\text{Pd}_{90}\text{Au}_{10}$  micropillar during compression (b).

$2.4nA$  (Figure 4.13 (b)). Final surface polishing was done at  $0.6nA$  (Figure 4.13 (c)). The approximate final pillar dimensions were  $15\mu m$  tall and  $5.5\mu m$  diameter. Compression tests were performed on the high temperature indentation system which is described in detail in Section 4.6.

For the compression tests, the highest test temperature was set to  $125^\circ\text{C}$ . This has been selected to lie below the relaxation temperature of  $130^\circ\text{C}$ ; the threshold temperature for excessive grain growth amounts to  $200^\circ\text{C}$  (as discussed in the following section). A series of ambient temperature tests was conducted before the initial heating in order to be able to exclude or eventually determine any effect of microstructural changes during the thermal treatment. Then the sample was heated up, starting with the highest test temperature of  $125^\circ\text{C}$ , followed by  $100^\circ\text{C}$ ,  $75^\circ\text{C}$  and  $50^\circ\text{C}$ . After the heat treatment, a second series of room temperature tests was conducted. The sequence of the applied thermal treatment is also illustrated in Figure 6.2.

In case of the SRJT, the initial strain rate was set to  $10^{-3}s^{-1}$  for each test up to an engineering strain of  $\sim 5\%$ , which was already well within the plastic regime. Between  $\sim 5 - 13\%$  engineering strain, each pillar was subjected to a sequence of strain

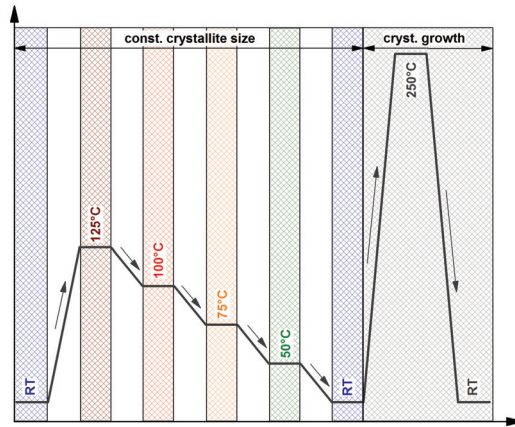


Figure 6.2.: Illustration of the applied test temperature sequence for nanocrystalline  $\text{Pd}_{90}\text{Au}_{10}$ .

rate changes over three orders of magnitude, ranging from  $10^{-4}\text{s}^{-1}$  to  $10^{-2}\text{s}^{-1}$ . The final strain rate beyond  $\sim 13\%$  engineering strain was again  $10^{-3}\text{s}^{-1}$  to demonstrate the behavior was reversible and not significantly changing with increasing strain. Four pillars were tested at each temperature, and the order of SRJ was changed for one pillar at each temperature to exclude any influence of the sequence of rates on the results. For the RLRT, a constant compression rate of  $10^{-3}\text{s}^{-1}$  was chosen. Several repeated relaxation cycles, each one consisting of five individual, 60s duration segments, were conducted in the elastic regime, at the transition from the elastic to plastic, in the early plastic and in the well-developed plastic regimes of the stress-strain curve.

### 6.2.2. In situ investigation of recrystallization and correlation to mechanical response

Subsequent to the above described elevated temperature experiments another set of tests was performed. In this second run, a series of heat treatments was performed in order to assess the limit of thermal stability of the nanostructure and the effect of grain growth on the materials mechanical response and activation behavior. Therefore, the specimen was cut into two pieces. One piece was mounted on a DHS1100 in situ heating stage (Anton Paar AG, Buchs, Switzerland) inside the diffractometer

in order to monitor apparent crystallite growth at temperatures beyond the limit of nanostructural stability. Grain sizes were determined using the Scherrer equation on the (111) peak of the  $\Theta - 2\Theta$  Bragg Brentano diffractograms (see Figure 4.9).

The specimen was directly heated up to 150°C and kept at that temperature for one hour before the XRD measurement to allow the microstructure to stabilize. Subsequent temperature increases were done in 25°C steps up to a final temperature of 250°C. Figure 6.3 illustrates the experimental sequence and the dependence of crystallite size on temperature. It can be seen that the crystallite size does not show any apparent changes up to a temperature around 200°C. Above 200°C the crystallites start to grow quickly up to a size of approximately 50nm. The results clearly indicate a threshold temperature for significant grain growth, which directly influences the mechanical behavior of the material. To connect the apparent grain growth with mechanical response experimentally, an array of twelve micropillars was prepared on the second piece of Pd<sub>90</sub>Au<sub>10</sub>. The pillars had the same dimensions as the previous ones and were cut in accord to the subsequently employed FIB protocol. Accordingly, the same heat treatment profile was applied to the specimen inside the SEM while mounted on the in situ indenter. Strain rate jump and load relaxation tests with the same experimental profile as described in the last section were performed at 250°C and after cooling down back to room temperature.

## 6.3. Results

### 6.3.1. Strain rate jump tests

Figure 6.4 illustrates the representative engineering stress-strain behavior observed during the SRJ tests on the thermally relaxed Pd<sub>90</sub>Au<sub>10</sub> specimen at different test temperatures. Strain rates were varied over three orders of magnitude from  $10^{-4}s^{-1}$  up to  $10^{-2}s^{-1}$  within each test. The jumps appear to be sharp with rather small transients as the strain rate is reduced and slightly longer transients as the strain rate is increased and in all cases the flow stress stabilizes quickly. From the sequence of the jumps, it is apparent that the increasing strain rates result in a marked increase in flow stress due to the pronounced SRS of nanocrystalline *fcc*-metals. The average flow stress level of the curves decreases with increasing test temperature in the constant-nanostructure regime up 125°C in a nearly linear fashion, which is nicely displayed in the almost equally spaced curves as shown in Figure 6.4. The decrease in flow stress is expected and indicates the strong thermal dependence of the dominant deformation mechanisms present in this type of material. This is also indicated

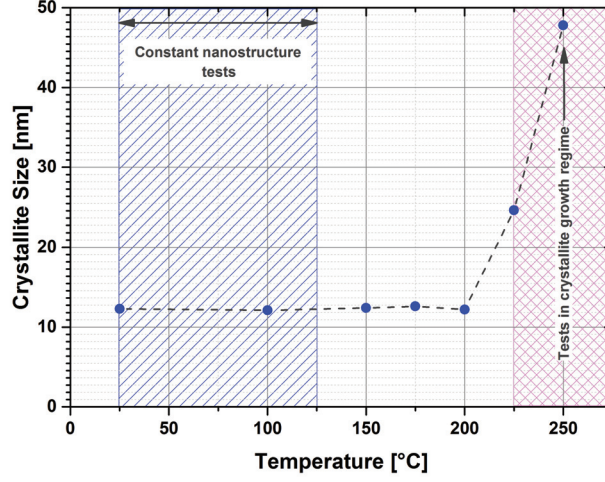


Figure 6.3.: In situ XRD observation of nanostructural stability of  $\text{Pd}_{90}\text{Au}_{10}$ . The structure remains stable below temperatures of approximately  $200^\circ\text{C}$ . Beyond this temperature excessive grain growth occurs. The blue array indicates the constant nanostructure regime in which the micropillar compression tests were performed.

by the well-pronounced jumps that appear larger with each temperature increment. After cooling down back to room temperature from  $125^\circ\text{C}$ , the material's response compares well to the initial test (not displayed) which indicated no apparent change in the nanostructure during the thermal cycle. As the test temperature reaches  $250^\circ\text{C}$  in the second test sequence, the flow stress level is further decreased. At the same time, the individual jumps are significantly smaller but still clearly observable. This indicates a marked change in nanostructure, as previously suggested from the XRD data acquired at that temperature. Consequently, the room temperature SRJT after the grain growth treatment shows a decrease in average flow stress level of  $\sim 20\%$  compared to the RT measurements before the grain growth with a further reduction in jump height.

For uniaxial mechanical tests the strain rate sensitivity (SRS) exponent  $m$  can be extracted by using the following equation [158]:

$$m = \left[ \frac{\partial(\ln\sigma)}{\partial(\ln\dot{\epsilon})} \right]_T \quad (6.1)$$

where  $\partial(\ln\sigma)$  is the change in flow stress as a function of the change in applied strain rate  $\partial(\ln\dot{\epsilon})$  at constant temperature  $T$ . The extraction of  $m$  values from the present



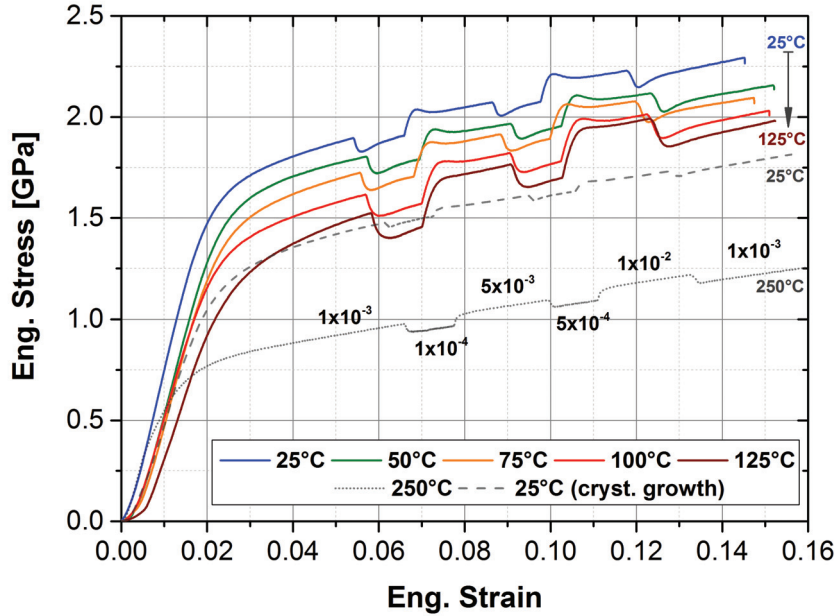


Figure 6.4.: Eng.stress vs. eng.strain curves of SRJ tests as a function of temperature on thermally-relaxed  $\text{Pd}_{90}\text{Au}_{10}$ . As the temperature increases, the overall flow stress level decreases and the relative jump height increases. For a better overview, the corresponding strain rates are indicated only for the 250°C curve.

data sets was carried out according to the two analysis methods described in Section 5.1. To compare all strain rate jump tests, Figure 6.5 provides an overview of the results in form of a  $\log(\text{stress})\text{-}\log(\text{strain})$  plot. The individual data points for each temperature line up well and can be fitted with a linear function the slope of which corresponds to the SRS exponent,  $m$ .

As the flow stress decreases with increasing test temperatures, the SRS becomes more pronounced which presents a change of slope of  $\sim 35\%$  per 25°C until a temperature of 75°C is reached. From 75°C to 125°C, the slope change is of the order of 50% which may indicate a transition in the deformation mechanisms, or their proportional fractions of the deformation, around these temperatures. At 250°C, the SRS decreases considerably with respect to the measurement at 125°C from  $m_{125^\circ\text{C}} = 0.0584$  to  $m_{250^\circ\text{C}, \text{cryst. growth}} = 0.0274$ . Again, this relative decrease of  $m$  is closely related to the change in nanostructure due to grain growth from an initial crystallite size of  $\sim 12\text{nm}$  to  $\sim 50\text{nm}$  after the heat treatment. In contrast, if we assume that a constant nanostructure were to be retained up to the highest test tem-

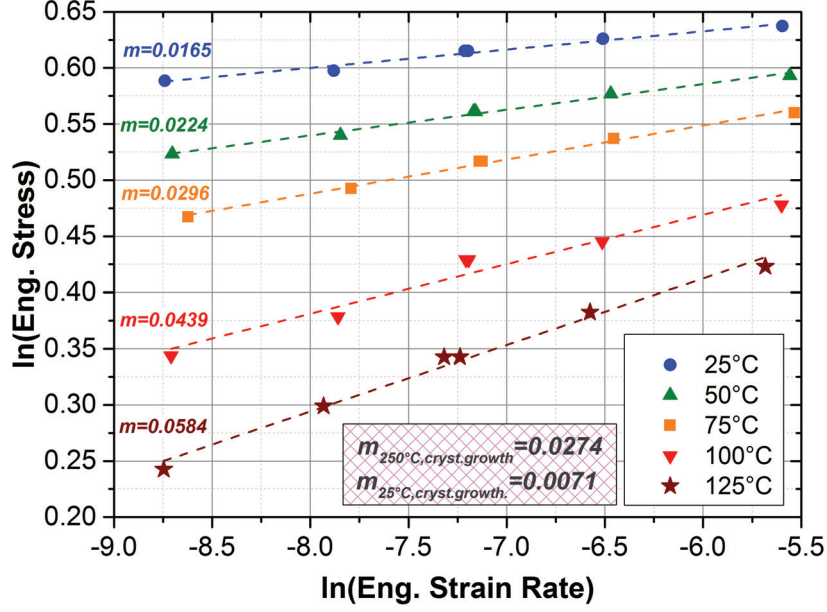


Figure 6.5.: Log(stress), plotted as a function of log(strain rate). The strain rate sensitivity exponent  $m$  increases with increasing temperature. For a better overview within the plot, the individual data points and the fitted slopes for the measurements at 250°C and at room temperature after crystallite growth are not shown. However, the extracted  $m$  values are given in the inset.

perature, a simple extrapolation of the obtained trend of the low temperature SRS exponents results in values of  $m \sim 0.17$  at 250°C. This extrapolated value is one order of magnitude higher than the actual values extracted from the measurement, which clearly suggests that the nanostructure of the material has significantly changed. The SRS at room temperature after grain growth is with  $m_{250^\circ\text{C},\text{cryst.growth}} = 0.0071$  less than half the initial value in the lower nanocrystalline size regime,  $m_{25^\circ\text{C}} = 0.0165$ .

Figure 6.6 displays the apparent activation volumes of Pd<sub>90</sub>Au<sub>10</sub> obtained from strain rate jump tests as a function of test temperature by using the following equation [94]:

$$V_{app,SRJ} = \frac{\sqrt{3}kT}{m\sigma_{flow}} \quad (6.2)$$

where  $k$  is the Boltzmann constant,  $T$  is the absolute test temperature and  $m$  is the determined strain rate sensitivity. The average flow stress level of the corresponding SRJ segment,  $\sigma_{flow}$ , is determined from a zero slope stress-strain curve that has been

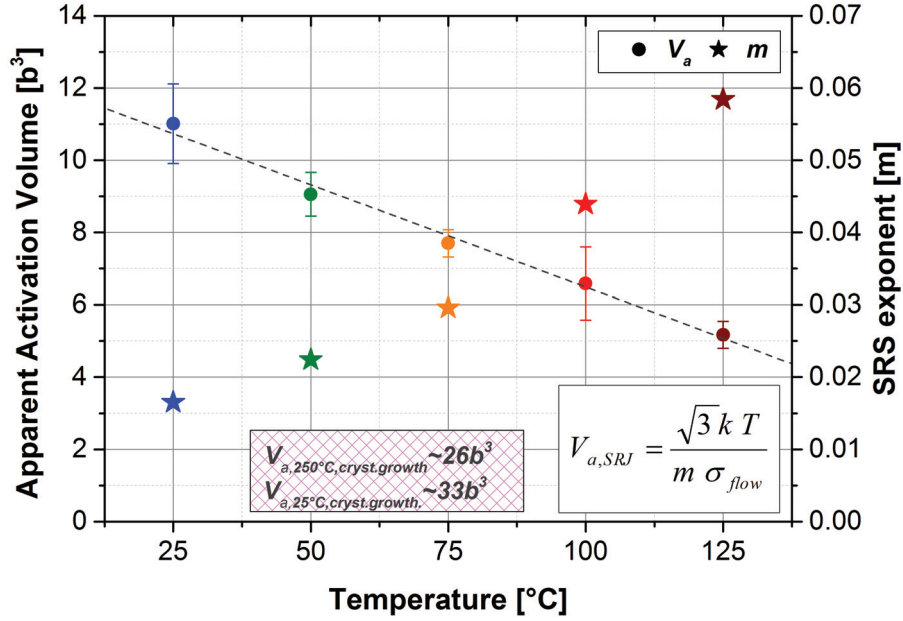


Figure 6.6.: Apparent activation volumes from strain rate jump tests, plotted as function of test temperature.

fitted through the experimental data [118, 94]. At room temperature, the values are around  $11b^3$ , without any difference before and after the first series of elevated temperature tests. With increasing test temperature, the apparent activation volume goes down in an almost linear trend until it reaches values around  $5b^3$  at  $125^\circ\text{C}$ .

In the second series of tests, where the sample was annealed at  $250^\circ\text{C}$ , the apparent activation volume increases significantly, reaching values of  $\sim 25b^3$ . This corresponds to the larger size of the grown crystallites allowing longer range dislocation mechanisms to account for a larger proportion of the deformation. Cooling down to room temperature again results in a further increase to  $\sim 32b^3$ .

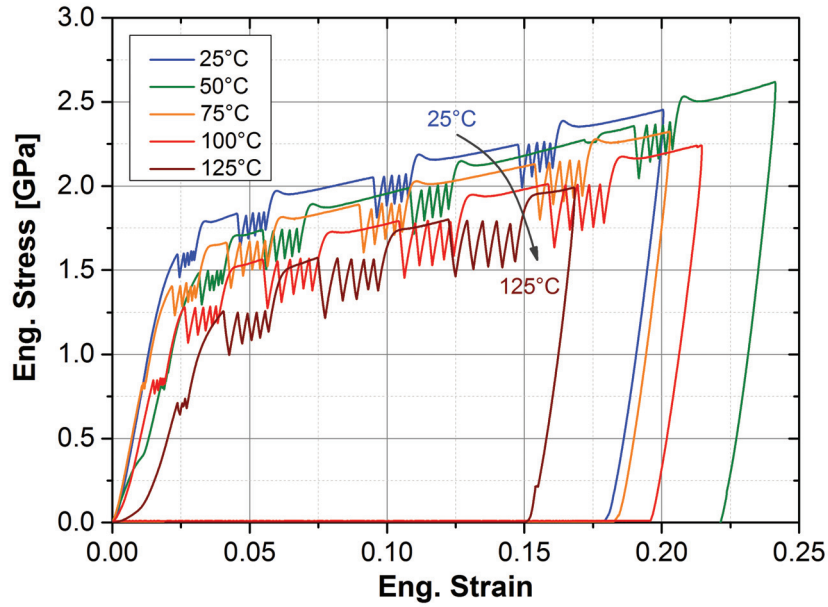
### 6.3.2. Repeated load relaxation tests

As already demonstrated by means of micropillar relaxation experiments on nanocrystalline nickel with a grain size of  $\sim 30\text{nm}$  in Section 5.3, microplasticity readily occurs well below the characteristic yield point of these materials. Hence, in the framework of this case study, a series of repeated load relaxation cycles were performed, following the same temperature profile as for the SRJ tests. On each pillar,

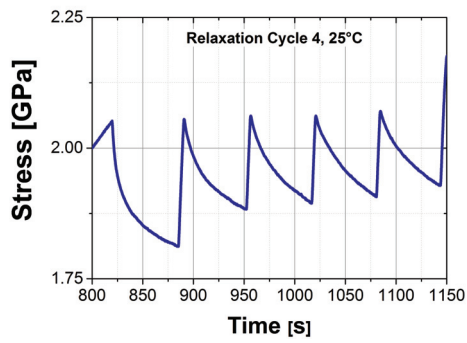
a sequence of four to five relaxation cycles were placed at relevant sections of the stress strain curves: in the apparent elastic regime, in the transition from elastic to plastic, the early plastic regime and finally at various stages in the fully developed plastic regime. Figure 6.7(a) shows representative engineering stress-strain curves of these tests. It can be easily observed that the overall flow stress level decreases reciprocally with test temperature, as already stated in the previous section. Compared to the nanocrystalline Nickel from Section 5.3, the room temperature load relaxation of Pd<sub>90</sub>Au<sub>10</sub> under the same experimental conditions is even more pronounced which may be directly attributed to the much smaller grain size. Within one minute, the stress in the intermediate elastic regime relaxes by  $\sim 6\%$ . Cycle four, which is in the well-developed plastic regime at a stress level of  $\sim 2GPa$ , provides relaxation up to  $\sim 12\%$ . Looking at the elevated temperature measurements, the amount of relaxation increases gradually with temperature. At 100°C, the values go up to  $\sim 19\%$ , again at a mean stress level of  $\sim 2GPa$  which corresponds to cycle five in this case.

A minimum least squares method was used to fit the experimental data according to the logarithmic decay function as given in Equation 5.15. Accordingly, from each individual relaxation segment, the apparent activation volume  $V_{a,r}$  and the time constant  $c$  were extracted. Figure 6.7 shows a representative example of a stress vs. time curve (b) of an entire relaxation cycle and the corresponding fit of the first segment (c). The overall quality of the fits were decent with correlation coefficients of the order of  $R^2 = 0.99$ . Whereas, the relaxation cycles in the apparent elastic regime resulted in R-values  $< 0.99$  in some cases. This may indicate that in the low strain regime below  $\approx 3.5\%$  onsets and transients related to competing deformation mechanisms become reflected in the stress relaxation.

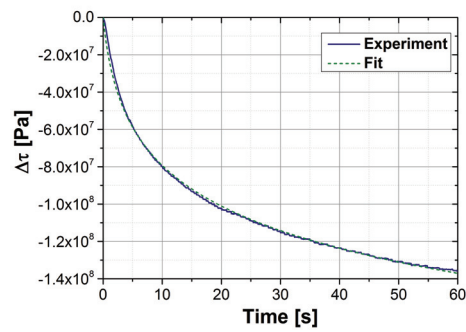
Figure 6.8 shows the plot of apparent and effective activation volume as a function of engineering strain as extracted from the load-relaxation tests on the thermally relaxed Pd<sub>90</sub>Au<sub>10</sub> specimen. In order to reduce the amount of data points in the plot, only the mean activation volumes with respect to the mean strain of the corresponding relaxation cycle is shown. The apparent activation volume was determined by fitting the experimental data of each relaxation segment to Equation 5.15. The effective activation volume was calculated over the transients between subsequent relaxation segments by means of Equation 5.16. The plot initially indicates a strong strain dependence of the apparent activation volume in the lower strain regime. Below  $\sim 4\%$  strain the values go up to  $\sim 32b^3$  (not shown on the plot) and show a strong scatter. Above this low strain regime, the scatter decreases and the average values for the apparent activation volumes at room temperature go down to approximately  $5b^3$ , independently of any further increase in strain. A similar behavior is



(a)



(b)



(c)

Figure 6.7.: (a) Eng. stress vs. eng. strain curves of RLR tests as a function of temperature on thermally relaxed  $\text{Pd}_{90}\text{Au}_{10}$ . As the temperature increases, the relative amount of relaxation with respect to stress increases. (b) Example of a stress relaxation cycle in the fully plastic flow regime as directly obtained from the experiment and the corresponding logarithmic fit of the first segment (c).

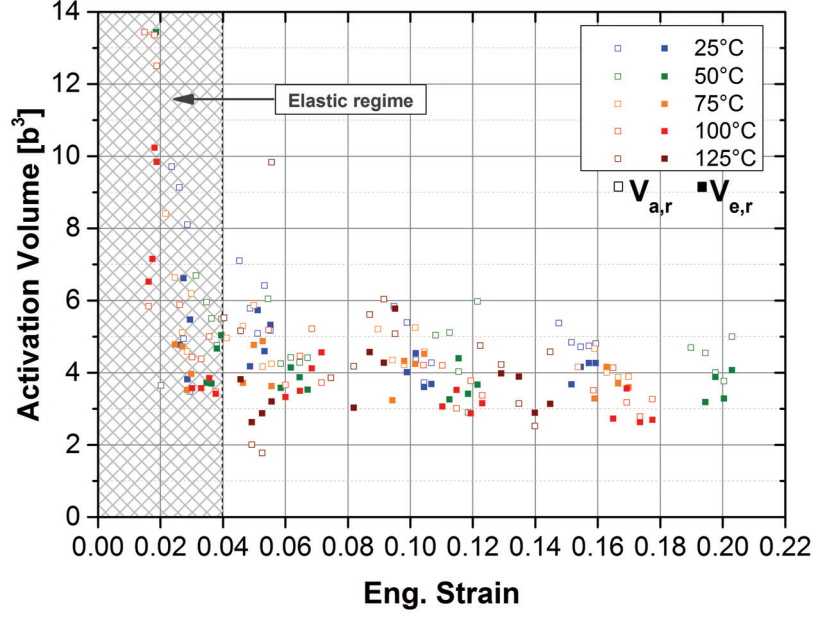


Figure 6.8.: Activation volumes as function of Eng. strain, obtained from repeated load-relaxation tests at variable test temperatures on thermally relaxed Pd<sub>90</sub>Au<sub>10</sub>. The hollow and solid symbols denote apparent and effective activation volumes, respectively.

found for the effective activation volume which has a lower overall scatter and values around  $4b^3$ . Increasing the test temperature shifts both, the apparent and the effective activation volumes down to slightly lower values in the order of  $V_{a,r,125^\circ\text{C}} \sim 4b^3$  and  $V_{e,r,125^\circ\text{C}} \sim 3b^3$ .

## 6.4. Discussion

### 6.4.1. Apparent deformation behavior

Figure 6.9(a) shows a representative micrograph of a Pd<sub>90</sub>Au<sub>10</sub> micropillar with a  $\sim 12\text{nm}$  crystallite size after compression at 125°C, whereas Figure 6.9(b) shows the same compression test after heat treatment at 250°C (image tilt angle 55°). Both pillars were deformed to approximately 25% strain. The deformation of the untreated pillar at 125°C was propagated quite homogeneously over the whole length, showing only little amount of strain concentration in the top part of the pillar. The pillar

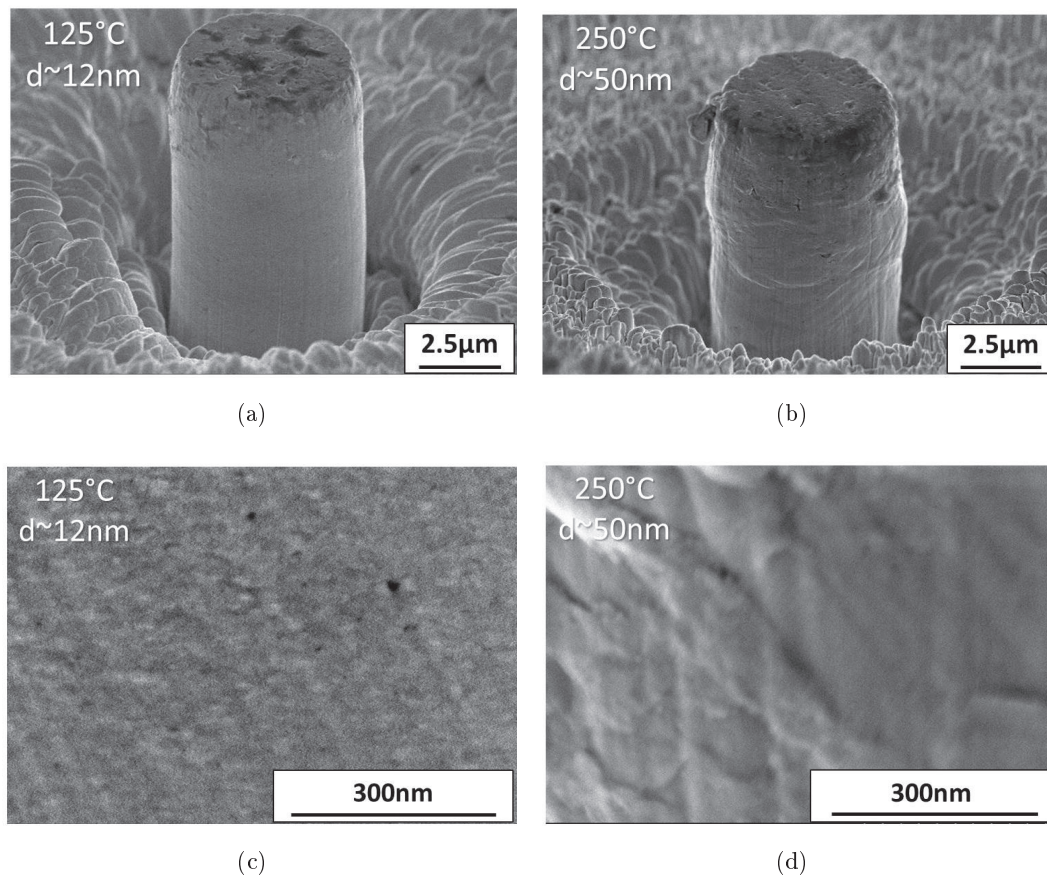


Figure 6.9.: SEM overview images of  $\text{Pd}_{90}\text{Au}_{10}$  micropillars after compression (a and b) and corresponding high resolution SEM images (c and d) at 125°C and 250°C, respectively. Crystallite growth clearly affects the apparent deformation behavior. Increased grain boundary mediated deformation manifests in coarse surface features after compression up to 25% strain.

surface remained smooth and does not show any obvious geometrical differences. This behavior seems to be invariant with temperature and deformation rate in the constant nanostructure regime, since all the tested micropillars up to 125°C look alike after compression. However, recrystallizing the nanostructure affects the apparent deformation behavior substantially. The surface structure of the heat treated pillar appears less smooth with larger domains in the size regime of  $< 0.5\mu m$  bulging out of the pillar surface. Although the crystallite size is still roughly ten times smaller than these features, their appearance suggests that the grains have grown. The bulk of the deformation seems to be accommodated by the upper 60 – 70% of the pillar which may be attributed to the slight pillar taper from the milling process.

In contrast, after a compression to such a substantial amount of strain, a single crystal *fcc* metal pillar would show dislocation-induced slip offsets traversing the entire cross section [94]. Slip bands would also be found on a BMG micropillar, but in this case they would be induced by localization of STZ's [184] and not dislocation activity. However, neither of these two materials would display similarly homogeneous deformation behavior as found in nanocrystalline materials. The closer observation of the post-compression surfaces in a Hitachi S-4800 high resolution SEM (Hitachi, Japan) on the Pd<sub>90</sub>Au<sub>10</sub> micropillar compressed at 125°C (Figure 6.9(c)) indicates no obvious surface features. The fine grain size of initially 12nm seems not to have grown excessively, neither as an effect of the high temperature experiments (which was further confirmed by post experimental XRD measurements) nor due to the FIB milling and polishing. No traces of slip or any anomalously deformed regions are present. The slight surface roughness may be an indicator for grain boundary mediated plasticity which causes grains to slide out of the free surface or enhanced STZ activity.

After the crystallites have grown at 250°C to a nominal size of  $> 45 \pm 10nm$ , the post-compression surface features of the micropillar clearly show traces of enhanced grain boundary-mediated plasticity as displayed in Figure 6.9(d). Entire crystallite domains are pushed out of the free surface of the micropillar. Such features have also been observed on nanocrystalline nickel in Section 5.1, where they have been attributed to grain boundary diffusion processes.

#### 6.4.2. Activation volume

In this study, we determined activation volumes by employing different evaluation protocols related to load relaxation tests, strain rate jump tests, and transients between subsequent relaxation events. Experiments were carried out on nominally



identical micropillars. Therefore, it is logical to assume that same rate controlling mechanisms are operative in the deforming pillars, provided that comparable strain, temperature, and strain rate prevail.

As already mentioned, only effective activation volumes can be determined from transient tests, whereas both strain rate jump and load relaxation tests deliver values for apparent activation volumes. Hence, we may speculate that a comparison of apparent activation volumes deduced from both types of tests may enhance our understanding of deformation behavior in nanocrystalline metals in the limit of crystallinity. Comparing Figure 6.6 and Figure 6.8, we realize that the extracted values of apparent activation volumes differ by a factor of 2–3, depending on which evaluation protocol has been utilized. Likewise, the temperature dependence of the apparent activation volume determined by strain rate jump tests is twice as big as that determined by stress relaxation tests. The difference between the results suggests that the testing scheme and the evaluation protocol have a significant influence on the determined apparent activation volumes. The key difference between both tests is the change of the applied strain rate. In the case of the stress relaxation tests, strain rate drops instantly to near zero, implying that total strain remains fixed during each relaxation segment, but a transformation of stored elastic strain to plastic strain occurs. Such a relaxation is facilitated exclusively by thermally activated plasticity mechanisms which have, due to the segment time of 60s, typical time constants similar to or below that value. The determined apparent activation volume, corresponding to the convolution of an ensemble of active mechanisms, is approximately  $4b^3$ . The observed temperature dependence of activation volume can also be interpreted in this context. Increasing the temperature should allow additional mechanisms having increased time constants, or increased activation volume, respectively, to contribute to the relaxation. Incorporating such a scenario into Equation 5.16, one would have to simply sum the weighted identical right hand side expressions with different time constants and activation volumes related to the respective mechanisms. A typical mechanism entering the sum might be simply a shear transformation [171] that involves an increased number of atoms taking part in the local shear event. Using Equation 5.16 as it stands to evaluate a single apparent activation volume, however, would lead to a decrease in activation volume at elevated temperatures, as shown by the analysis.

In contrast to the stress relaxation tests, the strain rate jump tests successively vary the applied strain rate. After each strain rate jump, a newly established steady state of plastic deformation prevails after a significant stress overshoot  $\Delta\dot{\epsilon} > 0$  or undershoot  $\Delta\dot{\epsilon} < 0$  (see Figure 6.4). Adopting the idea of an ensemble of athermal

and thermally-activated plasticity mechanisms with a range of activation volumes and time constants, a jump to a higher strain rate may suppress some thermally activated plasticity mechanisms with longer time constants, whereas a jump to lower strain rates may activate additional plasticity mechanisms. In fact, the potency and type of mechanisms, which are selected from the ensemble of possible mechanisms by the prescribed strain rate, manifest as higher or lower stress values in the newly established steady state. The initial stress increase during a jump to higher strain rates may reflect the fact that only athermal mechanisms, such as lattice elasticity, can instantly contribute to the higher strain rate. The increased stress in return lowers the effective activation energy barrier for the thermally activated mechanisms (c.f. Equation 5.14) and enables them to contribute to higher strain rates. The interplay between athermal mechanisms, stress variation and thermally activated mechanisms results in the transient behavior following the stress overshoot, which is essentially a stress relaxation under dynamic deformation conditions. The jump to lower strain rates can be explained analogously.

The fact that the over and undershoots become less pronounced with increasing temperature confirms that the share of thermally activated processes of the ensemble of all plasticity mechanisms becomes more dominant with increasing temperature. This is also reflected by the increased strain rate sensitivity and the convergence of the apparent activation volumes derived from both tests with increasing temperature to values of approximately  $4b^3$ .

### **6.4.3. Activation energy and possible related deformation mechanisms**

Besides the activation volume, the apparent activation energy is a relevant thermal activation parameter which can be used to identify active plasticity mechanisms. In contrast to the apparent activation volume, which is the average of the activation volumes of active mechanisms weighted by their contribution to the total shear strain rate, the apparent activation energy is sensitive to the active process with either the smallest or the highest activation energy, depending on whether they act in parallel or in series respectively [118, 150]. Based on a steady state creep approach, we previously extracted activation energies from high temperature micropillar SRJ tests on nanocrystalline Ni as shown in Section 5.1.3 and [118]. The obtained results are in close agreement with literature values for grain boundary diffusion in nickel.

A similar, but more general approach, to determine the apparent activation energy

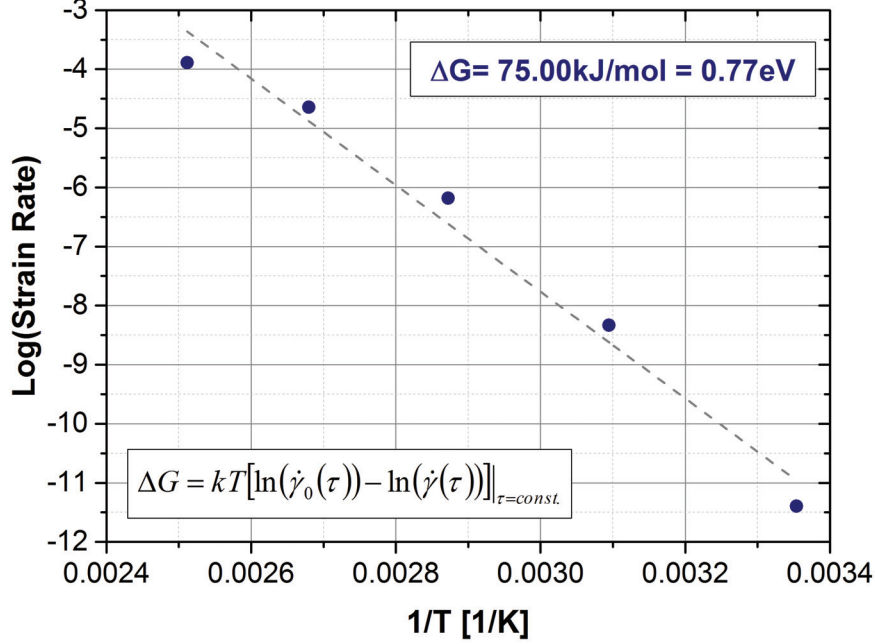


Figure 6.10.: Apparent activation energy for deformation calculated by plotting extrapolated strain rate, corresponding to the same stress level in log scale vs.  $1/T$

is to take the logarithm of Equation 5.12 and solve for  $\Delta G$  to obtain:

$$\Delta G(\tau) = kT [\ln(\dot{\gamma}_0(\tau)) - \ln(\dot{\gamma}(\tau))] |_{\tau=const.} \quad (6.3)$$

We also know from Equation 5.13 that  $\Delta G$  is a function of shear stress,  $\tau$ , which requires the determination of  $\Delta G$  to be performed at the same stress levels for each temperature. Since nanocrystalline Pd<sub>90</sub>Au<sub>10</sub> micropillars show a strong dependence of flow stress on test temperature, we had to slightly extrapolate measured stress values to achieve constant stress levels [118]. Figure 6.10 shows the  $\log(\dot{\epsilon})$  vs.  $1/T$  plot for the different test temperatures up to 125°C. The five data points were determined at a mean flow stress level  $\sigma_{\text{flow}} \approx 1.71 \text{ GPa}$  ( $\ln(\sigma_{\text{flow}}) = 0.5375$ ). From the slope of the curve fitted through these points, an apparent activation energy of  $\Delta G = 75 \text{ kJ/mol} = 0.77 \text{ eV}$  was extracted.

In nanocrystalline metals, care has to be taken when assigning a measured activation energy to a single deformation mechanism as the dominant mechanism, since the same value could be shared by several different mechanisms or represent a convolution of several competing mechanisms. In the context of the very few available

studies in the literature which deal with activation parameters of palladium and gold, the measured value ( $0.77eV$ ) is consistent with the activation energy of diffusion of Au in a PdAu multilayer with high intragranular defect density ( $0.76eV$ ) [185]. Although these numbers suggest a near perfect match to the activation energy extracted from Figure 6.10, it is rather unlikely that diffusion alone is the rate controlling mechanism for two reasons: differences in studied materials and inconsistency with model predictions. First, the material examined in [185] is a textured PdAu-multilayer with a fairly high intragranular defect density (the lattice diffusion coefficients were higher than the grain boundary diffusion coefficients), whereas in our case, we have a randomly textured nanocrystalline material. Secondly, if we use these diffusion coefficients [185] and the results of this study in different diffusion models, i.e. Ashby-Verral [186] or Coble creep [182], the resulting strain rates at room temperature and  $125^{\circ}C$  are in the order of  $10^6$  and  $10^3$  respectively. Both values are several orders of magnitude above the experimental findings as displayed in i.e. Figure 6.4, which implies that they do not contribute to plastic deformation in a dominant manner. Further, we assumed that  $\dot{\gamma}_0$  behaves in a constant manner. In view of the complex ensemble of active deformation mechanisms, where each one may have its own temperature, stress and/or strain rate dependence, assuming  $\dot{\gamma}_0$  to be constant may not be appropriate. Thus, if  $\dot{\gamma}_0$  were temperature dependent, this would result in a shift along the  $\ln(\dot{\gamma})$  direction in Figure 6.10, resulting in a different apparent activation energy.

Models for GBS (i.e. [164, 103] or Equation 3.2) yield results which are closer to our experimental findings: strain rates on the order of  $10^{-6}$  at room temperature and  $10^{-4}$  at  $125^{\circ}C$ , respectively. Nevertheless, these values are based on the assumptions from reference [185], and, as already mentioned, it is questionable that the diffusivity through the lattice is faster than through the grain boundaries. Hence, if one would interchange the diffusion coefficients the resulting strain rates would be in the order of unity and diminish the influence of GBS as a dominant mechanism. Further, GBS results in texture evolution due to preferred grain growth, which in turn opens pathways for dislocation-based phenomena in these larger grains. However, studies on HPT-deformed nanocrystalline palladium [83] revealed no texture formation, even at strains  $> 100\%$ . The TEM images shown in Figure 6.11 consolidate these assumptions as the post deformation nanostructures of the micropillars (after SRJT) neither at room temperature, nor at  $125^{\circ}C$  indicate localized grain growth. Also, the share of dislocations in the ensemble of deformation mechanisms in nanocrystalline PdAu has been quantified to be approximately 10% [120], which indicates it serves as an accommodation mechanism rather than the dominant deformation mechanism.

Table 6.1.: Calculated values for Mechanical work  $\Delta W$  and Helmholtz free energy  $\Delta F$ 

$T [C^\circ]$	$\sigma_{flow} [GPa]$	$V_{app,SRJ} [b^3]$	$\Delta W [eV]$	$\Delta F [eV]$
25	1.67	11.0	1.38	2.15
50	1.61	9.1	1.10	1.87
75	1.53	7.7	0.88	1.65
100	1.40	6.6	0.69	1.46
125	1.31	5.2	0.51	1.28

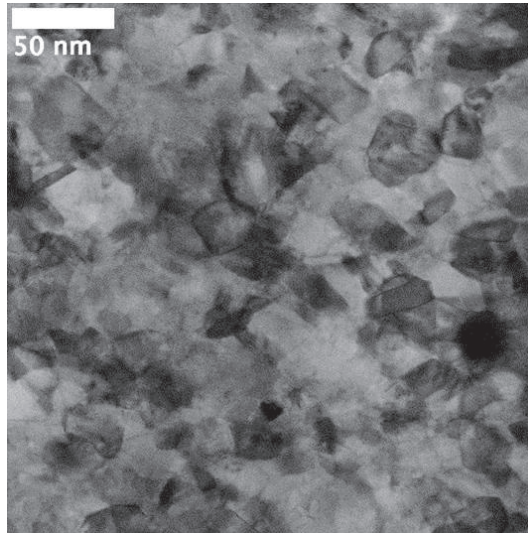
Thus, even though the range of activation volumes presented in the previous section ( $\sim 5 - 11b^3$ ) would also accommodate all the mechanisms discussed so far, including dislocation-mediated processes, none of them is actually expected to apply to an extent which would validate assignment as the dominant deformation mechanism. However, this does not mean that they are inactive.

Another approach to examine the plastic deformation of such fine-grained nanocrystalline metals is based on the activation of shear transformation zones (STZs), as they are usually accepted to propagate plastic flow in metallic glasses. Although the bulk of the investigated material is crystalline, the intergranular volume is approximately  $\sim 30\%$  (see Figure 3.2), which promotes the significance of intergranular- and STZ-mechanisms. For example, Grewer et al. [120] proposed STZs to carry  $\sim 65\%$  of the overall strain in nanocrystalline PdAu with  $10nm$  crystallite size, along with mildly increasing dislocation activity and decreasing grain boundary mediated mechanisms above the yield point. To compare our current results with literature data, it is helpful to compute the Helmholtz free energy,  $\Delta F = \Delta G + \Delta W$ . The mechanical work,  $\Delta W$ , done by the externally applied force can be calculated with the applied flow stress,  $\sigma_{flow}$ , and the apparent activation volume,  $V_{app,SRJ}$ , thusly

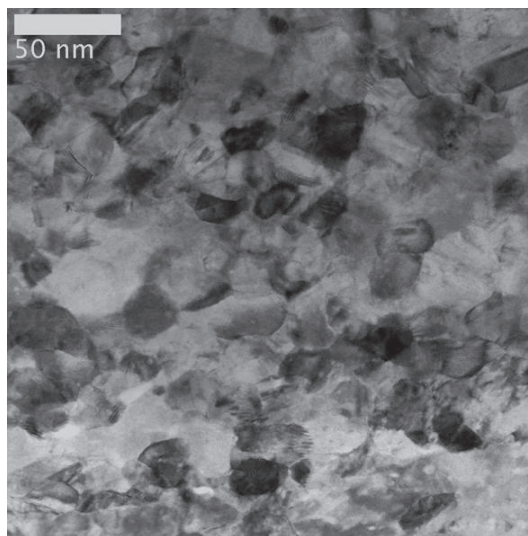
$$\Delta W = \frac{(\sigma_{flow})}{\sqrt{3}} V_{app,SRJ} \quad (6.4)$$

Due to the temperature dependence of  $\sigma_{flow}$  and  $V_{app,SRJ}$ ,  $\Delta W$  also depends on  $T$ , and we obtain the values for  $\Delta W$  and  $\Delta F$  that are listed in Table 6.1.

For Al-rich metallic glasses, an activation energy distribution of  $0.85 < \Delta F_{\Omega,STZ} < 1.26eV$  has been proposed [171]. There index  $\Omega_{STZ}$  denotes the number of atoms in the activated STZ, which is on the order of  $15 - 21$ , and an assumed critical shear strain of  $\Delta\gamma_c \approx 0.2$ . Hence, with  $V_{app,SRJ} = \Omega_{STZ}\Delta\gamma_c$ , we calculate the size,  $\Omega_{STZ}$ , of presumably active STZs in thermally relaxed nanocrystalline Pd<sub>90</sub>Au<sub>10</sub> to be around  $34 < \Omega_{STZ} < 76$  atoms. Consequently, the activation free energies



(a)



(b)

Figure 6.11.: Pd<sub>90</sub>Au<sub>10</sub> TEM cross sections (STEM) of micropillar nanostructure after compression to 25% strain (SRJ). The upper image (a) represents the deformed nanostructure before the elevated temperature experiments whereas image (b) was taken after the thermal treatment at 125°C. Both pillars show no indications of localized grain growth due to GBS or the thermal treatment.

$\Delta F$  in the present study for PdAu are slightly higher than the activation energies found in [171] for Al. The values are on the same order, but values for PdAu and Al cannot be directly compared. Furthermore, in the present case, as discussed in the previous paragraph, additional plasticity mechanisms like stress-driven GB migration or (partial) dislocation glide can be active in nanocrystalline metals [7], which may also contribute to the observed activation energy. Assuming that the contribution of STZs decreases and/or ceases at cryogenic temperatures, and thus the strain is primarily mediated by dislocations and/or stress driven GB migration, then activation energy in the lower temperature range would be expected to display higher values than extracted in this study. Hence, in an upcoming work, we will try to address this issue by performing similar deformation experiments at high strain rates and/or cryogenic temperatures to selectively impede certain thermally activated processes.

## 6.5. Conclusions

In the present study, the applicability of elevated temperature, uniaxial micropillar transient tests to probe the activation parameters was demonstrated on nanocrystalline Pd<sub>90</sub>Au<sub>10</sub> with a nominal crystallite size of 12nm. The strain rate sensitivity and activation volume were extracted from strain rate jump and repeated load relaxation tests at various temperatures, which enabled the activation energy  $\Delta G$  to be determined. The high geometric fidelity of the micropillars in combination with the large number of crystallites ( $> 10^8$ ) in a single pillar allowed investigation of the mechanical properties with the quality and reproducibility similar to the level of regular bulk tests. The presented combination - a novel, highly accurate dynamic test method with a highly pure, homogeneous nanocrystalline *fcc* metal - demonstrates the potential of this technique for accurately probing and simultaneously observing mechanical behavior at the lower boundary of crystallinity.

Post-compression imaging of the micropillars showed no evidence of stress-induced grain coarsening or slip bands. From the strain rate sensitivity analysis, it is unlikely that either grain boundary sliding ( $m \geq 0.3$ ) [183] or Coble creep ( $m \geq 1.0$ ) [182] are the dominant rate-limiting mechanism. The obtained effective activation volumes from stress relaxation tests up to 125°C were on the order of  $\sim 4b^3$ , which is consistent with intragranular as well as STZ-mediated plasticity. The values were fairly consistent over the entire test temperature and plastic strain range, suggesting that the overall relaxation mechanism remains the same. Further, analysis of the strain rate jump tests reveal a temperature dependent activation volume ranging from  $11b^3$

at room temperature to  $5b^3$  at 125°C, which reflects the temperature-dependent interplay of different externally driven deformation mechanisms.

An apparent activation energy value of  $\Delta G = 0.77eV$  has been extracted from strain rate jump tests. This value as a standalone cannot be attributed to a specific dominant deformation mechanism. Comparison to available literature data as well as to the other results from this study do not suggest diffusive mechanisms to be rate controlling. A range of activation free energies  $\Delta F$  of  $1.28 < \Delta F < 2.15eV$  can be determined, where lower values of  $\Delta F$  correspond to higher temperatures. Following the reasoning of Ju et al. [171] for metallic glasses, we estimated STZ sizes of  $34 < \Omega_{STZ} < 76$  atoms. Both, the activation free energies and the STZ sizes for nanocrystalline Pd<sub>90</sub>Au<sub>10</sub> are slightly larger than the values found for Al-rich metallic glasses but still similar in a congruent manner. However, a direct comparison of  $\Delta F$  for different material systems should be regarded with caution, especially since additional plasticity mechanisms are involved in the case of nanocrystalline material.



---

## 7. Technical relevance of nanocrystalline metals and their application in the Swiss watchmaking industry

### 7.1. Motivation

As mentioned in Chapter 1, the bulk of watchmaking metals is available in the form of rolled sheets which are then ground down to the desired thickness (usually in the order of few  $100\mu m$ ) before watch parts are machined. Large batches are mostly produced by stamping, whereas for prototyping and smaller batches also electrical discharge machining (EDM) or chemical etching processes are utilized. A tradeoff between the rather high costs of stamping tools vs. the machining and process costs for EDM needs to be found. Generally, all sheet metal-based processes are restricted to the availability of suitable materials and limit the design of parts to one single layer which prevails the integration of new functions into parts that require multiple layers and/or foreign material inserts like carbon, diamonds, rubies, sapphires, etc. To remain at the forefront of technological advancement, watchmaking companies in Switzerland are facing the challenge of integrating a wide range of new materials technologies into their manufacturing processes. This includes new materials for mechanical miniature parts such as silicon or galvanofomed nanocrystalline metal alloys, coating technologies such as atomic layer deposition (ALD) or diamond chemical vapor deposition (CVD) for components, and manufacturing technologies such as DRIE (Deep Reactive Ion Etching), LiGA, or laser machining. Key to the successful implementation of these new materials is the precise understanding of their basic mechanical properties: Young's modulus, elastic limit, creep, relaxation, fracture toughness etc. However, these properties and the process-property relationships are not understood on the required size-scale which is due to a general lack of mechanical testing methodologies for miniature parts and a lack of understanding of internal and external microstructure length scale effects.

Contrary to conventional poly-/micro-crystalline metals manufactured by stamp-

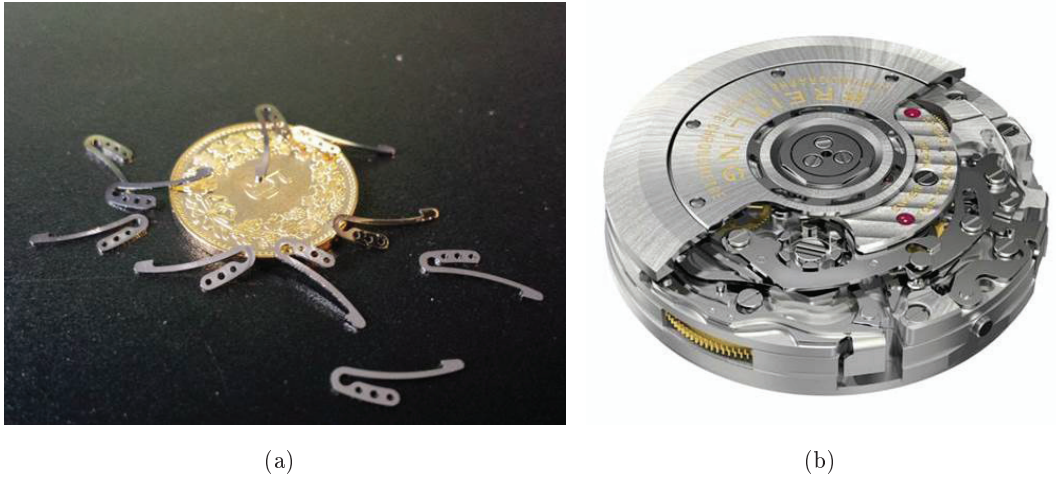


Figure 7.1.: (a) Nanocrystalline nickel watch micro-cantilevers, obtained from LiGA-process. (b) Mechanical wrist-watch movement (Courtesy: Breitling SA) which utilizes a large number of functional microcomponents.

ing, monocrystalline materials such as silicon or sapphire suffer from low fracture toughness whereas nanocrystalline (electrodeposited) materials which are in the focus of this study exhibit low resistance against time-dependent plasticity. Moreover, all new materials behave in an anisotropic manner. Coated components suffer from unknown system properties such as residual stress, limited adhesion, unknown tribological properties in micro-contacts, etc. Process damage in surface zones from DRIE or laser impact affects the mechanical properties. For these reasons, the design experience acquired over hundreds of years for conventional, stamped or hand-crafted materials cannot be transferred to these new technologies. Additionally, many watch manufacturers are forced to outsource development processes for cost reasons or change subcontractors due to interruptions in the supply chain.

Watchparts as depicted in Figure 7.1 (a) have to be precise and highly functional and their mechanical properties need to be known accurately. Otherwise, the precision of the watch is lost, and the required life-time predictions over 20 years cannot be made. From a design perspective alone, the LiGA technique appears to be the method of choice. It can be employed to fabricate precise and complex micromechanical components with high aspect ratios, multiple functional layers and incorporated foreign materials for functional and design reasons. Figure 7.1 (b) exemplarily shows a watch-movement, consisting of numerous micro-parts and different engineering materials to provide an idea about the complexity of the installed components. However,

the absence of LiGA materials which fulfill the required mechanical properties is currently a major drawback and limits the application of this process. Therefore, new electrodeposited materials meeting these requirements, i.e. high yield strength and Young's modulus, as well as improved relaxation- and creep properties have to be developed. The benchmark is an industrially available nanocrystalline nickel which is currently used for the suggested applications. Further it is required to develop and utilize test methods which are capable of reliably measuring mechanical properties on watchpart scale. In this context, the presented study was conducted partially within the framework of a CTI-project\* and focuses on the following major tasks:

- Identification of the key mechanical properties of electrodeposited materials with respect to watchmaking applications
- Development/utilization of suitable test devices to assess the process-property parameters on the size scale of watchparts and testing of a selection of application relevant materials.
- Alloying nickel with refractory metals to thermally stabilize the nanostructure and improve the material performance with respect to watchmaking-applications.

## 7.2. Mechanical properties for watch applications

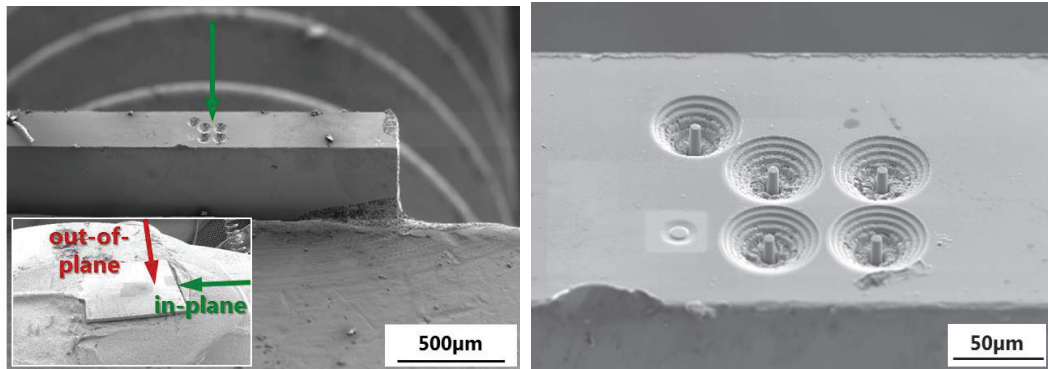
In this section, the key mechanical properties for watch applications are briefly reviewed. As the focus of this thesis is mainly put on electrodeposited nanocrystalline *fcc* metals, the details and examples given here are directly related to this group of materials. Further, due to the strongly pronounced time-dependent plastic behavior of nanocrystalline metals, the mechanical properties are discussed with respect to the parameters grain size and and strain rate.

### 7.2.1. Young's modulus

Young's modulus can be measured from stress-strain curve obtained from a standard tension or compression experiment, but commonly the modulus values used for mechanical design of watch components are taken from literature. Young's modulus is strongly dependent on texture in metals and semiconductors. For example, the modulus of single crystal nickel varies from  $\sim 136GPa$  to  $\sim 303GPa$  due to

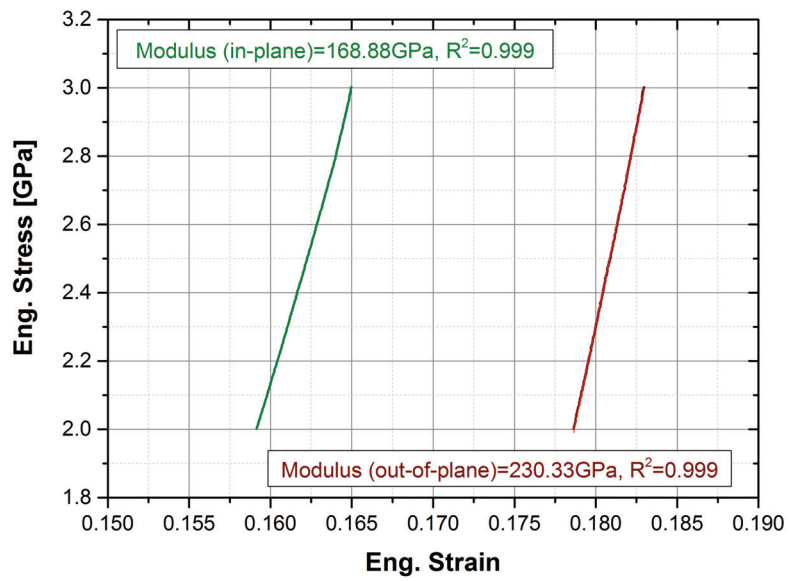
---

\*(CTI-140826): „Accelerated materials design of alloys for LiGA parts with high Young's modulus and creep resistance comparable to maraging steel“



(a)

(b)



(c)

Figure 7.2.: Micropillars, cut in „in-plane“ direction into the side of the gripping section of a nanocrystalline nickel micro tensile specimen (a) and (b). The normal axis of the micropillar corresponds to the tensile-axis. Comparison of modulus from unloading curves in-plane and out-of-plane (c).

difference in crystallographic orientation/texture as discussed in Section 3.1. Hence it is somewhat instructive to determine the modulus of watch microcomponents on actual watch part scale, using suitable miniaturized sample testing methods rather than considering the literature/material supplier property values for design purposes. Ideally the measurements are conducted with respect to the actual loading direction the component will face in service.

In order to experimentally investigate the influence of crystallographic texture on the Young's modulus of nanocrystalline nickel, two sets of micropillars were prepared (see Section 4.5.1) in the undeformed gripping section of a nanocrystalline nickel micro tensile bar (industrial reference grade, as deposited condition) with a strongly pronounced (111) growth texture (measured by XRD). One set of micropillars was cut perpendicular to the deposition plane, as usually done for the previously presented studies. The second set was milled into the sidewall of a gripping section such that the compression axis of the pillar is aligned parallel with the tensile axis of the specimen. Figure 7.2 (a) and (b) illustrate the in-plane orientation of the micropillars. The out-of-plane orientation is depicted in Figure 5.19. Both sets of pillars were compressed with a diamond flat punch tip at strain rates of  $\dot{\epsilon} = 0.001s^{-1}$ . Figure 7.2 shows the unloading curves of two representative experiments. Figure 7.2 (c) shows the upper segments of unloading curves from micropillar compression tests on one nanocrystalline nickel dogbone specimen (industrial reference, as deposited). The extracted modulus values are  $E_{out-of-plane} \sim 230GPa$  for the tests in growth direction and  $E_{in-plane} \sim 169GPa$  for the tests into the direction of the tensile axis. The values are  $\sim 36\%$  different from each other which clearly indicates the textural influence.

As mentioned in the introduction to this Chapter, Young's modulus is one of the most important material properties with respect to watch applications. Many watchparts fulfill spring functions in the form of small cantilever beams with a fixed and a loose end which are occasionally, or periodically, bent like for example the set lever in a chronograph movement or the rattrapante brake lever. When designing such components, the watchmanufacturers usually do not rely only on the elastic properties that are provided by the materials manufacturer. From their experience, they know that severe differences between average bulk properties and their specific component properties may exist. For the industrial reference nickel shown here in this thesis, the Young's modulus value provided by the manufacturer is  $E_{manufacturer} \sim 170GPa$  which corresponds well to the in-plane modulus measured here. However, no information about the measurement direction or method is provided there, and the directional differences are severe as can be concluded from Figure 7.2. However,

the industrial approaches to circumvent this discrepancy are very often proprietary, not standardized, and involve finite element modeling or large amounts of tests and design refinements to achieve the desired function. Nanoindentation, which probably is the most commonly utilized technique in the watch industry, is not sensitive to textural or orientation changes and as such not beneficial in this case. For this type of measurement, micropillar compression into the main loading direction of a watch component can assist in a more accurate and reliable determination of elastic properties, even though the effort of specimen preparation (focused ion beam milling) is comparably large.

### 7.2.2. Yield strength and hardness

Yield strength is another important property for designing watchparts. Plastic deformation of components needs to be avoided and a certain ruggedness, for example against large G-forces in the event of dropping a watch has to be ensured. Hence, the parts are designed usually with large safety factors and only face stresses up to a fraction of the materials nominal capability. Yield strength can be directly measured from a stress-strain curve obtained by a standard tension or compression experiment by applying a suitable yield criterion. For engineering applications, usually plastic deformations of 0.2% are accepted. For metals, hardness is usually related to yield strength by a constant factor of  $\sim 2.8$  ( $Hardness = 2.8 \cdot yield\ strength$ ). This is a common approximation and enables the use of indentation techniques for measuring strength. In contrast to Young's modulus, yield strength/hardness show a less pronounced dependence on texture. Hardness increases with decrease in grain size, because smaller grains inhibit dislocation activity in the grains. For polycrystalline metals, this is usually achieved by specific heat treatments or cold working in i.e. rolling processes. Especially in the case of nanocrystalline metals, where much finer grain sizes are achieved, this strength increase reaches up to a certain limit where dislocation based mechanisms cease and grain boundary mediated processes start to govern plastic behavior. As a result the hardness decreases again as visualized in Figure 3.1 (b)) or described by Equation 3.1.

In case of nanocrystalline metals, the assessment of yield strength is often only possible by miniaturized techniques, as the available quantities of materials prevent the use of common bulk techniques. However, even if bulk quantities are available for testing, as is usually the case for rolled sheets, it is necessary to perform tests on watch part scale. Figure 4.14 (a) illustrates the statistical relevance of micropillar tests as a function of two parameters: the materials internal size (grain size) and the

component size (diameter of the pillar). This example can easily be transferred to polycrystalline sheet metals and components on watch part scales. The grain size of such metal sheets (brass, maraging steel) is commonly in the order of several tens of microns, and the grain size may also depend on the preferential orientation of grains due to the rolling process. Assuming an ideal, random grain orientation and spherical grains with an average diameter of  $50\mu m$ , watch parts with a crosssectional diameter of  $50\mu m$  consists of only 50 to 100 grains/cross section. Hence, bulk properties may not be necessarily valid for watch applications. In this context, Section 7.3 presents a case study where a selection of commercially available watchmaking materials have been tested on component scale.

### 7.2.3. Time dependent plastic behavior: load relaxation and creep

#### Load relaxation

The high strength of nanocrystalline metals combined with the almost unlimited design freedom of the LiGA-process moved electrodeposited nanocrystalline metals in to the focus of interest of many watch manufacturers. However, a challenging disadvantage of the currently available materials is their strongly time-dependent plastic behavior, which originates from their very fine nanostructure and manifests in stress relaxation and creep, even at ambient temperatures. Watch parts experience high contact stresses and often fail by a combination of these mechanisms as their main purpose is to store mechanically produced energy over a certain period of time. While creep behavior [164, 101, 103, 165, 166] of nanocrystalline materials has already been studied by using conventional tensile or compression tests on bulk specimens, stress relaxation properties, on the other hand, have not received as much attention and are reported only in few studies [168, 169, 144]. Further, none of the mentioned studies conducted tests on the scale of micromechanical components. As such it is necessary to develop short term (or accelerated) tests to accurately predict long term behavior (over 20 years) for both, load-relaxation and creep.

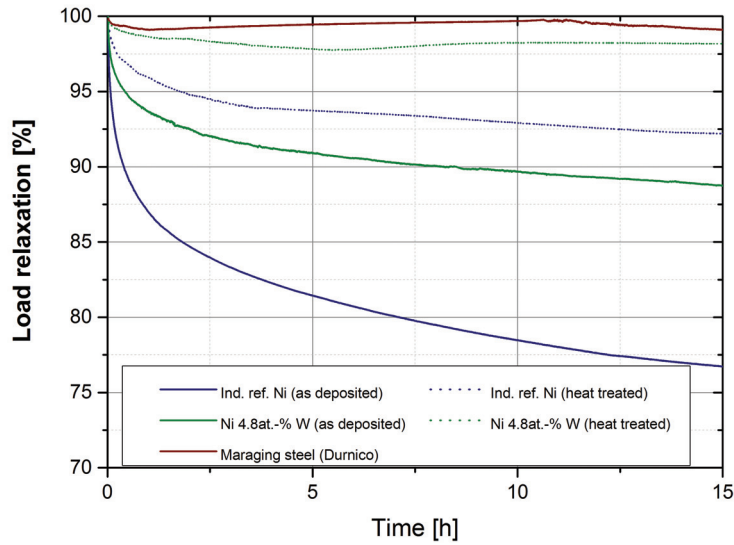
Load relaxation as a mechanism refers to the drop in applied stress/load of a specimen with the passage in time. For example, springs are often relied upon to exert a constant restoring force while held in a flexed position for sustained periods of time. Springs made from nanocrystalline nickel with a grain size of  $\sim 30nm$  will lose their restoring force over time, even at room temperature. When loaded near the yield point, the restoring force will decay by  $\sim 3 - 5\%$  even within 1 minute, and further decay  $\sim 10\%$  within a week. It is important to know the stress relaxation properties of watch components as a function of stress normalized by yield strength

for designing the movements using nanocrystalline metals. The more the stress approaches the yield strength, the more severe is the relaxation (see Figure 5.21). Stress relaxation as a function of applied stress normalized by the yield stress (applied stress/yield strength) needs to be mapped out for comparing different materials and for designing mechanical watch parts.

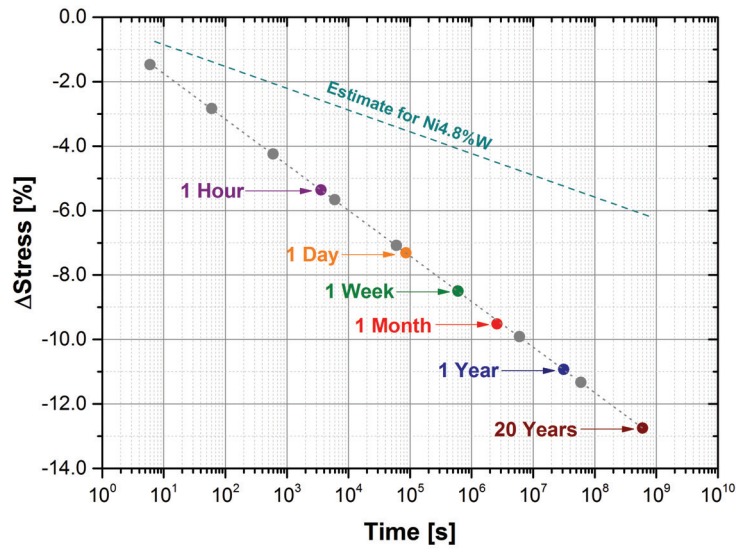
A first approach to the assessment of relaxation parameters on watch part scale in this work is illustrated in Figure 7.3 (a). Load relaxation curves are displayed that were obtained in uniaxial tension on micro specimens with gauge crosssections of  $\sim 150\mu m \times 200\mu m$ . The tested micro-tensile specimens were made of electrodeposited nanocrystalline Ni (blue) and NiW (green), both in as-deposited and heat-treated condition, and hot rolled maraging steel (Durnico) as a polycrystalline reference material. All the tests have been performed in the plastic regime just after reaching the yield point. For the sake of comparability, the yield points have been normalized and the load drop is given in %, since the corresponding yield stresses are different for the different materials. The curves suggest, for both electrodeposited materials, the heat treatment significantly decreases the tendency to relax, which may be an effect of slight grain growth during the heat treatment and the thermal relaxation of grain boundaries. Maraging steel is polycrystalline and does not exhibit pronounced time-dependent plastic behavior, which is expected for this material at low homologous temperatures. The NiW-alloy developed at Empa, which is discussed in Section 7.4, exhibits improved relaxation behavior compared to pure nanocrystalline nickel. After the thermal treatment, the relaxation of NiW is strongly decreased with values close to the rolled maraging steel. However, the loads that watchparts commonly face in a watch movement are typically only a fraction of the materials' elastic limit. This scenario is illustrated in Figure 7.3 (b) where the load relaxation of industrial reference nickel (as-deposited condition) at stresses of approximately 55% of the elastic limit are extrapolated as a function of time (log-scale) with respect to the logarithmic stress decay function (Equation 5.15) obtained from the micropillar tests in Section 5.3. After one hour, the load in the micropillar has already decreased for  $\sim 5.5\%$ , and after one day for a total of  $\sim 7.5\%$ . Due to the logarithmic character the initial load decrease is very fast but slows down with increasing time scale as the predicted load loss due to relaxation after 20 years is in the order of 13%.

For both materials, the average amount of relaxation decreases by approximately 50% after the materials have been heat treated (see Figure 7.3 (a)). This is likely a convoluted effect of slight grain growth and thermal relaxation of the grain boundaries. This is beneficial from an applicative perspective as the material relaxes less and more energy remains stored in a watch spring. Nevertheless, the relevant time





(a)



(b)

Figure 7.3.: Load-relaxation curves (room temperature) obtained in uniaxial tension above the yield stress on nanocrystalline nickel, nanocrystalline nickel-tungsten and maraging steel (a) and long term prediction of stress relaxation of nanocrystalline nickel and nickel-tungsten at 55% of the elastic limit (b).

scale of stress relaxation phenomena remains within hours where a comparably large portion of the stored energy is dissipated by quasi-elastic deformation, and hence no longer available for driving the watch movement.

## Creep

The second relevant time-dependent plasticity mechanism is creep. It is defined as the time-dependent change in strain as a function of applied stress. Watch parts under contact stresses release the external stress by changing their dimensions. This does present a major challenge, particularly for nanocrystalline materials that creep significantly due to high volume fraction of grain boundaries aiding diffusion. Creep is conventionally measured by loading a specimen with a static weight and measuring the change in dimensions with time (often over days, months or years). Characterizing the creep behavior of small components and miniaturized sample is difficult because creep rates are often in the range of  $\dot{\epsilon}_c = 10^{-6}s^{-1}$  to  $10^{-10}s^{-1}$ . For a  $5mm$  gauge length specimen, this translates into total dimensional change of  $18\mu m$  to only  $1.8nm$  per hour! So extremely precise and stable measurements systems must be used to study creep of small samples. A very basic setup which was developed during this thesis for testing LiGA dogbone specimen is shown in Figure 7.4. The setup is capable of holding a single specimen plus the desired weight and measuring over a duration of 36 hours. The strain is measured optically by a high-resolution camera. It should be noted that the nanocrystalline nickel specimen tested in Figure 7.4 has a nominal gauge cross section of  $250\mu m \times 300\mu m$  and requires a weight of  $> 12kg$  to reach static stresses around the materials yield stress.

The creep rates achieved in these measurements are in the order of  $\dot{\epsilon}_{creep} = 10^{-9}s^{-1}$ , which is in decent agreement with available literature values for primary creep of nanocrystalline nickel with comparable grain sizes (see i.e. [164]). Taking this result as a standalone value for a lifetime prediction of a watch part, Figure 7.5 illustrates two estimates for accepted deformations of 1% and 5%. According to these predictions a nanocrystalline nickel watch part facing the applied loads of this test would fail within a period of  $> 1year$  which is, in the context of required part lifetimes, not sufficient. However, with respect to these measurements two things should be noted: First of all, even after 36 hours, no steady state was established which is probably due to microstructural evolution (for instance grain growth) during the experiment. As it is indicated in Figure 7.4, where the slope of the curves decrease after approximately 15 hours, the secondary creep strain rates are usually much lower than those in the primary regime which would lead to slower deformation

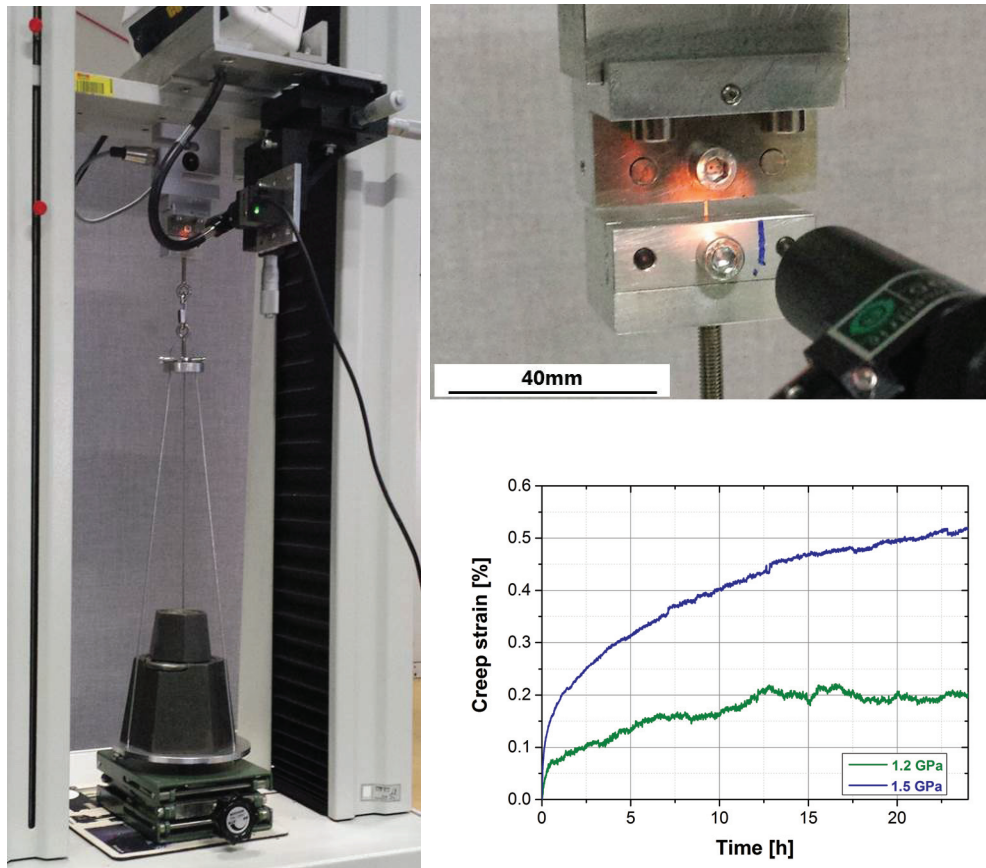


Figure 7.4.: First creep tests on a LiGA sample in air using vision tracking (digital image correlation) over a 24h period. The small LiGA sample (3mm gauge length and 300 $\mu$ m) could bear loads up to 12kg!! These creep tests can be improved and adapted to perform routine tests on industrial specimens using piezo actuation and by performing tests in SEM.

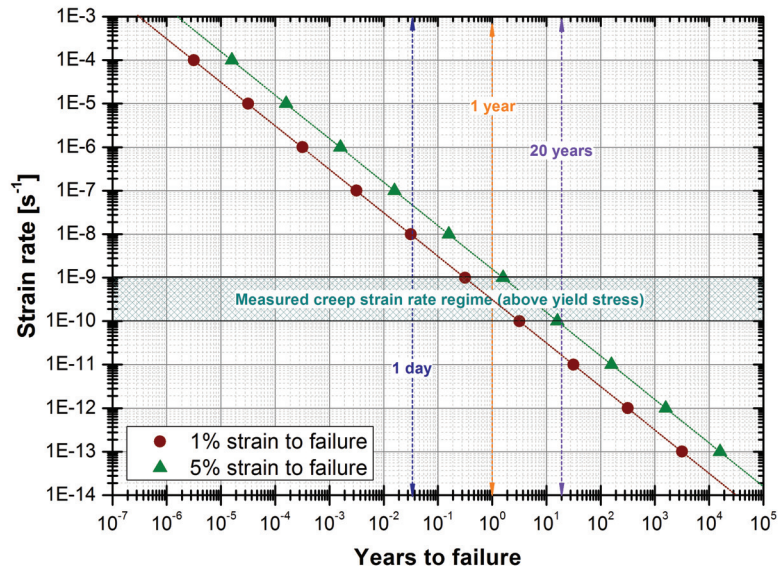


Figure 7.5.: Prediction of creep deformation as a function of time for accepted creep deformations of 1% and 5%. The experimentally assessed creep rates of  $\dot{\epsilon} = 10^{-9} s^{-1}$  are within the blue shaded frame.

after a certain test duration and thus a much longer component lifetime. Secondly, the stresses in this simple test were well above the materials' yield stress, in order to be able to resolve the small strains. Actual watch components are usually exposed to much lower stresses, at least well below the elastic limit, which will result in much smaller creep strain rates. Nevertheless, we are currently working on a protocol to assess creep properties by means of micropillar compression inside the SEM with the instrument described in Section 4.6 in order to achieve better strain resolutions at low creep stresses. The aim is to be able to capture creep events at a much earlier primary state and also test smaller volumes of materials, as for the presented tests, LiGA-micro parts need to be available which requires a large amount of process optimization.

### Summary

It can be said that both mechanisms, load relaxation and creep, are strongly related and convoluted as the same mechanisms govern both phenomena. The main differences are in the definition of the test protocol or loading conditions where ei-

ther constant strain for relaxation or constant load for creep are applied and in the time scales on which the mechanisms are activated. Creep traditionally requires long time scales to be established and higher loads. Relaxation is already active at lower stresses, as was demonstrated by the measurements in the elastic regime of nanocrystalline nickel, and hence considered to be the more relevant mechanism in the context of watchmaking applications. From a materials perspective, both mechanisms are heavily dependent on the materials' grain size, as smaller grains increase the intergranular volume and enhance diffusive mechanisms. A possible approach to hinder the diffusion along grain boundaries and improve the mechanical performance at the same time is to alloy nickel with refractory metals. This approach was introduced in Section 4.2 and will be further discussed in the last Section of this Chapter.

### **7.3. Case studies: Mechanical testing of watch making alloys on watchpart-scale**

This section provides a small overview over miniaturized conventional tests performed in the framework of a joint CTI-project between Empa and a Swiss watch manufacturer. The aim was to test different watch making materials on the scale of actual watch components, i.e. in the range of several hundreds of micrometers in cross section. Tasks were not only the actual assessment of mechanical properties but also the development and modification of suitable testing equipment. Only a few results are shown here in order to obey the confidentiality agreement. As most of the tested materials were produced by means of proprietary processes there are no material details provided in this section except for the bulk-specifications whenever available from the supplier.

#### **7.3.1. Micro tensile tests**

As already discussed in Section 5.2.3 and Section 5.2, uniaxial tensile tests are the most common tests for assessing mechanical parameters of engineering materials, but the bottle neck with respect to nanocrystalline metal thin films and micromechanical applications is the availability of suitable test specimens. In close collaboration with a major Swiss watchmaking company, a representative cross section of the most commonly available watchmaking alloys has been machined/deposited into the shape of dogbone tensile specimen (see i.e. Figure 5.9 for details). All steel and brass specimen were made by electrical discharge machining from commercially bought hot rolled sheet metal. The nanocrystalline nickel and nickel-alloy specimen

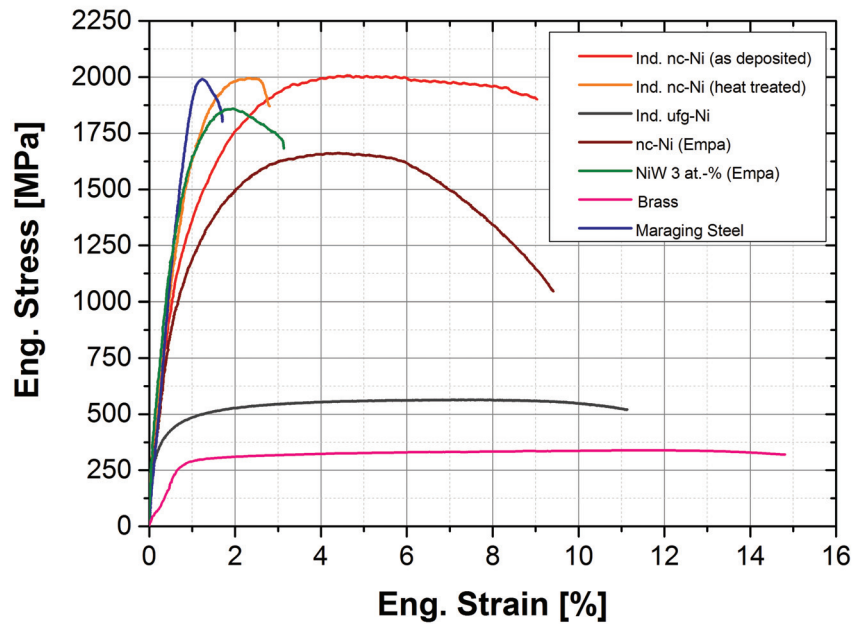


Figure 7.6.: Comparison of micro tensile stress-strain curves for a selection of metals/alloys used in mechanical watches.

were electrodeposited. The scope of this series of tests was to validate and compare our micro tensile tests to bulk values in the literature and to check how the nickel and nickel-tungsten deposited at EMPA compares to the industrial reference nickel. All tests were carried under identical conditions. The constant strain rate was set to  $\dot{\epsilon} = 0.001s^{-1}$  and the test temperature was 23°C. At least ten specimens per material were tested. Hardness measurements (Vickers 10) were performed on the non-deformed gripping sections of individual samples after the tensile tests in order to gain additional information. Figure 7.6 provides a representative overview over a selection of tested materials. The mechanical properties (Young’s modulus [unloading, not displayed], yield- and tensile strength, hardness) of all measured micro tensile samples are listed in Table 7.1. Mechanical bulk properties of the same materials proposed by the suppliers are given there as well. For the industrial nanocrystalline Nickel, the results obtained by the micro tensile tests generally are in good agreement with those given by the supplier, although the Young’s moduli as well as the yield strength are slightly below the values proposed there. Assuming that the strain rates applied for measuring the reference data were slightly higher than the strain rates

Table 7.1.: Mechanical properties of watchmaking alloys, assessed with uniaxial micro tensile tests. The italicized values are taken from supplier references if available.

<b>Material</b>	Young's modulus	Yield strength	Tensile strength	Hardness
	[GPa]	[MPa]	[MPa]	[HV]
<b>Ind. nc-Ni</b>	165	1146	2064	574
(as deposited)	<i>170</i>	<i>1600</i>	<i>2000</i>	<i>590</i>
<b>Ind. nc-Ni</b>	167	1300	1933	563
(heat treated)	<i>170</i>	<i>1600</i>	<i>2000</i>	<i>590</i>
<b>Ind. ufg-Ni</b>	78	645	803	219
<b>Brass</b>	92	410	510	156
	<i>96</i>	-	<i>&gt;470</i>	<i>159</i>
<b>Maraging steel</b>	188	1924	1983	598
(Durnico)	<i>195</i>	<i>1800-2100</i>	<i>1800-2100</i>	<i>500-600</i>
<b>Silicon (DRIE)</b>	171	-	-	-
(⟨110⟩-direction)	<i>170</i>	-	-	-

used here, this would explain the lower values obtained here. On the other hand, variations on modulus values in the order of 10% are in an acceptable range and here the variation is less than that. Although the rolled sheet metal specimens have grain sizes in the order of  $> 1\mu m$ , and therefore the number of grains in a specimen cross section is considerably smaller than in large bulk specimen, the results obtained in this study are fairly consistent. This suggests that the mechanical properties of these specimen do not change from bulk down to the tested size regime of this study. However what may have a significant influence, at least on the Young's modulus which is together with the yield strength the most important design parameters for watchparts, is the rolling texture of the sheet metal. All specimen tested here were cut parallel to the rolling texture of the metal sheets. It is therefore suggested to look into these textural effects by preparing and measuring specimen which have been cut perpendicular to the rolling direction.

### 7.3.2. Micro four point bend tests

Although tensile tests are representative for comparing mechanical properties of microcomponents, most watch components are not exposed to uniaxial tensile load. A much more common load case in actual applications is in-plane bending since many watch components have to fulfill a spring function. Our approach to assess these is

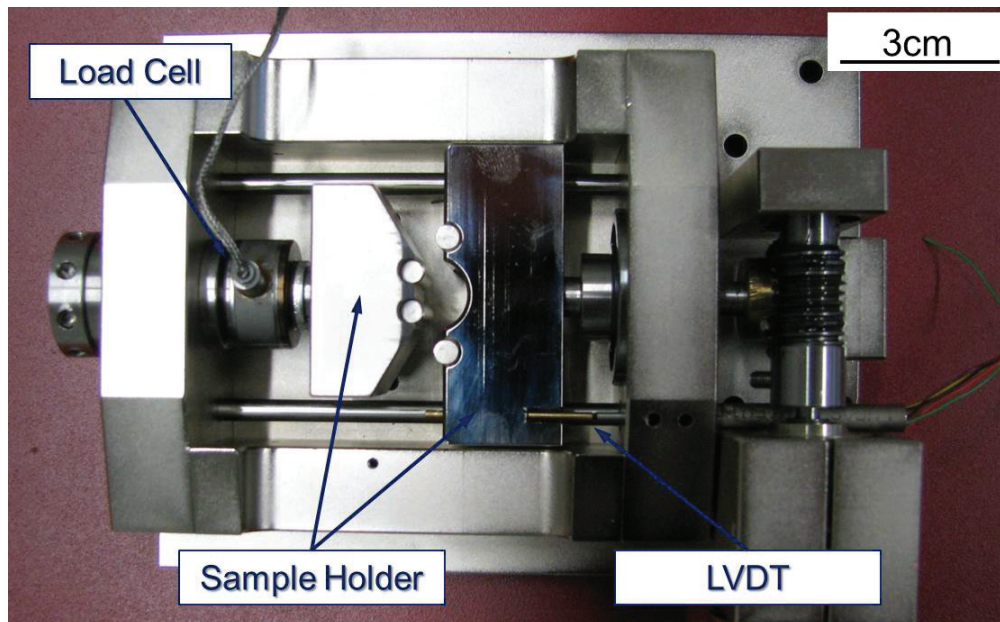
Table 7.2.: Mechanical properties of watchmaking alloys, assessed with four point bending tests. The italicized values are taken from supplier references if available.

<b>Material</b>	Flexural modulus <i>in plane</i> [GPa]	Flexural modulus <i>out of plane</i> [GPa]	Flexural modulus <i>reference values</i> [GPa]
<b>Ind. ref. Ni</b> (as deposited)	181	109	<i>155</i>
<b>Ind. ref. Ni</b> (heat treated)	187	101	
<b>Brass</b>	90	96	–
<b>Maraging steel</b> (Durnico)	192	211	–

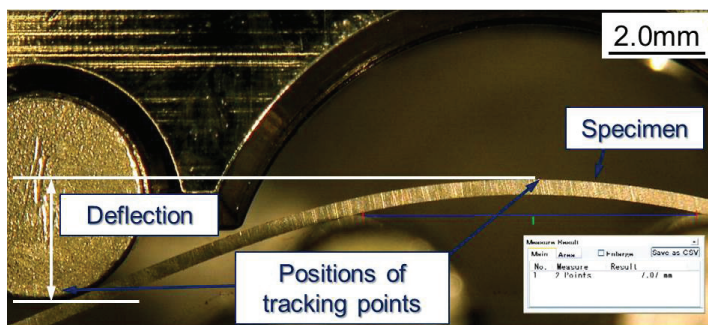
to perform micro scale four point bend tests on a suitable testing device. Based on the experience with the microtensile testing setup, a commercial Kammrath&Weiss bend tester was heavily modified. The basic setup is very similar to the tensile device described in Section 4.7, but it allows insertion of dedicated three- or four point bending chucks. A 150N load cell was installed as the expected loads in bending are considerably lower than in tension. Figure 7.7 (a) shows the device and its components. Figure 7.7 (b) was captured in situ with the digital microscope whereas Figure 7.7 (c) shows various bend test specimen before and after the tests. Table 7.2 compares the results obtained from the four point bend tests.

The only available supplier data on flexural moduli was denoted to  $155GPa$  for the nanocrystalline industrial reference nickel. Our in plane bend tests revealed mean values of  $E_{Ni flex, inplane} = 181GPa$  which are  $\sim 20\%$  higher then the given supplier values. Although modulus deviations in the order of 10% if measured by mechanical means can be expected, the difference in the presented case is already significant. Compared to the out of plane tests, where the results are  $E_{Ni flex, outofplane} = 109GPa$ , there is an even larger difference. Unfortunately, the supplier does not provide any details on the applied test procedure or the boundary conditions of the tests. From our side we are convinced that the results obtained from our tests are true for the following two reasons: first we already validated the performance of our DIC strain measurement for the tensile tests with standard materials and do not expect this not to perform differently in bending. Secondly, if we measure standard materials in bending mode, i.e. silicon with known orientations we obtain results that correspond to the literature for these materials. Further, our (in-plane) results fit well to simulated performance data the watch manufacturers

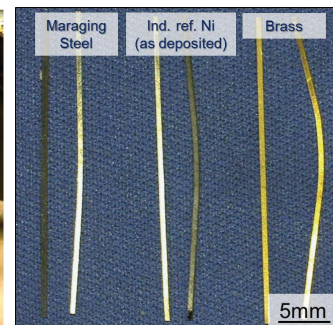




(a)



(b)



(c)

Figure 7.7.: (a) Modified micro-bend test device with four point bending chucks. (b) In situ image of a maraging steel specimen during a test. (c) Bend test specimen from watchmaking alloys, manufactured by EDM or electrodeposition.

use to design their components. Possible explanations for the difference between supplier values and the measured values from this study are various and speculative. One possibility is that during the commercialization and heavy modification process of the electrochemical bath impurities or textural changes have influenced the values after they have been proposed. They may also vary from batch to batch as different LiGA-mold designs yield different current densities which has a strong influence on the flexural properties. However, this question cannot be answered in the framework of this case study. Interestingly, the sheet metal specimen did not show any significant differences in flexural modulus, independently of in- or out of plane test direction which may be due to their not very strongly pronounced rolling texture.

#### **7.4. Development of nickel-tungsten alloys for watch components**

As already motivated in the introduction to this Chapter, the aim is to alloy electrodeposited nickel with refractory metals to improve the mechanical properties and thermal stability. The pronounced time-dependent plastic behavior of nanocrystalline metals (strain rate sensitivity, load relaxation, creep) is mostly dominated by grain boundary-mediated, diffusional plasticity [146] (see also Section 5 for details). Hence, slowly diffusing and thermally stable refractory metals (W, Mo, Ta, Re or Nb) can assist in suppressing the grain boundary diffusivity and reduce grain boundary volume by slightly increasing the mean grain size of the material.

Electrodeposits consisting of nickel and tungsten have already been a topic in number of studies as they combine improved thermal stability with preferable mechanical properties. The focus of these studies was mainly on the achievement of thin deposits  $< 10\mu m$  with a high tungsten content. Normally tungsten is a grain refiner, and smaller grains increase the materials hardness/strength due to the Hall-Petch effect [37, 38]. However, the grain refinement increases the grain boundary volume fraction. This influences the electrodeposition of thick films, since the films are highly stressed (mostly tension) and delaminate from the substrate. Although not fully understood, it is likely that the increased excess volume (vacancies/voids) that sits on the grain boundaries in the as deposited state of a laminate causes such stresses. Hence, the smaller the grain size, the larger the stress gradients become. For LiGA-applications, even though they are not as sensitive to internal stresses as free standing laminates due to the confined connected volumes of material, good adhesion and low internal stresses are still key parameters to achieve reasonable mi-

crocomponents from this technique. Thus we conducted this property optimization study with respect to performance expectations of an industrial deposition process: low residual stress, low W-content, grain size as small as possible for high strength but large enough to decrease grain boundary diffusivity. In case of this study which was part of a CTI-project in collaboration with a Swiss watch manufacturer another important material property is the texture of the deposits as these influence the Young's modulus. Hence we focus on the microstructural, textural and compositional stability of NiW electrodeposits with varying tungsten content up to 5at.-%. In Chapter 4.2 the electrochemical process is described. The variations in tungsten content were achieved by systematically changing the pulse-deposition conditions. The microstructural changes were investigated as a function of deposition parameters and composition.

#### 7.4.1. Microstructural characterization

Electrodeposition is a non-equilibrium process which often leads to the formation of defects or locally changed microstructure. While high resolution techniques like TEM provide detailed information about micro-/nanostructure features but only on a small and localized volume of material, XRD can access a much larger volume of material but the reliability of results strongly depends on the morphology of the microstructure. Consequently, both techniques as standalone methods do not provide reliable information about the overall structure of electrodeposits. To get an idea of the overall uniformity of the NiW-deposits we utilized FIB-imaging in this study, over large  $15\mu\text{m} \times 15\mu\text{m}$  cross sections.

Figure 7.8 shows the cross-sectional FIB images of NiW electrodeposits as a function of W content. The microstructure of the films was found to be strongly dependent on the W content but less on the electrodeposition parameters. From the bath without tungstate ions, Ni electrodeposit consists of uniformly distributed nanocrystalline microstructure (Figure 7.8 (a)). The surface of the deposit is very rough; many micrometer-sized nodules were observed on the surface. On the other hand, in case of NiW films, the surface is covered with sub-micrometer roughness even at concentration as low as 0.5at.-%. As seen in the FIB image (Figure 7.8 (b)), fiber-like, heterogeneous large grains were observed among nanocrystalline grains. This indicates a significant change in the film growth mechanism on addition of W. Similar microstructure was observed for all NiW samples with a W content up to 4at.-% (Figure 7.8 (c,d)). Further increase in W content results in a significant reduction in the size of heterogeneous large grains (Figure 7.8 (e)). At W content

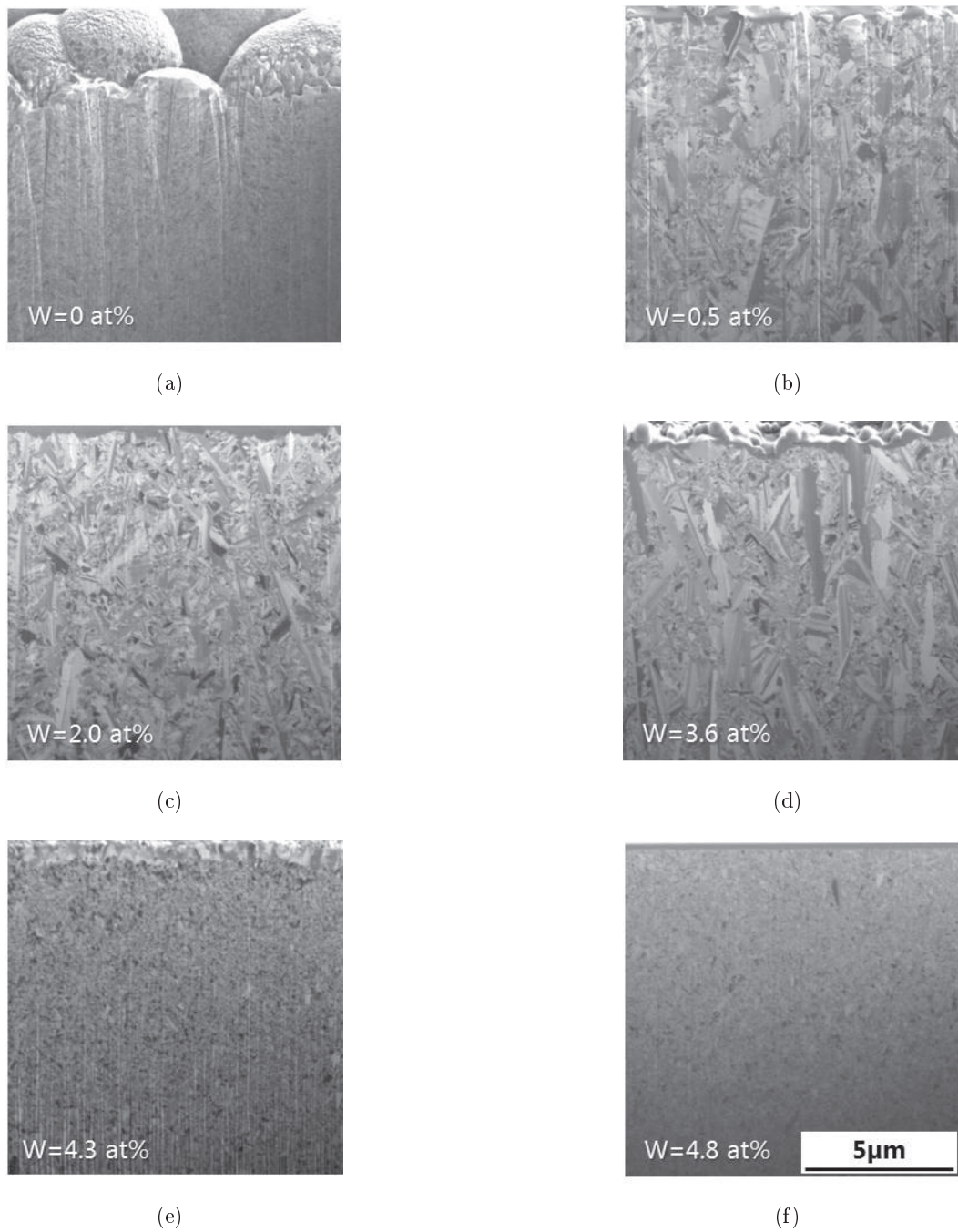


Figure 7.8.: Cross-sectional FIB images of NiW electrodeposits with different compositions. NiW deposits were prepared at mean current densities of  $J = -10\text{mA}/\text{cm}^2$  (a-e), and  $-15\text{mA}/\text{cm}^2$  (f) in the ammoniacal citrate baths containing 0 – 20g/L of W.

of 4.3at. – %, a significant decrease in the size and number of large grains is seen, while an increase in the volume fraction of nanocrystalline grains is observed (Figure 7.8 (e)). Finally, at 4.8at. – %, the deposit becomes almost completely nanocrystalline (Figure 7.8 (f)). This transitions from nanocrystalline grains (pure Ni) to heterogenous, nanotwinned grains (NiW from 0.5 to 4at. – % W content) and back to nanocrystalline microstructure (W content greater than 4.3at. – %) suggests two distinct growth mechanisms in this range of W concentration.

A possible interpretation of these findings is the existence of two competitive effects of W on Ni-alloy: the promotion of nanotwinned structures and the grain refinement. It has been reported previously that W addition significantly decreases the stacking fault energy of Ni [187]. This means that twins can be more easily formed in Ni-W than in pure Ni. In addition to this, application of pulse plating may also contribute to the formation of twinned grains. Reports exist on the formation of dense nanotwins in Cu by pulse plating [188, 189, 190]. During electrodeposition, the introduction of the „off-time“ induces the rearrangement of metal atoms to the energetically more stable state. In fact, the rough top surface of nt-NiW with sharp edges of needle like nt-grains are similar to that of nt-Cu from Hasegawa et al. [189], where the twins are oriented in the vertical direction to the growth surface. This indicates that nt-grains in NiW are formed by the mechanism similar to those in vertically nt-Cu. On the other hand, W is also known to restrict Ni grain growth, which in turn results in a decrease in grain size of films. Therefore the composition dependent change in microstructure can be explained by the balance of a change in stacking fault energy and the restriction of grain growth.

According to Tiarney et al. [191] the stacking fault energy decreases drastically with an increase of W content in the range between 0 to 2at. – %. Beyond this, the decrease rate in stacking fault energy of Ni is reduced. On the other hand, the growth restriction parameter increases proportionally up to the limiting solubility of the solute. Hence, when the W content is low (i.e. less than 4at. – %), nanotwinned NiW is formed because the inclusion of W affects the stacking fault energy of the film. However, the content is not sufficiently high to induce grain refinement. Traces of grain refinement were found in terms of small regions with nanocrystalline microstructure. However, when the W content is further increased, the grain refinement effect of W becomes more significant than twin formation, and the film becomes fully nanocrystalline.

Table 7.3.: Young's modulus and hardness of nanostructured Ni and NiW deposits.

Material	W content [at.-%]	Grain size [nm]	Young's modulus [GPa]	Hardness [GPa]
nc. Ni	0	46	187	5.45
nt. NiW	3.6	–	191	4.71
nc. NiW	4.8	21	199	6.43

#### 7.4.2. Indentation results

The same in situ indentation system as described in Section 5.2, equipped with a Berkovich diamond tip, was used for the indentation experiments. A proportional loading with  $\dot{P}/P = 0.03s^{-1}$  was applied to ensure a constant strain rate. Thermal drift was measured at 5% of maximum load during the unloading sequence. The maximum applied load was  $450mN$  in all cases [154]. The CSM method [153] as described in Section 5.2.2 was used since it allows to measure the mechanical properties as a function of the penetration depth. Hardness and indentation modulus were calculated using the Oliver and Pharr method [154].

Indentation hardness and modulus data are listed in Table 7.3 for comparison. A Poisson's ratio of  $\nu = 0.3$  was used for calculating the indentation modulus, which is approximately the same for all the three samples. This suggests that tungsten content has almost no influence on the modulus of the material. However, indentation testing is not very sensitive to changes in texture, which can have a major influence on the Young's modulus. In terms of the hardness, nc-NiW shows hardness superior to that of nc-Ni. According to Schuh [99], the contribution of solid solution strengthening is proportional to square root of the atomic concentration of W. This is estimated to be only  $\sim 40MPa$  even for a NiW alloy with W content of  $14.1at\%$ . This suggests that the solid solution strengthening is negligible for nc-NiW samples in this study, and that the hardening of nc-NiW is simply due to the refined grain size.

#### 7.4.3. Thermal stability

The thermal stability of the microstructure is of interest for practical applications as well as for assessing the potential improvement of time-dependent deformation properties. In order to study this aspect, we performed a series of thermal treatment experiments. In order to assure that the microstructural changes are purely from thermal treatment and not from sample variation, one sample of each condition was diced into several pieces. The pieces were annealed at different temperatures, and

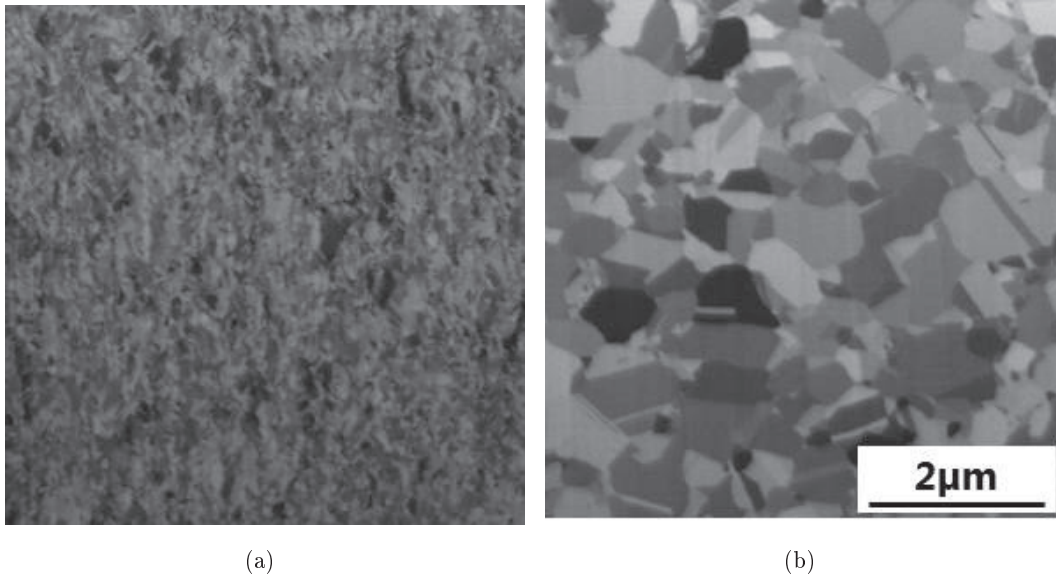


Figure 7.9.: Ion channeling contrast images of ncNi-nanostructure (industrial reference) in as deposited condition (a) and after thermal treatment at 250°C for 2 hours (b).

the microstructure of samples was investigated qualitatively by cross-sectional FIB observation and quantitatively by XRD measurements during heat treatment process up to 440°C, as described in detail in Section 6.2.2. For comparative reasons, the thermal behavior of industrial reference type nc-Ni was investigated first. Figure 7.9 (a) shows a cross sectional FIB image of nanocrystalline nickel in the as deposited condition. The mean grain size is approximately 46nm. After increasing the temperature up to 250°C for two hours, the nanostructure presents significant grain growth as can be seen in Figure 7.9 (b).

In contrast, Figure 7.10 shows the microstructural evolution of nc-NiW film with a W content of 4.8at% annealed at different temperatures. Qualitatively it was not possible to observe any visible changes in microstructure upon thermal treatment up to 350°C. The nanostructure visibly changed only after annealing at 400°C and higher. It is worth noting that the grain size after annealing at 450°C still remained much smaller than those of nc-Ni annealed at 250°C. These thermal treatment experiments clearly demonstrate that the grain boundaries in nc-NiW are much more stable than in nc-Ni.

Figure 7.11 shows the results of the XRD measurements for nanocrystalline nickel and nickel tungsten (4.8at. – %W). It should be noted that the grain size values in the curves have been normalized with respect to the initial grain sizes of each sample

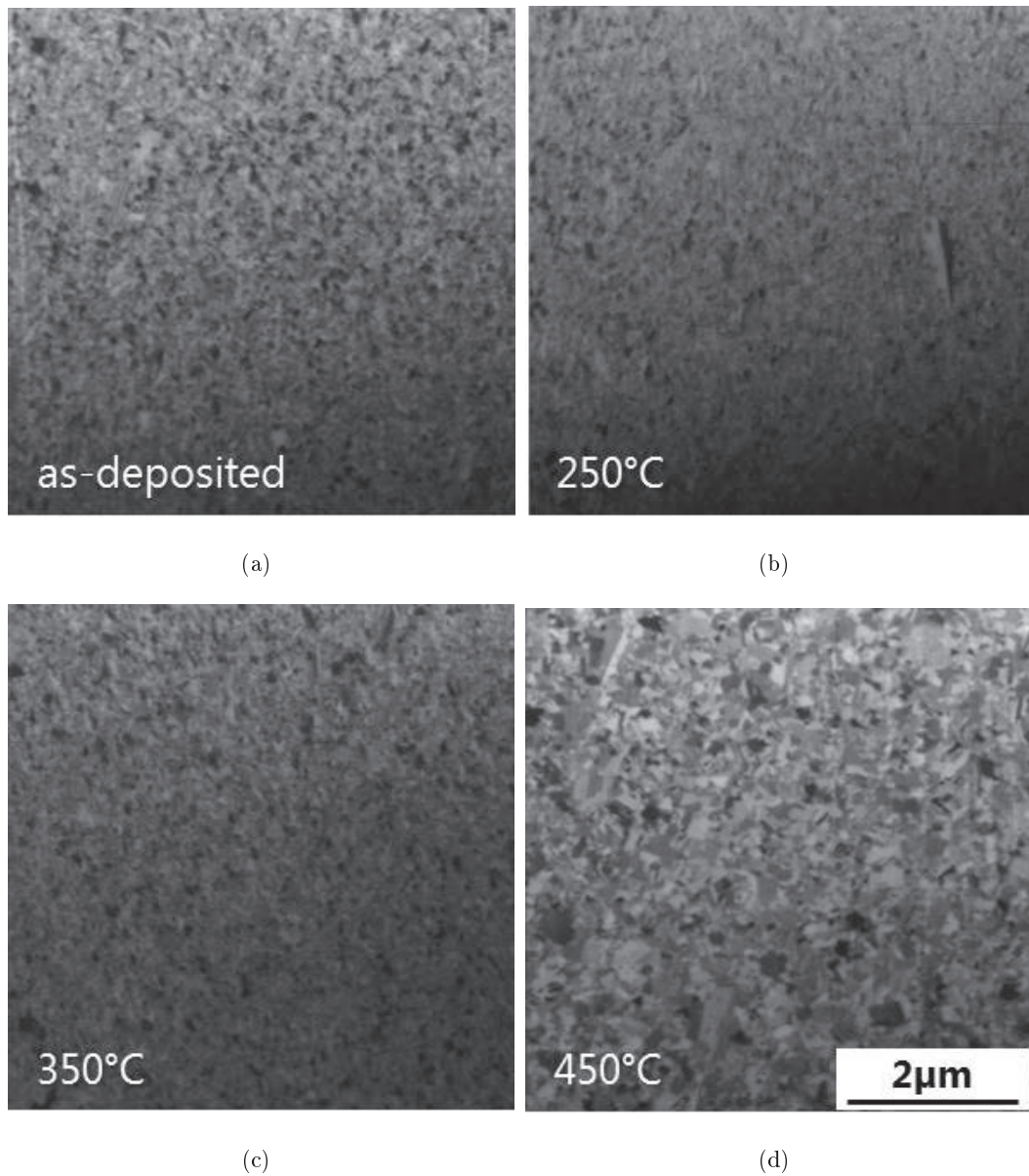


Figure 7.10.: Ion channeling contrast images of NiW-nanostructure (4.8at.-%W) in different states of thermal treatment (2 hour hold period). (a) as deposited (b) 250°C, (c) 350°C and 450°C.



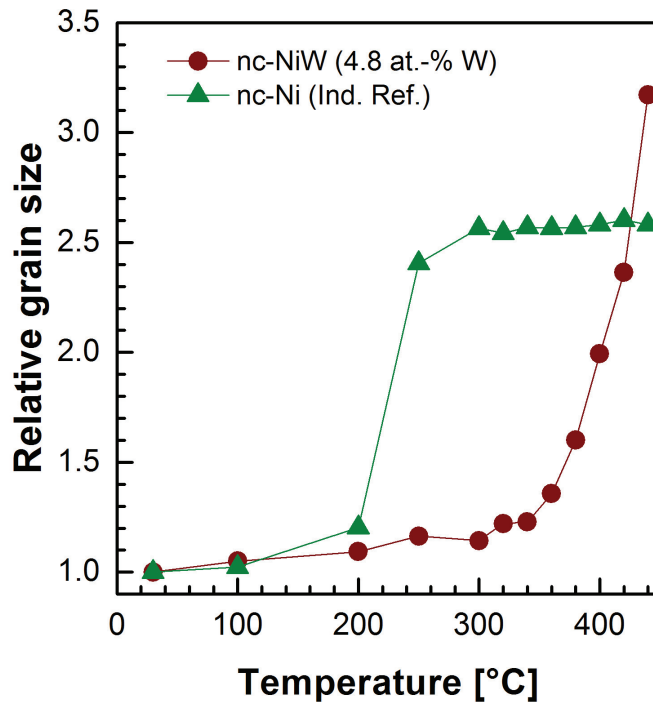


Figure 7.11.: Grain growth behavior during heat treatment. The temperatures were held constant for 2 hours at each step. Comparison of nc-NiW (4.8 at% W) and nc-Ni (Industrial reference).

in as deposited condition. The mean grain size values are listed in Table 7.3. The curves indicate that around a temperature of 200-220°C the nanostructures of both specimen start to change. For „pure“ nanocrystalline nickel the change is much more pronounced. Whereas, in the case of NiW, the changes in nanostructure are much more subtle up to at least 350°C. After that threshold, the nanostructure starts to grow slowly as well. These results correspond well to the crosssectional images (Figure 7.9 and 7.10). The results suggest an improvement of grain boundary stability due to the addition of W to Ni.

#### 7.4.4. Texture analysis

The micro structure was analyzed by means of XRD (BRUKER Discover D8, Bruker GmbH, Karlsruhe, Germany) with Cu-K $\alpha$  radiation at 40kV/40mA. The texture

coefficient is defined after Harris [192] as:

$$TC_{hkl} = \frac{I_{hkl}/I_{0,hkl}}{(1/n) \sum I_{hkl}/I_{0,hkl}} \quad (7.1)$$

, where  $I_{hkl}$  is the relative peak intensity from  $hkl$  reflection of the sample,  $I_{0,hkl}$  is that of randomly-oriented reference powder and  $n$  is the number of reflections [192]. For this study,  $\{111\}$ ,  $\{200\}$ ,  $\{220\}$ , and  $\{311\}$  reflections were used to calculate  $TC$  ( $n = 4$ ). Equation 7.1 shows that a  $TC_{hkl}$  equal to one means a random orientation distribution, while for preferred orientation,  $TC_{hkl}$  would deviate from one. A  $TC_{hkl}$  equal to four would mean a perfectly textured sample.

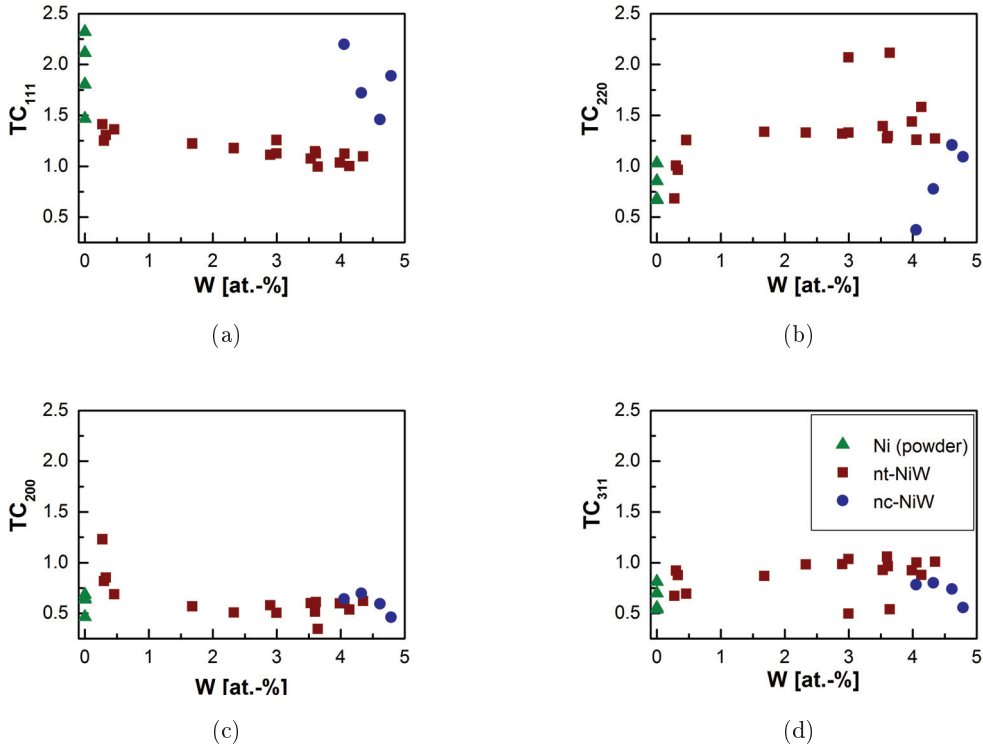


Figure 7.12.: Texture coefficients for (a)  $\{111\}$ , (b)  $\{200\}$ , (c)  $\{220\}$  and (d)  $\{311\}$  reflections of Ni and NiW alloy electrodeposits.

Figure 7.12 shows the calculated  $TC$  of Ni and NiW samples plotted as the function of W content. Pure Ni (triangle) shows higher  $TC$  for  $\{111\}$  than  $TC$ s for other texture, indicating that the deposit is  $\langle 111 \rangle$  textured, although the  $TC$  values show some scatter. For nanotwinned NiW films (squares), the  $TC_{111}$  is lower and  $TC_{220}$  is higher than in case of the Ni samples. This shows that the deposits structure

is more randomly oriented. As is also seen in the plot, all nt-NiW samples show similar *TCs* regardless of their W content. This is consistent with the fact that the microstructure of nt-NiW films with different W contents is similar to each other. A significant texture change was observed between nt-NiW and nc-NiW samples. The texture of nc-NiW films is  $\langle 111 \rangle$  similar to that for nc-Ni films. As was described earlier, nt-NiW samples consist of micron-sized nanotwinned grains interspersed within nanocrystalline grains. By comparing the texture and microstructure, it is speculated that nanocrystalline region is  $\langle 111 \rangle$  textured similarly to the nc-Ni and nc-NiW. The increase in polycrystalline nature of nt-NiW is associated with the random growth of nanotwinned grains.

Higher tungsten concentrations generally increase the Young's modulus in proportion to the W-concentration [193, 194] for polycrystalline bulk alloys. However, in the present case, even for the NiW alloy with the highest W-concentration (4.8at. – %), the theoretical modulus increase due to solid solution of W<sup>†</sup> is in the order of  $\sim 10GPa$ , which is rather small compared to the absolute modulus of the nanocrystalline material. However, as the textures of the three films are similar and the overall tungsten content is comparably low, the modulus values as assessed by nanoindentation (see previous Section) are not expected to change to a large extent in the investigated tungsten concentration regime.

#### 7.4.5. Discussion of NiW results

##### Electrodeposition and microstructure

The electrodeposition of NiW alloys exhibits microstructural transformation from nanocrystalline to nano-twinned, and further back to nanocrystalline microstructure with an increase of W content from 0at. – % to 5at. – %. The critical W content to obtain a nanocrystalline NiW film is around 4at. – %. Below this value, a film with a bimodal grain structure, consisting of randomly oriented nanotwinned micrometer grains and nanocrystalline grains was obtained, regardless of the deposition condition.

Numerous electrolyte compositions and bath parameters were tested in this study. Hence, the amount of deposited samples in the alloy development process is rather large ( $\sim 130$  samples). In a first approach, stable deposition conditions are established for the deposition of thin films on silicon wafer pieces with average dimensions of 20mm by 20mm. Once desired film properties are achieved, the next step is to

---

<sup>†</sup>Young's modulus of polycrystalline tungsten is 402GPa [195]

upscale the process to deposit thick films in LiGA-molds (see Section 4.1.2) which again requires numerous deposition runs to achieve components of desired quality with reproducible properties. Hence, with respect to the time frame of this work, only few LiGA-micro tensile specimens with selected W-contents of 3 to 4.8at. – % were produced and tested up to date. Up-scaling this process and producing larger amounts of thick LiGA-components to perform mechanical „micro-bulk“ tests in an extensive manner (micro-tensile and micropillar compression) is the next major task. Also, investigating the mechanical properties of the nanotwinned specimen with respect to active deformation mechanisms is an interesting task as pertinent literature predicts enhanced microstructural properties of nanotwinned copper and copper alloys [168, 33, 161, 32, 196].

### Thermal stability

Diffusive mechanisms along grain boundaries contribute to the enhanced plastic deformation of electrochemically pure nanocrystalline nickel significantly, which limits its application for micromechanical components. In watch movements, where moving parts are required to store energy under compressive/contact stresses, diffusion-based and strongly time-dependent plastic behavior are features that prevent the employment of nanocrystalline metals. As such, the core idea behind alloying nickel with the refractory metal tungsten was to improve the thermal stability of the material by hindering diffusive processes along grain boundaries, which will improve time-dependent mechanical properties (stress relaxation, creep). An indicator for the diffusivity in nanocrystalline metals is the propensity for grain growth. In Figure 7.11, the grain growth of nanocrystalline nickel is compared to the NiW-alloy with a tungsten content of 4.8at. – % by means of in situ XRD measurements. The nanostructure of pure nickel (green curve) is stable up to a temperature slightly above 200°C, and the nanograins start to grow significantly when this threshold temperature is exceeded. In contrast, the nanocrystalline structure of NiW (brown curve) is retained up to approximately 350°C before slight grain growth is observed. Comparative microstructural images are shown in Figure 7.9 (a-b) and Figure 7.10 (a-d) for nanocrystalline nickel and nickel-tungsten, respectively, which agree with the XRD observations. From a perspective of temperature alone, this marks an improvement of > 50%. Hence, these results are promising as they are a qualitative measure of the enhanced thermal stability of nanocrystalline NiW alloys.

### Mechanical properties and comparison to nanocrystalline nickel

To accelerate the mechanical characterization during the alloy development process nanoindentation measurements were performed on selected deposits. These measurements showed that the mechanical properties heavily depend on the microstructure. The strength increase of NiW in the nanocrystalline regime is primarily assigned to the nanostructural refinement, as discussed in Section 3.1.2, since tungsten acts as a grain refiner and the influence of solute atoms on strength is less pronounced in electrodeposits. If the obtained hardness values from the indentation measurements are converted into yield strength, ( $H = \sigma_y \cdot 2.8$ ), the results for „pure“ nickel are around  $\sigma_{y,Ni} = 1.98GPa$ . This is in good agreement with previously measured results from micropillar compression tests on industrial, reference grade nickel with similar grain size. Applying the same calculation for Ni4.8at. – %W results in slightly higher yield stresses of  $\sigma_{y,NiW} = 2.3GPa$ , but at a much smaller grain size. As already mentioned in the previous subsection, the Young’s moduli of the NiW alloys were not significantly higher than for pure nanocrystalline nickel. This can be assigned to the overall low tungsten concentration in the deposits as well as the identical texture. Nevertheless, although not much improved, the values are in the same order as those for industrial reference grade nickel, which is acceptable for applications in a watch as they are similar to maraging steel.

For the assessment of time-dependent plastic behavior, it was attempted to deposit one batch with sufficiently thick Ni4.8at. – %W specimen. Although the deposition parameters were not yet optimized for the LiGA-process, a total number of two freestanding micro tensile specimen with total thickness of  $100\mu m$  were extracted from the mask. One of the specimen was kept in as deposited condition, whereas the second specimen was subjected to a heat treatment at  $350^\circ C$  for two hours in order to thermally relax the grain boundaries without changing the microstructure, similar to the commercially available industrial reference nickel. The specimen were then tested along with commercially available nickel reference specimen and maraging steel specimen which were cut from rolled sheets. Figure 7.3 (a) shows the results of the measurements. The blue curves were obtained from nanocrystalline nickel in as deposited (blue curve) and heat treated (blue dotted curve) condition. Comparing these two curves to the respective green curves obtained from NiW, it can be seen that the relaxation behavior of the NiW-alloy is significantly improved. In the as deposited condition, the total amount of relaxation over 15 hours is in the order of 11% vs. 23% for pure nanocrystalline nickel. After the two materials received a thermal treatment, the relaxation properties of both were significantly improved.

In case of NiW, the total amount of relaxation after 15 hours is less than 2.5%, which is very similar to polycrystalline maraging steel (red curve), while the load in nanocrystalline nickel still relaxes approximately 7.5%. Extrapolating these results with respect to the logarithmic decay function, a stress level below the elastic limit results into Figure 7.3 (b). The average relaxation level of NiW is much lower than for nanocrystalline nickel, and the more shallow slope of the NiW-curve clearly indicates its slower relaxation. These results are only preliminary, and a thorough optimization of deposition parameters with respect to the LiGA-process needs to be conducted before further mechanical tests are feasible. However the results are encouraging as they clearly show that alloying nickel with tungsten influences the (time dependent) mechanical behavior into the desired direction. Hence, it is thought that in the near future, well-characterized NiW-alloy microcomponents can be utilized in watch movements.

---

## 8. Summary and outlook

The presented thesis provides two core contributions to the scientific community: the development of novel in situ transient techniques for mechanical property assessment on nanostructured materials and extended insights into deformation mechanisms under a variety of boundary conditions (temperature, time, stress, strain, strain rate). As nanostructured materials are usually not available in bulk quantities the measurement techniques were specifically developed to be applied on thin film materials. In this context micropillars were considered to be the favorable specimen type as uniaxial compression-based measurements provided a comparably simple and straightforward interpretation of experimental data. Focused ion beam milling was utilized as a key manufacturing method, which allowed to manufacture homogeneously shaped micropillar specimen with excellent geometric fidelity over a wide span of diameters that could be adjusted to the materials external and internal length scales. Further the combination of micropillar specimen and the high lateral resolution of the utilized Alemnis indentation system allowed to conduct site specific, precisely-localized measurements. Performing the measurements in the protected environment of a SEM prevented the influence of disturbing ex situ effects and specimen oxidation during elevated temperature tests. Further the continuous observation of specimen deformation was found to assist in the interpretation of experimental data. Although the presented results were mostly conducted on nanocrystalline nickel, it should be mentioned that the methods can be utilized for any type of nanostructured or amorphous materials like CVD/PVD multilayers, nanotwinned thin films or with some restrictions to specimen size even ufg-materials and single crystals. The following sections briefly summarize the presented methods and results with respect to scientific and industrial interest and give an outlook to possible future tasks.

### 8.1. Experimental small scale in situ techniques to assess plasticity mechanisms in nanocrystalline metals

A novel micropillar transient test technique - elevated temperature, strain rate jump (SRJ) tests - was successfully demonstrated on the Alemnis high temperature in-

dentation system. The investigated material was nanocrystalline nickel which was synthesized at Empa. In this particular test, the specimen were first subjected to a deformation at constant strain rates until the materials elastic limit was exceeded. As soon as the flow stress level had stabilized the strain rate was changed instantaneously over several orders of magnitude and the materials flow stress response was monitored. These „jumps“ were sequentially repeated. The SRJ curves allowed to extract the strain rate sensitivity (SRS) exponent,  $m$ , as well as the apparent activation volume,  $V_{app}$ . Both measures are indicative for the activated deformation mechanisms in the materials. The high temperature capability of the Alemnis indenter allowed the tests to be performed at elevated temperatures, which enabled the study of the evolution of activation parameters as a function of temperature and the extraction of the apparent activation energy,  $Q$  from SRJ.

Mechanical properties of nanocrystalline materials are known to be highly sensitive to nanostructural and compositional inhomogeneities and the way how they have been produced. Further, these materials are rarely available in bulk quantities which prevents the applicability of traditional bulk mechanical tests. Due to that mechanical properties reported for nanocrystalline metals are hard to compare amongst different studies and it was difficult to find suitable reference values. Hence, to assess and validate the utility of the micropillar compression strain rate jump tests, a follow up study was conducted which compared these newly developed elevated temperature micropillar SRJ to strain rate jump tests by means of more established techniques: nanoindentation and tensile tests. Here the approach to enable a direct comparability of results was to conduct all measurements on the same specimen from the same batch of materials at room temperature. This study also enabled a direct comparison of the effects of three different loading cases: uniaxial tension, uniaxial compression and hydrostatic compression. Accordingly, LiGA micro tensile specimen were synthesized and first tested on the miniaturized tensile setup with the previously introduced protocol. Afterward, postmortem microcompression and nanoindentation strain rate jump tests were conducted on the undeformed gripping sections of the tensile bars. Again the SRS exponent,  $m$ , and the apparent activation volumes,  $V_{app}$ , were successfully extracted.

The strongly time-dependent plastic behavior of nanocrystalline metals also manifests in susceptibility to creep and stress relaxation, even at room temperature. In addition, time dependent deformation is an important criterion for designing micro-components made of nanocrystalline materials as both, creep and stress relaxation contribute in a convoluted manner towards failure under contact stresses. Apart from the engineering aspect, time-dependent studies provide fundamental insights



into the rate controlling deformation mechanism(s) in these materials. A micropillar stress relaxation technique was developed to assess the time dependence of plasticity mechanisms on short time scales ( $< 1h$ ). In a single relaxation test, the load was monitored as the material was subjected to a certain displacement. At a desired point, the displacement was stopped, and the load decrease due to quasielastic recovery was monitored. From the analysis of a single load drop over time, the apparent activation volumes were extracted. However, over the the long relaxation segment duration under high stresses, an evolution of the nanostructure was possible which would have influenced this measure. To circumvent this, another novel micropillar technique, repeated/transient relaxation tests, were introduced where the specimen basically was subjected to a fast, quasi elastic reloading. Over the fast transient, the microstructural change was assumed to be negligible, which enabled the extraction of an effective activation volume. The measurements were also conducted under uniaxial tension on micro tensile specimen with good agreement between the two methods.

## 8.2. Observed deformation mechanisms in nanocrystalline metals

### Electrodeposited nanocrystalline nickel

The mechanical properties of nanocrystalline metals were known to be highly dependent on strain rate and temperature. To gain insight into the nature of the rate controlling deformation mechanisms with respect to temperature and time, a novel elevated temperature micropillar strain rate jump tests protocol was established and first demonstrated on nanocrystalline nickel. The test protocol allowed the extraction of various activation parameters which were indicative of the activated plasticity mechanisms in the selected temperature interval. From the individual „jumps“, the strain rate sensitivity (SRS) exponent,  $m$ , which was the measure of the dependence of change in flow stress,  $\sigma$ , as a function of change in applied strain rate,  $\dot{\epsilon}$ , has been extracted. The obtained values were  $m \sim 0.02$ . Similar values measured by bulk- or nanoindentation tests on nanocrystalline nickel were found in literature. The apparent activation volume,  $V_{app}$ , was also extracted from SRJ.  $V_{app}$  is directly related to plastic deformation and often used to obtain an idea of the governing rate controlling mechanism(s). The obtained values which were around  $\sim 13b^3$  were found to be consistent with literature results for nanocrystalline electrodeposited nickel. In this size regime of  $V_{app}$ , strongly pronounced dislocation-dislocation interactions

were unlikely as they usually required much larger values ( $> 1000b^3$ ). Purely diffusion based mechanisms on the other hand generally required much smaller values ( $< 1b^3$ ). Hence,  $V_{app}$  as a standalone measure was not sufficient to identify a particular mechanism, although values around  $\sim 10b^3$  indicate the decreased dominance of dislocation mediated plasticity. Due to grain size variations in electrodeposited nanocrystalline nickel, it was plausible that both of these mechanisms were simultaneously operative. An advantage of the elevated temperature measurements was that the apparent activation energy of deformation could be extracted. The obtained value,  $Q = 92kJ/mol$ , matched well with grain boundary diffusion activation energy for nickel suggesting it to be the rate controlling deformation mechanism. High resolution SEM images of the deformed pillars confirmed extensive grain boundary sliding and rotation to accommodate the plastic strain. However, slip traces were also observed in case of large grains as a result of the comparably wide grain size distribution in nanocrystalline electrodeposits. Nevertheless, the obtained results gave a strong indication for grain boundary mediated plasticity in nanocrystalline metals.

To compare the results obtained by elevated temperature micropillar strain rate jump tests against more conventional SRJ techniques (tension, nanoindentation), three different series of room temperature SRJ tests were conducted on the same nanocrystalline nickel specimen in order to study the comparability and consistency of the test results. The extracted SRS exponents,  $m \sim 0.02$  and apparent activation volumes,  $V_{app} \sim 10b^3$  from these three methods were found to be in excellent agreement within this study, as well as with the previously obtained results. This suggested that the rate controlling deformation mechanism(s) were apparently the same for all three loading cases. Post compression analysis of the nanocrystalline nickel micropillars by means of high resolution SEM confirmed the same surface features as previously observed by the elevated temperature tests. In contrast, the SRS results obtained from microcompression of single crystal nickel showed much lower strain rate sensitivity and considerably larger apparent activation volumes ( $V_{App,sx-Ni} \sim 350b^3$ ), which was indicative of significant dislocation-dislocation interactions in these pillars. This was also confirmed by the observation of multiple discrete slip steps, traversing the entire pillar diameter. The results obtained from this direct comparison suggested that the compared techniques were eligible to be reliably and interchangeably used to accurately measure strain rate sensitivity in a wide variety of materials. For materials with mechanical anisotropy, such as crystallographic texture, it was suggested that nanoindentation techniques may underestimate the magnitude of the anisotropy, and alternative techniques as tension and

microcompression were favored.

To estimate the strongly time-dependent plastic behaviour of nanocrystalline metals, microcompression stress relaxation experiments at room temperature were successfully performed on nano-crystalline nickel sample. The results were directly compared with bulk tensile relaxation measurements from the same batch of material. The activation volume for time-dependent plasticity provided an indication of the operative mechanism during a load relaxation segment. The apparent activation volume,  $V_{app}$ , was determined for each segment by fitting the experimental data to a logarithmic decay function while the effective activation volume,  $V_{eff}$ , was determined based on the jumps between relaxation segments.  $V_{app}$  showed a strong strain dependence in the low strain regime, transitioning from  $\sim 30 - 40b^3$  at  $\sim 1\%$  strain to values of  $11 - 13b^3$  at  $\sim 4\%$  strain. In spite of this sharp transition,  $V_{app}$  became remarkably stable at strains in excess of  $8\%$ , always producing values of  $\sim 7b^3$ . In contrast,  $V_{eff}$  showed little or no strain dependence over the entire range of strain, yielding almost constant values of  $\sim 7b^3$ . A possible interpretation of the constant  $V_{eff}$  values was that the fundamental deformation mechanism did not change significantly over the entire range of strains. The elevated apparent activation volumes at small strains were believed to be an artifact induced by the evolving microstructure. At such low strains the deformation microstructure (e.g. dislocation content) was not fully established yet and evolved rapidly during the relaxation segment. At higher strains, more sources have become activated, more dislocations were present and therefore the relative evolution was not as substantial over the same period of time.

Stress relaxation is one of several manifestations of viscoplasticity. The mechanisms that gave rise to stress relaxation were also assumed to give rise to strain rate sensitivity and creep behavior. A comparison between the apparent activation volumes extracted from relaxation tests strain rate jump experiments, independently of the loading case yielded always results in the order of  $\sim 10b^3$ , noting that a change of activation volume from  $\sim 5$  to  $20b^3$  was not generally interpreted as a substantial change in deformation mechanism. Thus activation volume provided a scalar metric that could be used to interpret the rate-limiting deformation mechanisms which were in accord to literature results for nanocrystalline nickel reported from other groups using both bulk and nanoindentation strain rate jump tests. Values in the vicinity of  $\sim 10b^3$  could be interpreted that the rate controlling step was the generation of dislocations from grain boundaries, rather than dislocation glide past obstacles. However, grain boundary-mediated dislocation nucleation may be an overly simplistic interpretation. For example, as previously observed with strain rate jump tests,

post deformation microstructures of micropillars showed both, evidence of dislocation slip steps and clear grain boundary ledges associated with grain boundary sliding. As strain rate jump tests, independently of the loading case, also yielded similar activation volumes it could be concluded that activation volumes alone may not be sufficient to rule out other forms of grain boundary mediated deformation.

### **Model system Palladium-Gold**

Pd<sub>90</sub>Au<sub>10</sub> was chosen as a nanocrystalline binary model system. The material was inertgas condensated which provided the advantage of extremely high purity and random texture. Unlike nanocrystalline electrodeposits, it exhibited an extremely small nominal crystallite size of only 12nm which was getting close to the interface between nanocrystalline and amorphous, as well as a narrow, log-normal grain size distribution. The absence of individual large grains was assumed to prevail the site specific activation of (dislocation based) deformation mechanisms which may be superimposed to the entire ensemble of active mechanisms. Because of these features inertgas condensated Pd<sub>90</sub>Au<sub>10</sub> was hoped to enable an enhanced and more clear observability of nanocrystalline behavior and assist to develop a better understanding of the deformation behavior of nanocrystalline metals.

The strain rate sensitivity and activation volume were extracted from strain rate jump and repeated load relaxation tests at various temperatures, which enabled the activation energy  $\Delta G$  to be determined. Post-compression imaging of the micropillars by means of SEM and TEM showed no evidence of stress-induced grain coarsening or slip bands. From the strain rate sensitivity analysis, it is unlikely that either grain boundary sliding ( $m \geq 0.3$ ) or Coble creep ( $m \geq 1.0$ ) are the dominant rate-limiting mechanisms. The obtained effective activation volumes from stress relaxation tests up to 125°C were on the order of  $\sim 4b^3$ , which is consistent with intragranular as well as shear transformation zone (STZ)-mediated plasticity which is usually an accepted mechanisms for the plastic deformation of metallic glasses. The values were fairly consistent over the entire test temperature and plastic strain range, suggesting that the overall relaxation mechanism remains the same. Further, analysis of the strain rate jump tests revealed a temperature dependent activation volume ranging from  $11b^3$  at room temperature to  $5b^3$  at 125°C, which reflects the temperature-dependent interplay of different externally driven deformation mechanisms.

An apparent activation energy value of  $\Delta G = 0.77eV$  has been extracted from strain rate jump tests. This value as a standalone cannot be attributed to a spe-

cific dominant deformation mechanism. Comparison to available literature data as well as to the other results from this study do not suggest diffusive mechanisms to be rate controlling. A range of Helmholtz activation free energies  $\Delta F$  of  $1.28 < \Delta F < 2.15 eV$  can be determined, where lower values of  $\Delta F$  correspond to higher temperatures. For metallic glasses, we estimated STZ sizes of  $34 < \Omega_{STZ} < 76$  atoms. Both, the activation free energies and the STZ sizes for nanocrystalline Pd<sub>90</sub>Au<sub>10</sub> are slightly larger than the values found for Al-rich metallic glasses but still similar in a congruent manner. However, a direct comparison of  $\Delta F$  for different material systems should be regarded with caution, especially since additional plasticity mechanisms are involved in the case of nanocrystalline material.

The presented combination - a novel, highly accurate dynamic test method with a highly pure, homogeneous nanocrystalline *fcc*-metal - demonstrated the techniques potential for accurately probing and simultaneously observing mechanical behavior at the lower boundary of crystallinity. Compared to nanocrystalline electrodeposited nickel, the results obtained from the presented model system did indeed allow for more clear observations. Transients were sharper and more pronounced with respect to temperature and strain rate. The extracted SRS-values were generally larger, which indicated a stronger rate dependence of the smaller, very homogeneous nanostructure. Average activation volumes, although still in a regime valid for dislocation mediated plasticity, were smaller than in nanocrystalline nickel and indicated a decreasing trend. The obtained post compression surface images did not show any apparent traces of slip or dislocation mediated plasticity. The results obtained for the presented model material fostered the indications of a plastic deformation behavior which was strongly mediated by mechanisms originating at the interfaces between grains.

### 8.3. Nanocrystalline metals for applications in Swiss watches

The lack of detailed understanding of basic mechanical properties (Young's modulus, elastic limit, creep, relaxation, fracture toughness etc.) has been identified as a limiting factor for the implementation of new watch manufacturing techniques (e.g. LiGA). There are two reasons for this: mechanical properties of nanocrystalline metals deviate from those of polycrystalline materials and the lack of suitable standardized small scale test techniques for measuring their properties. Despite their high hardness and strength, current LiGA materials do not fulfill the all the required

mechanical properties for watch applications, as they are known to exhibit low resistance against time dependent plasticity and behave in an anisotropic manner.

In a first step, the mechanical properties of commercially available nanocrystalline nickel, which is the current industrial benchmark, were assessed by means of the previously introduced small scale techniques: micro tensile- and micropillar compression tests. With respect to applications in mechanical watches, the focus was put on Young's modulus, elastic limit and time-dependent plasticity (creep and load relaxation) as these properties were identified to have the most significant influence on the performance of watch components. In particular electrodeposited material often possess a preferred crystallographic orientation into the direction of film growth which leads to a pronounced directional dependence of Young's modulus which, in case of nickel, was calculated to vary between 136 and 303GPa as demonstrated in Figure 3.3. The industrial reference nickel investigated in this thesis with its pronounced  $\langle 111 \rangle$ -texture provides an out-of-plane modulus of approximately 230GPa. However, due to manufacturing restrictions, the main loading direction of a watch part is always in-plane as illustrated in Figure 7.2 where the Young's modulus was quantified to approximately 170GPa. The difference between the values is  $\sim 25\%$  and as such needs to be taken into account in the design process of watch parts.

The second, and probably most important, mechanical property in the discussed context is time dependent-plasticity. All nanocrystalline metals show this feature which manifests in the loss of stored energy (load relaxation) or permanent plastic deformation (creep) over the entire temperature span watches are commonly exposed to. A marked difference between the two mechanisms is their timescale. Load relaxation occurs instantaneously after a stress has been applied and results mostly in a logarithmic stress decay due to quasi-elastic recovery. Whereas, creep is usually monitored under a constant stress condition over hours or years. Several series of tests in uniaxial tension and compression were conducted on nanocrystalline nickel in order to quantify the amount of relaxation at different loads below and above the materials yield stress. Figure 5.21 shows the materials behavior during a repeated micropillar compression test at various stress levels. Regardless of any quantification of relaxation, this Figure demonstrates instructively how pronounced this feature is in nanocrystalline nickel, and its evolution with increasing stress level. Extrapolating the results for the low stress regime allows for a simple component lifetime prediction since i.e. springs are often relied upon to exert a constant restoring force while held in a flexed position for sustained periods of time and hence will lose their restoring force over time. When loaded below the yield point, the restoring force will decay by  $\sim 3 - 5\%$  even within a few minutes, and further decay  $\sim 9\%$  within a week.

Although this mechanism usually does not lead to catastrophic failure of the component it severely affects the performance of a watch as the stored energy is dissipated and no longer available to empower the movement. Nevertheless, while measuring even small changes in load as required for the assessment of relaxation behavior, is comparably easy, precisely measuring small dimensional changes, as required for the assessment of creep, in watch components is rather tricky. Creep rates of nanocrystalline nickel components are often in the range of  $\dot{\epsilon}_c = 10^{-6} s^{-1}$  to  $10^{-10} s^{-1}$ . For a  $5mm$  gauge length specimen, this translates into total dimensional change of  $18\mu m$  to only  $1.8nm$  per hour. A preliminary approach for measuring creep on watch-part scale was shown in Figure 7.4. The image illustrates the enormous weight a nanocrystalline nickel microcomponent is capable to hold in comparison to its small size before it fails catastrophically. The creep rates achieved in these measurements were in the order of  $\dot{\epsilon}_{creep} = 10^{-9} s^{-1}$ , which was in decent agreement with available literature values for primary creep of nanocrystalline nickel with comparable grain sizes. These preliminary results were utilized for an estimate of how much deformation watchparts will see with passage of time as depicted in Figure 7.5. According to these predictions, a nanocrystalline nickel watch part facing the applied loads of this test would fail within a period of  $> 1year$  which is not sufficient in the context of required part lifetimes in a watch. However, with respect to these measurements, two things should be noted: First of all, even after 36 hours no steady state was established, which is probably due to microstructural evolution during the experiment. As it is indicated in Figure 7.4, where the slope of the curves decrease after approximately 15 hours, the secondary creep strain rates are usually much lower than those in the primary regime which would lead to slower deformation after a certain test duration and thus a much longer component lifetime. Secondly, the stresses in this very basic test were well above the materials yield stress which was a requirement to be able to resolve the small strains but actual watch components are usually exposed to much lower stresses which would result in smaller creep strain rates.

Further, a case study was presented where numerous commercially available watch-making materials were tested at specimen sizes comparable to actual watch parts. Specimen were manufactured from sheet metals by electrode discharge machining or electrodeposition into LiGA-molds. For the miniaturized uniaxial tensile test, dog-bone shaped specimens were utilized. The results are depicted in the stress-strain curves in Figure 7.6 and quantified in Table 7.1. Although uniaxial tensile results yield relevant engineering measures, a more common loading case for watch components is bending, as many of them are machined in the shape of cantilevers with one fixed and one free end and need to fulfill a spring function. Hence, a second

series of tests was conducted under four point bending. The results are given in Table 7.2. While the mechanical properties assessed in uniaxial tension are in good agreement with the mechanical properties given by the supplier, the results obtained from bend tests deviate considerably in case of the nanocrystalline nickel, which can be addressed to the previously mentioned influence of growth texture on Young's modulus.

Finally, an approach to improve the time-dependent plastic properties of nanocrystalline nickel by developing an electrodepositable nickel-based alloy with a sufficiently high content of tungsten was presented. Refractory metals like tungsten provide decent strength, thermal stability and are known to decrease diffusive processes along grain boundaries. At the same time tungsten is known to be a grain refiner which is beneficial for the materials strength. Microstructural investigations showed that the alloys structure changes as a function of deposition parameters and tungsten content. Low tungsten contents up to  $4at. - \%$  exhibited a twinned microstructure, whereas a fully nanocrystalline structure was obtained when the tungsten concentration exceeded this concentration. Over the whole range of compositions, the materials' overall texture did not change significantly, despite the addition of tungsten. As shown in Figure 7.1, the achieved tensile strength of Ni with  $3at. - \%$  W is, although the microstructure is twinned and not yet nanocrystalline, is already comparable to commercially produced nanocrystalline nickel and maraging steel. Further, Figure 7.3(a) shows the stress relaxation properties of nanocrystalline NiW with the highest achieved tungsten content. These improved approximately 70% in comparison to nanocrystalline nickel. This also corresponds well to the results of the thermal treatments depicted in Figure 7.11, which showed significantly less grain growth in nanocrystalline NiW at temperatures almost twice as high as the stability limit of pure nanocrystalline nickel. This yields promising opportunities for future studies. First of all the deposition process needs to be optimized for LiGA-molds. Afterward the characterization techniques proposed and developed in the framework of this thesis can be utilized for a thorough mechanical characterization of the deposits. Also the influence of twinned structures on the mechanical behavior and apparent deformation mechanisms is considered to be of scientific interest, as twin boundaries are capable of hindering dislocation motion similar to grain boundaries but without opening diffusive pathways.



## 8.4. Outlook

The high temperature capability of the Alemnis in situ indentation system opens the door to an enhanced and much deeper understanding of the complex interplay of time, temperature and structure on the mechanical properties of nanocrystalline materials. In combination with the continuous specimen observability and the presented variety of experimental protocols, this technique is extremely powerful and can assist in understanding deformation mechanisms in nanostructured materials. Nevertheless, in case of thermally activated deformation mechanisms, it can be useful to look into the opposite direction. Decreasing the test temperature in order to see where thermally activated mechanisms cease may be helpful for the deconvolution of the ensemble of active deformation mechanisms active at ambient and elevated temperatures. Hence, a future task is the development of a cryogenic setup which, similar to the existing high temperature setup, allows for precise temperature calibration and can be used in the protected environment of an electron microscope. With respect to the present capabilities of the Alemnis in situ indenter, a refined experimental protocol for the assessment of micropillar creep properties at ambient- and elevated temperatures needs to be established, which may yield useful results for the understanding of time-dependent plasticity in nanocrystalline materials on an intermediate timescale. An experimental requirement for creep measurements may be an increase in micropillar size as longer specimens allow for an enhanced displacement/strain resolution, in particular at low stresses. Looking at smaller pillars with an average height of up to  $\sim 2\mu\text{m}$ , another interesting development currently on-going at Empa is high-strain-rate testing. Such „ballistic“ tests, where strain rates up to  $\dot{\epsilon} = 10^6\text{s}^{-1}$  can be realized, may help to extrapolate strain rate sensitivity measurements and eventually expose deformation mechanisms with very small time constants.

From a specimen perspective, one bottleneck for micropillar compression testing is clearly the micropillar manufacturing by means of focused ion beam milling which is very time consuming. For small series of test specimens or intermediate checks of properties in a development process, this method is still applicable. However, for more elaborate studies on electrodeposited materials or quality control in industrialized processes, it may be beneficial to utilize the LiGA-process for directly depositing films in the shape of compression pillars. In a single deposition run, thousands of specimen could be produced. Ideally, the shape of electrodeposited pillars from a contour, surface quality and aspect ratio perspective would be directly suitable for testing. Nevertheless, if ideal pillar shapes cannot be achieved, it would be still beneficial to have large arrays with pre-shaped pillars that could be refined by means of

FIB in successive steps. Also, techniques like laser ablation or the recently available plasma-FIB are of interest in this context.

The presented development of NiW alloys is still preliminary and has a lot of potential for future work. The materials' nano structural features still need to be explored before up-scaling of the deposition process to suit it for LiGA-applications and, in the long run, introduce the process into an industrial production lines. The demonstrated micropillar techniques can be applied to conduct an in-depth study of the materials' thermal and thermo-mechanical stability as a function of tungsten content. What has also not been studied to a deeper extent yet is the influence of twinned structures on the mechanical properties. Most studies on this topic are dealing with room-temperature experiments on nanotwinned copper. As nanotwinned NiW may provide both, enhanced thermal stability and a less pronounced time-dependent plasticity, this may be another promising material/structure for watch applications in near future.

---

## A. Bibliography

- [1] COTTRELL, A.H.: *Theory of dislocations*. Progress in Metal Physics, 4:205–264, 1953.
- [2] KUMAR, K., H. VAN SWYGENHOVEN and S. SURESH: *Mechanical behavior of nanocrystalline metals and alloys 11 The Golden Jubilee Issue: Selected topics in Materials Science and Engineering: Past, Present and Future*, edited by S. Suresh. Acta Materialia, 51(19):5743–5774, November 2003.
- [3] ZHOU, Y., U. ERB and K.T. AUST: *The role of interface volume fractions in the nanocrystalline to amorphous transition in fully dense materials*. Philosophical Magazine, 87(36):5749–5761, 2007.
- [4] SANDERS, P.G., J.A. EASTMAN and J.R. WEERTMAN: *Elastic and tensile behavior of nanocrystalline copper and palladium*. Acta Materialia, 45(10):4019–4025, oct 1997.
- [5] CAROLINA, NORTH, T Y TSUI and G M PHARR: *On the elastic moduli of nanocrystalline Fe, Cu, Ni, and Cu-Ni alloys prepared by mechanical milling/alloying*. Journal of Materials Research, 10:2892–2896, 1995.
- [6] HEMKER, K.J and H LAST: *Microsample tensile testing of LIGA nickel for MEMS applications*. Materials Science and Engineering: A, 319-321:882–886, December 2001.
- [7] MEYERS, M.A., A. MISHRA and D.J. BENSON: *Mechanical properties of nanocrystalline materials*. Progress in Materials Science, 51(4):427–556, May 2006.
- [8] GIANOLA, D.S., S. VAN PETEGEM, M. LEGROS, S. BRANDSTETTER, H. VAN SWYGENHOVEN and K.J. HEMKER: *Stress-assisted discontinuous grain growth and its effect on the deformation behavior of nanocrystalline aluminum thin films*. Acta Materialia, 54(8):2253–2263, 2006.

- [9] ARGON, A.S.: *Plastic deformation in metallic glasses*. Acta Metallurgica, 27(1):47–58, 1979.
- [10] WHEELER, J.M. and J. MICHLER: *Elevated temperature, nano-mechanical testing in situ in the scanning electron microscope*. Review of Scientific Instruments, 84(4):045103, 2013.
- [11] WHEELER, J.M., P. BRODARD and J. MICHLER: *Elevated temperature, in situ indentation with calibrated contact temperatures*. Philosophical Magazine, 92(25-27):3128–3141, sep 2012.
- [12] MAIER, V., K. DURST and J. MÜLLER: *Nanoindentation strain-rate jump tests for determining the local strain-rate sensitivity in nanocrystalline Ni and ultrafine-grained Al*. Journal of Materials Research, 28:1421–1430, 2011.
- [13] ARGON, A.S.: *Strengthening mechanisms in crystal plasticity*. Oxford University Press Oxford, 2008.
- [14] CAILLARD, D. and J.L. MARTIN: *Thermally Activated Mechanisms in Crystal Plasticity*. Pergamon Materials Series, 8:3–433, 2003.
- [15] EVANS, A.G. and R.D. RAWLINGS: *The Thermally Activated Deformation of Crystalline Materials*. Physica Status Solidi (B), 34(1):9–31, 1969.
- [16] FRANK, F.C. and W.T. READ: *Multiplication Processes for Slow Moving Dislocations*. Phys. Rev., 79:722–723, Aug 1950.
- [17] SCHUH, C.A., T.C. HUFNAGEL and U. RAMAMURTY: *Mechanical behavior of amorphous alloys*. Acta Materialia, 55:4067–4109, 2007.
- [18] SUTTON, A.P. and R.W. BALLUFFI: *Interfaces in Crystalline Materials*. Oxford Classic Texts in the physical Sciences, 2006.
- [19] RÖSLER, J., H. HARDERS and M. BÄKER: *Mechanisches Verhalten der Werkstoffe*. Springer, 2003.
- [20] HULL, D. and D. J. BACON: *Introduction to dislocations*, volume 257. Pergamon Press Oxford, 1984.
- [21] BRENNER, S.S.: *Tensile strength of whiskers*. Journal of Applied Physics, 27(12):1484–1491, 1956.

- [22] OROWAN, E.: *Zur Kristallplastizität. I.* Zeitschrift für Physik, 89(9-10):605–613, 1934.
- [23] OROWAN, E.: *Zur Kristallplastizität. II.* Zeitschrift für Physik, 89(9-10):614–633, 1934.
- [24] OROWAN, E.: *Zur Kristallplastizität. III.* Zeitschrift für Physik, 89(9-10):634–659, 1934.
- [25] TAYLOR, G. I.: *The Mechanism of Plastic Deformation of Crystals. Part I. Theoretical.* Proceedings of the Royal Society of London A: Mathematical, Physical and Engineering Sciences, 145(855):362–387, 1934.
- [26] TAYLOR, G. I.: *The Mechanism of Plastic Deformation of Crystals. Part II. Comparison with Observations.* Proceedings of the Royal Society of London A: Mathematical, Physical and Engineering Sciences, 145(855):388–404, 1934.
- [27] POLANYI, M.: *Über eine Art Gitterstörung, die einen Kristall plastisch machen könnte.* Zeitschrift für Physik, 89(9-10):660–664, 1934.
- [28] HIRSCH, P.B., R.W. HORNE and M.J. WHELAN: *Direct observations of the arrangement and motion of dislocations in Aluminum.* Philos. Mag., 1:677, 1956.
- [29] KOCKS, W.F.: *Thermodynamics and kinetics of slip.* Progr. Mater. Sci., 19:291, 1975.
- [30] HAASEN, P.: *Physikalische metallkunde.* Springer-Verlag, 2013.
- [31] FRANK, F.C.: *On the Equations of Motion of Crystal Dislocations.* Proceedings of the Physical Society Section A, 62(2):131, 1949.
- [32] LU, L., Y. SHEN, X. CHEN, L. QIAN and K. LU: *Ultrahigh strength and high electrical conductivity in copper.* Science (New York, N.Y.), 304(5669):422–6, apr 2004.
- [33] LU, L., X. CHEN, X. HUANG and K. LU: *Revealing the Maximum Strength in Nanotwinned Copper.* Science (New York, N.Y.), 323(January):2007–2010, 2009.
- [34] ARZT, E.: *Size effects in materials due to microstructural and dimensional constraints: a comparative review.* Acta Materialia, 46(16):5611–5626, October 1998.

- [35] KRAFT, O. and C. A. VOLKERT: *Mechanical Testing of Thin Films and Small Structures*. Advanced Engineering Materials, 3(3):99–110, March 2001.
- [36] GREER, JULIA R. and JEFF TH.M. DE HOSSON: *Plasticity in small-sized metallic systems: Intrinsic versus extrinsic size effect*. Progress in Materials Science, 56(6):654–724, August 2011.
- [37] HALL, E.O.: *The Deformation and Ageing of Mild Steel: III Discussion of Results*. Proceedings of the Physical Society. Section B, 64:747, 1951.
- [38] PETCH, N.J.: *The cleavage strength of polycrystals*. Journal of iron and steel inst., 1953.
- [39] LI, J.C.M.: *Trans. TMS-AIME*. In 239, 1963.
- [40] WANG, N., Z. WANG, K.T. AUST and U. ERB: *Effect of grain size on mechanical properties of nanocrystalline materials*. Acta metall. mater., 43(2):519–528, 1995.
- [41] KOCH, C.C. and J. NARAYAN: *The inverse HP-effect - Fact or Artifact?* Mat Res Soc, 2001.
- [42] CHOKSHI, A.H., A. ROSEN, J. KARCH and H. GLEITER: *On the validity of the hall-petch relationship in nanocrystalline materials*. Scripta Metallurgica, 23(10):1679–1683, 1989.
- [43] EL-SHERIK, A.M., U. ERB, G. PALUMBO and K.T. AUST: *Deviations from hall-petch behaviour in as-prepared nanocrystalline nickel*. Scripta Metallurgica et Materialia, 27(9):1185–1188, 1992.
- [44] WEISSMUELLER, J. and J. MARKMANN: *Deforming Nanocrystalline Metals: New Insights, New Puzzles*. Advanced Engineering Materials, 7(4):202–207, April 2005.
- [45] OVIDKO, I.A. and A.G. SHEINERMAN: *Enhanced ductility of nanomaterials through optimization of grain boundary sliding and diffusion processes*. Acta Materialia, 57(7):2217–2228, April 2009.
- [46] VAN SWYGENHOVEN, H.: *Footprints of plastic deformation in nanocrystalline metals*. Materials Science and Engineering: A, 483-484(October 2006):33–39, June 2008.

- [47] SAADA, G.: *Hall-Petch revisited*. Materials Science and Engineering: A, 400-401(September 2004):146–149, July 2005.
- [48] CARLTON, C.E. and P.J. FERREIRA: *What is behind the inverse Hall-Petch effect in nanocrystalline materials?* Acta Materialia, 55(11):3749–3756, June 2007.
- [49] GUTKIN, M.YU., I.A. OVIDKO and N.V. SKIBA: *Crossover from grain boundary sliding to rotational deformation in nanocrystalline materials*. Acta Materialia, 51(14):4059–4071, August 2003.
- [50] GODON, A., J. CREUS, S. COHENDOZ, E. CONFORTO, X. FEAUGAS, P. GI-RAULT and C. SAVALL: *Effects of grain orientation on the Hall-Petch relationship in electrodeposited nickel with nanocrystalline grains*. Scripta Materialia, 62(6):403–406, March 2010.
- [51] RAJAGOPALAN, J., J.H. HAN and M.T.A. SAIF: *On plastic strain recovery in freestanding nanocrystalline metal thin films*. Scripta Materialia, 59(9):921–926, November 2008.
- [52] SAADA, G.: *Modelisation of plastic deformation of nanocrystalline solids-IA-166*. Materials Science and Engineering: A, 483-484:506–508, June 2008.
- [53] LU, K. and N. HANSEN: *Structural refinement and deformation mechanisms in nanostructured metals*. Scripta Materialia, 60(12):1033–1038, June 2009.
- [54] GU, P., B.K. KAD and M. DAO: *A modified model for deformation via partial dislocations and stacking faults at the nanoscale*. Scripta Materialia, 62(6):361–364, March 2010.
- [55] PADMANABHAN, K.A., G.P. DINDA, H. HAHN and H. GLEITER: *Inverse Hall-Petch effect and grain boundary sliding controlled flow in nanocrystalline materials*. Materials Science and Engineering: A, 452-453:462–468, April 2007.
- [56] VANDERMEER, R.A. and N. HANSEN: *Recovery kinetics of nanostructured aluminum: Model and experiment*. Acta Materialia, 56(19):5719–5727, November 2008.
- [57] BOUAZIZ, O., Y. ESTRIN, Y. BRECHET and J.D. EMBURY: *Critical grain size for dislocation storage and consequences for strain hardening of nanocrystalline materials*. Scripta Materialia, 63(5):477–479, September 2010.

- [58] SCHIØTZ, J. and K.W. JACOBSEN: *A maximum in the strength of nanocrystalline copper*. Science, 301(5638):1357–1359, 2003.
- [59] VAN SWYGENHOVEN, H. and P. M. DERLET: *Grain-boundary sliding in nanocrystalline fcc metals*. Physical Review B, 64(22):224105, nov 2001.
- [60] YAMAKOV, V., D. WOLF, S.R. PHILLPOT, A.K. MUKHERJEE and H. GLEITER: *Dislocation processes in the deformation of nanocrystalline aluminium by molecular-dynamics simulation*. Nature materials, 1(1):45–8, 2002.
- [61] BUDROVIC, Z., H. VAN SWYGENHOVEN, P. M. DERLET, S. VAN PETEGEM and B. SCHMITT: *Plastic deformation with reversible peak broadening in nanocrystalline nickel*. Science, 304(5668):273–276, 2004.
- [62] CHEN, M. AND MA, E., K.J. HEMKER, H. SHENG, Y. WANG and X. CHENG: *Deformation twinning in nanocrystalline aluminum*. Science, 300(5623):1275–1277, 2003.
- [63] LEGROS, M., B.R. ELLIOTT, M.N. RITTNER, J.R. WEERTMAN and K.J. HEMKER: *Microsample tensile testing of nanocrystalline metals*. Philosophical magazine A, 80(4):1017–1026, 2000.
- [64] ASARO, R.J. and S. SURESH: *Mechanistic models for the activation volume and rate sensitivity in metals with nanocrystalline grains and nano-scale twins*. Acta Materialia, 53(12):3369–3382, July 2005.
- [65] WOLF, D. ET.AL.: *Materials Interfaces: Atomic Level Structure and Properties*. John Wiley, New York, 1992.
- [66] WOLF, D.: *Correlation between the energy and structure of grain boundaries in b.c.c. metals I. Symmetrical boundaries on the (110) and (100) planes*. Philosophical Magazine Part B, 59(6):667–680, 1989.
- [67] LIFSHITZ, L.M.: *Structure of the Energy Spectrum of Impurity Bands in Disordered Solid Solutions*. Soviet Phys. JETP, 17(4):909, 1963.
- [68] RACHINGER, W. A.: *Relative Grain Translations in the Plastic Flow of Aluminum*. J. Inst. Metals, 81:33–41, 1952.
- [69] CAHN, JOHN W, YURI MISHIN and AKIRA SUZUKI: *Coupling grain boundary motion to shear deformation*. Acta materialia, 54(19):4953–4975, 2006.



- 
- [70] BALL, A. and M.M. HUTCHINSON: *Superplastic behaviour of rapidly solidified Al-5Mg-1.2 Cr alloy*. Journal of Materials Science, 3:1, 1969.
- [71] MOHAMED, F.A. and T.G. LANGDON: *Creep behaviour in the superplastic Pb-62% Sn eutectic*. Philosophical Magazine, 32(4):697–709, 1975.
- [72] MOHAMED, F.A. and T.G. LANGDON: *Creep at low stress levels in the superplastic Zn-22% Al eutectoid*. Acta Metallurgica, 23(1):117–124, 1975.
- [73] SCHIØTZ, J., F.D. DI TOLLA and K.W. JACOBSEN: *Softening of nanocrystalline metals at very small grain sizes*. Nature, 391(6667):561–563, 1998.
- [74] VAN SWYGENHOVEN, H. and A. CARO: *Plastic behavior of nanophase Ni: A molecular dynamics computer simulation*. Applied Physics Letters, 71(12):1652–1654, 1997.
- [75] VAN SWYGENHOVEN, H., M. SPACZER, A. CARO and D. FARKAS: *Competing plastic deformation mechanisms in nanophase metals*. Physical Review B, 60(1):22, 1999.
- [76] MA, E.: *Materials science. Watching the nanograins roll*. Science (New York, N.Y.), 305(5684):623–4, 2004.
- [77] SHAN, Z., E.A. STACH, J.M.K. WIEZOREK, J.A. KNAPP, D.M. FOLLSTAEDT and S.X. MAO: *Grain boundary-mediated plasticity in nanocrystalline nickel*. Science (New York, N.Y.), 305(5684):654–7, jul 2004.
- [78] RÖSNER, H., J. MARKMANN and J. WEISSMÜLLER: *Deformation twinning in nanocrystalline Pd*. Philosophical magazine letters, 84(5):321–334, 2004.
- [79] BAEHR, H.D. and S. KABELAC: *Thermodynamik: Grundlagen und technische Anwendungen*. Springer-Verlag, 2012.
- [80] JIN, M., A.M. MINOR and J.W. MORRIS JR.: *Strain-induced coarsening in nano-grained films*. Thin Solid Films, 515(6):3202 – 3207, 2007. {TMS} 2005 - Mechanical Behaviour of Thin Films and Small Structures TMS 2005.
- [81] ZHANG, K., J. R. WEERTMAN and J. A. EASTMAN: *The influence of time, temperature, and grain size on indentation creep in high-purity nanocrystalline and ultrafine grain copper*. Applied Physics Letters, 85(22):5197–5199, 2004.
- [82] SCHIØTZ, J.: *Strain-induced coarsening in nanocrystalline metals under cyclic deformation*. Materials Science and Engineering: A, 375 - 377:975 – 979, 2004.

- [83] IVANISENKO, YU, L. KURMANAEVA, J. WEISSMUELLER, K. YANG, J. MARKMANN, H. RÖSNER, T. SCHERER and H.-J. FECHT: *Deformation mechanisms in nanocrystalline palladium at large strains*. Acta Materialia, 57(11):3391–3401, 2009.
- [84] WEI, Q., D. JIA, K.T. RAMESH and E. MA: *Evolution and microstructure of shear bands in nanostructured Fe*. Applied physics letters, 81(7):1240–1242, 2002.
- [85] SABIROV, I., Y. ESTRIN, M.R. BARNETT, I. TIMOKHINA and P.D. HODGSON: *Tensile deformation of an ultrafine-grained aluminium alloy: Micro shear banding and grain boundary sliding*. Acta Materialia, 56(10):2223–2230, 2008.
- [86] IVANISENKO, Y., W. SKROTZKI, R. CHULIST, T. LIPPMANN and L. KURMANAEVA: *Texture development in a nanocrystalline Pd-Au alloy studied by synchrotron radiation*. Scripta Materialia, 66(3):131–134, 2012.
- [87] IVANISENKO, Y., T. WERZ, A. MINKOW, J. LOHMILLER, P.A. GRUBER, A. KOBLER, L. KURMANAEVA and H.-J. FECHT: *Observation of shear band formation in nanocrystalline Pd-Au alloy during in situ SEM compression testing*. Journal of Materials Science, 48(19):6841–6847, 2013.
- [88] ARGON, A.S. and L.T.O. SHI: *Development of visco-plastic deformation in metallic glasses*. Acta Metallurgica, 31:499–507, 1983.
- [89] TREXLER, M.M. and N.N. THADHANI: *Mechanical properties of bulk metallic glasses*. Progress in Materials Science, 55(8):759–839, 2010.
- [90] GREWER, M., J. MARKMANN, R. KAROS, W. ARNOLD and R. BIRNINGER: *Shear softening of grain boundaries in nanocrystalline Pd*. Acta Materialia, 59(4):1523–1529, 2011.
- [91] PAN, D. and A. INOUE: *Experimental characterization of shear transformation zones for plastic flow of bulk metallic glasses*. Proceedings of the National Academy of Sciences of the United States of America, 105:14769–14772, 2008.
- [92] GREWER, M.: *Plastische Verformungsprozesse in nanokristallinen Palladium-Gold-Legierungen: Dehnratenabhängige mechanische Prüfung und in-situ Diffraktion an Scherkompressionsproben*. PhD thesis, Naturwissenschaftlich-Technischen Fakultät II - Physik und Mechatronik - der Universität des Saarlandes, 2013.

- 
- [93] GREWER, M. and R. BIRRINGER: *Shear shuffling governs plastic flow in nanocrystalline metals: An analysis of thermal activation parameters*. Physical Review B - Condensed Matter and Materials Physics, 89(18), 2014.
- [94] WEHRS, J., G. MOHANTY, G. GUILLONNEAU, A. TAYLOR, X. MAEDER, D. FREY, L. PHILIPPE, S. MISCHLER, J.M. WHEELER and J. MICHLER: *Comparison of In Situ Micromechanical Strain-Rate Sensitivity Measurement Techniques*. Jom, 67(8):1684–1693, may 2015.
- [95] LUND, A.C. and C.A. SCHUH: *Strength asymmetry in nanocrystalline metals under multiaxial loading*. Acta Materialia, 53(11):3193–3205, jun 2005.
- [96] LOHMILLER, J., M. GREWER, C. BRAUN, A. KOBLER and C. KÜBEL: *Untangling dislocation and grain boundary mediated plasticity in nanocrystalline nickel*. Acta Materialia, 65:295–307, 2014.
- [97] ZHENG, Y.D., P.Q. DAI, W.C. XU and S.R. HU: *Effect of annealing on tensile properties of electrodeposited nanocrystalline Ni with broad grain size distribution*. Materials Science and Technology, 27(12):1793–1797, 2011.
- [98] SAILE, VOLKER: *LIGA and Its Applications: Introduction*, volume 7. Wiley, 2009.
- [99] SCHUH, C.A., T.G. NIEH and H. IWASAKI: *The effect of solid solution W additions on the mechanical properties of nanocrystalline Ni*. Acta Materialia, 51(2):431–443, jan 2003.
- [100] DALLA TORRE, F., H. VAN SWYGENHOVEN and M. VICTORIA: *Nanocrystalline electrodeposited Ni: microstructure and tensile properties*. Acta Materialia, 50(15):3957–3970, sep 2002.
- [101] YIN, W.M. and S.H. WHANG: *Creep in boron-doped nanocrystalline nickel*. Scripta Materialia, 44(4):569–574, mar 2001.
- [102] YIN, W.M., S.H. WHANG and R.A. MIRSHAMS: *Effect of interstitials on tensile strength and creep in nanostructured Ni*. Acta Materialia, 53(2):383–392, jan 2005.
- [103] YIN, W.M., S.H. WHANG, R. MIRSHAMS and C.H. XIAO: *Creep behavior of nanocrystalline nickel at 290 and 373 K*. Materials Science and Engineering: A, 301(1):18–22, mar 2001.

- [104] ROTH, H.A., C.L. DAVIS and R.C. THOMSON: *Modeling solid solution strengthening in nickel alloys*. Metallurgical and Materials Transactions A, 28(6):1329–1335, 1997.
- [105] DETOR, A. and C.A. SCHUH: *Tailoring and patterning the grain size of nanocrystalline alloys*. Acta Materialia, 55(1):371–379, jan 2007.
- [106] HAKAMADA, M., Y. NAKAMOTO, H. MATSUMOTO, H. IWASAKI, Y. CHEN, H. KUSUDA and M. MABUCHI: *Relationship between hardness and grain size in electrodeposited copper films*. Materials Science and Engineering: A, 457(1):120–126, 2007.
- [107] YAMASAKI, T.: *High-strength nanocrystalline Ni-W alloys produced by electrodeposition and their embrittlement behaviors during grain growth*. Scripta Materialia, 44(8):1497–1502, 2001.
- [108] YOUNES, O. and E. GILEADI: *Electroplating of Ni/W alloys I. Ammoniacal citrate baths*. Journal of The Electrochemical Society, 149(2):C100–C111, 2002.
- [109] SLAVCHEVA, E., W. MOKWA and U. SCHNAKENBERG: *Electrodeposition and properties of NiW films for MEMS application*. Electrochimica Acta, 50(28):5573–5580, 2005.
- [110] MIZUSHIMA, I., P.T. TANG, H.N. HANSEN and M.A.J. SOMERS: *Residual stress in Ni-W electrodeposits*. Electrochimica acta, 51(27):6128–6134, 2006.
- [111] BIRINGER, R.: *Nanocrystalline materials*. Materials Science and Engineering: A, 117:33–43, sep 1989.
- [112] OKAMOTO, H. and T.B. MASSALSKI: *The Au-Pd (Gold-Palladium) system*. Bulletin of Alloy Phase Diagrams, 6(3):229–235, 1985.
- [113] GIANNUZZI, L. and F.A. STEVIE: *Review of focused ion beam milling techniques for TEM specimen preparation*. Micron, page 30:197, 1999.
- [114] LANGFORD, J.I. and A.J.C. WILSON: *Scherrer after sixty years: a survey and some new results in the determination of crystallite size*. Journal of Applied Crystallography, pages 102–113, 1978.
- [115] SCHERRER, P: *Bestimmung der Grösse und der inneren Struktur von Kolloidteilchen mittels Röntgenstrahlen*. Nachrichten von der Gesellschaft der Wissenschaften, pages 98–100, 1918.

- 
- [116] EL MEL, A., M. BUFFIRE, N. BOUTS, E. GAUTRON, P.Y. TESSIER, K. HENZLER, P. GUTTMANN, S. KONSTANTINIDIS, C. BITTENCOURT and R. SNYDERS: *Growth control, structure, chemical state, and photoresponse of CuO-CdS core-shell heterostructure nanowires*. *Nanotechnology*, 24(26):265603, 2013.
- [117] THUVANDER, M., M. ABRAHAM, A. CEREZO and G.D.W. SMITH: *Thermal stability of electrodeposited nanocrystalline nickel and iron-nickel alloys*. *Materials science and technology*, 17(8):961–970, 2001.
- [118] MOHANTY, G., J.M. WHEELER, R. RAGHAVAN, J. WEHRS, M. HASEGAWA, S. MISCHLER, L. PHILIPPE and J. MICHLER: *Elevated temperature, strain rate jump microcompression of nanocrystalline nickel*. *Philosophical Magazine*, 95(January 2015):1–18, sep 2014.
- [119] AMES, M., M. GREWER, C. BRAUN and R. BIRRINGER: *Nanocrystalline metals go ductile under shear deformation*. *Materials Science and Engineering A*, 546:248–257, 2012.
- [120] GREWER, M., C. BRAUN, M.J. DECKARM, J. LOHMILLER, P.A. GRUBER, V. HONKIMÄKI and R. BIRRINGER: *Anatomizing deformation mechanisms in nanocrystalline Pd90Au10*. arXiv:1408.5049, 2016.
- [121] UCHIC, M.D. and D.M. DIMIDUK: *A methodology to investigate size scale effects in crystalline plasticity using uniaxial compression testing*. *Materials Science and Engineering: A*, 400:268–278, 2005.
- [122] BEI, H., S. SHIM, G.M. PHARR and E.P. GEORGE: *Effects of pre-strain on the compressive stress-strain response of Mo-alloy single-crystal micropillars*. *Acta Materialia*, 56(17):4762–4770, 2008.
- [123] WHEELER, J.M., L. THILLY, A. MOREL, A.A. TAYLOR, A. MONTAGNE, R. GHISLENI and J. MICHLER: *The plasticity of indium antimonide: Insights from variable temperature, strain rate jump micro-compression testing*. *Acta Materialia*, 106:283–289, 2016.
- [124] SOLER, R., J.M. MOLINA-ALDAREGUIA, J. SEGURADO, J. LLORCA, R.I. MERINO and V.M. ORERA: *Micropillar compression of LiF [111] single crystals: Effect of size, ion irradiation and misorientation*. *International Journal of Plasticity*, 36:50–63, 2012.

- [125] HÜTSCH, J. and E.T. LILLEODDEN: *The influence of focused-ion beam preparation technique on microcompression investigations: Lathe vs. annular milling*. Scripta Materialia, 77:49–51, 2014.
- [126] RAGHAVAN, R., J.M. WHEELER, D. ESQUE-DE LOS OJOS, K. THOMAS, E. ALMANDOZ, G.G. FUENTES and J. MICHLER: *Mechanical behavior of Cu/TiN multilayers at ambient and elevated temperatures: Stress-assisted diffusion of Cu*. Materials Science and Engineering: A, 620:375–382, jan 2015.
- [127] WHEELER, J.M., R. RAGHAVAN, V. CHAWLA, M. MORSTEIN and J. MICHLER: *Deformation of Hard Coatings at Elevated Temperatures*. Surface and Coatings Technology, 254:382–387, sep 2014.
- [128] WHEELER, J.M., R. RAGHAVAN, V. CHAWLA, J. ZECHNER, I. UTKE and J. MICHLER: *Failure mechanisms in metal-metal nanolaminates at elevated temperatures: Microcompression of Cu-W multilayers*. Scripta Materialia, 98:28–31, mar 2015.
- [129] SOLER, R., J.M. WHEELER, H.-J. CHANG, J. SEGURADO, J. MICHLER, J. LLORCA and J.M. MOLINA-ALDAREGUIA: *Understanding size effects on the strength of single crystals through high-temperature micropillar compression*. Acta Materialia, 81:50–57, 2014.
- [130] KORTE, S., J.S. BARNARD, R.J. STEARN and W.J. CLEGG: *Deformation of silicon-Insights from microcompression testing at 25-500°C*. International Journal of Plasticity, 27(11):1853–1866, nov 2011.
- [131] WHEELER, J.M., C. NIEDERBERGER, C. TESSAREK, S. CHRISTIANSEN and J. MICHLER: *Extraction of plasticity parameters of GaN with high temperature, in situ micro-compression*. International Journal of Plasticity, 40:140–151, jan 2013.
- [132] WHEELER, J.M., R. RAGHAVAN, J. WEHRS, Y. ZHANG, R. ERNI and J. MICHLER: *Approaching the limits of strength-measuring the uniaxial compressive strength of diamond at small scales*. Nano Letters, 2015.
- [133] YANG, B., C. MOTZ, M. RESTER and G. DEHM: *Yield stress influenced by the ratio of wire diameter to grain size - a competition between the effects of specimen microstructure and dimension in micro-sized polycrystalline copper wires*. Philosophical Magazine, 92(25-27):3243–3256, sep 2012.

- 
- [134] YANG, Y., J.C. YE, J. LU, F.X. LIU and P.K. LIAW: *Effects of specimen geometry and base material on the mechanical behavior of focused-ion-beam-fabricated metallic-glass micropillars*. Acta Materialia, 57(5):1613–1623, 2009.
- [135] RABE, R., J.M. BREGUET, P. SCHWALLER, S. STAUSS, F.J. HAUG and J. PATSCHEIDER: *Observation of fracture and plastic deformation during indentation and scratching inside the scanning electron microscope*. Thin Solid Films, 469–470(Special Issue):206–213, 2004.
- [136] LUCAS, B.D. and T. KANADE: *An iterative image registration technique with an application to stereo vision*. IJCAI, pages 121–130, 1981.
- [137] EBERL, CH., R. THOMPSON, D. GIANOLA, W. SHARPE JR and K. HEMKER: *Digital image correlation and tracking*. MatLabCentral, Mathworks file exchange server, FileID, 12413, 2006.
- [138] WANG, Y.M., S. CHENG, Q.M. WEI, E. MA, T.G. NIEH and A. HAMZA: *Effects of annealing and impurities on tensile properties of electrodeposited nanocrystalline Ni*. Scripta Materialia, 51(11):1023–1028, nov 2004.
- [139] NATTER, H., M. SCHMELZER and R. HEMPELMANN: *Nanocrystalline nickel and nickel-copper alloys: Synthesis, characterization, and thermal stability*. Journal of Materials research, 13(05):1186–1197, 1998.
- [140] WHEELER, J.M. and J. MICHLER: *Invited Article: Indenter materials for high temperature nanoindentation*. Review of Scientific Instruments, 84(10):101301, 2013.
- [141] SAHA, R. and W.D. NIX: *Effects of the substrate on the determination of thin film mechanical properties by nanoindentation*. Acta Materialia, 50(1):23–38, 2002.
- [142] WANG, Y., A. HAMZA and E. MA: *Temperature-dependent strain rate sensitivity and activation volume of nanocrystalline Ni*. Acta Materialia, 54(10):2715–2726, jun 2006.
- [143] DALLA TORRE, F., H. VAN SWYGENHOVEN, R. SCHÄUBLIN, P. SPÄTIG and M. VICTORIA: *Mechanical behaviour of nanocrystalline electrodeposited Ni above room temperature*. Scripta materialia, 53(1):23–27, 2005.
- [144] WEI, Q., S. CHENG, K.T. RAMESH and E. MA: *Effect of nanocrystalline and ultrafine grain sizes on the strain rate sensitivity and activation volume: fcc*

- versus bcc metals*. Materials Science and Engineering: A, 381(1-2):71–79, sep 2004.
- [145] SHEN, X., J. LIAN, Z. JIANG and Q. JIANG: *High strength and high ductility of electrodeposited nanocrystalline Ni with a broad grain size distribution*. Materials Science and Engineering: A, 487(1-2):410–416, jul 2008.
- [146] FROST, H.J. and M.F. ASHBY: *Deformation-mechanism maps*. Pergamon Press, 1982.
- [147] KOTTADA, R.S. and A.H. CHOKSHI: *Low temperature compressive creep in electrodeposited nanocrystalline nickel*. Scripta materialia, 53(8):887–892, 2005.
- [148] LI, Y.J., J. MUELLER, H.W. HÖPPEL, M. GÖKEN and W. BLUM: *Deformation kinetics of nanocrystalline nickel*. Acta Materialia, 55(17):5708–5717, 2007.
- [149] SHERBY, O.D. and P.E. ARMSTRONG: *Prediction of activation energies for creep and self-diffusion from hot hardness data*. Metallurgical and Materials Transactions B, 2(12):3479–3484, 1971.
- [150] GAROFALO, F.: *Fundamentals of creep and creep-rupture in metals*. Physics Today, 19(5):100, 1966.
- [151] BARRET, C.S. and T.B. MASSALSKI: *Structure of metals*. Pergamon Press Oxford, 1980.
- [152] WHEELER, J.M., V. MAIER, K. DURST, M. GÖKEN and J. MICHLER: *Activation parameters for deformation of ultrafine-grained aluminium as determined by indentation strain rate jumps at elevated temperature*. Materials Science and Engineering: A, 585:108–113, nov 2013.
- [153] ASIF, S.A.S., K.J. WAHL and R.J. COLTON: *Nanoindentation and contact stiffness measurement using force modulation with a capacitive load-displacement transducer*. Review of Scientific Instruments, 70(5):2408–2413, 1999.
- [154] OLIVER, W.C. and G.M. PHARR: *An improved technique for determining hardness and elastic-modulus using load and displacement sensing indentation experiments*. Journal of Materials Research, 7(6):1564–1583, jun 1992.



- [155] LUCAS, B.N. and W.C. OLIVER: *Indentation power-law creep of high-purity indium*. Metallurgical and Materials Transactions A, 30(March), 1999.
- [156] DIETER, G.E. and D. BACON: *Mechanical metallurgy*. McGraw-Hill, London, 1986.
- [157] CSIKOR, F.F., C. MOTZ, D. WEYGAND, M. ZAISER and S. ZAPPERI: *Dislocation avalanches, strain bursts, and the problem of plastic forming at the micrometer scale*. Science (New York, N.Y.), 318(5848):251–254, 2007.
- [158] HART, E.W.: *Theory of the tensile test*. Acta Metallurgica, 15(February), 1967.
- [159] GOODALL, R. and T.W. CLYNE: *A critical appraisal of the extraction of creep parameters from nanoindentation data obtained at room temperature*. Acta Materialia, 54(20):5489–5499, dec 2006.
- [160] VLASSAK, J.J. and W.D. NIX: *Indentation modulus of elastically anisotropic half spaces*. Philosophical Magazine A, 1993.
- [161] LU, L., R. SCHWAIGER, Z.W. SHAN, M. DAO, K. LU and S. SURESH: *Nano-sized twins induce high rate sensitivity of flow stress in pure copper*. Acta Materialia, 53(7):2169–2179, apr 2005.
- [162] VEHOFF, H., D. LEMAIRE, K. SCHÜLER, T. WASCHKIES and B. YANG: *The effect of grain size on strain rate sensitivity and activation volume—from nano to ufg nickel*. International Journal of Materials Research, 98(4):259–268, apr 2007.
- [163] JENNINGS, A. T., J. LI and J. R. GREER: *Emergence of strain-rate sensitivity in Cu nanopillars: Transition from dislocation multiplication to dislocation nucleation*. Acta Materialia, 59(14):5627–5637, aug 2011.
- [164] WANG, N., Z. WANG, K.T. AUST and U. ERB: *Room temperature creep behavior of nanocrystalline nickel produced by an electrodeposition technique*. Materials Science and Engineering: A, 237(2):150–158, September 1997.
- [165] MOHAMED, F.A. and Y. LI: *Creep and superplasticity in nanocrystalline materials: current understanding and future prospects*. Materials Science and Engineering: A, 298(1):1–15, 2001.

- [166] CAI, B., Q.P. KONG, L. LU and K. LU: *Low temperature creep of nanocrystalline pure copper*. Materials Science and Engineering: A, 286(1):188–192, 2000.
- [167] MAY, J., H.W. HÖPPEL and M. GÖKEN: *Strain rate sensitivity of ultrafine-grained aluminium processed by severe plastic deformation*. Scripta Materialia, 53(2):189–194, 2005.
- [168] LU, ., T. ZHU, Y. SHEN, M. DAO, K. LU and S. SURESH: *Stress relaxation and the structure size-dependence of plastic deformation in nanotwinned copper*. Acta Materialia, 57(17):5165–5173, 2009.
- [169] WANG, Y.M., A.V. HAMZA and E. MA: *Activation volume and density of mobile dislocations in plastically deforming nanocrystalline Ni*. Applied Physics Letters, 86(24):241917, 2005.
- [170] COTTRELL, A.H. and R.J. STOKES: *Effects of temperature on the plastic properties of aluminium crystals*. In *Proceedings of the Royal Society of London A: Mathematical, Physical and Engineering Sciences*, volume 233, pages 17–34. The Royal Society, 1955.
- [171] JU, J.D., D. JANG, A. NWANKPA and M. ATZMON: *An atomically quantized hierarchy of shear transformation zones in a metallic glass*. Journal of Applied Physics, 2011.
- [172] GU, P., M. DAO, R.J. ASARO and S. SURESH: *A unified mechanistic model for size-dependent deformation in nanocrystalline and nanotwinned metals*. Acta Materialia, 2011.
- [173] DURST, K. and V. MAIER: *Dynamic nanoindentation testing for studying thermally activated processes from single to nanocrystalline metals*. Current Opinion in Solid State and Materials Science, 19(6):340–353, dec 2015.
- [174] BOCHNIAK, W.: *The Cottrell-Stokes law for fcc single crystals*. Acta Metallurgica Et Materialia, 41(11):3133–3140, 1993.
- [175] MOHANTY, G., J. WEHR, B. BOYCE, A. TAYLOR, M. HASEGAWA, L. PHILIPPE and J. MICHLER: *Room temperature stress relaxation in nanocrystalline Ni measured by micropillar compression and miniature tension*. J. Mater. Res., 2016.

- [176] WANG, L. and B.C. PROROK: *Characterization of the strain rate dependent behavior of nanocrystalline gold films*. Journal of Materials Research, 23(01):55–65, jan 2011.
- [177] PALUMBO, G., S.J. THORPE and K.T. AUST: *On the contribution of triple junctions to the structure and properties of nanocrystalline materials*. Scripta Metallurgica et Materiala, 24(1):1347–1350, 1990.
- [178] VO, N.Q., R.S. AVERBACK, P. BELLON and A. CARO: *Limits of hardness at the nanoscale: Molecular dynamics simulations*. Physical Review B, 78(24):241402, dec 2008.
- [179] WEISSMÜLLER, J., J. MARKMANN, M. GREWER and R. BIRRINGER: *Kinematics of polycrystal deformation by grain boundary sliding*. Acta Materialia, 59(11):4366–4377, jun 2011.
- [180] CHINH, N.Q., P. SZOMMER, Z. HORITA and T.G. LANGDON: *Experimental Evidence for Grain-Boundary Sliding in Ultrafine-Grained Aluminum Processed by Severe Plastic Deformation*. Advanced Materials, 18(1):34–39, jan 2006.
- [181] ARGON, A. S. and S. YIP: *The strongest size*. Philosophical Magazine Letters, 86(11):713–720, nov 2006.
- [182] COBLE, R.L.: *A Model for Boundary Diffusion Controlled Creep in Polycrystalline Materials*. Journal of Applied Physics, 34(6):1679, 1963.
- [183] LANGDON, T.G.: *Grain boundary sliding revisited: Developments in sliding over four decades*. J Mater Sci., 41(41):597–609, 2006.
- [184] WHEELER, J.M., R. RAGHAVAN and J. MICHLER: *Temperature invariant flow stress during microcompression of a Zr-based bulk metallic glass*. Scripta Materialia, 67(2):125–128, 2012.
- [185] HALL, P.M., J.M. MORABITO and J.M. POATE: *Diffusion mechanisms in the Pd/Au thin film system and the correlation of resistivity changes with Auger electron spectroscopy and Rutherford backscattering profiles*. Thin Solid Films, 33(1):107–134, mar 1976.
- [186] ASHBY, M.F. and R.A. VERRALL: *Diffusion-accommodated flow and superplasticity*. Acta Metallurgica, 21(2):149–163, feb 1973.

- [187] SHANG, S.L., C.L. ZACHERL, H.Z. FANG, Y. WANG, Y. DU and Z.K. LIU: *Effects of alloying element and temperature on the stacking fault energies of dilute Ni-base superalloys*. Journal of Physics: Condensed Matter, 24(50):505403, 2012.
- [188] CHAN, T., Y. CHUEH and C. LIAO: *Manipulating the crystallographic texture of nanotwinned Cu films by electrodeposition*. Crystal Growth & Design, 11(11):4970–4974, 2011.
- [189] HASEGAWA, M., M. MIESZALA, Y. ZHANG, R. ERNI, J. MICHLER and L. PHILIPPE: *Orientation-controlled nanotwinned copper prepared by electrodeposition*. Electrochimica Acta, 178:458–467, 2015.
- [190] JANG, D., X. LI, H. GAO and J.R. GREER: *Deformation mechanisms in nanotwinned metal nanopillars*. Nature nanotechnology, 7(9):594–601, 2012.
- [191] TIEARNEY, T.C. and N.J. GRANT: *Measurement of structural parameters important in creep of Ni-Mo and Ni-W solid solutions*. Metallurgical transactions A, 13(10):1827–1836, 1982.
- [192] HARRIS, G.B.: *X. Quantitative measurement of preferred orientation in rolled uranium bars*. The London, Edinburgh, and Dublin Philosophical Magazine and Journal of Science, 43(336):113–123, 1952.
- [193] MISHIMA, Y., S. OCHIAI, N. HAMAOKA, M. YODOGAWA and T. SUZUKI: *Solid Solution Hardening of Nickel-Rose of Transition Metal and B-subgroup Solutes*. Transactions of the Japan institute of metals, 27(9):656–664, 1986.
- [194] RUPERT, T.J., J.C. TRENKLE and C.A. SCHUH: *Enhanced solid solution effects on the strength of nanocrystalline alloys*. Acta Materialia, 59(4):1619–1631, feb 2011.
- [195] LOWRIE, R. and A.M. GONAS: *Dynamic elastic properties of polycrystalline tungsten, 24–1800°C*. Journal of Applied Physics, 36(7):2189–2192, 1965.
- [196] LU, L., Z.S. YOU and K. LU: *Work hardening of polycrystalline Cu with nanoscale twins*. Scripta Materialia, 66(11):837–842, June 2012.

---

# Curriculum Vitae

---

## Personal information

---

Name:	Wehrs
Given name:	Juri Aljoscha
Gender:	male
Date of birth:	20.12.1984
City of birth:	Rheinfelden (Baden)
Nationality:	Germany
E-mail:	wehrsjuri@gmail.com

---

## Education

---

09/2001 to 07/2004	Technisches Gymnasium Lörrach, Germany
10/2005 to 04/2012	Braunschweig Institute of Technology Braunschweig, Germany  Undergraduate thesis in mechanical engineering Diploma thesis in material science
from 08/2012	Doctoral Student Laboratory for Mechanics of Materials and Nanostructures, Empa Thun, Switzerland

---